11-23-2021 2:30 PM

Effects of Gamma-Radiation on the Evolution of Copper Corrosion Dynamics in Deep Geological Repository Solution Environments

Lindsay J. Grandy, *The University of Western Ontario*

Supervisor: Wren, Jungsook C., *The University of Western Ontario*
A thesis submitted in partial fulfillment of the requirements for the Doctor of Philosophy degree in Chemistry

Recommended Citation

Grandy, Lindsay J., "Effects of Gamma-Radiation on the Evolution of Copper Corrosion Dynamics in Deep Geological Repository Solution Environments" (2021). *Electronic Thesis and Dissertation Repository*. 8257.
https://ir.lib.uwo.ca/etd/8257

ABSTRACT

The Canadian plan for permanent disposal of used nuclear fuel involves a used fuel container (UFC), a carbon steel vessel with a copper coating to provide the corrosion protection. The corrosion conditions for the copper layer of the UFC are expected to involve small, stagnant water volumes, pH values between 6 and 9, and a continuous flux of γ-radiation emitted from the radionuclides trapped in the fuel matrix. While γ-radiation does not affect the copper metal directly, humid air and water will radiolytically decompose into redox-active and acidic species which will be produced at constant concentrations and can alter the corrosion behaviour of the copper coating. A fundamental understanding of the corrosion behaviour in the presence of γ-radiation is needed to predict the long-term corrosion progression of the copper layer of the UFC with confidence and assure its long-term integrity.

This work investigates the combined effects of γ-radiation and solution conditions (initial pH, cover gas composition, and solution depth) on the dynamics of copper corrosion. The results show that the elementary steps involved in the overall metal oxidation process change as corrosion progresses (i.e., multiple steady-states during corrosion process), from which four distinct corrosion stages can be identified, each with characteristic corrosion product time-dependent behaviour. This work showed that the solution conditions – including the presence of radiation – do not change the stepwise behaviour of the corrosion stage; however, the solution conditions affect the rates of the elementary reactions in each stage, thereby affecting the overall metal oxidation rate. It is changes in the rates, rather than in the nature of the elementary reactions, that influence how fast the overall corrosion dynamics evolve through the different dynamic stages.

This study has shown that the relationship between the copper dissolution and pH during copper corrosion can be correlated to the $Cu(OH)_2$ solubility equilibrium in all studied solution conditions. This key thermodynamic relationship can help simplify the long-term modeling of the corroding system. Additionally, this work has clearly shown that the system experiences feedback loops that render the linear extrapolation of corrosion rate inaccurate. The elementary steps and the thermodynamic limitations for copper concentration values identified in this study provides a simplified approach toward developing a high-fidelity corrosion model.

SUMMARY FOR LAY AUDIENCE

The Canadian plan for the permanent disposal of used nuclear fuel involves a used fuel container (UFC), a carbon steel vessel with a copper coating to provide external corrosion protection. The copper layer will be exposed to a continuous flux of γ-radiation emitted from the decay of radionuclides in the used fuel. Although the γ-radiation does not affect the metal directly, any trapped water or humid air near the UFC will decompose to produce redox-active and acidic species that can affect the corrosion of the copper coating. A fundamental understanding of the copper corrosion behaviour in the presence of γ-radiation is needed to predict the long-term corrosion progression of the copper layer of the UFC with confidence and assure its long-term integrity.

In this thesis, a copper corrosion mechanism is proposed that can explain the combined effects of solution parameters and γ-radiation on the overall corrosion rate. The effects of radiation were decoupled by performing corrosion experiments in solutions containing the important radiolysis species (i.e., H_2O_2, H^+, and NO_3^-) as well as in solutions in the presence of radiation. The solution parameters investigated were the initial pH, cover gas composition, and solution depth/volume in the presence and absence of radiation.

The results show that the solution parameters do not change the elementary reactions that determine the corrosion rate, but they may change the rates of the elementary reactions and the durations of the corrosion stages. This study has also demonstrated the importance of cupric ion solubility in determining the long-term corrosion behaviour. The work presented in this thesis will contribute to the development of a robust corrosion model that can accurately predict the extent of long-term radiolytic corrosion of the copper layer of the UFC.

Keywords:

Radiation Chemistry · Copper · Corrosion Mechanism · Nuclear Waste Disposal ·
Gamma Radiation · Water Radiolysis · Corrosion Dynamics

CO-AUTHORSHIP STATEMENT

This thesis includes published data in Chapter 6 and 8.

For all the chapters, I am the main author and Prof. J.C. Wren is co-author.

Dr. J. Joseph and G. Whitaker assisted with editing.

For all chapters, Dr. J. Joseph helped with post-test solution analysis.

ACKNOWLEDGEMENTS

I wish to express my sincere gratitude to my supervisor, Dr. Jungsook Wren, for her support and guidance throughout my studies. She created an environment within her group where students were able to explore scientific concepts without fear of ridicule.

I would also like to thank Dr. Jiju Joseph for selflessly being there for all the group members, both academically and personally. Thank you to Giles Whitaker for tirelessly editing all my writing and for showing me that just because I’m a native English speaker does not mean I can write perfectly in the English language. Thank you to Dr. Nick Payne for being a mentor throughout the last years of my graduate school journey.

I would like to thank the entire Wren group, aka my work family, for always being there for me and for providing a supportive environment where I can grow. Thank you for the countless conversations (and arguments) about corrosion and thank you for the moments away from the lab. I would not have stayed sane if it were not for my loving group members.

I would like to thank my boyfriend Jon, who provided the constant assurance that I needed (and it was a lot) to successfully complete this thesis.

Importantly, I need to thank my family – my mom, my dad, Charlotte, and Ben. They are the source of my confidence, my pride, and my joy. I would not be who I am without them.

TABLE OF CONTENTS

LIST OF TABLES

LIST OF FIGURES

LIST OF SYMBOLS

a	Chemical activity
$Cu^0_{(m)}$	Copper atom bound to the solid metal phase
$Cu^{2+}_{(sol'n)}$	Dissolved cupric ions (including all hydrolysis products)
$Cu^{II}_{(sol'n)}$	All dissolved and dispersed cupric ions
$Cu(OH)_{2(solv)}$	Fully solvated $Cu(OH)_2$ molecule
$Cu(OH)_{2(colloid)}$	Solid $Cu(OH)_2$ particles dispersed in solution
d_{sol}	Solution depth (cm)
D_R	Radiation dose rate (Gy/h)
E^0	Standard electrochemical potential (V)
E^{eq}	Equilibrium potential (V)
F	Faraday constant (s A/mol)
I_{corr}	Corrosion current (A)
k	Rate constant
Ox	Oxidant
Red	Reductant
R	Ideal gas constant
S1	Dynamic corrosion Stage 1
S2	Dynamic corrosion Stage 2
S3	Dynamic corrosion Stage 3

LIST OF ABBREVIATIONS

BCC	Base Centered Cubic
CS	Carbon Steel
DGR	Deep Geological Repository
FCC	Face Centered Cubic
FIB	Focused Ion Beam
EDX	Energy Dispersive X-ray Spectrometry
ICP-OES	Inductively Coupled Plasma Optical Emission Spectroscopy
LET	Linear Energy Transfer (keV/μm)
ORR	Oxygen Reduction Reaction
PVC	Polyvinyl Chloride
NWMO	Nuclear Waste Management Organization
RDS	Rate-Determining Step
SEM	Scanning Electron Microscopy
SKB	The Swedish Nuclear Waste Management Company
SSW	Surface Science Western
UFC	Used Fuel Container
UV-Vis	Ultraviolet and Visible

CHAPTER 1. INTRODUCTION

1.1 BACKGROUND AND MOTIVATON

Nuclear power is a low-carbon energy source that provides about 10% of global electricity production.[1,2] In Canada, nuclear power accounts for 15% of the country's and 60% of Ontario's electricity supply. However, the permanent safe disposal of used nuclear fuel must be addressed. Many options have been considered and deep geological repositories (DGRs) are generally considered the best approach for long-term waste disposal in many countries.[3,4] Canada's plan for the permanent disposal of used nuclear fuel includes a deep geological repository (DGR), approximately 500 meters underground, using a multiple-barrier system as shown in **Figure 1.1**.[5,6]

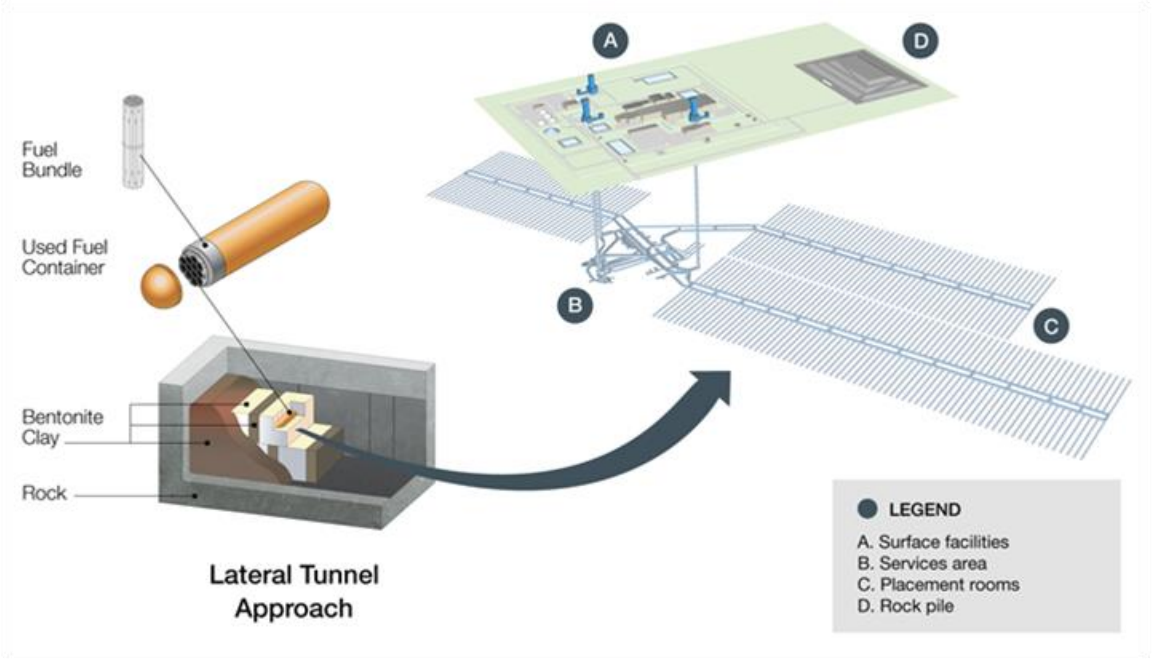

Figure 1.1 Schematic of the multi-barrier system to be used for long-term storage of used nuclear fuel.[6]

In Canada, it is the Nuclear Waste Management Organization (NWMO) that is responsible for designing and implementing the DGR. The key engineered barrier is the used fuel container (UFC). Previous UFC designs loaded the fuel into a carbon steel (CS) inner vessel with 8 – 10 cm thick walls, which was emplaced in a copper (Cu) outer shell with 2.5

cm walls (left, **Figure 1.2**). The current UFC design is optimised for Canada Deuterium Uranium (CANDU®) fuel bundles and smaller in dimensions that facilitate easier handling and emplacement in the DGR. The CS vessel wall thickness was reduced, and the outer copper shell is replaced with a 3-4 mm integrally applied copper coating.[5,7-9] The hemispherical head shape increases the mechanical strength for the container and the thinner CS and copper layers reduce cost and materials required. With thinner container walls, the radiation dose rate on the outside of the current UFC design is higher compared to previous designs.[10]

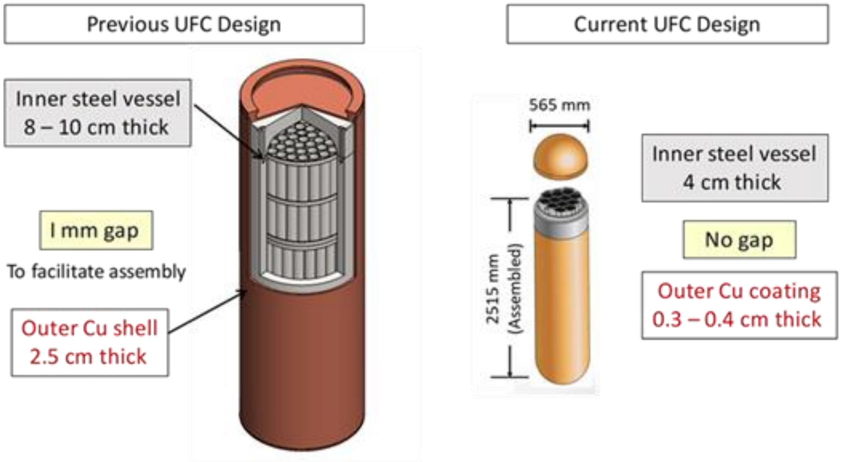

Figure 1.2 Schematics of the previous and current Canadian UFC designs.

CS was chosen for the inner vessel material due to its high strength and low susceptibility to localized corrosion.[11] Copper was selected to act as a corrosion barrier material due to its thermodynamic stability in the anoxic long-term condition anticipated in the DGR.[5,12] The corrosion conditions that the copper layer will experience are not commonly studied in corrosion research: small water volume to surface area ratios, stagnant conditions, neutral to alkaline pH solutions, and a continuous, low flux of γ-radiation. Additionally, in the first hundred years after emplacement, the UFC will experience changing environments ranging from humid air with no condensed water on the surface to humid air in equilibrium with bulk water droplets/films on the surface, which could provide the required aqueous medium for corrosion to occur.[5,11,13] It is crucial to have a good understanding of how the copper layer will behave in the unique and changing DGR conditions so that the depth of corrosion can be predicted with confidence.

Predicting the corrosion rate of copper under DGR conditions and over periods of time not easily studied experimentally is very challenging. Corrosion models must be developed based on a fundamental understanding of the rate-determining elementary reactions and the parameters they depend on (and not simply empirical observations), to be able to accurately extrapolate the corrosion rate beyond the experimental timescale. Experiments must be performed systematically, not necessarily to mimic the expected environmental conditions exactly, but to ascertain the rate-determining parameters.

Previous studies have shown that the chemical reactions and transport processes in the interfacial solution region can become increasingly important if solution species accumulate during corrosion.[14-16] Feedback loops can arise, resulting in non-linear chemical dynamics, complicating the analysis of observed behaviour. The linear extrapolation of corrosion rate in a system where feedback loops exist will not provide accurate long-term corrosion rate/depth.[14,17-19] Furthermore, the corrosion rate may not have a linear dependence on solution parameters (e.g. pH, anion concentration) as would be expected with classical linear dynamics.[16]

The outer copper coating of the UFC will be exposed to a continuous flux of γ-radiation emitted from the fission and neutron activation products trapped in the spent fuel matrix. The dose rates of α- and β-radiation at the copper surface are negligible and will not affect copper corrosion. The γ-radiation dose rate at the outside copper layer has been calculated to be 2.3 Gy/h after 10 years of emplacement, and decay slowly to a background level of 0.2 Gy/h after 100 years.[10,13] The γ-radiation interacts with humid air and water trapped next to the copper surface producing redox active species that can affect the corrosion of the copper layer. Any radiation energy absorbed directly by $Cu^0_{(m)}$ is dissipated as heat without inducing any chemical changes.[13,20-23]

The chemically reactive radiolysis products will determine the aqueous redox conditions of the water and influence the corrosion kinetics in radiation-exposed systems.[24-28] These species can affect the corrosion rate and corrosion pathways and create conditions in which feedback loops can be established or enhance existing systemic feedback loops. The net production rates of radiolytic species on the timescale of metal oxidation depend on the radiation dose rate and the concentrations of solute species, including H^+, O_2 and reactive anions (e.g., Cl^-, NO_3^-).[10,20,29,30] Thus, solution parameters and γ-radiation must be studied in conjunction to have a clear understanding of the effects of radiation.

1.2 THESIS OBJECTIVES AND METHODS

The objective of this thesis work is to explore the combined effects of γ-radiation and the solution environment on the dynamics of copper corrosion and to develop a copper corrosion mechanism that can be used for more accurate prediction of the corrosion allowance of the copper coating of the UFC in the first few hundred years after emplacement in the DGR, when the radiation level is still significant. To develop the mechanism, the rate-determining step(s) and the key elementary processes that control the overall rate must be identified. The effect of radiation and solution parameters on each key elementary process can then be determined.

In this thesis, solution parameters were varied systematically, with and without exposure to γ-radiation, and solution and surface changes were followed as a function of time. The parameters chosen were those that affect mass transport and/or solution reactions rates. The variables studied in this work include cover gas composition, initial pH, solution depth/volume and γ-radiation. The effects of key radiolysis products were decoupled through systematic studies involving both radiolytic production and chemical addition to develop a fundamental understanding of the effects of the radiolysis products.

1.3 THESIS OUTLINE

- **Chapter 1**: Background information on the project and the thesis motivation, objective, and outline are presented.
- **Chapter 2**: Materials background, literature review, and theoretical background are presented for the properties of copper and its corrosion, radiation chemistry and radiolytic corrosion, and non-linear chemical phenomena.
- **Chapter 3**: The experimental methods used in Chapters 4 – 8 are described.
- **Chapter 4**: The relationship between the dissolved copper concentration and pH is investigated in all the redox and solution conditions studied in this thesis. How this relationship evolves with time is determined. The objective of this chapter is to

determine whether a specific relationship between pH and dissolved copper can be established and what the effects of solution parameters are on the relationship.

- **Chapter 5**: The individual effects of the key radiolysis products, i.e., H_2O_2, H^+, and NO_3^-, on copper corrosion are investigated. Specifically, how these species affect copper dissolution and oxide precipitation in early corrosion times is elucidated. The results from this chapter allow for the effects of radiolysis species to be decoupled when analyzing copper corrosion in the presence of radiation.
- **Chapter 6**: The effects of γ-radiation on the copper corrosion dynamics are investigated in small CO_2-free droplet solutions. A copper corrosion mechanism is proposed by investigating the time-dependent behaviour of corrosion products (i.e., dissolved copper concentration, pH, and solid deposits) in the presence and absence of radiation. This chapter gives important insight into how a constant flux of γ-radiation affects the rates and durations of stages of copper corrosion.
- **Chapter 7**: The effects of cover gas on copper corrosion dynamics in the absence and presence of γ-radiation are investigated. The cover gases examined are aerated (with CO_2), 21% O_2 balance Ar, and deaerated, and the results are compared to those from the CO_2-free air environment analyzed in **Chapter 6** to elucidate the combined effects of cover gas and γ-radiation.
- **Chapter 8**: The effects of a higher initial pH and solution depth/volume on the copper corrosion dynamics are investigated. There parameters were studied because they affect the mass transport conditions of cupric ions and are conditions relevant to the DGR environment.
- **Chapter 9**: The summary and major conclusions of this thesis are presented along with a brief discussion on future work.

1.4 REFERENCES

1 Brook, B. W., Alonso, A., Meneley, D. A., Misak, J., Blees, T., van Erp, J. B. Why Nuclear Energy is Sustainable and Has to be Part of the Energy Mix. *Sustainable Materials and Technologies* **1-2**, 8-16, (2014).

2 *The Canadian Nuclear Factbook 2020*. (Canadian Nuclear Association, 2020).

3 *Inventory of Radioactive Waste in Canada*. (Natural Resources Canada, 2016).

4 *Programs Around the World for Managing Used Nuclear Fuel*. (NWMO, 2020).

5 Hall, D. S., Keech, P. G. An Overview of the Canadian Corrosion Program for the Long-Term Management of Nuclear Waste. *Corros. Eng. Sci. Technol.* **52**, 2-5, (2017).

6 Abrahamsen-Mills, L., Small, J. *State of Science Review: Modelling Microbial Effects to Assess Long-Term Performance of a DGR* (NWMO, 2019).

7 Wren, J. C., Jean, A., Naghizadeh, M., Grandy, L., Morco, R., Joseph, J. M., Behazin, M., Keech, P. G. Radiation Induced Corrosion of Copper in Deep Geological Repositories in *WM2019: 45 Annual Waste Management Conference.* 1-15 (Office of Scientific and Technical Information).

8 Keech, P. G., Behazin, M., Binns, W. J., Briggs, S. An Update on the Copper Corrosion Program for the Long-Term Management of Used Nuclear Fuel in Canada. *Mater. Corros.* **72**, 25-31, (2020).

9 Standish, T. E. "Galvanic Corrosion of Copper-Coated Carbon Steel for Used Nuclear Fuel Containers" Doctor of Philosophy, The University of Western Ontario, Electronic Thesis and Dissertation Repository. (2019). 6705.

10 Morco, R. P. "Gamma-Radiolysis Kinetics and Its Role in the Overall Dynamics of Materials Degradation " Doctor of Philosophy, The University of Western Ontario, Electronic Thesis and Dissertation Repository. (2020). 7248.

11 Wu, M., Behazin, M., Nam, J., Keech, P. *Internal Corrosion of Used Fuel Container*. (Nuclear Waste Management Organizaiton, 2019).

12 King, F. *Critical Review of the Literature on the Corrosion of Copper by Water*. (SKB, 2010).

13 Morco, R. P., Joseph, J. M., Hall, D. S., Medri, C., Shoesmith, D. W., Wren, J. C. Modelling of Radiolytic Production of HNO_3 Relevant to Corrosion of a Used Fuel Container in Deep Geologic Repository Environments. *Corros. Eng. Sci. Technol.* **52**, 141-147, (2017).

14 Shin, Y. G. "Nonlinear Dynamics of Carbon Steel Corrosion under Gamma Radiation" Doctor of Philosophy, The University of Western Ontario, Electronic Thesis and Dissertation Repository. (2020). 7339.

15 Guo, D. "Corrosion Dynamics of Carbon Steel" Doctor of Philosophy, University of Western Ontario, Electronic Thesis and Dissertation Repository. (2018). 5897.

16 Naghizadeh, M. "Copper Corrosion Dynamics under Deep Geologic Repository Conditions" Doctor of Philosophy, The University of Western Ontario, Electronic Thesis and Dissertation Repository. (2021). 7894.

17 Emami, M. A., Bigham, M. Mechanism of Corrosion Due to Unalloyed Copper Inclusion in Ancient Bronzes. *Surf. Eng.* **29**, 128-133, (2013).

18 Ambrose, J., Barradas, R. G., Shoesmith, D. W. Rotating Copper Disk Electrode Studies of the Mechanism of the Dissolution-Passivation Step on Copper in Alkaline Solutions. *J. Electroanal. Chem. Interfacial Electrochem.* **47**, 65-80, (1973).

19 Ibrahim, B., Zagidulin, D., Behazin, M., Ramamurthy, S., Wren, J. C., Shoesmith, D. W. The Corrosion of Copper in Irradiated and Unirradiated Humid Air. *Corros. Sci.* **141**, 53-62, (2018).

20 Joseph, J. M., Choi, B. S., Yakabuskie, P., Wren, J. C. A Combined Experimental and Model Analysis on the Effect of pH and $O_{2(aq)}$ on Gamma-Radiolytically Produced H_2 and H_2O_2. *Radiat. Phys. Chem.* **77**, 1009-1020, (2008).

21 Spinks, J. W. T., Woods, R. J. *An Introduction to Radiation Chemistry*. 2nd edn, (Wiley, 1976).

22 Farhataziz, Rodgers, M. A. J. *Radiation Chemistry: Principles and Applications*. (VCH Publishers, 1987).

23 O'Donnell, J. H. *Principles of Radiation Chemistry*. (American Elsevier, 1970).

24 Musa, A. Y., Wren, J. C. Combined Effect of Gamma-Radiation and pH on Corrosion of Ni-Cr-Fe Alloy Inconel 600. *Corros. Sci.* **109**, 1-12, (2016).

25 Daub, K., Zhang, X., Noël, J. J., Wren, J. Gamma-Radiation-Induced Corrosion of Carbon Steel in Neutral and Mildly Basic Water at 150°C. *Corros. Sci.* **53**, 11-16, (2011).

26 Daub, K., Zhang, X., Noël, J. J., Wren, J. C. Effects of γ-Radiation Versus H_2O_2 on Carbon Steel Corrosion. *Electrochim. Acta* **55**, 2767-2776, (2010).

27 Behazin, M., Noël, J. J., Wren, J. C. Combined Effects of pH and γ-Irradiation on the Corrosion of Co-Cr Alloy Stellite-6. *Electrochim. Acta* **134**, 399-410, (2014).

28 Knapp, Q. W., Wren, J. C. Film Formation on Type-316L Stainless Steel as a Function of Potential: Probing the Role of Gamma-Radiation. *Electrochim. Acta* **80**, 90-99, (2012).

29 Yakabuskie, P., Joseph, J., Wren, J. The Effect of Interfacial Mass Transfer on Steady-State Water Radiolysis. *Radiat. Phys. Chem.* **79**, 777-785, (2010).

30 Yakabuskie, P. A., Joseph, J. M., Stuart, C. R., Wren, J. C. Long-Term γ-Radiolysis Kinetics of NO_3^- and NO_2^- Solutions. *J. Phys. Chem. A* **115**, 4270-4278, (2011).

CHAPTER 2. TECHNICAL BACKGROUND

2.1 COPPER BACKGROUND

Copper metal, $Cu^0_{(m)}$, is soft, malleable, and ductile with good electrical and thermal conductivity and highly resistant to corrosion. Its electronic configuration is $[Ar]3d^{10}4s^1$ and the lone 4s electron explains many of coppers unique physical properties, such as its high electrical conductivity and its natural orange-red colour. Copper is produced as a polycrystalline solid which can increase its strength for practical applications. The individual $Cu^0_{(m)}$ grain sizes depend on the metal pre-treatment and an example of the appearance of the wrought copper grains is shown in the SEM image in **Figure 2.1**.[1,2]

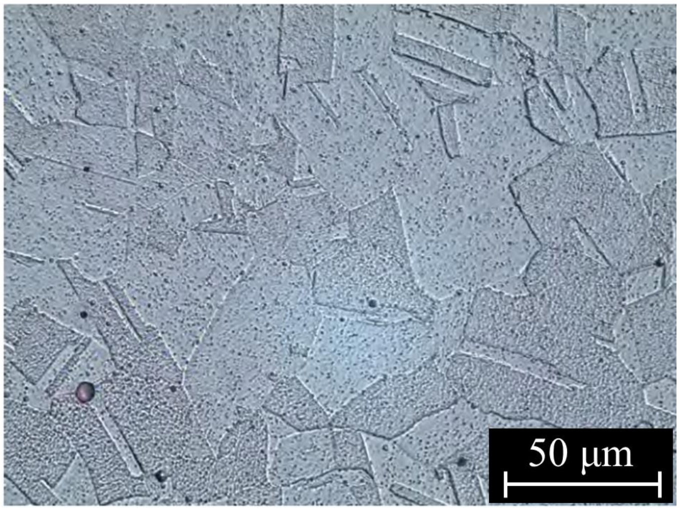

Figure 2.1 Wrought copper microstructure.[1]

2.1.1 Aqueous Copper Species

The main aqueous copper species are cuprous (Cu^+) and cupric (Cu^{2+}). The extent to which a copper cation can dissolve in a particular solution is based on the anions present, the pH, and the temperature of the solution, and is illustrated by its solubility diagram. The diagrams are constructed based on a solid in equilibrium with its dissolved constituents as a function of pH (at a given temperature) or temperature (at a given pH).[3,4]

A hydrated copper ion will undergo hydrolysis in aqueous solutions (**Eq. 2.1**) due to the strong bonds that are formed between metal atoms and oxygen and because the OH^- ligand is always available in water. The concentration of available OH^- (i.e., pH) determines the extent of hydrolysis for a particular copper ion.[3,4] The hydrolysis products for copper ions can be complicated, very often including polyatomic atoms (e.g. $Cu_2(OH)_2^{2+}$), but are generally considered as those shown in **Eq. 2.1**.[4,5]

$$(Cu\cdot(H_2O)_6)^+ \rightleftharpoons (Cu(OH)\cdot(H_2O)_5) + H^+ + H_2O \rightleftharpoons (Cu(OH)_2\cdot(H_2O)_4)^- + 2\ H^+ + 2\ H_2O \qquad (2.1a)$$

$$(Cu\cdot(H_2O)_6)^{2+} \rightleftharpoons (Cu(OH)\cdot(H_2O)_5)^+ + H^+ + H_2O \rightleftharpoons (Cu(OH)_2\cdot(H_2O)_4) + 2\ H^+ + 2\ H_2O \rightleftharpoons (Cu(OH)_3\cdot(H_2O)_3)^- + 3\ H^+ + 3\ H_2O \qquad (2.1b)$$

The hydrolysis products are usually written without the H_2O ligand for simplicity. The solubility curve for a particular copper ion includes all hydrolysis products, which creates the parabolic shape as a function of pH shown in **Figure 2.2**.[3,4] All hydrolysis products are collectively referred to as "$Cu^+_{(sol'n)}$" for cuprous species, and "$Cu^{2+}_{(sol'n)}$" for cupric species:

$$Cu^+_{(sol'n)} \equiv Cu^+ + Cu(OH) + Cu(OH)_2^- \qquad (2.2a)$$

$$Cu^{2+}_{(sol'n)} \equiv Cu^{2+} + Cu(OH)^+ + Cu(OH)_2 + Cu(OH)_3^- \qquad (2.2b)$$

Figure 2.2 shows the solubility diagram for $Cu^+_{(sol'n)}/CuOH$ and $Cu^{2+}_{(sol'n)}/Cu(OH)_2$. The solubility of $Cu^+_{(sol'n)}$ is orders of magnitude lower than that of $Cu^{2+}_{(sol'n)}$ when pH < 8.0, indicating that $Cu^{2+}_{(sol'n)}$ is the dominant species in solution in this pH range.[4,6] When a solution becomes supersaturated with copper ions, the neutral hydrolysis ($Cu(OH)$ or $Cu(OH)_2$) product precipitates to maintain the solubility equilibrium.

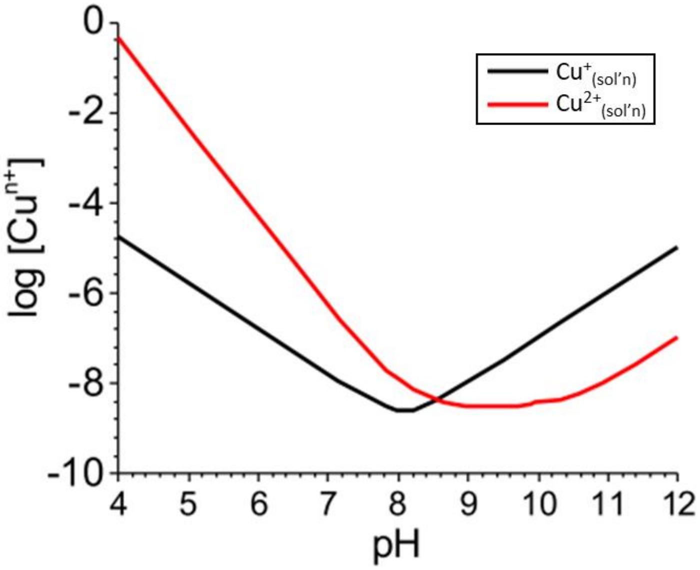

Figure 2.2 Solubility of cuprous ($Cu^+_{(sol'n)}$) and cupric ($Cu^{2+}_{(sol'n)}$) species in water at 25˚C.

Another important consideration for aqueous species is their diffusion. Diffusion of a species is a function of its concentration gradient and diffusion coefficient, according to Fick's first law of diffusion.[7] The diffusion coefficient is a proportionality constant between the diffusion flux and the magnitude of a concentration gradient for a particular species in a particular medium, described in area per unit time (e.g., cm^2/s), and can be used to determine the relative diffusion speeds of species. In a viscous media, diffusion is slower than that in water and diffusion in a porous media is the diffusion through the pore volume, determined by the pore size and connectedness.[8] The diffusion of cupric ion species is slow compared to that of oxidants and OH^-/H^+, as illustrated in **Table 2.1**.

Table 2.1 Diffusion coefficients for relevant species in water at 25 ˚C.[9]

Species	Diffusion coefficient (at 25°C) ($\times 10^{-5}$ cm^2/s)
$O_{2(aq)}$	2.10
H_2O_2	1.5
Cu^+	1.20
$Cu(OH)_2$	0.77

$Cu(OH)^+$	0.73
$Cu^{2+}_{(aq)}$	0.71
$Cu_2(OH)_2^{2+}$	0.50

2.1.2 Cupric Hydroxide

Cupric hydroxide, $Cu(OH)_2$, is bluish green in colour (**Figure 2.3a**) and has been reported to be polymorphic, most commonly fibrous shaped or colloidal.[2,6,10-12] The properties of $Cu(OH)_2$ are dependent on how it was formed and the age of the precipitate.[13] The colloidal form of $Cu(OH)_2$ is often unavoidable without specifically controlling the environment, due to strong hydrogen bonds with water.[14-16] $Cu(OH)_2$ colloids have been observed to aggregate into a hydrogel simply through saturating a basic solution with a cupric salt and adding a species to enhance cupric ion hydrolysis, for example cupric acetate with ammonia,[11] cupric chloride with propylene oxide (an image of the hydrogel grown in this well is shown in **Figure 2.3b**),[15] and cupric acetate with ammonium carbonate.[17]

The propensity of Cu^{2+} to form polynuclear hydroxide complexes (most reported is $Cu_2(OH)_2^{2+}$, but also $Cu_2(OH)^{3+}$ and $Cu_3(OH)_4^{2+}$) even at low Cu^{2+} concentrations is an entropic effect and contributes to the formation of colloids and gels.[6,18] Indeed the formation of these colloids and gel networks have contributed to the large variations in the reported solubility constant for $Cu(OH)_2$. Aging of $Cu(OH)_2$ particles is also another source of error when determining its solubility properties as the transition from $Cu(OH)_2$ to hydrous oxide to solid CuO is not obvious through spectroscopy or other analysis techniques.[6,13]

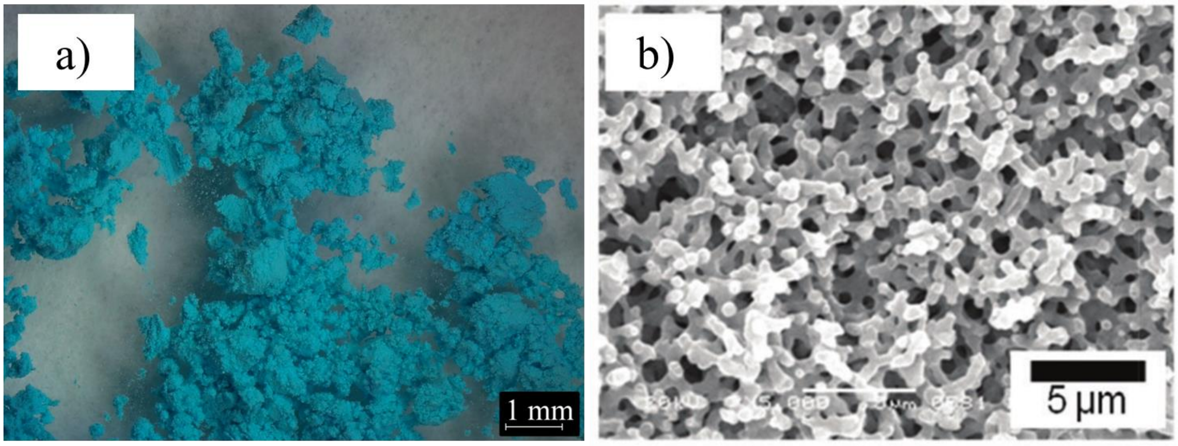

Figure 2.3 a) Optical and b) SEM[15] images of copper(II) hydroxide, $Cu(OH)_2$.

2.1.3 Cuprous Oxide

Cuprous oxide (called cuprite as a mineral), Cu_2O, is the main oxide of copper formed during corrosion. Cu_2O is a semiconductor with a bandgap energy range of 2.0 – 2.2 eV, corresponding to yellow light.[19] Cu_2O can range in colour from pink to deep red depending on the crystal size and can appear darker, even black, if it contains impurities, such as hydrogen during atmospheric corrosion.[3,20] While small Cu_2O crystals are reported to be yellow, the yellow species has also been attributed to the metastable (kinetically stable) species CuOH.[21,22]

Like its colour, other physical properties of Cu_2O can vary substantially. Cu_2O has been grown in many different shapes, such as cubic,[16,23,24] octahedral,[25,26] hopper cubes,[27,28] and hollow crystals.[29-32] Whether Cu_2O is a p- or n-type semiconductor depends on the growth mechanism and parameters, for example anodically grown Cu_2O exhibits p-type properties while naturally grown Cu_2O in the same solution can either be p-type or a duplex layer of n- and p-type depending on growth time. Cu_2O exhibits an n-type behaviour when its grown via deposition of soluble Cu^+ or Cu^{2+}.[19,20,33] Since the properties can vary substantially, Cu_2O has a wide range of applications, such as biosensors,[32] solar energy conversion,[34] gas sensing,[35,36] catalysis,[37-39] electrode materials for lithium ion batteries,[40,41] and others.

Synthesis of Cu_2O crystals through chemical reduction of $Cu^{2+}_{(aq)}$ has been widely studied, where a cupric salt (sulphate, nitrate, acetate, or chloride) is reduced to Cu^+ using a mild reducing agent, such as sodium ascorbate,[23,24] hydrazine,[25,29,30] and glucose.[16,26] Exposing a Cu^{2+}-saturated solution to γ-radiation is also a common synthesis method.[42] Different concentrations of these chemical additives, as well as addition of surfactants (e.g. cetyltrimethylammonium, sodium dodecyl sulfate, polyvinylpyrrolidone), increased temperatures, pH variations and reaction time can be used to tune the size and morphology of the resulting Cu_2O crystals.[24,26,32] CuOH has been shown to be an intermediate in the synthesis of Cu_2O crystals.[42-44]

The Cu atoms in Cu_2O are FCC packed, while the O atoms are BCC packed. The unit cell of Cu_2O is shown in **Figure 2.4**, along with some crystallographic planes.[45,46] Growth of a single Cu_2O crystal occurs based on the surface lattice energies, as indicated in **Figure 2.4**, where the {113} plane has the fastest growth rate and the {111} has the slowest (unless the reactivity of a surface is altered by the presence of additives that preferentially adsorb on particular crystallographic planes).[45,46] A plane with a faster growth rate will diminish faster during crystal growth. Cu_2O single crystals initially grow in cubes with 6 faces of {100} planes but slowly will change shape into truncated cubes, truncated octahedrons, and eventually to octahedrons, with 8 facets of the thermodynamically most stable {111} planes (**Figure 2.5**). Longer growth time will lead to crystals with many faces and eventually spheres.[28,45] More shapes are possible due to competition between precipitation/crystallization and diffusion, including branching structures and hopper-cubes.[28,47] Both kinetics and thermodynamics play an important role in determining the shape of Cu_2O.

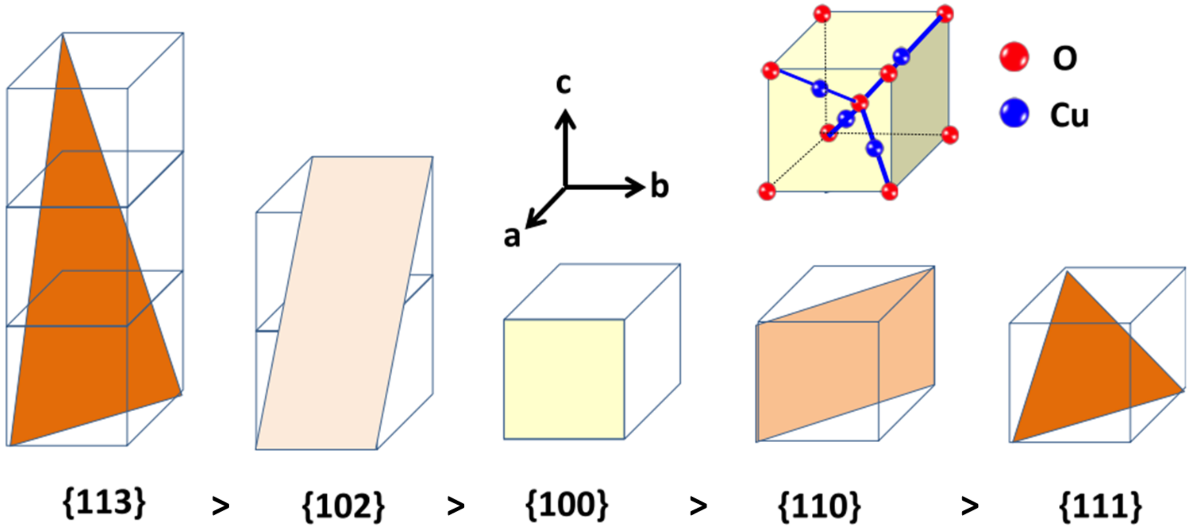

Figure 2.4 Cu_2O unit cell, with FCC Cu and BCC O, along with some crystallographic planes of Cu_2O in order of highest to lowest surface lattice energy.[45]

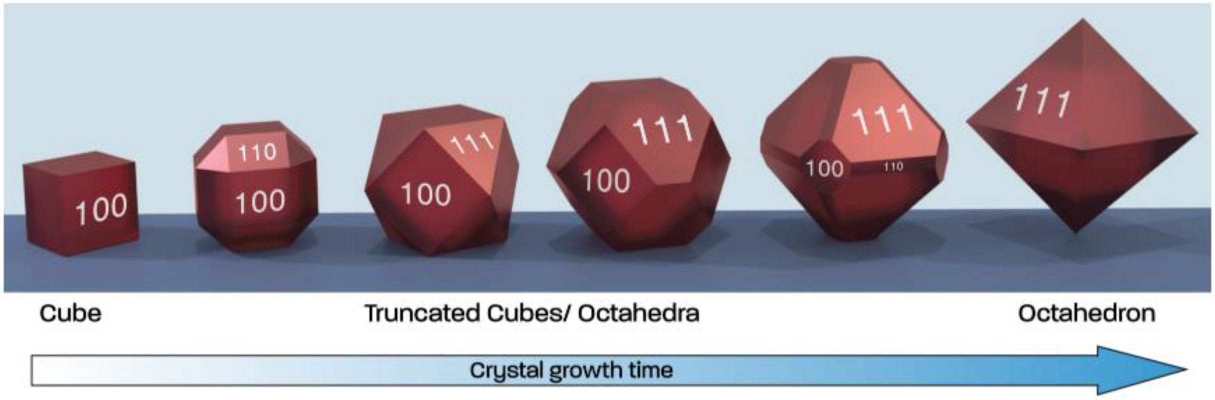

Figure 2.5 Time dependent growth of Cu_2O, from cubes to octahedron.[45]

2.1.4 Other Solid Cupric Species

At room temperature, CuO is less stable than Cu_2O. CuO, as a mineral called tenorite, is a semiconductor with a bandgap of 1.3 –1.9 eV, and is black in colour.[19] It is formed by heating Cu^0 in air or other Cu(II) solids at more than 300 ºC.[48] While CuO has occasionally been reported during room temperature Cu^0 corrosion, $Cu(OH)_2$ is kinetically favoured and is hard to differentiate from CuO using spectroscopic techniques.[49-51]

Cupric ions in solution easily complex with carbonate to produce malachite, $Cu_2(CO_3)(OH)_2$, or azurite, $Cu_3(CO_3)_2(OH)_2$ (sometimes written as $CuCO_3{\bullet}Cu(OH)_2$ and $2CuCO_3{\bullet}Cu(OH)_2$, respectively). $CuCO_3$ as a solid product quickly reacts with moisture in the air to produce basic Cu carbonates.[52] Azurite is bright blue (**Figure 2.6a**) and is more rare than malachite. Malachite is bright green (**Figure 2.6b**) and is a common copper corrosion product.[53,54] In fact, malachite is common in patinas, contributing to the green colour of the Statue of Liberty for example.[55] The formation of its banding patterns (**Figure 2.6b**) have been a source of interest in geology and has been attributed to non-linear chemical oscillatory behaviour, such as in the Belousov-Zhabotinsky (B-Z) reaction.[53,56]

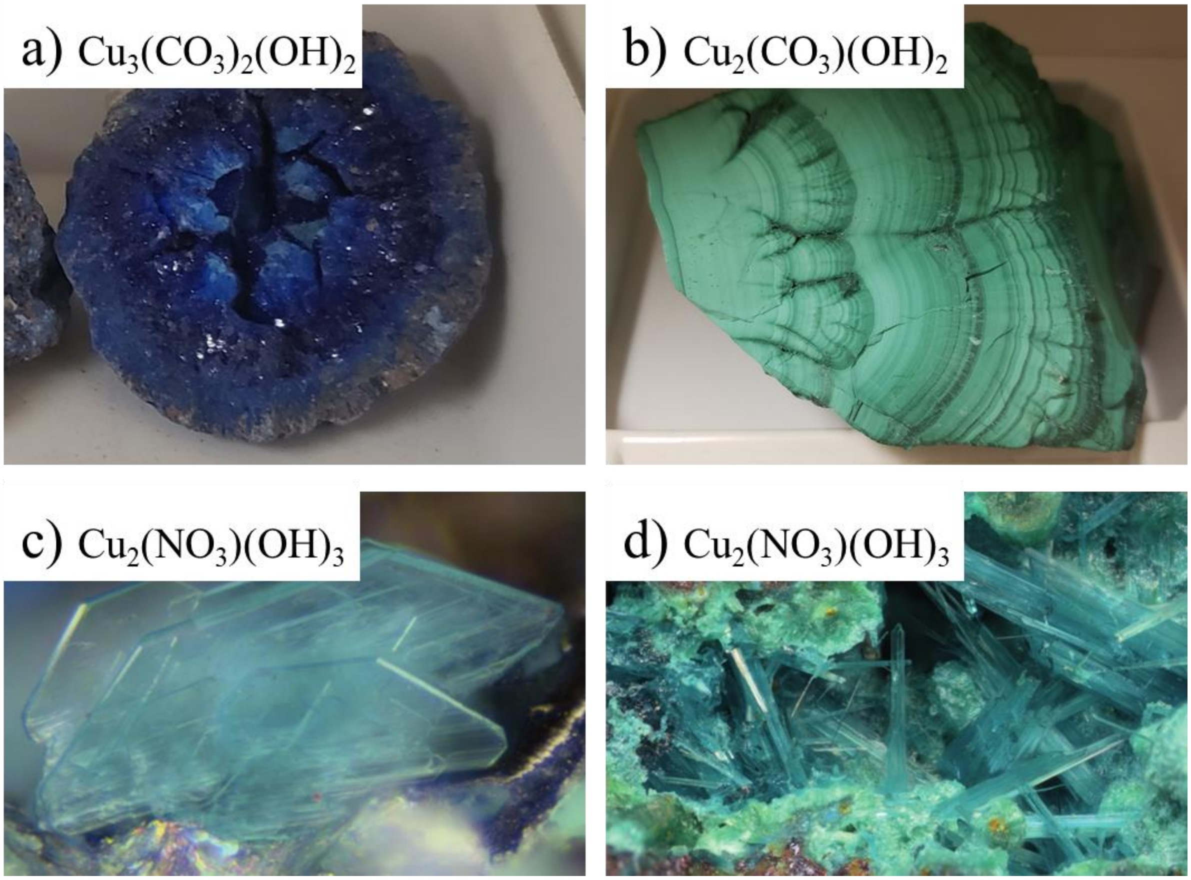

Figure 2.6 Optical images of basic cupric carbonate minerals (a,b) and basic cupric nitrate minerals(c,d[57]). a) Azurite, $Cu_3(CO_3)_2(OH)_2$, b) Malachite, $Cu_2(CO_3)(OH)_2$, c) Gerhardtite, $Cu_2(NO_3)(OH)_3$, and d) Rouaite, $Cu_2(NO_3)(OH)_3$.

Copper nitrates are a very common corrosion product when in the presence of NO_3^-. Pure $Cu(NO)_3$ is found in either tri- or hexahydrate form and is a blue, highly soluble salt. Anhydrous nitrate is difficult to produce as decomposition into basic copper (II) nitrate is preferential over dehydration.[58] Basic copper (II) nitrate minerals are rare in nature – as they are usually complexed with other anions such as chloride – but have been seen to include likasite, $Cu_3NO_3(OH)_5{\bullet}2H_2O$, and the polymorphs gerhardtite (orthorhombic) and rouaite (monoclinic), $Cu_2(NO_3)(OH)_3$ (sometimes written as $Cu(NO_3)_2{\bullet}3Cu(OH)_2$) (**Figure 2.6c, d**).[59,60] Likeasite is the most thermodynamically stable of the copper nitrates but the conditions in which it is produced (highly alkaline and high Cu^{2+} concentrations) are uncommon. The polymorphs are formed in solutions at near neutral pH, with gerhardtite being the most stable.[58]

2.2 RADIATION CHEMISTRY

2.2.1 Types of Radiation

Radiation chemistry deals with the chemical effects produced in a system when exposed to high energy ionizing radiation. The types of ionizing radiation include high-energy charged particles, e.g. alpha (α) and beta (β) particles, and electromagnetic waves, e.g. gamma (γ) rays, because they have energies in the range of keV to MeV which is many orders of magnitude higher than the excitation and ionization energy of atoms or molecules (tens of eV).[2]

Ionizing radiation interacts with matter, A, by indiscriminately colliding with electrons bound to atoms and molecules, transferring its kinetic energy to cause ionization (**Eq. 2.3a**) and/or excitation (**Eq. 2.3b**), which will then thermalize.

$$A \overset{\gamma}{\rightsquigarrow} A^{\bullet +} + e^- \tag{2.3a}$$

$$A \overset{\gamma}{\rightsquigarrow} A^* \tag{2.3b}$$

For comparison, a photon with less energy (e.g. a visible light photon) will excite a specific dissolved molecule, while high-energy radiation excites or ionizes many molecules along the path of radiation within the material, called the radiation track. Penetration depth of radiation is dependent on the energy of the particle as well as the density of the interacting medium.[61-64]

Charged particles interact with matter mainly through Coulomb forces between their charge and the atomic electrons. α particles, the nuclei of helium atoms, are emitted by radioactive nuclei with a discrete energy that is characteristic of the radioactive decay process.[61-63] Along the collision track, α particles interact through inelastic collisions with only small amounts of energy being lost with each collision due to their large size compared to the electrons they interact with. However, the large collision cross-section with electrons leads to a short penetration depth with a dense collection of excited and ionized particles, shown in **Figure 2.7a**. [61-63]

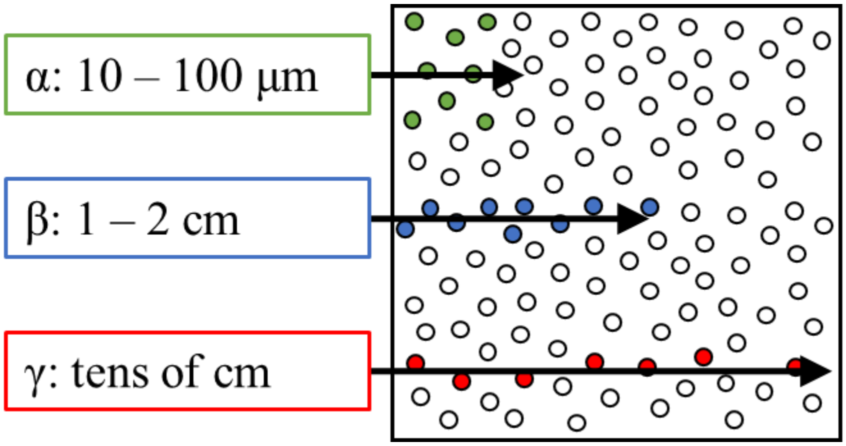

Figure 2.7 Penetration depth in water for α, β, and γ particles (distance not to scale).[61]

β particles are high-energy electrons or positrons emitted by atomic nuclei during beta decay. A particular radioactive nucleus emits β particles with an energy range from 0 to a maximum energy that is characteristic of the element and have a large penetration depth, compared to that for α particles (**Figure 2.7**). Because the mass of the β particle is identical to the scattering electrons, almost half of the kinetic energy is transferred per collision and can be deflected at a large angle. Due to the large transfer of energy, the scattered secondary electrons (formed via **Eq. 2.3a**) can interact with other electrons, propagating the energy in many directions but with reduced efficiency with each cascade. This creates many pockets of excited or ionized particles along the radiation track.[61-63]

γ-rays are a form of electromagnetic radiation with an energy between 0.001 and 8 MeV. A given γ-radiation source can emit multiple γ-rays during decay with specific, characteristic energies. A γ-photon with energy over 0.01 MeV transfers its energy to interacting matter mainly through Compton scattering.[61-63] Compton scattering results in the ejection of a 'primary' electron with a very high kinetic energy (close to that of the initial γ-photon). The primary electron is also referred to as a "hot" or "fast" electron. The high-energy primary electron continues to travel along the direction carried by the momentum gained during Compton scattering. At this point, the propagation is identical to that of a β particle and any chemical effects induced by β- and γ-radiation with the same absorbed energy are essentially the same. The probability of inelastic Compton scattering to produce a primary electron is low, thus the penetration depth of a γ-ray is large (**Figure 2.7**).[61-64]

With each collision of the primary electron, it transfers on average ~ 100 eV to a secondary electron. Because the ionization energy of most atoms and molecules is less than tens of eV, each secondary electron can also ionize or excite 2-3 atoms or molecules nearby. Each collision of the primary electron with atoms and molecules creates a cluster of 2-3 ion/electron pairs or excited molecules, known as a spur. If the spur can expand before the ions and electrons recombine or the excited molecules return to the ground states, the energy transferred from ionizing radiation to matter will not induce significant chemical changes. However, if the interacting medium is highly dielectric, such as water, the ions and electrons can be easily separated, and radiation can induce significant chemical reactions.[61-64]

2.2.2 Primary Water Radiolysis Processes

Interactions of high energy radiation with matter is indiscriminate, meaning that molecules are ionized/excited only based on their relative abundance and it is called a "solvent-orientated process". The interactions described in **Section 2.2.1** are direct or primary radiation effects (ionization and excitation of molecules); there are also indirect or secondary radiation effects (chemical reactions caused by ionized/excited molecules). That is, direct radiation effects will affect the solvent, while solutes in dilute concentrations will primarily be indirectly affected.[61-64] Discussions on direct radiation effects then can be narrowed to water for aqueous solutions.

The radiation track of a primary electron is illustrated in **Figure 2.8**. The primary electron will interact with several water molecules before thermalizing, as described for β-particles. Each initial interaction (~ 10^{-16} s) yields the water radical cation (**Eq. 2.4a**) and excited water molecules (**Eq. 2.5a**). Coulombic forces between species can lead to recombination of water, which reduces the net chemical decomposition caused by absorption of radiation energy. They can also react between themselves and with other water molecules.

$$H_2O \overset{\gamma}{\rightsquigarrow} H_2O^{\bullet+} + e^{-} \tag{2.4a}$$

$$H_2O^{\bullet+} + H_2O \rightarrow HO^{\bullet} + H_3O^{+} \tag{2.4b}$$

$$e^{-} + n\, H_2O \rightarrow e^{-}_{(aq)} \tag{2.4c}$$

$$H_2O \overset{\gamma}{\rightsquigarrow} H_2O^{*} \tag{2.5a}$$

$$H_2O^{*} \rightarrow H^{\bullet} + HO^{\bullet} \tag{2.5b}$$

The water radical cation quickly (~ 10^{-14} s) loses a proton to a neighbouring water molecule (**Eq. 2.4b**). The electron formed after ionizing water (the secondary electron) could have enough energy to create a short radiation track before thermalizing and hydrating (**Eq. 2.4c**). Excited water dissociates to yield atomic hydrogen and hydroxyl radicals (~ 10^{-13} s) (**Eq. 2.5b**).[61,64] These decomposition products (**Eq. 2.4 – 2.5**) are located together to make up spurs, which are distributed unevenly throughout the radiation track.

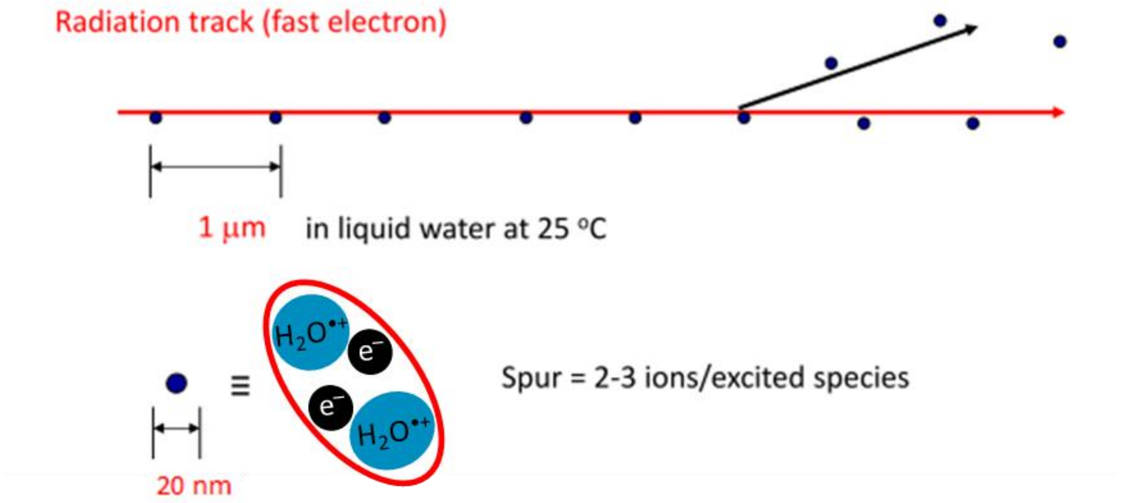

Figure 2.8 Illustration of the radiation track of a fast electron in liquid water and the resulting spurs consisting of ionized water and secondary electrons (spur size not to scale).[61]

As the species diffuse out from the spur, they become free ions and free radicals. These species can have relatively long lifetimes in water (due to the high dielectric constant).[61-64] They can react with species from adjacent spurs (depending on the density of spurs) and with solvent molecules. Approximately 100 ns after the initial interaction, the species within spurs had diffused out and reacted resulting in all the products being homogeneously distributed in solution. The chemical yields at ~ 100 ns are referred to as the primary radiolysis yields and the radiolytic decomposition products as the primary radiolysis products. The primary radiolysis yields are dependent on the total absorbed radiation dose and thus, are expressed in G-values or the number of molecules of product formed per 100 eV of energy absorbed, with the standard units of μmol/J. The primary radiolysis products for water decomposition are shown in **Eq. 2.6** with the G-values in brackets in units of μmol/J.[61,64-66]

$$H_2O_{(l)}\ (-0.40) \overset{\gamma}{\rightsquigarrow} HO^{\bullet}\ (0.27),\ H^{+}\ (0.26),\ e^{-}_{(aq)}\ (0.26),\ H^{\bullet}\ (0.06),\ H_2\ (0.04),\ H_2O_2\ (0.07) \tag{2.6}$$

2.2.3 Long-Term Radiolysis

Once formed ($t > 100$ ns), the primary radiolysis products are homogeneously distributed and will continue to react with species in solution (including solvent molecules, solutes, and dissolved gases).[61,63] Consequently, their concentrations will continuously change until a steady state has been established, which takes on the timescale of minutes (long compared to that in which primary radiolysis products are formed). The concentrations of radiolysis products at this stage can be determined using traditional homogeneous rate and mass transport equations, although the large number of chemical species that can be formed from even a simple system renders it complex. About 50 elementary reactions are required to determine the rate of formation and steady-state concentrations of water radiolysis products.[65] The steady-state concentrations of water radiolysis products are strongly influenced by the initial pH and dissolved species.[63,65-69] It is the steady-state concentrations, not the primary radiolysis yields, that impact interfacial chemical processes, i.e. corrosion, which have large activation energies and proceed relatively slowly.[45,70-72] The steady-state concentration values can be disturbed by chemical reactions that occur on a longer timescale, such as acid-base equilibria and interfacial phase transfer reactions.[63,65]

2.2.4 Humid Air Radiolysis

The G-values for humid-air radiolysis products, like water radiolysis products, are well established.[61,73] The main products of radiolytic decomposition of humid air (**Eq. 2.7**) are dependant on the relative humidity (RH) and irradiation time.

$$H_2O_{(g)},\ N_{2(g)},\ O_{2(g)} \overset{\gamma}{\rightsquigarrow} NO_x,\ HNO_3 \qquad (2.7)$$

At > 10% RH the radiolysis main products are $\bullet OH_{(g)}$, $\bullet HO_{2(g)}$ at short times, due to water vapour radiolysis, and HNO_3 at longer times, through the combination of $\bullet OH_{(g)}$ and $NO_{2(g)}$.[73] HNO_3 condenses on available surfaces and/or dissolves into solution, making it an important radiolysis product during aqueous corrosion. The concentration of dissolved HNO_3 formed via humid air radiolysis is not affected by the relative humidity but does depend on the radiation dose rate.

Its dissociation in solution decreases the solution pH and adds nitrate, a complexing anion that can participate in electrochemical reactions during corrosion.[73,74]

2.2.5 Radiation Relevant to Nuclear Waste Disposal

The UFC will be exposed to a continuous flux of ionizing radiation emitted from the radioactive fission and neutron-activation products trapped in the used fuel matrix (mainly the decay of ^{137}Cs with a half-life of 30 years). The ionizing radiation from radionuclides include α- and β-particles and γ-photons with energy in the range of 0.1 to 10 MeV. The fuel cladding material (zirconium alloys) and thick (4.6 cm) carbon steel vessel effectively shields α- and β-particles from reaching the exterior of the UFC. Thus, γ-radiation is of main interest concerning the corrosion of the copper coating of the UFC.[65,66] The dose rate – the quantity of radiation absorbed per unit time – at the outer surface of the UFC is expected to be ~2 Gy/h at the time of emplacement in the DGR, but decay exponentially with time to 0.1 Gy/h in 100 years (**Figure 2.9**), where gray (Gy) is equal to the absorption of one joule of radiation energy per kilogram of matter (water, in this case).[73]

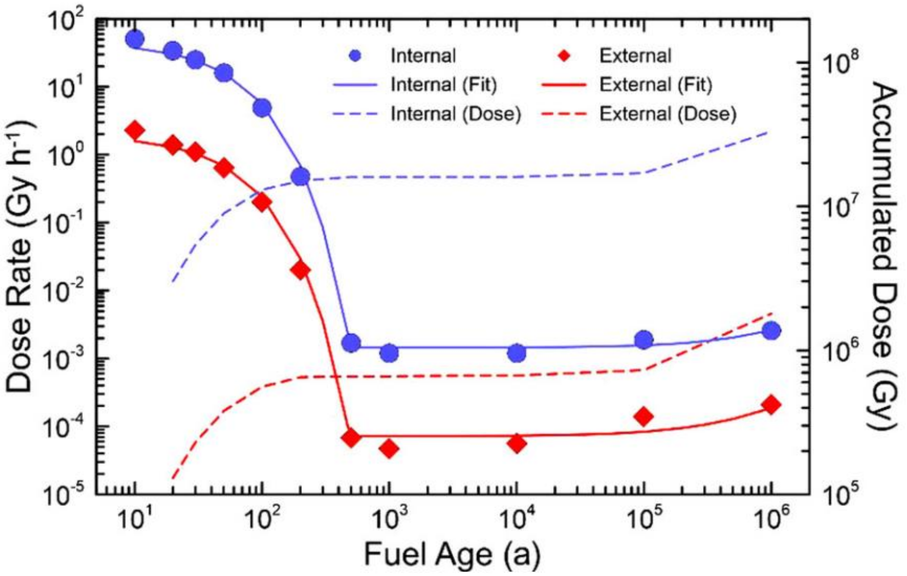

Figure 2.9 Calculated γ-radiation dose rate and accumulated doses at the internal (carbon steel) and external (copper) surfaces of the UFC starting with 10-year-old fuel.[73]

When exposed to ionizing radiation both $Cu^0_{(m)}$ and the surrounding water absorb the radiation energy, but the energy transferred to the metal is dissipated as heat without inducing chemical changes.[65,66] The main effect of the presence of radiation, then, is due to the humid air and water radiolysis products (**Eq. 2.6 – 2.7**).[61] The concentrations of radiolytically produced species were modelled at the dose rate used in this thesis (2 kGy/h), shown in **Figure 2.10**. The model only considers water and humid air system, i.e. without a $Cu^0_{(m)}$ surface. H_2O_2 is the main radiolytic product in the first ~ 10 h of exposure, formed mostly from water radiolysis. As humid air radiolysis forms HNO_3, it dissolves into available water and its concentration quickly surpasses that of H_2O_2. The concentration trend of NO_2^- is the same as NO_3^- as its main formation pathway is through NO_3^- reduction.[65,73]

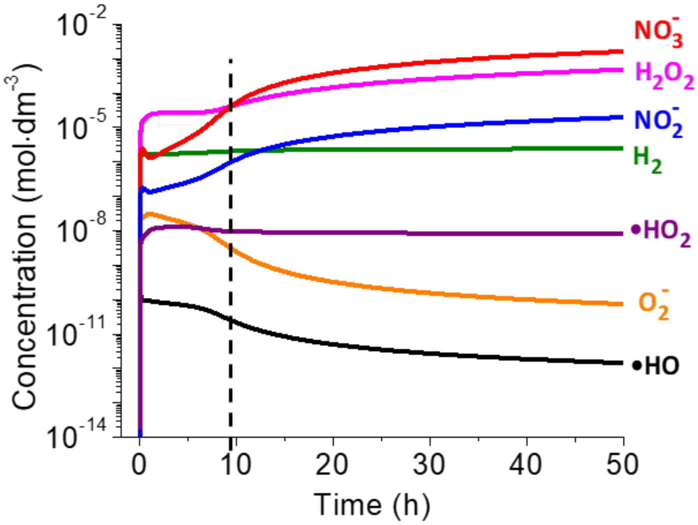

Figure 2.10 Simulated production of water and humid air radiolysis species in the presence of 2 kGy/h γ-radiation (in the absence of copper corrosion).[73] The dashed vertical line indicates a change in the dominant radiolysis product from H_2O_2 to NO_3^-.

2.3 COPPER CORROSION

2.3.1 Copper Redox Chemistry

Copper can take on many oxidation states, with the main states under ambient conditions being 0, +1, and +2. Redox half-reactions between copper species are shown in **Eq. 2.8** – **2.10** along with their standard electrode potentials (E^0).[3,75]

$$Cu^{+}_{(aq)} + e^{-} \rightleftharpoons Cu^{0}_{(m)} \qquad E^0 = 0.521\ V_{SHE} \qquad (2.8)$$

$$Cu^{2+}_{(aq)} + 2\ e^{-} \rightleftharpoons Cu^{0}_{(m)} \qquad E^0 = 0.337\ V_{SHE} \qquad (2.9)$$

$$Cu^{2+}_{(aq)} + e^{-} \rightleftharpoons Cu^{+}_{(aq)} \qquad E^0 = 0.153\ V_{SHE} \qquad (2.10)$$

The standard electrode potential of a half reaction is the potential at which the half reaction is in equilibrium with respect to the standard hydrogen electrode (SHE) at standard conditions and indicates the spontaneity of the reaction.[75] The standard electrochemical potentials for the half reactions between the copper species indicate that the oxidation of Cu^0 to the higher oxidation state, i.e. Cu^{2+}, is more favourable than oxidation to Cu^+ and the interconversion between Cu^+ and Cu^{2+} has a lower energy barrier than either Cu^+/Cu^0 or Cu^{2+}/Cu^0. Despite the general assumption that electrochemical reactions occur in one-electron steps, Cu^0 oxidation to Cu^{2+} is favourable compared to that to Cu^+. These distinct redox properties of copper species render Cu^0 corrosion a difficult process to study electrochemically.[33]

Copper half-reactions between the main solid species (oxides/hydroxides) are shown in **Eq. 2.11** – **2.13**, where similar potential relationships exist between the copper oxidation states.[75]

$$Cu_2O_{(s)} + H_2O + 2\ e^{-} \rightleftharpoons 2\ Cu^{0}_{(m)} + 2\ OH^{-} \qquad E^0 = -0.360\ V_{SHE} \qquad (2.11)$$

$$Cu(OH)_{2(s)} + 2\ e^{-} \rightleftharpoons Cu^{0}_{(m)} + 2\ OH^{-} \qquad E^0 = -0.222\ V_{SHE} \qquad (2.12)$$

$$2\ Cu(OH)_{2(s)} + 2\ e^{-} \rightleftharpoons Cu_2O_{(s)} + 2\ OH^{-} + H_2O \qquad E^0 = -0.080\ V_{SHE} \qquad (2.13)$$

The standard electrode potentials for copper (**Eq. 2.8 – 2.13**) render its oxidation in anoxic pure water thermodynamically impossible, which is an attractive quality in many applications, including nuclear waste disposal.[3,74,76] The standard electrode potentials do not take into account the conditions of the studied system, thus must be adjusted to equilibrium potentials (E^{eq}) using the Nernst equation (**Eq. 2.14**), where z represents the number of moles of electrons transferred in the reaction and F is Faraday's constant (96485 C/mol).[75]

$$E^{eq} = E^0 - \frac{RT}{zF} \cdot \ln\left(\frac{a_{red}}{a_{ox}}\right) \tag{2.14}$$

Importantly, the Nernst equation adjusts the standard electrode potential for the activity (a) of the reduced (red) and oxidized (ox) species at the electrode surface at equilibrium. The activity of the involved species can change throughout the corrosion process and thus the thermodynamically allowed reactions can change with corrosion time. While thermodynamic properties provide the driving force(s), corrosion is a kinetic process and should not be assumed to be at thermodynamic equilibrium.

2.3.2 Corrosion Background

Metal corrosion in aqueous environments involves charge transfer reactions, including the metal (M) oxidation and solution species (Ox) reduction half-reactions.

$$\mathrm{M} + \mathrm{Ox} \rightarrow \mathrm{M}^{n+} + \mathrm{Red} \tag{2.15}$$

The overall reaction is thermodynamically driven due to a difference in chemical potential between the metal and the solution it is in contact with. In general, the current during this reaction is governed by the rates of (i) electron transfer at the electrode surface, (ii) surface reactions, including adsorption and desorption processes, (iii) chemical reactions preceding or following the electron transfer (homogenous, such as protonation, or heterogenous, such as catalytic decomposition), and (iv) mass transfer of metal cations from metal surface to the solution phase (and oxidants from the solution phase to the surface). The rate constant (k) of a charge transfer reaction at the electrode surface depends on the electrode potential.

Long-term corrosion involves not just the initial charge transfer (**Eq. 2.15**) but subsequent electrochemical and/or chemical reactions that can be categorized as oxidation-reduction, chemical reactions without electron transfer, and species transport; all of which take place on different temporal and spatial scales. For example, the redox reactions and some chemical reactions (e.g., hydrolysis) occur on the order of seconds or minutes, whereas the formation of oxides could take hours or even days.[77,78] As metal ions are produced, they have two possible pathways: diffusion into the bulk solution (transport) or oxide formation (chemical reaction) on the surface. The predominance of one of these pathways is determined by solution parameters and corrosion time.

Pourbaix diagrams (E^{eq} vs. pH) are thermodynamic stability diagrams for a given corroding system in given conditions. They are useful in determining the thermodynamically possible species during corrosion; however, they vastly change with temperature, aqueous concentration, presence of additives, and solid and aqueous species considered, and therefore must be used with caution. Importantly, the concentration of oxidants and metal atoms in corrosion systems is continuously changing. Even in a simple corroding system, the concentration of Cu^{n+} in solution starts very small and can increase significantly as $Cu^0_{(m)}$ oxidizes and dissolves. Likewise, corrosion in unbuffered solutions causes the pH to increase as the reduction reaction produces OH^- (or consumes H^+). That is, naturally progressing corrosion systems are not under thermodynamic equilibrium. While Pourbaix diagrams can determine what the final state of the corroding system will be and what reactions are thermodynamically allowed, they cannot provide rate or mechanistic corrosion information.[3] A good example is Cu_2O, which is thermodynamically stable in a specific range of potentials at certain pH values, however the direct oxidation of Cu^0 to Cu_2O is only possible at high temperatures.[79] Similarly, while CuO is more thermodynamically stable in a wide variety of potentials and pH values, the formation of $Cu(OH)_2$ is known to be kinetically favoured.[33]

Generally, corrosion rate is determined experimentally usually using electrochemical methods, such as Tafel extrapolation, or by weight loss measurements. Tafel extrapolations determine the instantaneous corrosion rate through the linear extrapolation of a polarization curve, as shown in **Figure 2.11**. Determining the corrosion rate in this way is only valid under very particular conditions, including that the system is under activation control, and that there are no additional reactions occurring at the electrode surface due to the changing potential.[75,80] Weight loss experiments are those that involve dissolving solid species formed on the metal surface, weighing the sample, and comparing that weight to that of the sample before corrosion. The weight loss is then used to determine the corrosion rate in terms of the amount of metal that has been oxidized. This method is satisfactory if the focus is exclusively on the degradation of the metal within the experimental times. The extrapolation to longer times is only valid with the assumption that the rate of mass loss is linear for the entirety of corrosion.

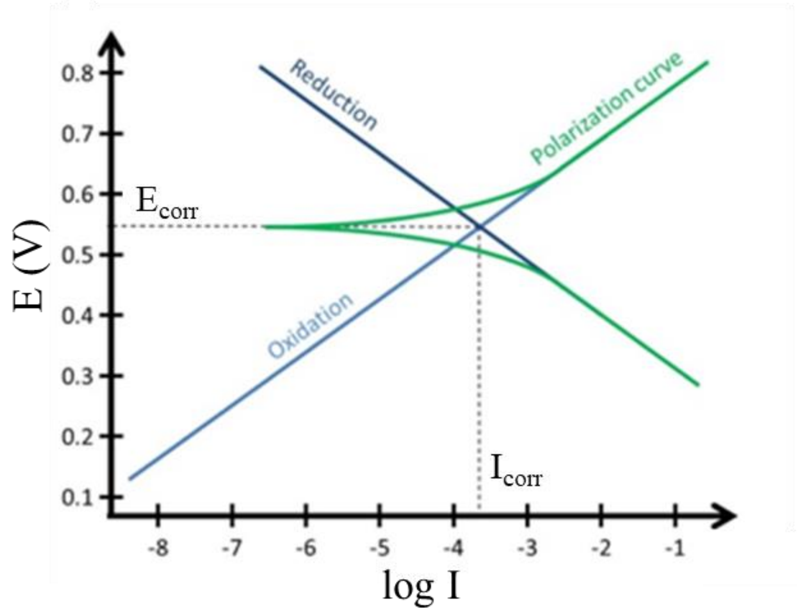

Figure 2.11 Linear Tafel extrapolation of corrosion current (I_{corr}).

There are many types of corrosion categorized based on physical observations of the metal degradation. Uniform corrosion occurs equally across the exposed metal surface. In this type of corrosion there are no preferential areas of attack and it is easy to quantify the amount of material loss. Localized corrosion is a blanket term for corrosion that occurs preferentially in a particular location either due to variances in the metal surface or environmental considerations. In this type of corrosion, the location of net oxidation and location of net reduction must be physically separated. For example, pitting is a severe localized corrosion attack that can be hard to predict and be catastrophic for the material. Having a protective layer (usually an oxide film) on the metal surface which breaks down in one location is a prerequisite for pitting corrosion. The location of the breakdown, i.e., the pit, creates a concentrated area for underlying metal oxidation and dissolution, permanently separating the anode (metal in the pit) from the cathode (the rest of the surface, covered with a passive film). Intergranular corrosion is another common type of observed localized corrosion, where the boundaries of the metal grains are more susceptible to attack compared the center of the grains because the atoms on the boundaries are higher in energy than those in the bulk.[81]

2.3.3 Aqueous Copper Corrosion

O_2 is the most common $Cu^0_{(m)}$ oxidant. The oxygen reduction reaction (ORR) on metal surfaces is a fundamental process studied in many fields of electrochemistry and many reaction pathways for ORR have been proposed.[75,82-85] H_2O_2 has been proven to be an intermediate in the ORR on metal surfaces, suggesting O_2 reduction on metal surfaces is a two-step process in which the first step is rate determining.[86]

$$O_2 + 2\,H^+ + 2\,e^- \rightleftharpoons H_2O_2 \tag{2.16a}$$

$$H_2O_2 + 2\,H^+ + 2\,e^- \rightleftharpoons 2\,H_2O \tag{2.16b}$$

Aqueous copper oxidation at room temperature generally results in dissolved copper cations. Depending on the anions present in water and the corrosion duration, different soluble and/or insoluble complexes or oxides can form.[87] Cu_2O is almost always reported to be a solid copper corrosion product and thus a common assumption is that the oxidation of Cu^0 forms Cu_2O directly.[78]

Corrosion studies on pure, unalloyed $Cu^0_{(m)}$ are uncommon and those that exist are done in large volumes of alkaline or acidic solutions.[88,89] Common applications of Cu^0 involve flowing water (e.g. pipes, on roofs), which can significantly change the corrosion dynamics compared to stagnant water (relevant to DGR conditions).[77,90] Many studies investigate the effects of parameters such as pH, dissolved O_2 concentration, and anion concentration, however studying the time-dependent corrosion evolution and these parameters is rare.[90,91]

Furthermore, copper corrosion studies in the presence of radiation are limited.[92] This thesis investigates the corrosion dynamics of copper in the presence of γ-radiation at near-neutral initial pH solutions with anions only naturally present in pure water (i.e. bi/carbonate from dissolved CO_2 and radiolytically produced NO_3^-), thus a review of current literature focuses on these conditions.

2.3.4 Effect of pH on Copper Corrosion

Solution pH is an important parameter in corrosion research. H^+ is a reactant in reduction reactions (**Eq. 2.16**) and as such its concentration can change the kinetics of the reaction. Additionally, the pH of a solution will affect solubility of copper ions (**Figure 2.2**), which can change both the driving force for reactions (by changing equilibrium concentrations) and the kinetics of reactions that result in soluble copper species. The effect of pH on other solution parameters is not necessarily linear due to feedback loops developed throughout corrosion, and as such comparisons between studies with different conditions are not always straightforward.

Corrosion studies investigating the pH effects often ignore the effects of corrosion time – and thus the kinetic effects of corrosion – by taking measurements after only one time point. For example, Feng et al.[91,93] investigated the effects of pH by performing experiments in three different pH values (5, 7.6, and 10) by taking measurements after only 24 hours. They determined that for each pH, there was a different corrosion mechanism and different corrosion film morphology.[94]

Other studies (which consider kinetic effects to varying degrees) have found that copper corrosion rate is at its minimum in solutions with pH ~ 8.5 – the pH at which Cu^{n+} solubility is at its lowest.[95,96] In solutions of all pH values, diffusion and copper ion solubility has been identified as an important consideration in determining corrosion rate and film formation.[78,93-95,97-102] While the diffusion limiting species is often assumed to be O_2, many studies show that rate limitations due to Cu^{n+} diffusion is more likely.[93,95,97-99,103]

2.3.5 Copper Corrosion in Carbonate Solutions

Ives and Rawson (1962)[90,104-106] wrote a four-part paper investigating the thermodynamics, kinetics, and electrochemical theory of copper corrosion in naturally aerated water (that is, saturated with O_2 and CO_2). In particular, they examined the Cu_2O film thickness and dissolved Cu^{2+} concentration as a function of O_2 and CO_2 partial pressure at various time points.[90] They did not separate the effects of CO_2 partial pressure from the resulting pH effect but did report the pH values. At all studied CO_2 partial pressures, they found that the Cu_2O film growth and the Cu^{2+} dissolution remained in step, attributed to the reverse disproportionation of Cu_2O, i.e. Cu^0 reaction with $Cu^{2+}_{(aq)}$ to form Cu_2O (**Eq. 2.17**).

$$Cu^0_{(m)} + Cu^{2+}_{(aq)} + 2\ OH^- \rightleftharpoons Cu_2O_{(s)} + H_2O \tag{2.17}$$

Although not explicitly discussed, they showed that at high CO_2 partial pressures the Cu_2O film growth and Cu^{2+} dissolution was independent of CO_2 (and thus HCO_3^- and CO_3^{2-} concentration), while at lower CO_2 partial pressures the film growth and dissolution increased with increasing CO_2 pressure. This correlation has been seen by many authors but it is unclear if this is an effect of the CO_2 or pH.[107]

A large area of research related to copper corrosion in the presence of HCO_3^- and CO_3^{2-} is the effects on pitting corrosion, specifically the growth of a protective film precursor. The conditions under which copper grows a passive film – likely a duplex film of Cu_2O/CuO or $Cu_2O/Cu(OH)_2$ – are not well-defined. HCO_3^- has been shown to both cause passivation and promote active dissolution.[102,108-110] The controversy may be due to the dual nature of bicarbonate based on the solution pH. That is, in acidic solutions bicarbonate promotes dissolution (and corrosion rate), whereas in alkaline solutions (reportedly ≥ 8.1) passivation is observed.[102,110] Increased dissolution at lower pH values is attributed to the complexation of Cu^{2+} with HCO_3^-, while the mechanism of passivation by HCO_3^- is contentious.[102,109,110] Some authors report that the passivation is due to the formation of basic copper carbonate films while others report that HCO_3^- adsorbs and stabilizes the passivating oxide or hydroxide film(s).[108,110] Some authors suspect that it is in fact the HCO^-/CO_3^{2-} ratio, not their individual concentration, that determines the passivation or dissolution of the underlying metal.[111]

2.3.6 Copper Corrosion in Nitrate Solutions

The complete nitrate reduction involves 8 electrons.

$$NO_3^- + 9\ H^+ + 8\ e^- \rightleftharpoons NH_3 + 3\ H_2O \tag{2.18}$$

Due to the high stability of many of the reaction intermediates, the reduction proceeds through a sequence of multi-step electron transfer reactions.[112] The nitrate reduction processes involve different intermediate steps depending on the nature of the electrode material, electrolyte pH, electrode potential, the presence of molecular or ionic additives in solution.[112-115] Nitrate reduction on different copper planes has different activities, thus a polycrystalline Cu^0 electrode may lead to several nitrate reduction products, although it is commonly accepted that the first reduction step is rate determining due to slow nitrate adsorption on the surfaces of transition metals (**Eq. 2.19**).[113,115,116]

$$NO_3^- + 2\ H^+ + 2\ e^- \rightleftharpoons NO_2^- + H_2O \tag{2.19}$$

Nitrite (NO_2^-) is commonly detected as a by-product during Cu^0 corrosion in the presence of nitrate (**Eq. 2.19**).[100,113,115] It is a weak acid with a pKa = 3.35 and its stability of nitrate is affected by the solution pH. Nitrite is stable in near-neutral and alkaline solutions but in acidic solutions, decomposition via **Eq. 2.20** or disproportionation via **Eq. 2.21** decreases its concentration.[117-119]

$$2\ HNO_2 \rightleftharpoons NO + NO_2 + H_2O \tag{2.20}$$

$$3\ HNO_2 \rightleftharpoons H^+ + NO_3^- + 2\ NO + H_2O \tag{2.21}$$

These reactions do not participate in electrochemical corrosion reactions but can be involved in chemical solution reactions. On metal surfaces, chemisorbed NO_2 can also undergo further reduction to form NO (**Eq. 2.22**).[117,119,120]

$$NO_2^-{}_{(ads)} + 2\,H^+ + e^- \rightleftharpoons NO_{(ads)} + H_2O \qquad (2.22)$$

Turnbull et al. (2017)[100] studied Cu^0 corrosion exposed to small volumes of acidic nitrate solutions. They found that nitrate reduction to nitrite participates in the oxidation of Cu^0, but that O_2 is the dominant oxidant. They proposed a corrosion mechanism involving three stages which depend on the solution reaching Cu^{2+} saturation. In subsequent papers, Turnbull et al.[121] used much larger solution volumes (with low pH values, ranging from 0.5 – 2), removing the effects of saturation, i.e. only studying their first stage when Cu^0 oxidizes and dissolves as Cu^{2+}.[100] From these experiments, they determined that the rate of Cu^0 corrosion in the first stage was independent of both the NO_3^- concentration and the H^+ concentration.[106,121] When using small water volumes, they determined the second stage of their proposed mechanism involves Cu_2O precipitation and the third involves the coprecipitation of NO_3^- with Cu^{2+} forming a layer on top of the Cu_2O crystals already on the surface. The third stage indicates that, although NO_3^- participates in the oxidation of Cu^0 to some degree, a significant amount remains in solution to coprecipitate with Cu^{2+} later in corrosion.

2.3.7 Copper Corrosion in the Presence of γ-Radiation

Corrosion studies in the presence of radiation are limited. Those that exist do not report corrosion rates or report only radiation-induced rate, without the unirradiated corrosion rate for comparison. Thus, understanding the impact of radiation is difficult. It is not possible to find consistent mechanistic explanations for the effect of radiation on the corrosion process.

Of the existing radiation-induced copper corrosion literature, results are conflicting. Even which species is the main oxidant for copper corrosion in the presence of radiation is contentious.[70,122] The controversy lies in the unexplained observation that more copper dissolution occurs in solutions exposed to radiation compared to in chemical solutions containing the same molecular oxidants.[72,123] The higher dissolution has been explained to be due to radiolytically-produced radical species, e.g. •OH, or, more recently, radiolytically produced O_2.[72,122,123] Radiolytically-produced H_2O_2 has been shown to be a stable species that exists in solution long enough to react with the metal surface and is considered the main oxidant for radiolytic copper corrosion.[65,70,71,123-125] H_2O_2 oxidation (**Eq. 2.23**) is both kinetically and thermodynamically favoured over O_2 reduction (**Eq. 2.16**).[126]

$$H_2O_2 + 2\,H^+ + 2\,e^- \rightleftharpoons 2\,H_2O \qquad E^0 = 1.776\ V_{SHE} \tag{2.23}$$

A key difference between solutions containing radiolysis products and solutions in the presence of radiation is that the latter has species that are continuously produced opposed to a chemical solution of these species in which they are decomposing over time. Additionally, key radiolysis products, i.e. H_2O_2 and NO_3^-, can couple with both the oxidation of Cu^0 and Cu(I), and reduction of Cu(II) and Cu(I).[100,127] However, the reduction of copper ions is only significant when their concentrations in solution are high, i.e., after long corrosion times. Only with their continuous production at all corrosion times (i.e., in the presence of radiation) can the short and long-term effects of radiolysis products be studied.

The presence of radiation during corrosion can cause phenomena that are not otherwise observed. For example, Bessho et al.[71] found the production of colloids and particulate copper species during copper vessel corrosion in the presence of γ-radiation. The species first formed at the copper/water interface then grew into the bulk solution and eventually dissociated from the surface after growing larger than 200 nm. While the authors speculated these species were copper oxides, no characterization was performed. Soroka et al.[21] also found colloidal formation in the presence of γ-radiation and determined it was cuprous hydroxide. In their case, Cu^{2+} was reduced to colloidal CuOH then formed the more stable Cu_2O. They reported the colloidal CuOH as a yellow precipitate, which is consistent with previous reports of hydrated Cu_2O.[12,128] The formation of these colloids in the presence of γ-radiation is commonly exploited for synthesis of metallic and metal oxide nanoparticles.[16,42,129,130]

Another phenomenon commonly seen during copper corrosion in the presence of radiation is patterns in the oxide layer; some examples are shown in **Figure 2.12**. These patterns are observed but their formation is not often discussed in depth.[131,132] Despite no correlation between the patterns and the underlying metallic structure (such as grain size), the patterns are often assumed to be associated with copper metal variances or a separation of cathodic and anodic sites on the metal.[45,72]

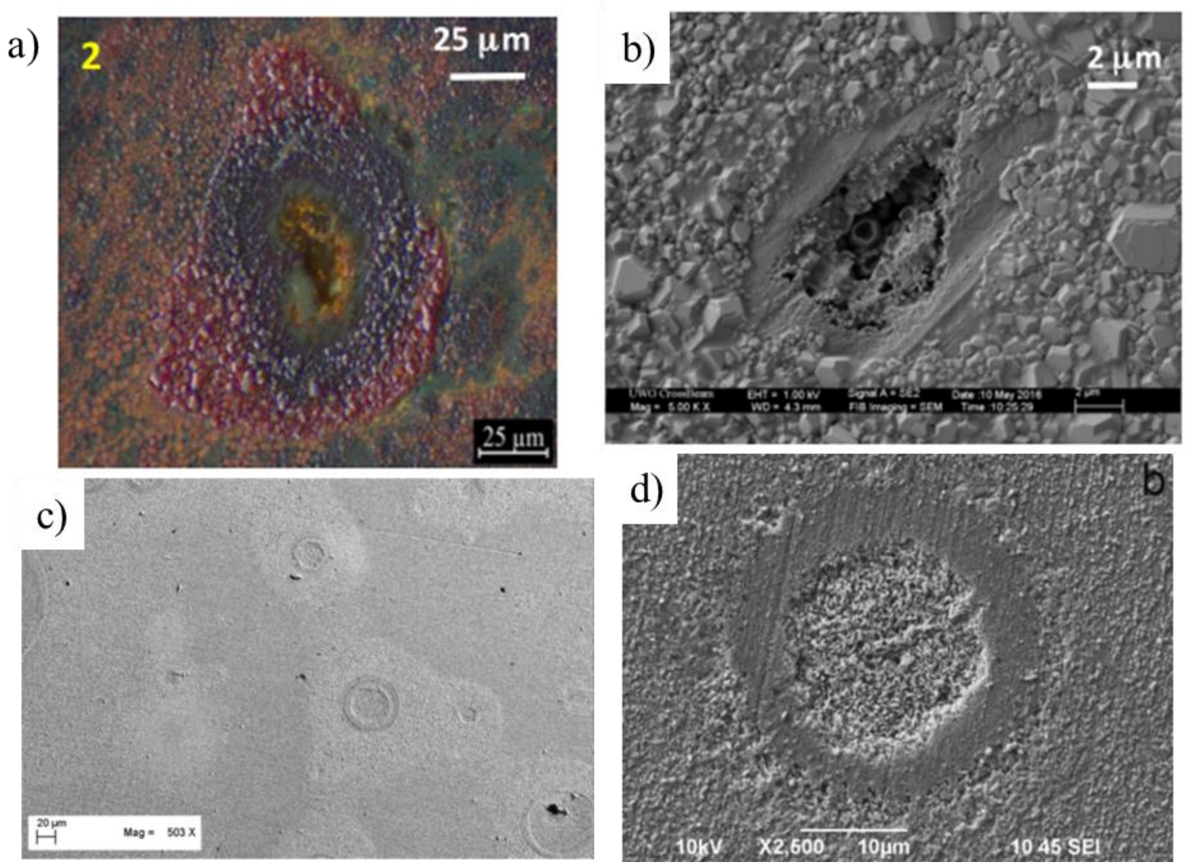

Figure 2.12 Patterns formed in Cu_2O film during radiation-induced corrosion. a,b[45] c[132] d[131]

2.4 PARTICLE RIPENING PHENOMENA

2.4.1 Ostwald Ripening

A two-phase system is thermodynamically unstable due to the large free energy associated with surfaces. Ostwald ripening is a thermodynamically driven crystal aging process that decreases the overall surface area of a system.[133,134] The driving force is the difference in solubilities of different sizes of particles. That is, the constituents in smaller particles, with a high surface energy, will mostly desorb from the surface while the constituents of larger particles, with higher lattice energy, will mostly adsorb.[135,136] Ostwald ripening is generally described for a homogeneous mixture in which the movement of crystal constituents is random. However, the adsorption of constituents on large crystals creates a slight concentration gradient in the local solution causing the continual growth of large crystals while small crystals cease to exist.[133] Small particles are kinetically favoured on short timescales, and the transformation of these particles into larger ones is thermodynamically favoured and will dominate after longer timescales.

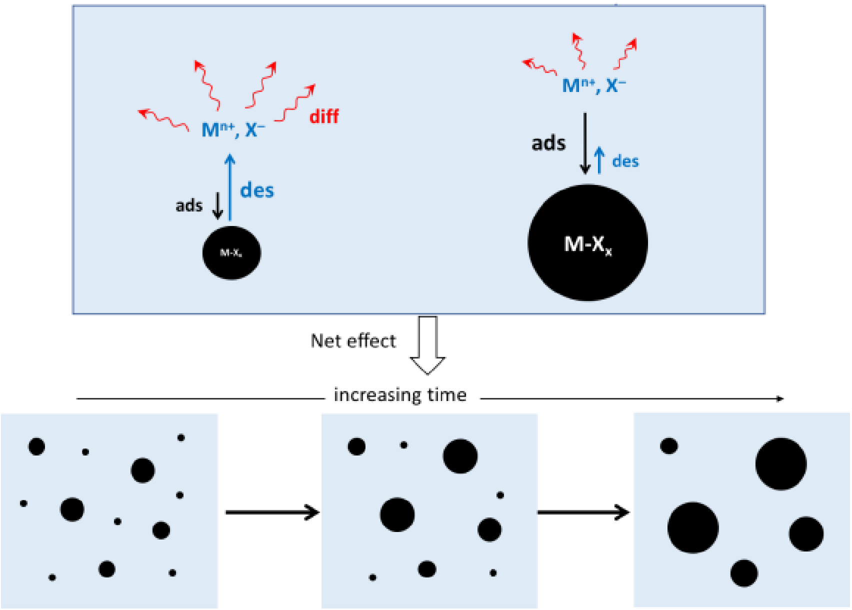

Figure 2.13 Schematic of the adsorption (ads) and desorption (des) processes on small and large particles and the effect of Ostwald ripening with increasing time.[136]

2.4.2 Liesegang Band Formation via Ostwald Ripening

In a closed system, the total mass of particles during crystal growth is conserved during Ostwald ripening. In a system in which the crystal constituent ions are continuously injected and transported through the system, the different adsorption-desorption isotherms from particles of different sizes and the transport of the ions can lead to growth and transport of bands of aggregated crystal particles, known as Liesegang rings or bands. Although the formation mechanism of Liesegang bands is not well established, the process is dependent on the coupling of reaction and diffusion processes, which can only occur in a slow transport medium such as porous rock (e.g., malachite) or a gel.[53,56,137-139]

Liesegang bands are typically monochromatic, alternating between precipitated salt and the absence of precipitation (where solution is unsaturated), schematically shown in **Figure 2.14**. Small crystals are continuously formed, due to the continuous injection of crystal constituents, and their aging via Ostwald ripening occurs in parallel. Large particles grow by absorbing the smaller particles around them, which leaves a volume void of crystals. The small particles that have formed further from the larger particles will undergo Ostwald ripening similar to the process of the first band.[136,138,139]

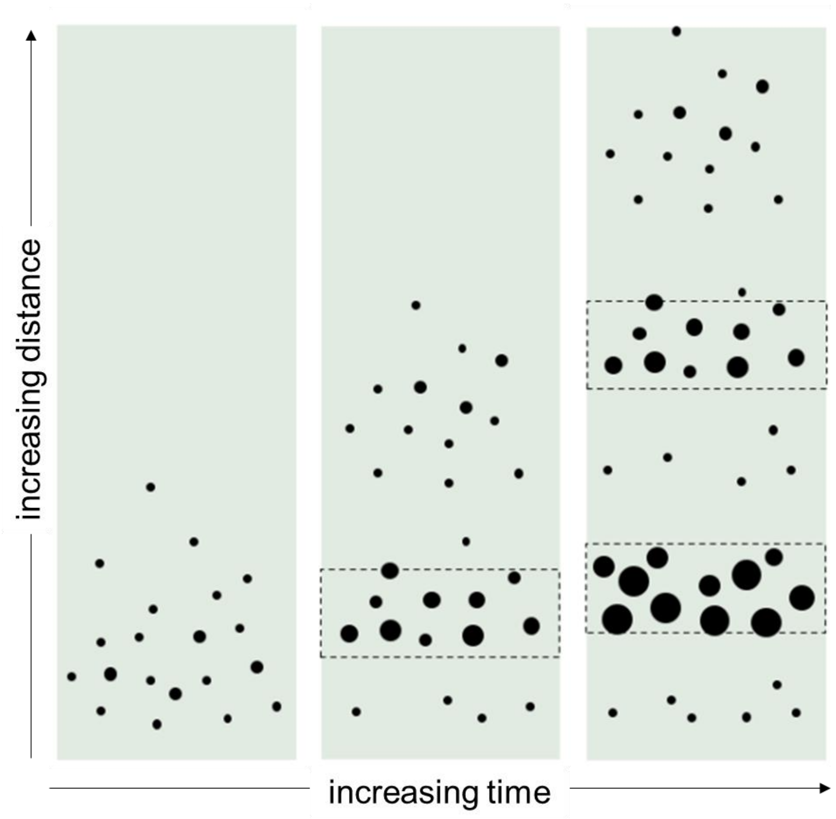

Figure 2.14 Schematic representation of the formation of Liesegang banding patterns.[136]

2.5 REFERENCES

1 Konečná, R., Fintová, S. *Copper and Copper Alloys: Casting, Classification and Characteristic Microstructures* in *Copper Alloys - Early Applications and Current Performance - Enhancing Processes* (ed Dr. Luca Collini) (InTech, 2012).

2 Greenwood, N. N., Earnshaw, A. *Chemistry of the Elements*. 2nd edn, (Butterworth-Heinemann, 1997).

3 Zoubov, N. D., Vanleugenhaghe, C., Pourbaix, M. *Copper* in *Atlas of Electrochemical Equilibria in Aqueous Solutions* Ch. 14.1, 384-392 (NACE International Cebelcor, 1974).

4 Baes, C. F., Mesmer, R. E. *The Hydrolysis of Cations*. (Wiley, 1976).

5 Pranowo, H. D., Bambang Setiaji, A. H., Rode, B. M. Cu^+ in Liquid Ammonia and in Water: Intermolecular Potential Function and Monte Carlo Simulation. *J. Phys. Chem. A* **103**, 11115-11120, (1999).

6 Powell, K. J., Brown, P. L., Byrne, R. H., Gajda, T., Hefter, G., Sjöberg, S., Wanner, H. Chemical Speciation of Environmentally Significant Metals with Inorganic Ligands. Part 2: The Cu^{2+}-OH^-, Cl^-, CO_3^{2-}, SO_4^{2-}, and PO_4^{3-} Systems. *Pure Appl. Chem.* **79**, 895-950, (2007).

7 Fick, A. On Liquid Diffusion. *Lond. Edinb. Dubl. Phil. Mag.* **10**, 30-39, (1855).

8 Grathwohl, P. *Diffusion in Natural Porous Media: Contaminant Transport, Sorption/Desorption and Dissolution Kinetics*. (Kluwer Academic Publishers, 1998).

9 Taxén, C. *Pitting Corrosion of Copper: Equilibrium-Mass Transport Limitations*. (SKB, 2011).

10 Oswald, H. R., Reller, A., Schmalle, H. W., Dubler, E. Structure of Copper(II) Hydroxide, $Cu(OH)_2$. *Acta Cryst. C* **46**, 2279-2284, (1990).

11 Henry, M., Bonhomme, C., Livage, J. Synthesis and Characterisation of Copper(II) Hydroxide Gels. *J. Sol-Gel Sci. Technol.* **6**, 155-167, (1996).

12 Rogers, A. F. A Review of the Amorphous Minerals. *J. Geol.* **25**, 515-541, (1917).

13 Hidmi, L., Edwards, M. Role of Temperature and pH in $Cu(OH)_2$ Solubility. *Environ. Sci. Technol.* **33**, 2607-2610, (1999).

14 Candal, R. J., Regazzoni, A. E., Blesa, M. A. Precipitation of Copper(II) Hydrous Oxides and Copper(II) Basic Salts. *J. Mater. Chem.* **2**, 657-661, (1992).

15 Fukumoto, S., Nakanishi, K., Kanamori, K. Direct Preparation and Conversion of Copper Hydroxide-Based Monolithic Xerogels with Hierarchical Pores. *New J. Chem.* **39**, 6771-6777, (2015).

16 Wang, D., Wu, Y., Bai, Z. Preparation of Ultrafine Cu_2O Powders with Different Morphologies from $Cu(OH)_2$ Gel. *J Mater Sci* **48**, 7696-7702, (2013).

17 Dörner, L., Cancellieri, C., Rheingans, B., Walter, M., Kägi, R., Schmutz, P., Kovalenko, M. V., Jeurgens, L. P. H. Cost-Effective Sol-Gel Synthesis of Porous CuO Nanoparticle Aggregates with Tunable Specific Surface Area. *Sci. Rep.* **9**, 11758, (2019).

18 Gustafson, R., Martell, A. Formation of Polynuclear Complexes in Aqueous Solution. *Ann. N.Y. Acad. Sci.* **88**, 322-331, (2006).

19 Nunes, D., Pimentel, A., Santos, L., Barquinha, P., Pereira, L., Fortunato, E., Martins, R. *Structural, Optical, and Electronic Properties of Metal Oxide Nanostructures* in *Metal Oxide Nanostructures* (eds Daniela Nunes *et al.*) Ch. 3, 59-102 (Elsevier, 2019).

20 Leygraf, C., Chang, T., Herting, G., Odnevall Wallinder, I. The Origin and Evolution of Copper Patina Colour. *Corros. Sci.* **157**, 337-346, (2019).

21 Soroka, I. L., Shchukarev, A., Jonsson, M., Tarakina, N. V., Korzhavyi, P. A. Cuprous Hydroxide in a Solid Form: Does It Exist? *Dalton Trans.* **42**, 9585-9594, (2013).

22 Korzhavyi, P. A., Johansson, B. *Thermodynamic Properties of Copper Compounds with Oxygen and Hydrogen from First Principles*. (SKB, 2010).

23 Gou, L., Murphy, C. J. Solution-Phase Synthesis of Cu_2O Nanocubes. *Nano Lett.* **3**, 231-234, (2003).

24 Thoka, S., Lee, A.-T., Huang, M. H. Scalable Synthesis of Size-Tunable Small Cu_2O Nanocubes and Octahedra for Facet-Dependent Optical Characterization and Pseudomorphic Conversion to Cu Nanocrystals. *ACS Sustain. Chem. Eng.* **7**, 10467-10476, (2019).

25 Xu, H., Wang, W., Zhu, W. Shape Evolution and Size-Controllable Synthesis of Cu_2O Octahedra and Their Morphology-Dependent Photocatalytic Properties. *J. Phys. Chem. B* **110**, 13829-13834, (2006).

26 Liang, X., Gao, L., Yang, S., Sun, J. Facile Synthesis and Shape Evolution of Single-Crystal Cuprous Oxide. *Adv. Mater.* **21**, 2068-2071, (2009).

27 Chen, K., Song, S., Xue, D. Hopper-Like Framework Growth Evolution in a Cubic System: A Case Study of Cu_2O. *J. Appl. Crystallogr.* **46**, (2013).

28 Chen, K., Sun, C., Song, S., Xue, D. Polymorphic Crystallization of Cu_2O Compound. *CrystEngComm* **16**, 5257-5267, (2014).

29 Chen, K., Song, S., Xue, D. Chemical Reaction Controlled Synthesis of Cu_2O Hollow Octahedra and Core–Shell Structures. *CrystEngComm* **15**, 10028-10033, (2013).

30 Feng, L., Zhang, C., Gao, G., Cui, D. Facile Synthesis of Hollow Cu_2O Octahedral and Spherical Nanocrystals and Their Morphology-Dependent Photocatalytic Properties. *Nanoscale Res. Lett.* **7**, 276, (2012).

31 Lu, C., Qi, L., Yang, J., Wang, X., Zhang, D., Xie, J., Ma, J. One-Pot Synthesis of Octahedral Cu_2O Nanocages via a Catalytic Solution Route. *Adv. Mater.* **17**, 2562-2567, (2005).

32 Zhu, H., Wang, J., Xu, G. Fast Synthesis of Cu_2O Hollow Microspheres and Their Application in DNA Biosensor of Hepatitis B Virus. *Cryst. Growth Des.* **9**, 633-638, (2009).

33 King, F. *Corrosion of Copper in Alkaline Chloride Environments*. (SKB, 2002).

34 Wick, R., Tilley, S. D. Photovoltaic and Photoelectrochemical Solar Energy Conversion with Cu_2O. *J. Phys. Chem. C* **119**, 26243-26257, (2015).

35 Wan, X., Wang, J., Zhu, L., Tang, J. Gas Sensing Properties of Cu_2O and its Particle Size and Morphology-Dependent Gas-Detection Sensitivity. *J. Mater. Chem. A* **2**, 13641-13647, (2014).

36 Zhang, J., Liu, J., Peng, Q., Wang, X., Li, Y. Nearly Monodisperse Cu_2O and CuO Nanospheres: Preparation and Applications for Sensitive Gas Sensors. *Chem. Mater.* **18**, 867-871, (2006).

37 Huang, W., Liu, Q., Zhou, Z., Li, Y., Ling, Y., Wang, Y., Tu, Y., Wang, B., Zhou, X., Deng, D., Yang, B., Yang, Y., Liu, Z., Bao, X., Yang, F. Tuning the Activities of Cuprous Oxide Nanostructures via the Oxide-Metal Interaction. *Nat. Commun.* **11**, 2312, (2020).

38 Wan, L., Zhou, Q., Wang, X., Wood, T. E., Wang, L., Duchesne, P. N., Guo, J., Yan, X., Xia, M., Li, Y. F., Jelle, A. A., Ulmer, U., Jia, J., Li, T., Sun, W., Ozin, G. A. Cu_2O Nanocubes with Mixed Oxidation-State Facets for (Photo)catalytic Hydrogenation of Carbon Dioxide. *Nat. Catal.* **2**, 889-898, (2019).

39 Wu, Y., McNulty, I., Liu, C., Lau, K. C., Liu, Q., Paulikas, A., Sun, C.-J., Cai, Z., Guest, J., Ren, Y., Stamenkovic, V., Curtiss, L., Liu, Y., Rajh, T. Facet-Dependent

Active Sites of a Single Cu_2O Particle Photocatalyst for CO_2 Reduction to Methanol. *Nat. Energy* **4**, 1-12, (2019).

40 Chen, K., Song, S., Xue, D. Faceted Cu_2O Structures with Enhanced Li-Ion Battery Anode Performances. *CrystEngComm* **17**, 2110-2117, (2015).

41 Zhang, L., Li, Q., Xue, H., Pang, H. Fabrication of Cu_2O-based Materials for Lithium-Ion Batteries. *ChemSusChem* **11**, 1581-1599, (2018).

42 Hai, Z., Zhu, C., Huang, J., Liu, H., Chen, J. Controllable Synthesis of CuO Nanowires and Cu_2O Crystals with Shape Evolution via γ-Irradiation. *Inorg. Chem.* **49**, 7217-7219, (2010).

43 Nakayama, S., Kaji, T., Notoya, T., Osakai, T. Mechanistic Study of the Reduction of Copper Oxides in Alkaline Solutions by Electrochemical Impedance Spectroscopy. *Electrochim. Acta* **53**, 3493-3499, (2008).

44 Bárta, J., Pospíšil, M., Čuba, V. Photo- and Radiation-Induced Preparation of Nanocrystalline Copper and Cuprous Oxide Catalysts. *J. Radioanal. Nucl. Chem.* **286**, 611-618, (2010).

45 Jean, A. M. "Evolution of Cu_2O Morphology During Copper Corrosion in the Presence of Gamma-Radiation" M.Sc., The University of Western Ontario, Electronic Thesis and Dissertation Repository. (2017). 4593.

46 Korzhavyi, P. A., Johansson, B. *Literature Review on the Properties of Cuprous Oxide Cu_2O and the Process of Copper Oxidation*. (SKB, 2011).

47 Desarnaud, J., Derluyn, H., Carmeliet, J., Bonn, D., Shahidzadeh, N. Hopper Growth of Salt Crystals. *J. Phys. Chem. Lett.* **9**, 2961-2966, (2018).

48 Brauer, G. *Handbook of Preparative Inorganic Chemistry*. Second edn, (Academic Press, Inc., 1963).

49 Zhou, F., Li, Z., Shenoy, G. J., Li, L., Liu, H. Enhanced Room-Temperature Corrosion of Copper in the Presence of Graphene. *ACS Nano* **7**, 6939-6947, (2013).

50 Deng, Y., Handoko, A. D., Du, Y., Xi, S., Yeo, B. S. *In Situ* Raman Spectroscopy of Copper and Copper Oxide Surfaces during Electrochemical Oxygen Evolution Reaction: Identification of Cu^{III} Oxides as Catalytically Active Species. *ACS Catal.* **6**, 2473-2481, (2016).

51 Biesinger, M. C. Advanced Analysis of Copper X-Ray Photoelectron Spectra. *Surf. Interface Anal.* **49**, 1325-1334, (2017).

52 Grauer, R. *Solubility Products of M(II)-Carbonates*. (National Cooperative for the Disposal of Radioactive Waste (Nagra), 1999).

53 Papineau, D. Chemically Oscillating Reactions in the Formation of Botryoidal Malachite. *Am. Mineral.* **105**, 447-454, (2020).

54 Vink, B. W. Stability Relations of Malachite and Azurite. *Mineral. Mag.* **50**, 41-47, (2018).

55 Kuntzleman, T. S., Cullen, D. M., Milam, S., Ragan, D. Rapid Formation of Copper Patinas: A Simple Chemical Demonstration of Why the Statue of Liberty Is Green. *J. Chem. Educ.* **97**, 2244-2248, (2020).

56 Orlik, M. Self-Organization in Nonlinear Dynamical Systems and Its Relation to the Materials Science. *J. Solid State Electrochem.* **13**, 245-261, (2009).

57 Mari, G., Martin, R. F. La Gerhardtite et la Rouaïte: Découvertes et Juxtapositions à Roua. *Riviera Scientifiqu* **104**, 37-50, (2020).

58 Zhang, J., Richardson, H. W.*Copper Compounds* in *ULLMANN'S Encyclopedia of Industrial Chemistry* (Wiley-VCH Verlag GmbH & Co., 2016).

59 Frost, R. L., Leverett, P., Williams, P. A., Weier, M. L., Erickson, K. L. Raman Spectroscopy of Gerhardtite at 298 and 77 K. *J. Raman Spectrosc.* **35**, 991-996, (2004).

60 Yoder, C., Bushong, E., Liu, X., Weidner, V., McWilliams, P., Martin, K., Lorgunpai, J., Haller, J., Schaeffer, R. The Synthesis and Solubility of the Copper Hydroxyl Nitrates: Gerhardtite, Rouaite and Likasite. *Mineral. Mag.* **74**, 433-440, (2010).

61 Spinks, J. W. T., Woods, R. J. *An Introduction to Radiation Chemistry*. 2nd edn, (Wiley, 1976).

62 O'Donnell, J. H. *Principles of Radiation Chemistry*. (American Elsevier, 1970).

63 Wren, J. C. *Steady-State Radiolysis: Effects of Dissolved Additives* in *Nuclear Energy and the Environment* Vol. 1046 *ACS Symposium Series* (eds C. M. Wai & B. J. Mincher) 271-295 (2010).

64 Bobrowski, K. *Radiation Chemistry of Liquid Systems* in *Applications of Ionizing Radiation in Materials Processing* Vol. 1 (eds Yongxia Sun & Andrzej G. Chmielewski) Ch. 4, 81 - 116 (Institute of Nuclear Chemistry and Technology, 2017).

65 Joseph, J. M., Choi, B. S., Yakabuskie, P., Wren, J. C. A Combined Experimental and Model Analysis on the Effect of pH and $O_{2(aq)}$ on Gamma-Radiolytically Produced H_2 and H_2O_2. *Radiat. Phys. Chem.* **77**, 1009-1020, (2008).

66 Yakabuskie, P., Joseph, J., Wren, J. The Effect of Interfacial Mass Transfer on Steady-State Water Radiolysis. *Radiat. Phys. Chem.* **79**, 777-785, (2010).

67 Yakabuskie, P. A., Joseph, J. M., Stuart, C. R., Wren, J. C. Long-Term γ-Radiolysis Kinetics of NO_3^- and NO_2^- Solutions. *J. Phys. Chem. A* **115**, 4270-4278, (2011).

68 Wren, J. C., Glowa, G. A. A Simplified Kinetic Model for the Degradation of 2-Butanone in Aerated Aqueous Solutions under Steady-State Gamma-Radiolysis. *Radiat. Phys. Chem.* **58**, 341-356, (2000).

69 Ferradini, C., Jay-Gerin, J.-P. The Effect of pH on Water Radiolysis: A Still Open Question — A Minireview. *Res. Chem. Intermed.* **26**, 549-565, (2000).

70 Daub, K., Zhang, X., Noël, J. J., Wren, J. C. Effects of γ-Radiation Versus H_2O_2 on Carbon Steel Corrosion. *Electrochim. Acta* **55**, 2767-2776, (2010).

71 Bessho, K., Oki, Y., Akimune, N., Matsumura, H., Masumoto, K., Sekimoto, S., Osada, N., Kinoshita, N., Monjushiro, H., Shibata, S. Corrosion of Copper in Water and Colloid Formation Under Intense Radiation Field. *J. Radioanal. Nucl. Chem.* **303**, 1117-1121, (2015).

72 Björkbacka, Å., Hosseinpour, S., Johnson, M., Leygraf, C., Jonsson, M. Radiation Induced Corrosion of Copper for Spent Nuclear Fuel Storage. *Radiat. Phys. Chem.* **92**, 80-86, (2013).

73 Morco, R. P., Joseph, J. M., Hall, D. S., Medri, C., Shoesmith, D. W., Wren, J. C. Modelling of Radiolytic Production of HNO_3 Relevant to Corrosion of a Used Fuel Container in Deep Geologic Repository Environments. *Corros. Eng. Sci. Technol.* **52**, 141-147, (2017).

74 Hall, D. S., Keech, P. G. An Overview of the Canadian Corrosion Program for the Long-Term Management of Nuclear Waste. *Corros. Eng. Sci. Technol.* **52**, 2-5, (2017).

75 Bard, A. J., Faulkner, L. R. *Electrochemical Methods: Fundamentals and Applications*. 2nd edn, (John Wiley, 2001).

76 King, F. *Critical Review of the Literature on the Corrosion of Copper by Water*. (SKB, 2010).

77 Merkel, T. H., Pehkonen, S. O. General Corrosion of Copper in Domestic Drinking Water Installations: Scientific Background and Mechanistic Understanding. *Corros. Eng. Sci. Technol.* **41**, 21-37, (2006).

78 Vargas, I. T., Fischer, D. A., Alsina, M. A., Pavissich, J. P., Pastén, P. A., Pizarro, G. E. Copper Corrosion and Biocorrosion Events in Premise Plumbing. *Materials* **10**, (2017).

79 Beverskog, B., Puigdomenech, I. Revised Pourbaix Diagrams for Copper at 25 to 300°C. *J. Electrochem. Soc.* **144**, 3476-3483, (1997).

80 McCafferty, E. Validation of Corrosion Rates Measured by the Tafel Extrapolation Method. *Corros. Sci.* **47**, 3202-3215, (2005).

81 Scully, J. C. *The Fundamentals of Corrosion*. Second edn, (Elsevier Science & Technology Books, 1975).

82 Wroblowa, H. S., Yen Chi, P., Razumney, G. Electroreduction of Oxygen: A New Mechanistic Criterion. *J. Electroanal. Chem. Interfacial Electrochem.* **69**, 195-201, (1976).

83 Hsueh, K. L., Chin, D. T., Srinivasan, S. Electrode Kinetics of Oxygen Reduction: A Theoretical and Experimental Analysis of the Rotating Ring-Disc Electrode Method. *J. Electroanal. Chem. Interfacial Electrochem.* **153**, 79-95, (1983).

84 Brandt, E. Electrochemistry of Oxygen and Hydrogen Peroxide at Clean and at Halide-Covered Polycrystalline Silver. *J. Electroanal. Chem.* **150**, 97-109, (1983).

85 Zhang, Q., Liu, P., Zhu, Z., Zhang, J., Cao, F. The Study of the H_2O_2 During Oxygen Reduction Process on Typically Corroding Metal Surface Using Tip Generation-Substrate Collection Mode of SECM. *Corros. Sci.* **164**, 108312, (2020).

86 Delahay, P. A Polarographic Method for the Indirect Determination of Polarization Curves for Oxygen Reduction on Various Metals. *J. Electrochem. Soc.* **97**, 198, (1950).

87 Cuppett, J. D., Duncan, S. E., Dietrich, A. M. Evaluation of Copper Speciation and Water Quality Factors That Affect Aqueous Copper Tasting Response. *Chem. Senses* **31**, 689-697, (2006).

88 Leckie, H. P. The Anodic Polarization Behavior of Copper. *J. Electrochem. Soc.* **117**, 1478, (1970).

89 King, F., Lilja, C., Vähänen, M. Progress in the Understanding of the Long-Term Corrosion Behaviour of Copper Canisters. *J. Nucl. Mater.* **438**, 228-237, (2013).

90 Ives, D. J. G., Rawson, A. E. Copper Corrosion: II. Kinetic Studies. *J. Electrochem. Soc.* **109**, 452, (1962).

91 Feng, Y., Tan, K. L., Hsieh, A. K., Teo, W. K., Siow, K. S. Corrosion Mechanisms and Products of Copper in Aqueous Solutions at Various pH Values. *Corros. Sci.* **53**, 389-398, (1997).

92 Keech, P. G., Behazin, M., Binns, W. J., Briggs, S. An Update on the Copper Corrosion Program for the Long-Term Management of Used Nuclear Fuel in Canada. *Mater. Corros.* **72**, 25-31, (2020).

93 Feng, Y., Teo, W. K., Siow, K. S., Tan, K. l., Hsieh, A. K. The Corrosion Behaviour of Copper in Neutral Tap Water. Part I: Corrosion Mechanisms. *Corros. Sci.* **38**, 369-385, (1996).

94 Merkel, T. H., Groß, H.-J., Werner, W., Dahlke, T., Reicherter, S., Beuchle, G., Eberle, S. H. Copper Corrosion By-Product Release in Long-Term Stagnation Experiments. *Water Res.* **36**, 1547-1555, (2002).

95 Brusic, V., Frisch, M. A., Eldridge, B. N., Novak, F. P., Kaufman, F. B., Rush, B. M., Frankel, G. S. Copper Corrosion With and Without Inhibitors. *J. Electrochem. Soc.* **138**, 2253-2259, (1991).

96 Dortwegt, R., Maughan, E. The Chemistry of Copper in Water and Related Studies Planned at the Advanced Photon Source in *Proceedings of the 2001 Particle Accelerator Conference.* 1456-1458.

97 Feng, Y., Teo, W. K., Siow, K. S., Hsieh, A. K. The Corrosion Behaviour of Copper in Neutral Tap Water. Part II: Determination of Corrosion Rates. *Corros. Sci.* **38**, 387-395, (1996).

98 Metikoš-Huković, M., Babić, R., Marinović, A. Spectrochemical Characterization of Benzotriazole on Copper. *J. Electrochem. Soc.* **145**, 4045-4051, (1998).

99 Folquer, M. E., Ribotta, S. B., Real, S. G., Gassa, L. M. Study of Copper Dissolution and Passivation Processes by Electrochemical Impedance Spectroscopy. *Corrosion* **58**, 240-247, (2002).

100 Turnbull, J., Szukalo, R., Behazin, M., Hall, D., Zagidulin, D., Ramamurthy, S., Wren, J. C., Shoesmith, D. W. The Effects of Cathodic Reagent Concentration and Small Solution Volumes on the Corrosion of Copper in Dilute Nitric Acid Solutions. *Corrosion* **74**, 326-336, (2017).

101 Calle, G. R., Vargas, I. T., Alsina, M. A., Pastén, P. A., Pizarro, G. E. Enhanced Copper Release from Pipes by Alternating Stagnation and Flow Events. *Environ. Sci. Technol.* **41**, 7430-7436, (2007).

102 Edwards, M., Schock, M. R., Meyer, T. E. Alkalinity, pH, and Copper Corrosion By-Product Release. *J. Am. Water Works Assoc.* **88**, 81-94, (1996).

103 Peters, D. W. *Corrosion and Passivation of Copper* in *Handbook of Cleaning in Semiconductor Manufacturing: Fundamental and Applications* (eds Karen A. Reinhardt & Richard F. Reidy) Ch. 11, 395-428 (Scrivener Publishing LLC. , 2010).

104 Ives, D. J. G., Rawson, A. E. Copper Corrosion: I . Thermodynamic Aspects. *J. Electrochem. Soc.* **109**, 447, (1962).

105 Ives, D. J. G., Rawson, A. E. Copper Corrosion: III . Electrochemical Theory of General Corrosion. *J. Electrochem. Soc.* **109**, 458, (1962).

106 Ives, D. J. G., Rawson, A. E. Copper Corrosion: IV . The Effects of Saline Additions. *J. Electrochem. Soc.* **109**, 462, (1962).

107 Sobue, K., Sugahara, A., Nakata, T., Imai, H., Magaino, S. Effect of Free Carbon Dioxide on Corrosion Behavior of Copper in Simulated Water. *Surf. Coat. Technol.* **169-170**, 662-665, (2003).

108 King, F., Ahonen, L., Taxén, C., Vuorinen, U., Werme, L. *Copper Corrosion Under Expected Conditions in a Deep Geologic Repository*. (SKB, 2001).

109 Sirikia, P., Saario, T., Makela, K., Laitinen, T., Bojinov, M. *Electric and Electrochemical Properties of Surface Films Formed on Copper in the Presence of Bicarbonate Anions*. (VTT Manufacturing Technology, 1999).

110 Ribotta, S. B., Folquer, M. E., Vilche, J. R. Influence of Bicarbonate Ions on the Stability of Prepassive Layers Formed on Copper in Carbonate-Bicarbonate Buffers. *Corrosion* **51**, 682-688, (1995).

111 González, S., Pérez, M., Barrera, M., González Elipe, A. R., Souto, R. M. Mechanism of Copper Passivation in Aqueous Sodium Carbonate−Bicarbonate Solution Derived from Combined X-ray Photoelectron Spectroscopic and Electrochemical Data. *J. Phys. Chem. B* **102**, 5483-5489, (1998).

112 Bae, S.-E., Stewart, K. L., Gewirth, A. A. Nitrate Adsorption and Reduction on Cu(100) in Acidic Solution. *J. Am. Chem. Soc.* **129**, 10171-10180, (2007).

113 Dima, G. E., de Vooys, A. C. A., Koper, M. T. M. Electrocatalytic Reduction of Nitrate at Low Concentration on Coinage and Transition-Metal Electrodes in Acid Solutions. *J. Electroanal. Chem.* **554-555**, 15-23, (2003).

114 de Vooys, A. C. A., Koper, M. T. M., van Santen, R. A., van Veen, J. A. R. Mechanistic Study on the Electrocatalytic Reduction of Nitric Oxide on Transition-Metal Electrodes. *J. Catal.* **202**, 387-394, (2001).

115 Pérez-Gallent, E., Figueiredo, M. C., Katsounaros, I., Koper, M. T. M. Electrocatalytic Reduction of Nitrate on Copper Single Crystals in Acidic and Alkaline Solutions. *Electrochim. Acta* **227**, 77-84, (2017).

116 Bae, S.-E., Gewirth, A. A. Differential Reactivity of Cu(111) and Cu(100) During Nitrate Reduction in Acid Electrolyte. *Faraday Discuss.* **140**, 113-123, (2009).

117 Evans, U. R. Behaviour of Metals in Nitric Acid. *Trans. Faraday Soc.* **40**, 120-130, (1944).

118 Lewis, G. N., Edgar, A. The Equilibrium Between Nitric Acid, Nitrous Acid and Nitric Oxide. *J. Am. Chem. Soc.* **33**, 292-299, (1911).

119 Turnbull, J., Szukalo, R., Zagidulin, D., Shoesmith, D. Nitrite Effects on Copper Corrosion in Nitric Acid Solutions. *Corros. Sci.* **179**, 109147, (2021).

120 Rosca, V., Duca, M., de Groot, M. T., Koper, M. T. M. Nitrogen Cycle Electrocatalysis. *Chem. Rev.* **109**, 2209-2244, (2009).

121 Turnbull, J., Szukalo, R., Zagidulin, D., Biesinger, M., Shoesmith, D. The Kinetics of Copper Corrosion in Nitric Acid. *Mater. Corros.* **72**, 1-13, (2020).

122 Soroka, I., Chae, N., Jonsson, M. On the Mechanism of γ-Radiation-Induced Corrosion of Copper in Water. *Corros. Sci.* **182**, 109279, (2021).

123 Björkbacka, Å., Yang, M., Gasparrini, C., Leygraf, C., Jonsson, M. Kinetics and Mechanisms of Reactions Between H_2O_2 and Copper and Copper Oxides. *Dalton Trans.* **44**, 16045-16051, (2015).

124 Knapp, Q. W., Wren, J. C. Film Formation on Type-316L Stainless Steel as a Function of Potential: Probing the Role of Gamma-Radiation. *Electrochim. Acta* **80**, 90-99, (2012).

125 Behazin, M., Noël, J. J., Wren, J. C. Combined Effects of pH and γ-Irradiation on the Corrosion of Co-Cr Alloy Stellite-6. *Electrochim. Acta* **134**, 399-410, (2014).

126 Borden, W. T., Hoffmann, R., Stuyver, T., Chen, B. Dioxygen: What Makes This Triplet Diradical Kinetically Persistent? *J. Am. Chem. Soc.* **139**, 9010-9018, (2017).

127 Björkbacka, Å., Johnson, C. M., Leygraf, C., Jonsson, M. Radiation Induced Corrosion of Copper in Humid Air and Argon Atmospheres. *J. Electrochem. Soc.* **164**, C201-C206, (2017).

128 Khatouri, J., Mostafavi, M., Amblard, J., Belloni, J. Radiation-Induced Copper Aggregates and Oligomers. *Chem. Phys. Lett.* **191**, 351-356, (1992).

129 Flores-Rojas, G. G., López-Saucedo, F., Bucio, E. Gamma-Irradiation Applied in the Synthesis of Metallic and Organic Nanoparticles: A Short Review. *Radiat. Phys. Chem.* **169**, 107962, (2020).

130 Alrehaily, L. M., Joseph, J. M., Biesinger, M. C., Guzonas, D. A., Wren, J. C. Gamma-Radiolysis-Assisted Cobalt Oxide Nanoparticle Formation. *Phys. Chem. Chem. Phys.* **15**, 1014-1024, (2013).

131 Björkbacka, Å., Saman, H., Leygraf, C., Jonsson, M. Radiation Induced Corrosion of Copper in Anoxic Aqueous Solution. *Electrochem. Solid-State Lett.* **15**, C5-C7, (2012).

132 Björkbacka, Å., Johnson, C. M., Leygraf, C., Jonsson, M. Role of the Oxide Layer in Radiation-Induced Corrosion of Copper in Anoxic Water. *J. Phys. Chem. C* **120**, 11450-11455, (2016).

133 Kahlweit, M. Ostwald Ripening of Precipitates. *Adv. Colloid Interface Sci.* **5**, 1-35, (1975).

134 Yao, J. H., Elder, K. R., Guo, H., Grant, M. Theory and Simulation of Ostwald Ripening. *Physical Review B* **47**, 14110-14125, (1993).

135 Lifshitz, I. M., Slyozov, V. V. The Kinetics of Precipitation From Supersaturated Solid Solutions. *J. Phys. Chem. Solids* **19**, 35-50, (1961).

136 Shin, Y. G. "Nonlinear Dynamics of Carbon Steel Corrosion under Gamma Radiation" Doctor of Philosophy, The University of Western Ontario, Electronic Thesis and Dissertation Repository. (2020). 7339.

137 Stern, K. H. The Liesegang Phenomenon. *Chem. Rev.* **54**, 79-99, (1954).

138 Sadek, S., Sultan, R. *Liesegang Patterns in Nature: A Diverse Scenery Across the Sciences* in *Precipitation Patterns in Reaction-Diffusion Systems* (ed Istvan Lagzi) Ch. 1, 1-43 (Research Signpost, 2011).

139 Smith, D. On Ostwald's Supersaturation Theory of Rhythmic Precipitation (Liesegang's Rings). *J. Chem. Phys.* **81**, 3102-3115, (1984).

CHAPTER 3. EXPERIMENTAL DETAILS

This chapter describes the principles of the experimental techniques used for the work presented in this thesis. Additional experimental details specific to each chapter are provided in those chapters.

3.1 SAMPLE PREPARATION

3.1.1 Materials and Solutions

All experiments were performed with high purity copper (99.9% purity) coupons made from wrought copper samples (provided by SKB, the Swedish Nuclear Waste Management Company) with an exposed surface area of 0.785 cm^2. The coupons were ground using silicon carbide papers (Buehler, Inc., Wooster, OH) with grit size 400, 800, and 1200 in succession, washing with pure water and drying with argon gas between each grit size and before starting each experiment. For experiments that used water volumes larger than 100 μL (i.e. **Chapter 5** and **8**), the coupon was contained within a polyvinyl chloride (PVC) shrink tube (Techflex, Sparta, NJ); more details are given in the respective chapter.

All solutions used in this study were prepared using water purified with a NANOpure Diamond UV ultra-pure water system (Barnstead International, Dubuque, IA) to give a resistivity of 18.2 MΩ·cm. Solutions were purged with compressed zero air (i.e., air with 0 ppm CO_2) (Praxair, Danbury, CT), 21% O_2 (balance Ar) (Praxair, Danbury, CT), or ultra high purity $Ar_{(g)}$ (Praxair, Danbury, CT), as specified in each chapter, for 1 h.

3.1.2 Exposure Procedure

The coupons were placed in 20 mL vials and sealed with an aluminum crimp cap with a polytetrafluoroethylene (PTFE)-coated silicone septum (Thermo Fisher Scientific, Waltham, MA). The vials were purged with compressed zero air (Praxair, Danbury, CT), 21% O_2 (balance Ar) (Praxair, Danbury, CT), or ultra high purity $Ar_{(g)}$ (Praxair, Danbury, CT), as specified in each chapter, for 30 minutes. The solution was then placed on the copper surface through the septum using a syringe. Vials were irradiated using a MDS Nordion (Ottawa, ON) Gamma Cell 220 Excel ^{60}Co irradiator, as described in the next section. A second set of experiments was performed under the same conditions but without irradiation, by leaving the vials on the benchtop.

3.1.3 Post-Test Analysis

Individual vials were removed from the irradiation chamber at regular time intervals for aqueous and surface analysis. The solution was collected using a plastic Pasteur pipette, transferred to a 4 mL dram vial and the pH was measured using a ThermoScientific Orion 9110DJWP Double Junction Micro-pH Electrode. The surface was washed with 5 mL of pure water, then the coupon was removed and dried with Ar. The two solutions were then combined for inductively coupled plasma optical emission spectroscopy (ICP-OES) analysis. The coupon was stored in a vacuum chamber until surface analysis was performed.

Surface analysis consisted of high-resolution optical microscopy, scanning electron microscopy (SEM), focused-ion beam (FIB) milling, and Raman spectroscopy, all discussed in detail in this chapter. Optical microscopy was used because it provides information about thin hydroxide/oxide layers formed on the surface due to the strong absorbance of visible light by copper complexes. Additionally, optical images allow the whole coupon surface can be seen at once giving information about the average solid deposits across the surface at that time. SEM provides topographical information about the surface and FIB milling allows investigation of the metal-oxide interface. Characterization of the oxide surface was performed by Raman spectroscopy and energy dispersive X-ray spectroscopy (EDX).

3.2 GAMMA CELL IRRADIATOR

Radiation experiments were performed using a MDS Nordion (Ottawa, ON) Gamma Cell 220 Excel ^{60}Co irradiator, shown in **Figure 3.1a,b**. The radiation source, ^{60}Co, is contained in a cylindrical array of stainless steel "pencils" surrounded by a steel-encased lead shell. Samples are loaded into a motorized stage that vertically enters and exits the sample irradiation area. This is to permit safe loading of samples without exposure to the radiation source.

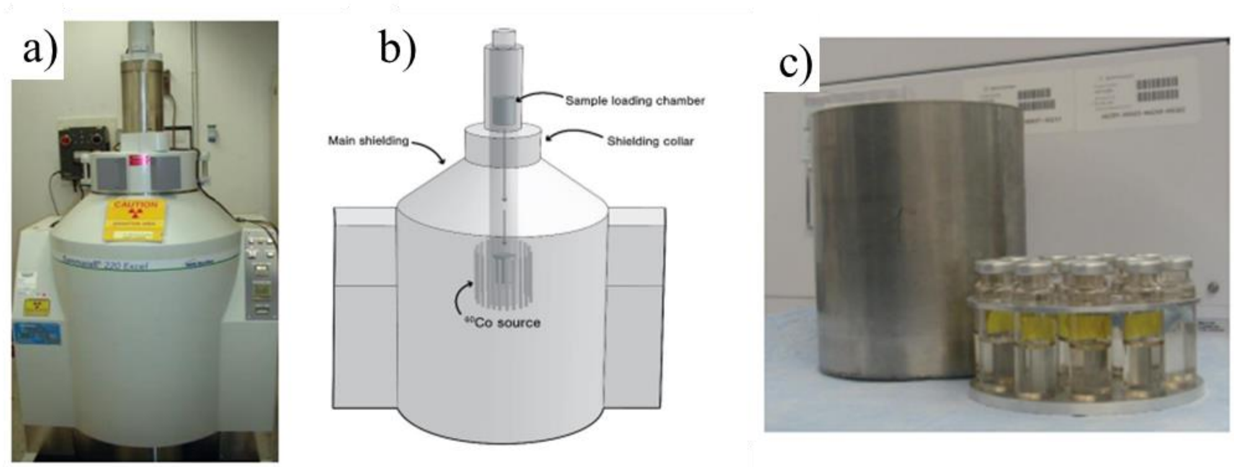

Figure 3.1 a) Picture and b) schematic of ^{60}Co gamma cell irradiator and c) custom-designed sample holder.

Cobalt-60 has a half-life of 5.3 years, undergoing beta decay according to **Eq. 3.1** emitting two gamma photons with energies of 1.17 and 1.33 MeV. The beta particle (e^-) emitted has a maximum energy of 0.32 MeV, but cannot penetrate the stainless steel pencils to interact with samples in the gamma cell irradiator.[1]

$$^{60}_{27}Co \rightarrow {}^{60}_{28}Ni + e^- + \bar{\nu} + 2\,\gamma \tag{3.1}$$

Sample vials were placed in a custom-designed sample holder, shown in **Figure 3.1c**, to ensure that all samples received the same dose throughout the irradiation period. Over the 4 years of experimentation performed in this thesis, the absorbed radiation dose rate in the irradiation chamber ranged from 2.1 – 1.4 kGy/h, where 1 Gy is equivalent to 1 J of energy absorbed per kg of water. The radiation dose used in these studies is approximately 1000× the dose rate expected in DGR conditions on the outside of the UFC.[2]

3.3 SAMPLE ANALYSIS

3.3.1 Optical Microscopy

Optical microscopy is used in this thesis because it provides information about thin hydroxide/oxide layers formed on the surface due to the strong reflectance of visible light by copper complexes. That is, the colour provides chemical information for the solid species on the surface, which is discussed in detail in **Section 6.3.1**. Additionally, optical images allow for the whole coupon surface to be imaged simultaneously which allows spatial variations to be perceived.

Optical microscopes use a series of lenses to focus on a sample illuminated by visible light and produce magnified images.[3] A Leica (Wetzlar, Germany) DVM6A digital microscope was used to perform the analysis presented in this thesis. The objective lens (PlanAPO FOV 12.55) with a 46× to 675× magnification has an integrated ring light and a coaxial LED illumination. The microscope has a digital camera, in place of an eyepiece, and thus the images produced are displayed on a computer monitor using the Leica LAS X Basic Functions software.

3.3.2 Scanning Electron Microscopy

Scanning electron microscopy (SEM) was used to analyze the morphology of the oxides formed during corrosion. In SEM (**Figure 3.2a**), a focused beam of high-energy electrons scans the surface of a sample, while the electrons interact with and decelerate within the sample. There are several detection modes, with the most common being the detection of secondary electrons (SE). SE are those resulting from the ionization of the material, and, with low incident electron energies, only SE from the top few nanometers of the sample will be detected. The number of SE (the intensity of the signal) is used to develop a morphological image of the surface.[3,4]

Another common mode is detecting backscattered electrons (BSE), which are created through elastic interactions with the sample, and thus can escape from greater depths from within the sample compared to SE. The intensity of the BSE signal is proportional to atomic number of the sample and the resulting image yields information about distribution of elements within the sample. That is, materials with a higher atomic number will appear brighter than those with a lower atomic number.[3-5]

SEM was performed at the Western Nanofabrication Facility using Zeiss (Oberkochen, Germany) LEO 1530 and 1540XB instruments. The latter is a dual beam field emission SEM and FIB, which was also used for the FIB milling (**Section 3.3.3**) and is fitted with an Oxford Instruments X-ray system for elemental mapping (**Section 3.3.4**). The electron high tension (EHT) or accelerating voltage used was 1 kV.

3.3.3 Focused Ion Beam Milling

Focused ion beam (FIB) milling is a very precise cutting technique achieved using a gallium ion beam to sputter atoms at the surface of the sample. The sample stage is tilted to face the FIB column, as shown in **Figure 3.2b**, to ensure the ions are hitting the material perpendicular to the surface. The Ga^+ beam has an accelerating voltage between 5 to 50 keV, chosen based on the desired amount of material to be removed, and has a precision of 5 nm.[6]

FIB milling was used in this project to investigate the cross-section of the interface between the bulk copper and the surface. Information on the porosity and oxide thickness can be obtained with this method. Secondary electron SEM images of the FIB milled cross-section were obtained using the Zeiss LEO 1540XB FIB/SEM at the Western Nanofabrication Facility.

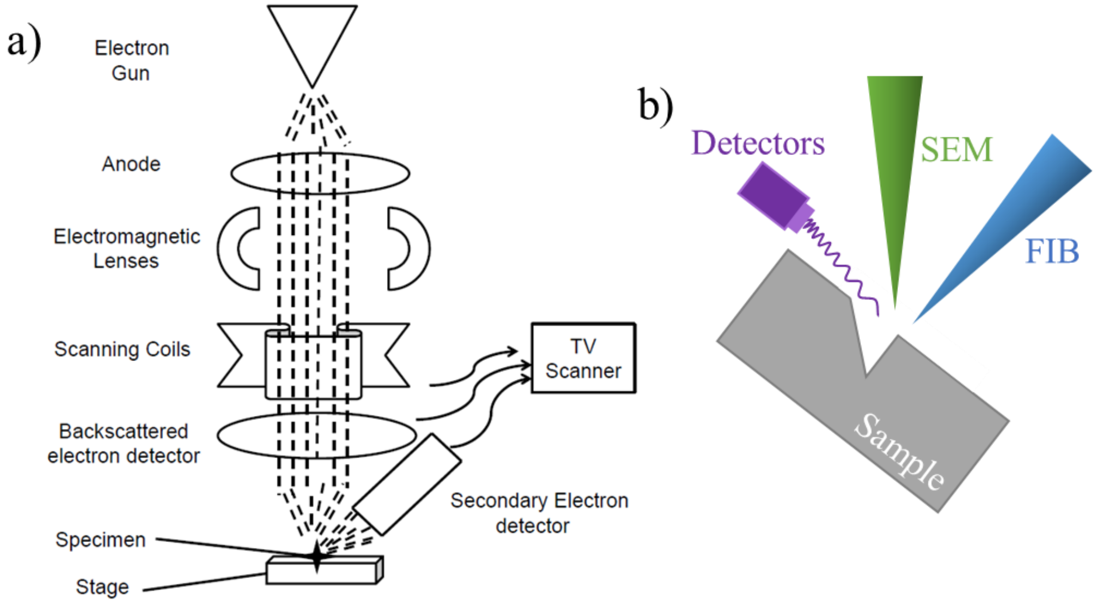

Figure 3.2 Schematic of a) SEM[7] and b) dual-beam FIB and SEM.

3.3.4 Energy Dispersive X-Ray Spectroscopy

Energy dispersive X-ray spectroscopy (EDX or EDS) is a chemical characterization technique, usually connected to an electron microscopy instrument, such as SEM. The sample is exposed to a high-voltage electron beam, which ejects an inner shell electron from the sample. The relaxation process involves a higher shell electron filling the electron hole, and this process releases characteristic X-rays. From these X-rays, the elements on the surface can be identified and their distribution mapped. Depending on the accelerating voltage of the electron beam and the sample being investigated, X-rays escape from a depth of 1 − 2 μm.[5] Furthermore, more insulating samples can decelerate and deflect the incoming electron beam, decreasing the number of X-rays that come from that material.[8] EDX analyses presented in this thesis were performed at the Western Nanofabrication Facility using Zeiss LEO 1540XB instrument fitted with an Oxford Instruments (Abingdon, UK) Si-PIN photodiode X-ray detector.

3.3.5 Raman Spectroscopy

Raman spectroscopy was used in this thesis to characterize the solid products formed during corrosion. It is an analytical technique used to determine the molecular vibrational modes of the sample and thus, often compared to infrared spectroscopy. However, Raman spectroscopy is favoured for samples exposed to aqueous solutions, as water is only weakly Raman active. A laser (most commonly visible light) is used to induce a change in polarizability of the electron cloud around a molecule. The incident photons can be elastically scattered, which is referred to as Rayleigh scattering (filtered out during Raman spectroscopy), or inelastically scattered, referred to as Raman scattering. The Raman scattering gives information about the sample's vibrational modes and determined using the difference in energy between the incident photon and the scattered photon.[4,9,10]

During Raman scattering, an electron is excited to a virtual electronic energy level corresponding to the energy of the incident photon (ν_0). The final state of the excited electron is in the same electronic energy level but different vibrational energy level. Illustrated in **Figure 3.3**, when the final state is higher in energy than the initial one, it is called "Stokes Raman scattering", while in "anti-Stokes Raman scattering" the final state is lower in energy than the initial one. The scattered photon is either lower (Stokes) or higher (anti-Stokes) in energy compared to the incident photon, and this change in energy is referred to as the Raman shift. The Stokes Raman shift is more probable and thus commonly measured in Raman spectroscopy.[4,9,10]

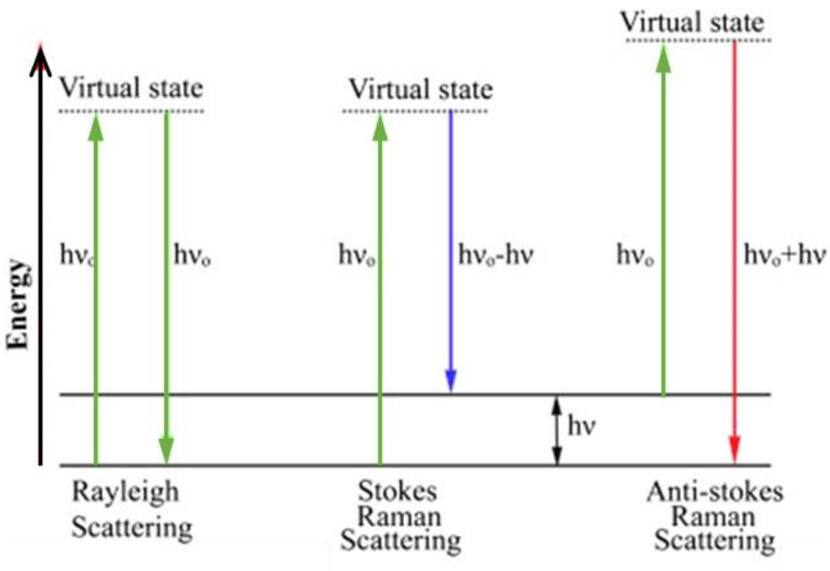

Figure 3.3 Illustration of Rayleigh scattering (elastic), Stokes and anti-Stokes Raman scattering (inelastic) that occurs during Raman spectroscopy. Adapted from N. John and S. George.[10]

The Raman spectrum yields a vibrational fingerprint which is characteristic of the molecule. The intensity of the Raman peaks in a spectrum are proportional to induced change in polarizability of the bond, which is equally as characteristic of molecules as the Raman shift. Thus, the Raman shift and relative intensity of the peaks in the Raman spectrum should be analyzed to accurately determine the molecules present in an unknown sample. The Raman shift is usually presented in inverse wavelength ($1/\lambda$) units called wavenumbers (cm^{-1}). A Renishaw (Wotton-under-Edge, UK) InVia Reflex Model 2000 Raman spectrometer with a holographic notch filter and 1800 l/mm grating was used to perform the experiments presented in this thesis. It is equipped with a MellesGriot (Carlsbad, CA) 35 mW HeNe laser with a wavelength of 633 nm and was used at 10 % power to ensure minimal surface degradation. The spot size was approximately 1 μm with a penetration depth of 2 – 3 μm, and all spectra were calibrated against the 521 cm^{-1} peak of silicon. Thermo Scientific (Walthan, MA) GRAMS 386 Raman software was used to collect and manipulate the spectra. This analysis was performed at Surface Science Western.

3.4 SOLUTION ANALYSIS

3.4.1 Micro-pH Electrode

The pH of solutions was measured before and after each experiment using a Thermo Scientific (Waltham, MA) Orion 9110DJWP Double Junction Micro-pH Electrode designed for small solution volumes with a ± 0.02 pH accuracy. The difference in potential between the pH electrode, which is inserted into the sample solution, and the reference electrode is measured then converted into pH (i.e., the hydrogen ion activity) using the Nernst equation. The pH meter was calibrated daily using a 2-point calibration curve using buffer solutions of 2.0, 4.0, 7.0, and 10.0, depending on the sample pH.

3.4.2 Inductively Coupled Plasma Optical Emission Spectroscopy

Inductively coupled plasma optical emission spectroscopy (ICP-OES) was used in the work presented in this thesis to quantify the amount of dissolved copper present in solution. An inductively coupled plasma torch (**Figure 3.4b**) is employed, which is composed of Ar plasma formed from an intense oscillating electromagnetic field in a Tesla coil. The liquid sample (aqueous in this thesis) is introduced directly into the plasma through a nebulizer (creating a mist, **Figure 3.4b**). The ions and electrons in the plasma decompose the sample into atoms which ionize and recombine several times within the plasma. During recombination, ions release photons with a characteristic wavelength. The intensity of the signal at a particular wavelength is proportional to the concentration of the corresponding element. The concentration of the sample is determined using a calibration curve obtained using samples of known concentrations.[4,11]

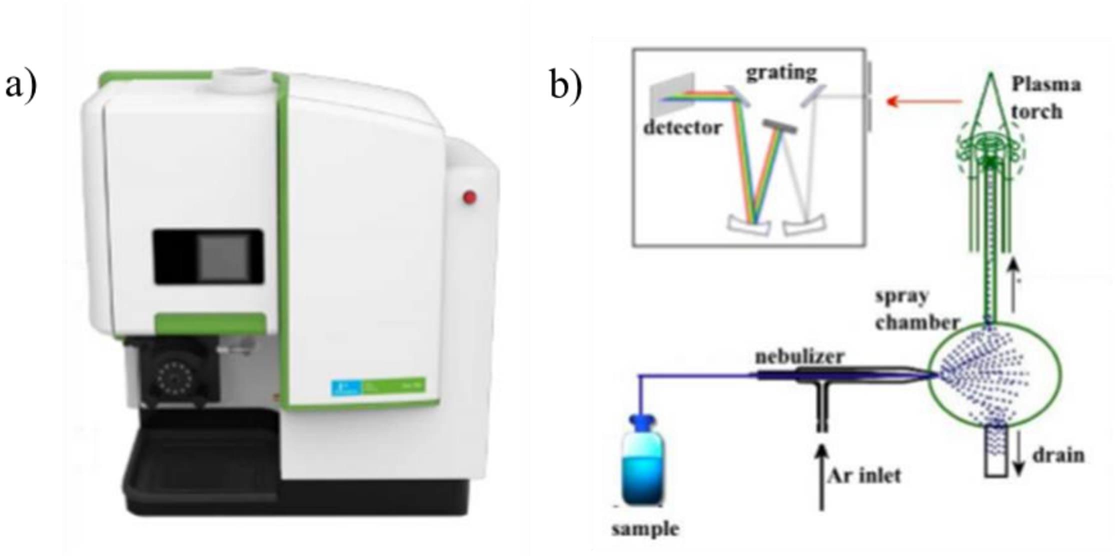

Figure 3.4 a) ICP-OES instrument and b) a schematic of the sample injection method and plasma torch.[12]

In this work the test solutions were analyzed using a PerkinElmer (Waltham, MA) Avio 200 ICP-OES (**Figure 3.4a**) with a Scott/Cross flow nebulizer and a charge-coupled device (CCD) detector. Particles in solution were digested using 2 % nitric acid (Sigma Aldrich, St. Louis, MO) prior to analysis. The detection limit for copper ions using this method is 6.3 pM at a wavelength of 327.4 nm. The four-point calibration curves used $CuSO_4$ (Sigma Aldrich, St. Louis, MO) standards at low (0.001 – 0.020 mM) or high (0.020 – 5.00 mM) concentrations, depending on the test solution, shown in **Figure 3.5**. The relative standard deviation on all measured concentrations was < 5 %, indicating a high precision.

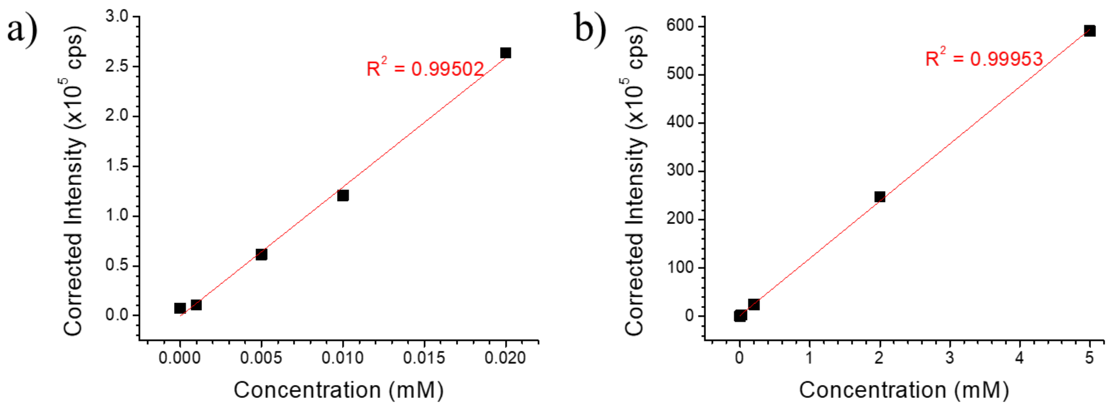

Figure 3.5 ICP-OES calibration curves for a) low (0.001 – 0.020 mM) and b) high (0.020 – 5.00 mM) Cu^{2+} standards.

3.4.3 Ultraviolet-Visible Spectrophotometry

Ultraviolet-visible (UV-Vis) spectroscopy was used in this thesis to quantify the concentration of H_2O_2 in the test solutions. In this technique, the sample solution is exposed to a wide range of light ranging from UV (190 – 380 nm) to visible (380 – 750 nm). Molecules in the solution can be electronically excited by a particular wavelength of light that corresponds to the energy difference of the transition. The absorption of this light lowers the intensity at that wavelength, which is detected by a diode array detector on the opposite side of the sample. The ratio of the incident light intensity (I_0) to the transmitted light intensity (I) is called the absorbance. The absorbance (A) at a particular wavelength is used to calculate the concentration (c in M) of the corresponding molecule through the Beer-Lambert law (**Eq. 3.2**), where ε is the molar extinction coefficient (M^{-1} cm^{-1}) and l is the path length through the sample (cm).[4]

$$A = log\frac{I_0}{I} = \varepsilon \cdot c \cdot l \tag{3.2}$$

The UV-Vis spectroscopy tests done in this thesis were performed using a diode array spectrophotometer (BioLogic Science Instruments, Seyssinet-Pariset, France). Determination of the H_2O_2 concentration was performed using the Ghormley triiodide method.[13] In this method, I^- is oxidized to I_3^- by H_2O_2 in the presence of a molybdate catalyst and excess I^-. The absorbance of I_3^- is measured spectrophotometrically at 352 nm with a molar extinction coefficient of 25,500 M^{-1} cm^{-1}. The H_2O_2 concentration is then determined by the stoichiometry of the reaction between I_3^- and H_2O_2 (**Eq. 3.3**).

$$3\ I^- + H_2O_2 + 2\ H^+ \rightarrow I_3^- + 2\ H_2O \tag{3.3}$$

3.5 REFERENCES

1 ICRP. *Nuclear Decay Data for Dosimetric Calculations*. (ICRP, 2008).

2 Morco, R. P., Joseph, J. M., Hall, D. S., Medri, C., Shoesmith, D. W., Wren, J. C. Modelling of Radiolytic Production of HNO_3 Relevant to Corrosion of a Used Fuel Container in Deep Geologic Repository Environments. *Corros. Eng. Sci. Technol.* **52**, 141-147, (2017).

3 Egerton, R. F. *Physical Principles of Electron Microscopy, An Introduction to TEM, SEM, and AEM*. (Springer, 2005).

4 Skoog, D. A., Holler, F. J., Nieman, T. A. *Principles of Instrumental Analysis*. 5th edn, (Harcourt Brace College Publishers, 1998).

5 Goldstein, J., Newbury, D. E., Joy, D. C., Lyman, C. E., Echlin, P., Lifshin, E., Sawyer, L., Michael, J. R. *Scanning Electron Microscopy and X-Ray Microanalysis*. Third edn, (Springer US, 2003).

6 Young, R. J., Moore, M. V. *Dual-Beam (FIB-SEM) Systems* in *Introduction to Focused Ion Beams: Instrumentation, Theory, Techniques and Practice* (eds Lucille A. Giannuzzi & Fred A. Stevie) 247-268 (Springer US, 2005).

7 Tare, M., Puli, O., Oros, S., Singh, A. Drosophila Adult Eye Model to Teach Scanning Electron Microscopy in an Undergraduate Cell Biology Laboratory. *Dros. Inf. Serv.* **92**, 174-180, (2009).

8 Imashuku, S., Sakatoku, S., Kawai, J. Effect of Electrical Charging on Scanning Electron Microscopy-Energy Dispersive X-Ray Spectroscopy Analysis of Insulating Materials. *Spectrochim. Acta B* **86**, 94-98, (2013).

9 Smith, E., Dent, G. *Modern Raman Spectroscopy: A Practical Approach*. Second edn, (John Wiley & Sons, 2019).

10 John, N., George, S. *Raman Spectroscopy* in *Spectroscopic Methods for Nanomaterials Characterization* (eds Sabu Thomas, Raju Thomas, Ajesh K. Zachariah, & Raghvendra Kumar Mishra) Ch. 5, 95-127 (Elsevier, 2017).

11 Boss, C. B., Fredeen, K. J. *Concepts, Instrumentation and Techniques in Inductively Coupled Plasma Optical Emission Spectrometry*. (Perkin Elmer, 1999).

12 Caruso, F., Mantellato, S., Palacios, M., Flatt, R. J. ICP-OES Method for the Characterization of Cement Pore Solutions and Their Modification by Polycarboxylate-Based Superplasticizers. *Cem. Concr. Res.* **91**, 52-60, (2017).

13 Ghormley, J. A., Stewart, A. C. Effects of γ-Radiation on Ice. *J. Am. Chem. Soc.* **78**, 2934-2939, (1956).

CHAPTER 4: EVOLUTION OF THE [$Cu^{II}_{(sol'n)}$]-pH RELATIONSHIP

4.1 INTRODUCTION

Corrosion is the process of metal loss, which can involve many chemical reactions including interfacial charge and mass transfer processes. Copper corrosion occurs through the oxidation of the solid metal ($Cu^0_{(m)}$) to soluble metal cation (Cu^{2+}), coupled with the reduction of oxidant (e.g., O_2 to OH^-), at the metal-solution interface ($z = 0$, where z is the distance from the metal surface) (**Eq. 4.1**) and the transport of species between the interface ($z = 0$) and the bulk solution ($z = \delta_{diff}$) (**Eq. 4.2**).

Interfacial charge and mass transfer reactions at $z = 0$:

Ox. half-reaction: $Cu^0_{(m)} \rightleftarrows Cu^{2+} + 2\ e^-$ (4.1a)

Red. half-reaction: $O_2 + 2\ H_2O + 4\ e^- \rightleftarrows 4\ OH^-$ (4.1b)

Overall reaction: $2\ Cu^0_{(m)} + O_2 + 2\ H_2O \rightleftarrows 2\ Cu^{2+} + 4\ OH^-$ (4.1c)

The subscript (m) represents the metal phase, and the species without phase designations are all solvated species. The electrochemical potential of the corroding system in **Eq. 4.1** changes throughout the corrosion process due to a changing concentration of Cu^{2+} in the solution adjacent to the metal surface. If the metal cation concentration in the interfacial solution is known, the electrochemical potential of the system at a given time may be calculated based on the standard electrode potentials reported in **Chapter 2** using the Nernst equation.

Transport of reactants and products through the diffusion layer ($0 < z < \delta_{diff}$):

$Cu^{2+}|_{z = 0} \rightsquigarrow Cu^{2+}|_{z = \delta_{diff}}$ (4.2a)

$O_2|_{z = \delta_{diff}} \rightsquigarrow O_2|_{z = 0}$ (4.2b)

$OH^-|_{z = 0} \rightsquigarrow OH^-|_{z = \delta_{diff}}$ (4.2c)

where δ_{diff} is the diffusion length. The solution from $z = 0$ to $z = \delta_{diff}$ will be referred to as the interfacial solution. The bulk solution phase begins where the redox species (O_2, OH^- and Cu^{2+}) can be treated as homogeneously distributed, i.e., the bulk solution begins at $z = \delta_{diff}$.

Because the overall process of corrosion involves interfacial electron and mass transfer reactions and mass transport through the solution phase, the rate of corrosion depends strongly on the redox and transport conditions of the solution in contact with the metal.

Unlike an electrochemical process on an inert electrode, corrosion involves interfacial transfer of metal atoms as well as electrons. Metal cations are continuously produced at the metal-solution interface, followed by their mass transport into the bulk solution. Although there are two possible dissolved ion species that can be produced from copper oxidation at room temperature, the cupric ion (Cu^{2+}) is more stable than the cuprous ion (Cu^{+}) in water at $pH < 9.0$.[1] If cupric ions are able to accumulate in solution (e.g., in stagnant solutions, small volumes), their solution reactions and transport processes can become increasingly important with time and establish cyclic feedback loops with preceding processes (including charge transfer at the metal surface). The solution reactions and transport processes of metal cations are significantly affected by solution parameters, including pH, ionic strength, temperature, and the presence of anions.

Recent studies on transition metal corrosion,[2-7] including the studies presented in this thesis, have demonstrated that the diffusion and hydrolysis of metal cations can have a significant effect on the corrosion evolution. These solution reactions can lead to precipitation of solid metal hydroxide, initially as nano-sized colloid particles which aggregate and grow into a hydrogel network. The metal hydroxide colloid precursor precipitates out of the solution phase as a solid phase (hydrogel network) when the concentration of the metal cation exceeds the solubility of the metal hydroxide salt (i.e., the solution must first be supersaturated with metal cations before the metal hydroxide hydrogel can precipitate). The hydrogel network consists of a semi-stationary phase made of loosely connected colloids with pores through which aqueous solution and dissolved species can diffuse.[4,5,8] Once a layer of hydrogel covers a corroding metal surface, it can have a significant effect on the overall transport of metal cations from the metal surface where they are produced to the bulk solution. This slower metal cation transport can also promote redox reactions between the metal cation and the metal. Thus, once a hydrogel layer begins to cover the surface, the overall metal oxidation (or metal loss) rate can change significantly.

In solution, transition metal cations are present in more than one chemical form due to the hydrolysis equilibrium[9]:

$$Cu^{2+} + 2\ OH^{-} \rightleftharpoons Cu(OH)^{+} + OH^{-} \rightleftharpoons Cu(OH)_{2(solv)} + H_2O \rightleftharpoons Cu(OH)_3^{-} + H^{+} \qquad (4.3)$$

where all of the cupric species are solvated species, but the phase designation using subscript (solv) is given only to the neutral species $Cu(OH)_2$ to distinguish it from its solid form. The hydrolysis equilibrium, being an acid-base equilibrium, is established very quickly. Hence, once in solution, the dissolved cupric ion exists in various chemical forms and all the hydrolyzed species will be henceforth collectively referred to as $Cu^{2+}_{(sol'n)}$.

$$Cu^{2+}_{(sol'n)} \equiv Cu^{2+} + Cu(OH)^{+} + Cu(OH)_{2(solv)} + Cu(OH)_3^{-} \qquad (4.4)$$

The relative amounts of the different chemical forms of $Cu^{2+}_{(sol'n)}$ are determined by the pKa values of the hydrolysis equilibria (**Eq. 4.3**) and hence, are a function of the total dissolved cupric ion concentration ($[Cu^{2+}_{(sol'n)}]$) and $[OH^{-}]$. However, due to the many hydrolysis products, the solubility (the solid-product equilibrium constant, K_{sp}) of transition metals does not have a simple 2nd order dependence on $[OH^{-}]$ over the entire pH range. Nevertheless, the solubility of transition metal hydroxides as a function of pH at ambient temperatures has been well studied.[9] The solubility of cupric and cuprous ions at room temperature is shown in **Figure 4.1**.

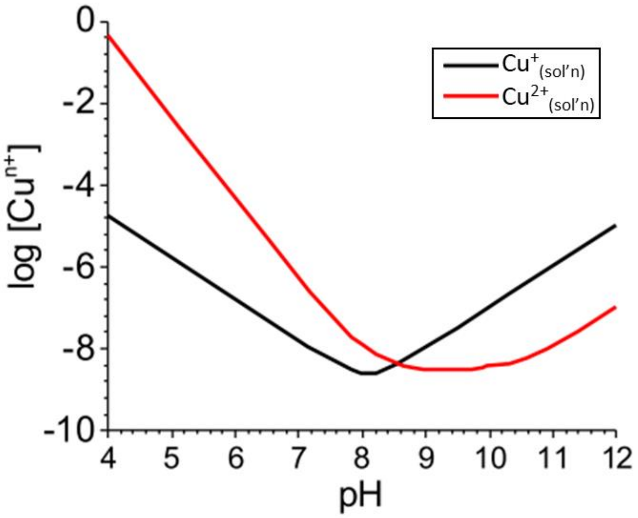

Figure 4.1 Solubility of cuprous ions ($Cu^{+}_{(sol'n)}$) and cupric ions ($Cu^{2+}_{(sol'n)}$) in water at 25 ºC.

When the total dissolved cupric ion concentration exceeds its saturation limit, the solubility of $Cu(OH)_{2(solid)}$, it can begin to precipitate:

$$Cu^{2+}_{(sol'n)} + x\,OH^{-} \rightarrow\rightarrow Cu(OH)_{2(colloid)} \rightarrow\rightarrow Cu(OH)_{2(hydrogel)} \tag{4.5}$$

Whether or not a metal hydroxide hydrogel layer can be formed on the metal surface therefore depends on whether the $Cu^{2+}_{(sol'n)}$ formed by the corrosion reactions can accumulate to its saturation limit in the interfacial solution. Whether the saturation limit can be reached or not, in turn, depends on the net production of $Cu^{2+}_{(sol'n)}$ (via interfacial charge transfer at the interface followed by its transport into the bulk solution) and the pH in the interfacial solution.

In this chapter we investigated the corrosion dynamics of copper during the early times in each set of solution conditions studied in this thesis. In early corrosion times, copper is oxidized to form mainly dissolved cupric ions, and this period will be referred to as Stage 1 throughout this thesis. The subsequent stage involves the formation of metal hydroxide hydrogel and will be referred to as Stage 2 throughout this thesis. Because the overall corrosion process also consumes H^+ (or produces OH^-), the copper corrosion dynamics in stagnant small volume solutions were studied by analyzing the time-dependent behaviours of $[H^+]$ as well as dissolved metal concentration $[Cu^{II}_{(sol'n)}]$. By studying the corrosion behaviours common in each set of solution conditions, we can establish the time dependences of $[H^+]$ and $[Cu^{2+}_{(sol'n)}]$ as a function of initial pH_0 and solution redox environment, from which we can determine the elementary rate-determining steps involved in corrosion in Stages 1 and 2. We are also interested in determining whether the relationship of $[Cu^{II}_{(sol'n)}]$ versus $[H^+]$ evolves with time and, if so, does it follow that of the metal cation solubility versus $[H^+]$. These results can then help to determine whether copper corrosion evolves beyond Stage 1 to hydrogel production and beyond in each studied set of solution conditions, and whether detailed corrosion dynamic modeling past Stage 2 is necessary for prediction of the long-term corrosion behaviour.

4.2 EXPERIMENTAL

4.2.1 Materials and Solutions

All experiments were performed with high purity copper (99.9% purity) coupons made from wrought copper samples (provided by SKB, the Swedish Nuclear Waste Management

Company) with an exposed surface area of 0.785 cm^2. The top surface of the copper coupons was ground using silicon carbide papers with grit size 400, 800, and 1200 in succession. The coupons were then washed with deionized water, dried under flowing $Ar_{(g)}$, and placed in a 20 mL vial sealed with an aluminum crimp cap with a polytetrafluoroethylene (PTFE)-coated silicone septum (Thermo Fisher Scientific, Waltham, MA). More information on this procedure is provided in **Section 3.1**. All solutions used in this study were prepared using water purified with a NANOpure Diamond UV ultra-pure water system (Barnstead International, Dubuque, IA) to give a resistivity of 18.2 MΩ·cm.

A range of different experimental conditions are explored in this chapter, drawn from the other chapters of this thesis. The experimental details for each chapter are summarized in **Table 4.1**.

Table 4.1 Summary of experimental conditions for each chapter.

	Chapter 5	Chapter 6	Chapter 7	Chapter 8
Initial pH	4, 7	7	7	9 (droplet) 7 (volumes)
Cover gas	Aerated	CO_2-free	Variable	Variable Aerated
Radiation	Absent	Absent and Present	Absent and Present	Absent and Present
Solution Volume (mL)	2	0.1 droplet	0.1 droplet	0.1 droplet (pH 9) 0.5 – 2 (pH 7)

4.2.2 Post-Test Analyses

Experiments were terminated by removing the solution from the coupon surface using a Pasteur pipette. The pH of this solution was determined using a Thermo Scientific Orion 9110DJWP Double Junction Micro-pH Electrode with a ± 0.02 pH accuracy. The solution was then diluted so the dissolved copper concentration could be quantified using inductively coupled plasma optical emission spectroscopy (ICP-OES) (PerkinElmer Avio 200 ICP-OES) with < 5 % relative standard deviation. More information on the procedure for solution analysis can be found in **Section 3.4**. The instrumental uncertainty is negligible compared to the individual data points and to the variation due to corrosion processes (explained in detail in **Chapter 6**) and thus, instrumental errors bars on plots are omitted.

4.3 RESULTS AND DISCUSSION

4.3.1 Time-Dependent Changes in [$Cu^{II}_{(sol'n)}$] and pH

Corrosion occurs through many different elementary steps and the step(s) that determines the overall rate (the rate determining step, RDS) can change with time. Initially, the metal oxidation half-reaction to form the soluble cupric ion is coupled with the reduction of dissolved oxidant (e.g., O_2 or H_2O_2) to form OH^-.

$$Cu^0_{(m)} + ½ \, O_2 + H_2O \rightleftarrows Cu^{2+} + 2\,OH^- \qquad z = 0 \qquad (4.6a)$$

$$Cu^0_{(m)} + H_2O_2 \rightleftarrows Cu^{2+} + 2\,OH^- \qquad z = 0 \qquad (4.6b)$$

The full redox reactions may be reversible, as suggested by the "⇄" arrows, but they are not necessarily at equilibrium.

After their formation at the metal surface, the products of **Eq. 4.6** (i.e., Cu^{2+} and OH^-) diffuse through the interfacial solution (**Eq. 4.2**). While diffusing away, cupric ions remain in hydrolysis equilibria (**Eq. 4.3**), and the main form of the cupric ions thus changes not only with corrosion time (t), but also distance from the metal surface (z). The concentrations of the initial corrosion products, [$Cu^{2+}_{(sol'n)}$] and [OH^-], will be higher at $z = 0$ where they are produced than in the bulk solution. Along their diffusion path (i.e., in the interfacial solution), the relative concentrations of $Cu^{2+}_{(sol'n)}$ and OH^- can vary and therefore the main chemical form of $Cu^{2+}_{(sol'n)}$ will also vary with z in the interfacial solution. OH^- will also participate in any other acid-base or hydrolysis equilibria that exist in solution, e.g., the CO_2/HCO_3^- acid-base equilibrium.

Experimentally, $[H^+]_t$ is determined from pH_t ($-\log[H^+]_t$). The dissolved species concentrations, i.e., $[Cu^{II}_{(sol'n)}]_t$ and $[OH^-]_t/[H^+]_t$, that are experimentally determined, are the z-

averaged values over the thickness of the solution layer (d_{sol}), and therefore the exact concentrations at distances z are unknown.

$$[\mathrm{H}^+]_t = \frac{1}{d_{sol}} \cdot \int_{z=0}^{d_{sol}} \left([\mathrm{H}^+]_{z,t} \cdot dz\right) \tag{4.7a}$$

$$[\mathrm{Cu^{II}}_{(\mathrm{sol'n})}]_t = \frac{1}{d_{sol}} \cdot \int_{z=0}^{d_{sol}} \left([\mathrm{Cu^{II}}_{(\mathrm{sol'n})}]_{z,t} \cdot dz\right) \tag{4.7b}$$

The measured z-averaged cupric ion concentration is referred to as $[\mathrm{Cu^{II}}_{(\mathrm{sol'n})}]$ and can also include dispersed solid colloidal particles, as discussed later.

The initial concentration of H^+ ($[\mathrm{H}^+]_0$) can impact the corrosion progression because it affects the position of the cupric ion hydrolysis equilibria in Stage 1. For example, in previous studies it was shown that when the initial bulk pH (pH_0) is low (≤ 2.0), $[\mathrm{OH}^-]_t$ produced via **Eq. 4.6** is much lower than $[\mathrm{H}^+]_0$ at $z = 0$ and therefore, pH_t is not significantly affected. Because pH_t remains low, the hydrolysis equilibrium results in the formation of mainly unhydrolyzed Cu^{2+} at $z = 0$.[4] In fact, because $[\mathrm{H}^+]_0$ is high at all z, the net production of OH^- (via **Eqs. 4.3** and **4.6**) will not significantly affect $[\mathrm{H}^+]_t$ at any z for a very long time and the $[\mathrm{H}^+]_t$ at any z after a given t can be considered to be the same as $[\mathrm{H}^+]_0$:

$$[\mathrm{H}^+]_t = [\mathrm{H}^+]_0 + \Delta[\mathrm{H}^+]_t \approx [\mathrm{H}^+]_0 \qquad \text{at any } z \text{ and } t \text{ when } \mathrm{pH}_0 \leq 2.0 \tag{4.8}$$

where $\Delta[\mathrm{H}^+]_t$ represents the increase in proton concentration over duration t. Thus, for a low pH_0, the pH_t of the solution is not affected as corrosion progresses and remains close to pH_0 for a long time.

The solubility of $\mathrm{Cu(OH)}_{2(\mathrm{solid})}$ is high at low pH values (**Figure 4.1**). Thus, in solutions with $\mathrm{pH}_0 \leq 2.0$, $[\mathrm{Cu}^{2+}_{(\mathrm{sol'n})}]_t$ remains far from the $\mathrm{Cu(OH)}_2$ solubility limit and no precipitation of cupric ions occurs at any z for a very long time (and precipitation may never occur at low pH_0 under high convection conditions). Hence, metal cations that are transferred into solution would all be in the dissolved state at any z and are mainly in the form of Cu^{2+}:

$$[\mathrm{Cu^{II}}_{(\mathrm{sol'n})}]_t \approx [\mathrm{Cu}^{2+}_{(\mathrm{sol'n})}]_t \approx [\mathrm{Cu}^{2+}]_t \qquad \text{in Stage 1 for } \mathrm{pH}_0 \leq 2.0 \tag{4.9}$$

In solutions initially free of copper ions, the amount of $\mathrm{Cu}^{2+}_{(\mathrm{sol'n})}$ produced in solution is equal to its increase ($\Delta[\mathrm{Cu}^{2+}_{(\mathrm{sol'n})}]_t$):

$$[\mathrm{Cu}^{2+}{}_{(\mathrm{sol'n})}]_t = [\mathrm{Cu}^{2+}{}_{(\mathrm{sol'n})}]_0 + \Delta[\mathrm{Cu}^{2+}{}_{(\mathrm{sol'n})}]_t = \Delta[\mathrm{Cu}^{2+}{}_{(\mathrm{sol'n})}]_t \qquad (4.10)$$

Mass and charge conservation further dictate that the decrease in the *z*-averaged $[\mathrm{H}^+]_t$ ($-\Delta[\mathrm{H}^+]_t$) would be twice the increase in $\Delta[\mathrm{Cu}^{\mathrm{II}}{}_{(\mathrm{sol'n})}]_t$:

$$\Delta[\mathrm{Cu}^{\mathrm{II}}{}_{(\mathrm{sol'n})}]_t \approx -2\,\Delta[\mathrm{H}^+]_t \qquad \text{in \underline{Stage 1} for } \mathrm{pH}_0 \leq 2.0 \qquad (4.11)$$

while $\Delta[\mathrm{H}^+]_t$ remains negligible compared to $[\mathrm{H}^+]_0$ when $\mathrm{pH}_0 \leq 2.0$ in stagnant small volume solutions (**Eq. 4.8**).

At higher pH_0, the time-dependent behaviours of $[\mathrm{H}^+]/[\mathrm{OH}^-]$ and $[\mathrm{Cu}^{\mathrm{II}}{}_{(\mathrm{sol'n})}]$ in Stage 1 deviate from those expected at very acidic pH_0 (≤ 2.0). However, during a naturally corroding process, $[\mathrm{Cu}^{\mathrm{II}}{}_{(\mathrm{sol'n})}]$ and $[\mathrm{OH}^-]$ do not change independent from each other. More details on the corrosion progression with time (the corrosion mechanism) for each set of solution conditions will be presented in the subsequent chapters.

4.3.2 Effects of Acidic and Neutral pH Solutions without Radiation

In **Chapter 5**, the individual effects of key radiolysis products ($\mathrm{H_2O_2}$, $\mathrm{NO_3^-}$, and $\mathrm{H^+}$) on Stages 1 and 2 were investigated. The time-dependent behaviours of $[\mathrm{Cu}^{\mathrm{II}}{}_{(\mathrm{sol'n})}]$ and pH are shown in **Figures 4.2** and **4.3**, grouped by pH_0. The oxidant was either $\mathrm{O_2}$ (pure water) or $\mathrm{H_2O_2}$ (0.1 mM and 10 mM) with a solution volume of 2.0 mL (solution depth of 2.50 cm).

The time-dependent behaviours of pH and $[\mathrm{Cu}^{\mathrm{II}}{}_{(\mathrm{sol'n})}]$ in solutions with $\mathrm{pH}_0 = 4.0$ (**Figure 4.2**) show a quick initial increase followed by a plateau at a maximum value. The plateau of $[\mathrm{Cu}^{\mathrm{II}}{}_{(\mathrm{sol'n})}]$ ($[\mathrm{Cu}^{\mathrm{II}}{}_{(\mathrm{sol'n})}]_{\mathrm{max}}$) is indicated by the red dotted line in **Figure 4.2** at 0.12 ± 0.05 mM ($\log([\mathrm{Cu}^{\mathrm{II}}{}_{(\mathrm{sol'n})}]) = -3.9$), which also corresponds to the initial proton concentration value ($\mathrm{pH}_0 = 4.0$, $[\mathrm{H}^+] = 0.10$ mM) (**Eq. 4.12**).

$$[\mathrm{Cu}^{\mathrm{II}}{}_{(\mathrm{sol'n})}]_{\mathrm{max}} \approx [\mathrm{H}^+]_0 \qquad \text{for } \mathrm{pH}_0 = 4.0 \qquad (4.12)$$

This equivalence is maintained for both solutions, despite two orders of magnitude difference in the concentration of initial oxidant (0.1 mM compared to 10 mM $\mathrm{H_2O_2}$). The final pH value ('$\mathrm{pH_f}$') was 5.8 ± 0.2 (blue dotted line in **Figure 4.1**), which is the pH at which the maximum copper concentration is at its saturation capacity, as discussed in detail below.

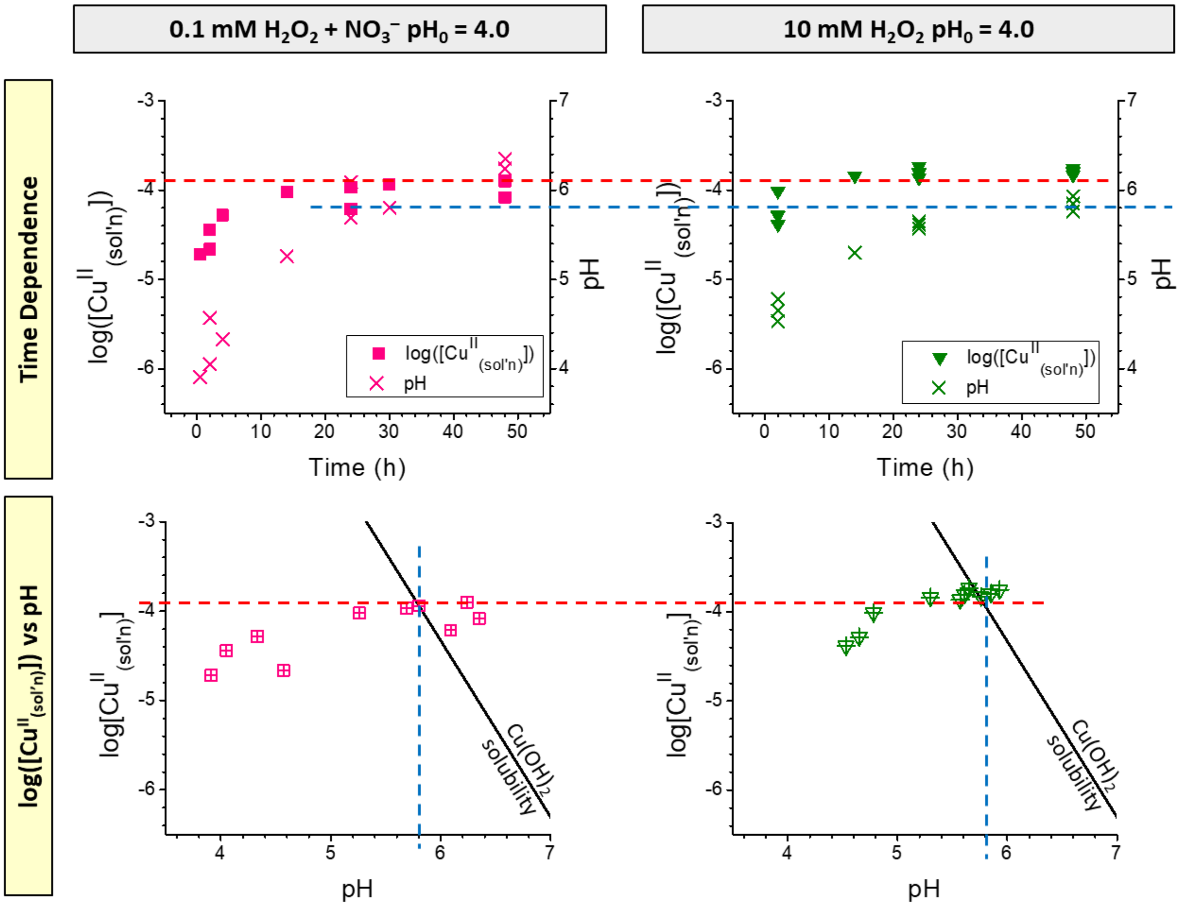

Figure 4.2 Time-dependent behaviour of $[Cu^{II}_{(sol'n)}]$ and pH (upper row) and the $\log([Cu^{II}_{(sol'n)}])$-pH relationship (bottom row) in 2.0 mL solutions of H_2O_2 with $pH_0 = 4.0$ without radiation. The red dotted line indicates $[Cu^{II}_{(sol'n)}]_{max}$ and the blue dotted line indicates pH_f.

The increase in $[Cu^{II}_{(sol'n)}]_t$ and pH_t with time is a result of metal oxidation coupled with oxidant (in this case, H_2O_2) reduction, which occur at the metal surface (z = 0) (**Eq. 4.6b**). In solutions with $pH_0 = 4.0$, pH increased with t (**Figure 4.2**), indicating that the amount of OH^- produced via **Eq. 4.3b** was non-negligible compared to $[H^+]_0$, and $[H^+]_t$ was lower than $[H^+]_0$:

$$[H^+]_t < [H^+]_0 \qquad \text{for } pH_0 = 4.0 \qquad (4.13)$$

The initial increase in pH_t was observed when t < 14 h (**Figure 4.2**), which is referred to as Stage 1.

In Stage 1, the time-dependent increase in $[Cu^{II}_{(sol'n)}]$ (**Figure 4.2**) was approximately equal to the decrease in $[H^+]_t$ (or increase in $[OH^-]_t$).

$$\Delta[Cu^{II}_{(sol'n)}]_t \approx -\Delta[H^+]_t \qquad \text{in Stage 1 for } pH_0 = 4.0 \qquad (4.14)$$

The lower $[H^+]_0$ and decreasing $[H^+]_t$ with time result in the hydrolysis equilibrium (**Eq. 4.3**) shifting to the right. The same rates of increase in $[Cu^{II}_{(sol'n)}]_t$ and decrease in $[H^+]_t$ indicate that the z-averaged chemical form of $Cu^{2+}_{(sol'n)}$ is initially $Cu(OH)^+$ rather than Cu^{2+}.

As OH^- and $Cu^{2+}_{(sol'n)}$ are produced and accumulate at z = 0, the hydrolysis equilibrium shifts further to the right and $Cu(OH)_{2(solv)}$ begins to form. Once the solubility limit is exceeded, $Cu(OH)_2$ precipitates as a solid species. Previous studies have shown that precipitation of $Cu(OH)_2$ will initially be as colloid particles ($Cu(OH)_{2(colloid)}$) that remain dispersed in the solution where they were produced.[1,10] The dispersed colloid particles contribute to $[Cu^{II}_{(sol'n)}]$ and the measured copper concentration continues to increase with corrosion time as these colloids precipitate. The colloid particles have a negligible effect on the initial redox reaction (**Eq. 4.6**) and cupric ion hydrolysis equilibrium (**Eq. 4.3**). However, the shift in hydrolysis equilibrium means the consumption of $[H^+]_t$ is no longer equal to the production of $[Cu^{2+}_{(sol'n)}]_t$ and the measured pH_t increase slows.

As cupric ion species diffuse from the surface into the bulk solution, the saturated volume adjacent to the metal surface expands. As the colloid density increases within the saturated volume, the frequency of collision between the colloid particles increases. When the colloid particles collide, they aggregate into a hydrogel and can precipitate onto the surface. The hydrogel contains a solid network of $Cu(OH)_2$ colloid particles and a mobile phase of Cu^{2+}-saturated solution, and is discussed in more depth later.[4,5] The precipitation of the $Cu(OH)_2$ hydrogel layer marks the start of Stage 2. Because saturation is a requirement for the start of Stage 2, it is seldom observed in solutions with $pH_0 \leq 2.0$ or in flowing solutions, as discussed in the previous section.

Previous studies[4] have found that the precipitation of the $Cu(OH)_2$ hydrogel on the metal surface limits the transport of cupric ions, but not OH^-, H^+, or H_2O through the interfacial solution, which is discussed in depth in **Chapter 6**. Thus, due to the growth of the hydrogel layer at the metal surface, the increase in [$Cu^{II}_{(sol'n)}$] slows substantially, but [OH^-] continues to increase even after long times, i.e., when t ≥ 14 h (**Figure 4.2**).

The log([$Cu^{II}_{(sol'n)}$])-pH relationship for $pH_0 = 4.0$ shows an increase in [$Cu^{II}_{(sol'n)}$] with pH, until [$Cu^{II}_{(sol'n)}$]$_{max}$ (red dotted line in **Figure 4.2**) is reached. After [$Cu^{II}_{(sol'n)}$] reached its maximum value (dictated by the value of $[H^+]_0$, **Eq. 4.12**), $[OH^-]_t$ increased to satisfy the $Cu(OH)_2$ solubility equilibrium because $Cu^{2+}_{(sol'n)}$ diffusion through the hydrogel network is slow. The production of OH^- continued until the dissolved cupric ions (which include all hydrolysis products) were in quasi-equilibrium with the solid $Cu(OH)_2$ at the interfacial solution.

$$Cu^{2+}_{(sol'n)} + x\ OH^- \rightleftharpoons Cu(OH)_{2(solid)} \qquad (4.15)$$

Once the solubility limit was reached, neither [$Cu^{II}_{(sol'n)}$] nor pH changed substantially. This shows that the final values of [$Cu^{II}_{(sol'n)}$] and [H^+] are controlled by the $Cu(OH)_2$ solubility equilibrium. However, the exact values of [$Cu^{II}_{(sol'n)}$] and [H^+] at the solubility equilibrium are based on the initial conditions and how the corrosion system evolves. In $pH_0 = 4.0$ solutions, [$Cu^{II}_{(sol'n)}$]$_{max}$ is dictated by pH_0 (**Eq. 4.12**) and pH_f is dictated by [$Cu^{II}_{(sol'n)}$]$_{max}$ reaching its saturation capacity (i.e., the pH_f is controlled by the hydrolysis equilibrium of $Cu(OH)_2$, which acts as an acid-base buffer).

The time-dependent behaviours of [$Cu^{II}_{(sol'n)}$] and pH in solutions with a pH_0 near neutral (7.0) are shown in **Figure 4.3**. [$Cu^{II}_{(sol'n)}$]$_{max}$ is indicated by the red dotted line at 0.03 ± 0.01 mM (log([$Cu^{II}_{(sol'n)}$]) = – 4.6), which does not correspond to $[H^+]_0$ as it did in solutions with $pH_0 = 4.0$ (**Eq. 4.12**). However, as observed previously, pH_f (indicated by the blue dotted line) corresponds to the pH at which [$Cu^{II}_{(sol'n)}$]$_{max}$ was at saturation.

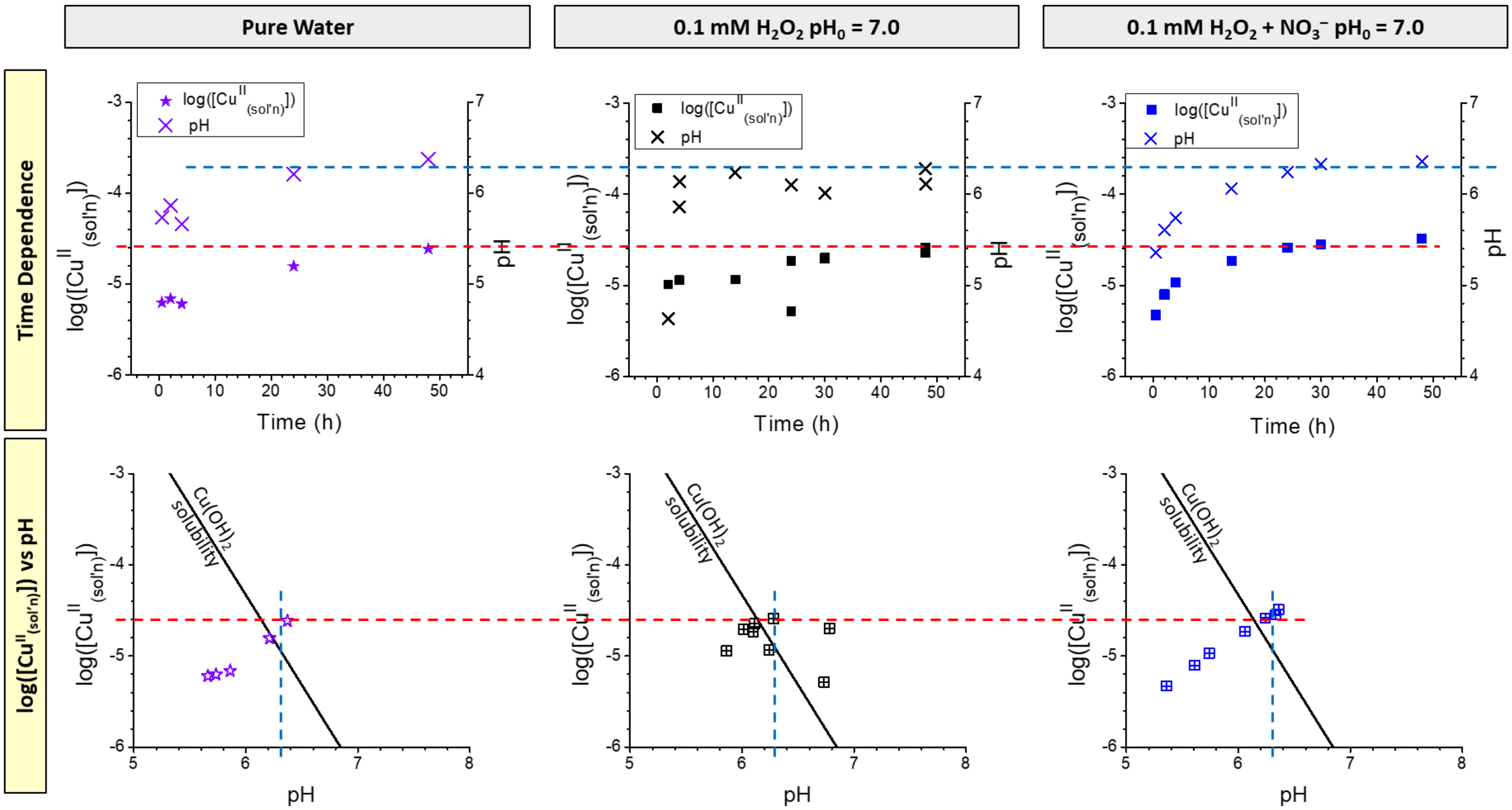

Figure 4.3 Time-dependent behaviour of [Cu$^{II}_{(sol'n)}$] and pH (upper row) and the log([Cu$^{II}_{(sol'n)}$]-pH (bottom row) relationship in 2.0 mL solutions of water and H_2O_2 with near neutral pH_0 without radiation. The red dotted line indicates [Cu$^{II}_{(sol'n)}$]$_{max}$ and the blue dotted line indicates pH_f.

In near neutral solutions, a small addition of OH^- or H^+ can drastically change the pH as the solution is near the equivalence point of H_2O (7.0). Hence, the production of a small amount of OH^- via **Eq. 4.6** can significantly change the $[OH^-]$ at $z = 0$ in a short period of time (shorter than a millisecond timescale for most solution reactions). The fast and substantial increase in $[OH^-]_t$ at $z = 0$ pushes the hydrolysis equilibrium (**Eq. 4.3**) to the far right, to form $Cu(OH)_3^-$. Due to the fast rate of cupric ion hydrolysis, the overall redox reaction at $z = 0$ that occurs through the interfacial mass transfer (**Eq. 4.6**) followed by the fast hydrolysis to $Cu(OH)_3^-$, can be considered as a single elementary step.

$$Cu^0_{(m)} + H_2O_2 + H_2O \rightarrow Cu(OH)_3^- + H^+ \qquad \text{in } \underline{\text{Stage 1a}} \text{ for } 6.0 \leq pH_0 \leq 9.0 \qquad (4.16)$$

Hence, the initial overall process can be considered to occur via **Eq. 4.16** and transport of $Cu(OH)_3^-$ and H^+ from $z = 0$ to $z = \delta_{diff}$ is taking place. Hence, the z-averaged chemical form of $Cu^{2+}_{(sol'n)}$ in solutions with near neutral pH_0 is initially $Cu(OH)_3^-$ rather than Cu^{2+} or $Cu(OH)^+$.

$$[Cu^{II}_{(sol'n)}]_t \approx [Cu(OH)_3^-]_t \qquad \text{in } \underline{\text{Stage 1a}} \text{ for } 6.0 \leq pH_0 \leq 9.0 \qquad (4.17)$$

Because of the low $[H^+]_0$ when pH_0 is neutral, the concentration of H^+ produced via **Eq. 4.16** is more than initially present in solution:

$$[H^+]_t > [H^+]_0 \qquad \text{in } \underline{\text{Stage 1a}} \text{ for } 6.0 \leq pH_0 \leq 9.0 \qquad (4.18)$$

The increase in $[H^+]_t$ at initial times results in the decrease in pH_t, observed when t = 16 h in **Figure 4.2**, when the measured pH was below 7.0 (4.6 – 5.8). At the same time, the formation of $Cu(OH)_3^-$ results in an increase in $[Cu^{II}_{(sol'n)}]_t$, which should be the same as the increase in $[H^+]_t$.

$$\Delta[Cu^{II}_{(sol'n)}]_t \approx \Delta[H^+]_t \qquad \text{in } \underline{\text{Stage 1a}} \text{ for } 6.0 \leq pH_0 \leq 9.0 \qquad (4.19)$$

This equivalence was observed in solutions with no other established acid-base equilibria, such as the carbonate acid-base equilibria, i.e., in CO_2-free solutions as discussed in **Chapter 6**. However, in solutions saturated with normal air containing CO_2 (such as those used for **Figure 4.3**), the change in $[H^+]_t$ is influenced by the bicarbonate buffering system. In this case, $\Delta[H^+]_t$

is not determined by only the redox reaction (**Eq. 4.16**) and hence, no simple relationship of $\Delta[H^+]_t$ versus $\Delta[Cu^{II}{}_{(sol'n)}]_t$ can be determined. The time during which the main cupric ion form is $Cu(OH)_3^-$ and pH is decreasing with time is referred to as Stage 1a. The studies presented in this thesis indicate that the observations described for Stage 1a are consistent for pH_0 values between 6.0 and 9.0 in small solution volumes.

As $Cu(OH)_3^-$ and H^+ diffuse from the metal surface into the bulk solution, $[H^+]$ at any *z* increases with time. The increase in $[H^+]_t$ causes the cupric ion hydrolysis equilibrium (**Eq. 4.2**) to shift more and more to the left with time in Stage 1b.

$$Cu(OH)_3^- + H^+ \rightarrow Cu(OH)_{2(solv)} + H_2O \rightarrow Cu(OH)^+ + OH^- \quad \text{in Stage 1b for } 6.0 \leq pH_0 \leq 9.0 \qquad (4.20)$$

As a result, the *z*-averaged chemical form shifts from $Cu(OH)_3^-$ to $Cu(OH)_{2(solv)}$ and then to $Cu(OH)^+$, which consumes H^+. That is, the change in $[H^+]$ and $[Cu^{2+}{}_{(sol'n)}]$ with corrosion time are not independent of each other. In Stage 1a, pH initially decreases, but after reaching a minimum near 16 h, it increases with time.

With the bicarbonate buffering system present in naturally aerated conditions (saturated with CO_2), the increase in $[OH^-]_t$ cannot be correlated to the increase in $[Cu^{II}{}_{(sol'n)}]$, as discussed above. The final pH value in the $pH_0 = 7.0$ solutions presented in **Figure 4.3** was 6.3 ± 0.1, corresponding to the pKa of HCO_3^-.

Previous studies,[2,4] and the studies presented in this section indicate that regardless of pH_0, the elementary steps to consider in determining the overall corrosion rate in Stage 1 (both Stage 1a and Stage 1b for near neutral solutions) include the initial redox reaction (**Eq. 4.6**), the diffusion of products through the interfacial solution (**Eq. 4.2**), and the cupric ion hydrolysis equilibria (**Eq. 4.3**). In Stage 1, when metal oxidation produces mainly dissolved (and dispersed) metal species, the overall rate of metal loss (corrosion) should be the same as the overall increase in dissolved metal cations with time:

$$\upsilon_{corr-st1} = -\frac{1}{A_{int}} \cdot \frac{d(m_{Cu})_t}{dt} = \frac{V_{sol}}{A_{int}} \cdot \frac{d\left(\int\left(\left[\mathrm{Cu}^{2+}{}_{(\mathrm{sol'n})}\right]_{z,t} \cdot dz\right)\right)}{dt} \qquad (4.21)$$

where $\upsilon_{corr-st1}$ represents the corrosion rate per unit surface area in Stage 1, m_{Cu} represents the mass of the metal at time t, $\int\left(\left[\mathrm{Cu}^{2+}{}_{(\mathrm{sol'n})}\right]_{z,t}\cdot dz\right)$ represents the z-averaged $[\mathrm{Cu}^{2+}{}_{(\mathrm{sol'n})}]$ at time t, and A_{int} and V_{sol} represent the interfacial surface area and solution volume, respectively. The overall corrosion rate in Stage 1 can then be determined from the observed time dependence of $[\mathrm{Cu}^{\mathrm{II}}{}_{(\mathrm{sol'n})}]_t$, i.e., the metal dissolution rate (υ_{diss}):

$$\upsilon_{corr-st1} \approx \upsilon_{diss} = \frac{V_{sol}}{A_{int}}\cdot\frac{d\left[Cu^{II}_{(sol'n)}\right]}{dt} \tag{4.22}$$

The equivalences in **Eqs. 4.21** and **4.22** arise from the most fundamental chemical rate law that mass and charge must be conserved during a natural process. These equations do not tell the dependences of $\upsilon_{corr-st1}$ on solution conditions, such as [Ox] and pH.

Because corrosion involves metal oxidation coupled with oxidant reduction, the $\upsilon_{corr-st1}$ in air-saturated solutions may depend on $[\mathrm{O_2}]_t$ and $[\mathrm{OH}^-]_t$. As these species are consumed or produced by corrosion reactions, their concentrations will change as corrosion progresses. However, if the changes are small compared to their initial concentrations, it is reasonable to approximate their concentrations at a given time as being the same as $[\mathrm{O_2}]_0$ and $[\mathrm{OH}^-]_0$. This is indeed the case for $[\mathrm{O_2}]_\mathrm{t}$ ($\approx [\mathrm{O_2}]_0$) in air-saturated droplet solutions with the headspace filled with air (see further discussion in **Chapter 7**). However, as is shown in this chapter, it is not the case for $[\mathrm{OH}^-]_\mathrm{t}$ (or $[\mathrm{H}^+]_\mathrm{t}$) when $\mathrm{pH}_0 > 2.0$ in stagnant, small volume solutions, because $[\mathrm{OH}^-]_t$ is determined not only by the initial redox reactions (**Eq. 4.6**) but also the cupric ion hydrolysis equilibria (**Eq. 4.2**) and any other pH-controlling acid-base equilibrium reactions that exist in solution.

Thus, if the corrosion rate was directly dependent on $[\mathrm{OH}^-]_t$, the corrosion rate (and thus the copper dissolution rate) would change with time. Instead, $[\mathrm{Cu}^{\mathrm{II}}{}_{(\mathrm{sol'n})}]$ is constant with time in Stage 1 for all studied pH_0, despite large pH_t changes. Furthermore, the time-dependent pH behaviour changes with pH_0, but this change is not due to different elementary steps (i.e. change in corrosion mechanism) or due to an increase in the rate of corrosion with increasing $[\mathrm{H}^+]_t$. Instead, the observed effects of pH_0 on the corrosion behaviour arise because the OH^- produced (or H^+ consumed) during corrosion reactions induces a different change in $[\mathrm{H}^+]_t$

depending on $[H^+]_0$ and accordingly, shifts the cupric ion hydrolysis equilibria. The different time-dependent behaviour of pH_t and $[Cu^{II}_{(sol'n)}]_t$ results in different final thermodynamic states based on pH_0, as discussed further at the end of this section.

The overall rate equation for metal loss in Stage 1 based on solution parameters can be constructed based on classical (electro-) chemical reaction rate and mass flux equations for $[Cu^{2+}_{(sol'n)}]_{z,t}$ for the individual elementary steps. This requires determining the kinetic parameters, such as reaction order and rate constant, for each elementary step, formulating the rate equation for $[Cu^{2+}_{(sol'n)}]_{z,t}$ as a function of the kinetic parameters for each step, and coupling the rate equations of individual steps to construct the overall rate equation. The overall partial differential rate equation can then be solved using computational software (e.g., COMSOL Multiphysics) to predict the overall metal loss over a given service duration in the anticipated ranges of solution conditions. Although this thesis project will contribute to the development of the copper corrosion rate model, completing it is beyond the scope of this project.

In solutions with low pH_0 (**Figure 4.2**), the interfacial solution reaches cupric ion supersaturation before the bulk solution does, resulting in precipitation at the interface as the saturated volume expands. In solutions with near neutral pH_0 (**Figure 4.3**), the sensitivity of the solution to slight changes in $[H^+]$ and the strong feedback between $[Cu^{2+}_{(sol'n)}]$ changes and $[H^+]$ changes with time, resulting in the colloids being more dispersed throughout the entire solution. Thus, the collision frequency is low (due to a larger saturated volume than in $pH_0 =$ 4.0 solutions) and when $Cu(OH)_{2(solv)}$ precipitates, it does so at all z. The colloid particles remain dispersed in the bulk solution and contribute to $[Cu^{II}_{(sol'n)}]$. The colloid particles agglomerate as their concentration increases and will eventually precipitate as a hydrogel on the surface.

The aggregation of $Cu(OH)_2$ particles and precipitation of $Cu(OH)_2$ hydrogel may be expected to be accompanied by a decrease in $[Cu^{II}_{(sol'n)}]$ with time. Instead, it is constant due to the production and dissolution of $Cu^{2+}_{(sol'n)}$ at a rate equal to that of the precipitation of the $Cu(OH)_2$ hydrogel from solution. This indicates that in Stage 2 the overall metal oxidation rate is determined by the production and growth of the hydrogel and the main elementary reactions to consider when determining the rate in Stage 2 include the initial redox reaction (**Eq. 4.6**), the diffusion of products through the interfacial solution (**Eq. 4.2**), the cupric ion hydrolysis equilibria (**Eq. 4.3**), and the overall precipitation of $Cu(OH)_2$ colloid particles and hydrogel. The metal oxidation rate can no longer be equated to the dissolution rate and becomes a nonlinear equation based on the hydrogel growth, discussed in detail in **Chapter 6**.

The log([$Cu^{II}_{(sol'n)}$])-pH relationship for near-neutral pH_0 solutions (bottom row, **Figure 4.3**) shows that the copper concentration increases with pH at log([$Cu^{II}_{(sol'n)}$])-pH values left of the $Cu(OH)_2$ solubility curve. The log([$Cu^{II}_{(sol'n)}$]) and pH values around the $Cu(OH)_2$ solubility curve do not change substantially. Because the precipitation of $Cu(OH)_2$ colloid particles occurs in the bulk solution, the collision frequency between colloid particles is low and the hydrogel growth occurs within the bulk solution (not in the interfacial solution). Thus, without a $Cu^{2+}_{(sol'n)}$-selective transport barrier (the hydrogel layer) at the metal surface, both [$Cu^{II}_{(sol'n)}$] and [OH^-] increase simultaneously to satisfy the $Cu(OH)_2$ solubility equilibrium. Once they do so, the equilibrium is maintained even with slight variations in pH.

The results presented in this section show that the elementary reactions that control the corrosion rate in the early stages of corrosion do not change with pH_0. Regardless of initial conditions (specifically pH_0 in this section), the log([$Cu^{II}_{(sol'n)}$])-pH relationship at long corrosion times will trend towards the solubility-pH curve of $Cu(OH)_2$. However, the initial conditions ($pH_0 > 2.0$) determine where on the $Cu(OH)_2$ solubility curve the system will end.

4.3.3 Effects of Radiation in Small Water Droplets

In **Chapters 6**, **7**, and **8**, corrosion in the absence (**Figure 4.4**) and presence (**Figure 4.5**) of radiation when copper was exposed to a small droplet of pH_0 of 7.0 and 9.0 in a variety of cover gas conditions was investigated.

The time-dependent behaviours of [$Cu^{II}_{(sol'n)}$] and pH after corrosion in the absence of radiation are presented in **Figure 4.4**, where similar behaviours were observed in both pH_0 values (7.0 and 9.0). Despite the variety of cover gas compositions, the range of [$Cu^{II}_{(sol'n)}$] values were similar, remaining between 0.04 mM and 1.60 mM (log([$Cu^{II}_{(sol'n)}$] = −4.4 to −2.8) in all solutions. This narrow range of [$Cu^{II}_{(sol'n)}$] values was similarly unaffected by the large changes in pH_t with corrosion time, further illustrating the minimal effect of pH_t on the corrosion *rate* (although the length of stages and main corrosion products changes with pH_t). The number of moles of cupric ions produced in these droplet solutions (2 to 80 nmol) is very similar to that observed in 2.0 mL solutions with the same solution depth and pH_0 (**Figure 4.8** in **Section 4.3.4**) (10 to 50 nmol). This explains why, unlike in the larger solutions, the droplet solutions quickly become supersaturated with cupric ions, which will be explained in more detail later. The time-dependent variations in copper concentration are dependent on solution conditions (and pH evolution), but the overall time dependence of $[Cu^{II}_{(sol'n)}]$ comprises an initial increase in Stage 1 with the production of dissolved species (for approximately $t < 50$ h) followed by a plateau at longer corrosion times due to production and growth of the $Cu(OH)_2$ hydrogel.

The pH in solutions free of CO_2 (black in **Figure 4.4**) initially decreased in Stage 1a, during which the redox process results in the formation of H^+ and $Cu(OH)_3^-$ (**Eq. 4.16**), then increased as the hydrolysis equilibrium shifted towards the formation of $Cu(OH)^+$ and $Cu(OH)_{2(solv)}$ (**Eq. 4.21**). With no other acid-base equilibria in solution (other than that of water), the weak acid-base equilibria of the cupric ion species controlled the pH, which remained at the pKa of $Cu(OH)^+$ once hydrogel began to form (8.4 ± 0.1 in Stage 2 in CO_2-free solutions).

When CO_2 is present in solution (blue and green data in **Figure 4.4**), a competition develops between the acid-base equilibria of $Cu(OH)^+$ and of HCO_3^- due to the changing $[H^+]_t$ in different corrosion stages. Initially, pH_t is buffered at the pKa of $Cu(OH)^+$ in Stage 1b and $Cu(OH)_2$ precipitates due to its low solubility at this pH. As $Cu(OH)_2$ precipitates, the slight decrease in OH^- causes pH_t to decrease substantially to reach the pKa of HCO_3^- ($HCO_3^- + H^+ \rightleftharpoons H_2CO_3$), because bicarbonate has a larger buffering capacity than $Cu(OH)^+$.[9] At this lower pH, the cupric ion solubility is higher, and the dissolved particles may reprecipitate and the pH_t may again increase. The second increase in pH was observed in solutions with CO_2 at longer times (**Figure 4.4**).

Thus, the minimum pH reached depends on the acid-base equilibrium of other pH-controlling agents. In the absence of any dissolved CO_2, water dissociation and the Cu^{2+} hydrolysis are the main reactions that control the pH_t during corrosion in Stage 1. However, when the droplet solution was prepared with CO_2-containing air, the minimum pH_t reached was close to the pKa of bicarbonate (the exact value reached depends on the buffering capacity, i.e., the total amount of CO_2 dissolved). Hence, the minimum pH_t reached in the solution saturated with CO_2-free air is higher than that reached in solution saturated with normal air. This further confirms that the Cu^{2+} hydrolysis equilibrium contributes significantly to the overall rate of proton consumption, while its effect on the overall rate of dissolution is negligible.

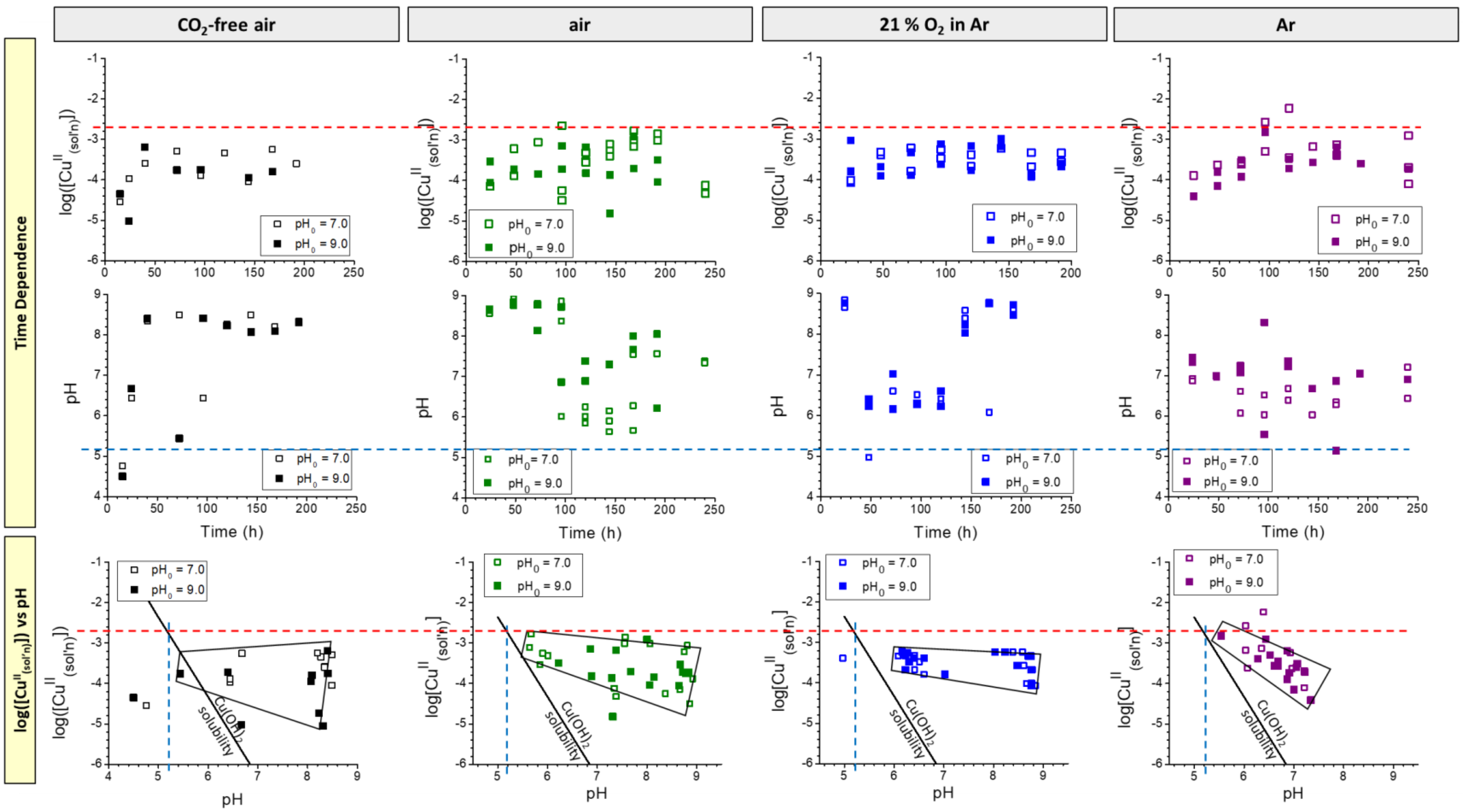

Figure 4.4 Time-dependent behaviour of [Cu^{II}$_{(sol'n)}$] and pH (upper row) and the log([Cu^{II}$_{(sol'n)}$])-pH relationship (bottom row) in 100 μL water droplet with different cover gas environments without radiation. The red dotted line indicates [Cu^{II}$_{(sol'n)}$]$_{max}$ and the blue dotted line indicate the pH at which [Cu^{II}$_{(sol'n)}$]$_{max}$ is at saturation.

The solution volumes used in this section were much smaller (0.1 mL compared to 2.0 mL used in **Section 4.3.2**) and thus, δ_{diff} was limited (see further discussion on the effect of diffusion length in **Section 4.3.4**). With a small diffusion length, the feedback loop between $[Cu^{2+}_{(sol'n)}]$ changes and $[H^+]$ changes with time are more pronounced in the *z*-averaged measured values.

At the very high $[H^+]_t$ reached near the metal surface ($z = 0$) in <u>Stage 1a</u> (**Eq. 4.16**), the solubility of $Cu(OH)_{2(solid)}$ is high. Because the pH of minimum solubility is 8.4 for $Cu(OH)_{2(solid)}$, the $Cu(OH)_2$ solubility decreases with increasing pH when pH < 8.4. The pH in the interfacial solution is lower (and thus the solubility is higher) than in the bulk solution. Thus, as $Cu^{2+}_{(sol'n)}$ transports from $z = 0$ into the bulk solution ($z = \delta_{diff}$) (primarily as $Cu(OH)_3^-$), it experiences an increasingly lower solubility. However, $Cu^{2+}_{(sol'n)}$ has been already transported to the bulk solution and $[Cu^{2+}_{(sol'n)}]$ can exceed the solubility limit at the pH_t of the bulk solution. Indeed, $[Cu^{II}_{(sol'n)}]$ was above the $Cu(OH)_2$ solubility limit at the pH_t (bottom row in **Figure 4.4**). This supersaturation induces precipitation of $Cu(OH)_2$ as colloidal particles in the bulk solution, which remain dispersed in solution and are included in $[Cu^{II}_{(sol'n)}]$. The measured cupric ion concentration includes the dissolved cupric ions and the colloid particles, and thus $[Cu^{II}_{(sol'n)}]_t$ does not change with pH_t as much as expected and instead the range of values of $[Cu^{II}_{(sol'n)}]$ is narrow. The proportion of cupric ions that exist in the dissolved state ($Cu^{2+}_{(sol'n)}$) compared to the colloidal form varies with pH_t.

The general $\log([Cu^{II}_{(sol'n)}])$-pH relationship is illustrated by the black trapezoid in **Figure 4.4**. The $\log([Cu^{II}_{(sol'n)}])$-pH values are to the right of the solubility curve indicating the total amount of copper that has dissolved/dispersed into the solution is higher than the solubility of $Cu(OH)_2$ at the pH_t of the solution at the same corrosion time. The metastable supersaturated solution is due to the formation of $Cu(OH)_2$ colloid particles dispersed in the bulk solution, as discussed above.

The amount of $Cu(OH)_2$ colloid formation ($Cu^{2+}_{(sol'n)}$ precipitation) is proportional to pH and thus, at high pH values, the solution was more supersaturated than at lower values. This flattened the observed $\log([Cu^{II}_{(sol'n)}])$-pH relationship compared to the solubility curve. There is a large range of $[Cu^{II}_{(sol'n)}]$ values at the high pH values as the colloid particles may remain in solution or may agglomerate and precipitate from solution (and no longer be included in the measured value) and the relative amount depends on the corrosion time. This widens the y-values (log([$Cu^{II}_{(sol'n)}$])) at high x-values (pH), creating the trapezoid shape. At lower pH values, the log([$Cu^{II}_{(sol'n)}$])-pH relationship approaches the solubility curve where [$Cu^{II}_{(sol'n)}$]$_{max}$ is at saturation (the intersection between the red and the blue dotted lines in **Figure 4.4**).

In the presence of radiation, the time-dependent behaviours of [$Cu^{II}_{(sol'n)}$] and pH (**Figure 4.5**) are independent of pH_0 and [O_2]. Despite the significantly different initial test conditions in the experiments carried out, the [$Cu^{II}_{(sol'n)}$]$_t$ and pH_t changes with time are very similar. The additional acidic products in solution formed via water and humid air radiolysis cause the pH_f to be much lower than in unirradiated solutions. The pH_f is indicated by the blue dotted line in **Figure 4.5** at 4.4 ± 0.5 (although the pH_f varied depending on cover gas compositions, as discussed in **Chapter 7**). Although acidic radiolysis products caused a decrease in pH_t, corrosion reactions (mass/charge transfer reactions, hydrolysis reactions, etc) still contribute to the pH_f value (the pH_f of a solution without a corroding system is 2.7, shown in **Appendix A**). [$Cu^{II}_{(sol'n)}$]$_{max}$ is indicated by the red dotted line in **Figure 4.5** at 63.1 mM (log([$Cu^{II}_{(sol'n)}$] = –1.2). The pH at which [$Cu^{II}_{(sol'n)}$]$_{max}$ is saturated is the pH_f (the intersecting blue and red lines in the bottom row of **Figure 4.5**).

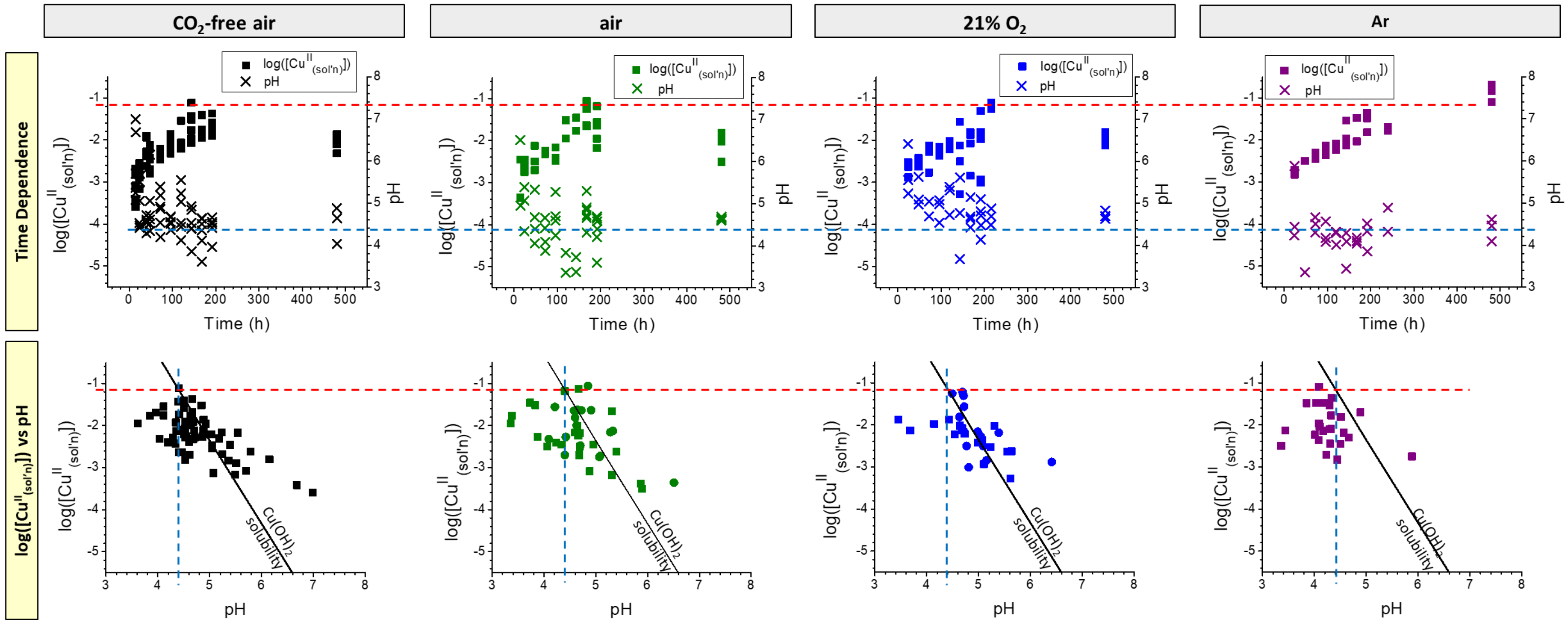

Figure 4.5 Time-dependent behaviour of [Cu^{II}$_{(sol'n)}$] and pH (upper row) and the [Cu^{II}$_{(sol'n)}$]-pH relationship (bottom row) in 100 μL water droplet with different cover gas environments in the presence of radiation. The red dotted line indicates [Cu^{II}$_{(sol'n)}$]$_{max}$ and the blue dotted line indicate the pH at which [Cu^{II}$_{(sol'n)}$]$_{max}$ is at saturation.

The initial metal oxidation half-reaction coupled with the solution oxidant reduction half-reaction results in the formation of $Cu(OH)_3^-$ and H^+ (**Eq. 4.16**) during Stage 1a. The decrease in pH_t as the species diffuse from $z = 0$ cause a shift in the cupric ion hydrolysis towards the formation of $Cu(OH)_{2(solv)}$ and $Cu(OH)^+$ (**Eq. 4.20**). The production and dissolution of acidic products via humid air radiolysis cause the solution to increase in acidity quicker than in unirradiated solutions and therefore, the shift in hydrolysis equilibrium $Cu(OH)_{2(solv)}$ and $Cu(OH)^+$ starts earlier than when radiation is absent (i.e., a shorter Stage 1a). The rate of $-\Delta[H^+]_t$ due to metal oxidation and the shift in cupric ion hydrolysis was slightly lower than the rate of $\Delta[H^+]_t$ due to radiolysis products, and thus the pH_t decreased rather than increased with time in Stage 1b (**Figure 4.5**).

Because the production of H^+ via radiolysis occurs in the bulk solution, the pH_t in the bulk solution is higher than in the interfacial solution. This causes the colloid and hydrogel formation to occur in the interfacial solution. Furthermore, in the presence of radiation, the agglomeration and precipitation of these colloid particles is fast. Water radiolysis produces reactive species, including $\bullet O_2^-$, that induce colloid agglomeration and increase the rate of hydrogel formation, which is discussed further in **Chapter 6**.[11-13] With faster precipitation and growth of the solid-phase $Cu(OH)_2$, the solubility quasi-equilibrium can quickly be achieved. The growth of the hydrogel in Stage 2 was accompanied by a plateau in $[Cu^{II}_{(sol'n)}]_t$ with time. Following the hydrogel growth, $[Cu^{II}_{(sol'n)}]$ increased further due to slight fluctuations in pH_t, as discussed in depth in **Chapter 6**. Once the $Cu(OH)_2$ solubility equilibrium was established it was maintained despite fluctuations in pH_t and an increase in $[Cu^{II}_{(sol'n)}]_t$ with time.

The $\log([Cu^{II}_{(sol'n)}])$-pH relationship (**Figure 4.5**) at high pH values (which corresponds to early corrosion times) show that the solution is supersaturated due to early formation of $Cu(OH)_2$ colloid particles (also observed in unirradiated solutions). At pH values lower than 6.0, the $Cu(OH)_2$ solubility equilibrium is maintained, due to the fast formation of $Cu(OH)_2$ hydrogel which can establish the solubility quasi-equilibrium with the dissolved species. Once the $Cu(OH)_2$ solubility equilibrium is achieved, it is maintained despite further pH_t variations. In an open, corroding system, the equilibrium values are not expected to be conformed to exactly (and instead are referred to as a 'quasi-equilibrium') and the distribution around the solubility curve is on average ± 1 pH unit and ± 0.5 order of magnitude around $[Cu^{II}_{(sol'n)}]$.

These results show that the solubility equilibrium dictates [$Cu^{II}_{(sol'n)}$] after long corrosion times in both irradiated and unirradiated solutions. The implication of the log([$Cu^{II}_{(sol'n)}$])-pH trend towards the solubility limit, regardless of the oxidizing power of the solution, is that the maximum [$Cu^{II}_{(sol'n)}$] can be predicted if the steady state pH or minimum pH is known. However, the initial conditions as well as how $Cu^{2+}_{(sol'n)}$ and pH change with time must be understood in order to predict the final state of the solution (where on the solubility curve the log([$Cu^{II}_{(sol'n)}$])-pH lies).

Figure 4.6 compares the same cover gas compositions in the presence and absence of radiation (pH_0 = 7.0), where the black trapezoid indicates the general observed log([$Cu^{II}_{(sol'n)}$])-pH trend. Without radiation, all measured [$Cu^{II}_{(sol'n)}$] values were above the saturation limit for the corresponding pH, while in the presence of radiation the log([$Cu^{II}_{(sol'n)}$])-pH relationship closely follows the $Cu(OH)_2$ solubility equilibrium. The different log([$Cu^{II}_{(sol'n)}$])-pH relationships are a result of the time-dependent evolution of the two species, as discused in depth above. [$Cu^{II}_{(sol'n)}$]$_{max}$ without radiation is approximately equal to the minimum [$Cu^{II}_{(sol'n)}$] with radiation because the minimum pH without radiation is approximate equal to the pH_{max} with radiation. These results demonstrate that there is a strong correlation between the pH evolution and copper dissolution throughout corrosion in both irradiated and unirradiated solutions.

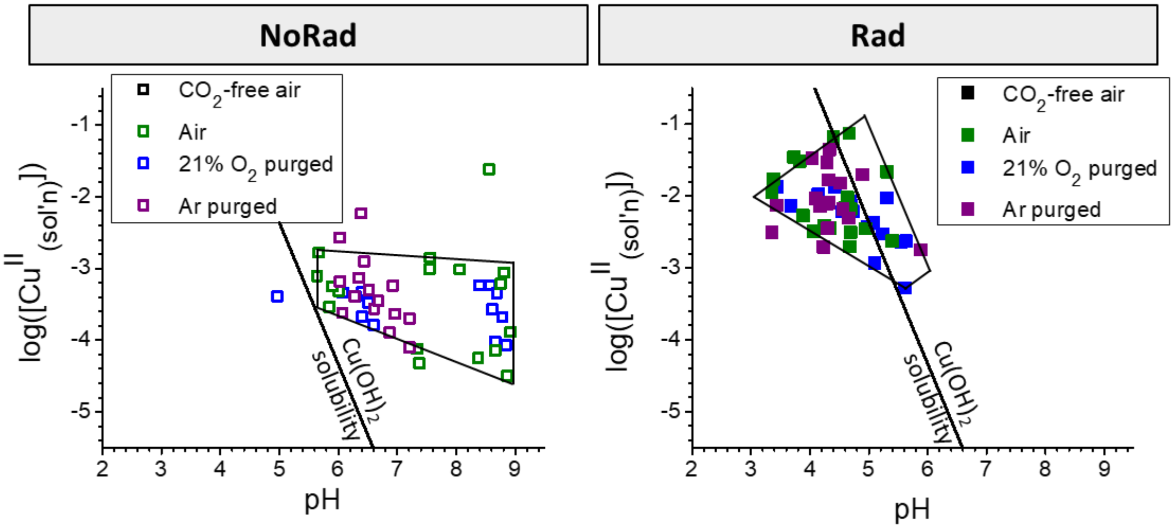

Figure 4.6 The log([$Cu^{II}_{(sol'n)}$])-pH relationship after copper was exposed to a 100 μL water droplet solution (pH_0 = 7.0) with various cover gas environments in the absence (NoRad) and presence (Rad) of radiation. The black trapezoid indicates the general observed log([$Cu^{II}_{(sol'n)}$])-pH relationship.

4.3.4 Effects of Solution Depth in the Presence of Radiation

The length of Stage 1 is dependent on how quickly Cu^{2+} can accumulate in solution, reach the solubility limit of $Cu(OH)_{2(solid)}$, and begin precipitating. In solutions with a small depth, such as the small water droplets used for the study presented in the previous section, $Cu^{2+}_{(sol'n)}$ can accumulate quickly and Stage 1 is short. In solutions with a large depth, Stage 1 is prolonged as it takes more time for the solution to reach the cupric ion saturation capacity if the dissolution rate is the same. Many studies on copper corrosion are done in large solution volumes, and as a result, only the corrosion behaviour in Stage 1 can be studied.[4] **Chapter 8** investigates the effects of solution depth (d_{sol}) on the corrosion dynamics in the presence of radiation using d_{sol} values between 0.25 and 2.50 cm.

In small solution depths (defined in this study as $d_{sol} \leq 0.25$ cm, regardless of solution volume), the diffusion layer ($0 < z < \delta_{diff}$) is a non-negligible proportion of the overall d_{sol}, schematically shown in **Figure 4.7**. The diffusion layer thickness is dependent on the diffusing ion and for a given ion it is the same regardless of solution volume. In stagnant solutions, the Nernst diffusion layer is approximately 0.2 – 0.5 mm.[14] In small d_{sol} solutions, the thickness of the diffusion layer, where large concentration gradients exist, is not negligible compared to the thickness of the solution layer. Conversely, in large depths (defined in this study as $d_{sol} \geq 0.80$ cm), the concentrations within the diffusion layer do not contribute significantly to the measured species values. In fact, the interfacial solution can be considered a point source of $Cu^{2+}{}_{(sol'n)}$ and other dissolved species formed via interfacial charge transfer (e.g., H^+/OH^-).

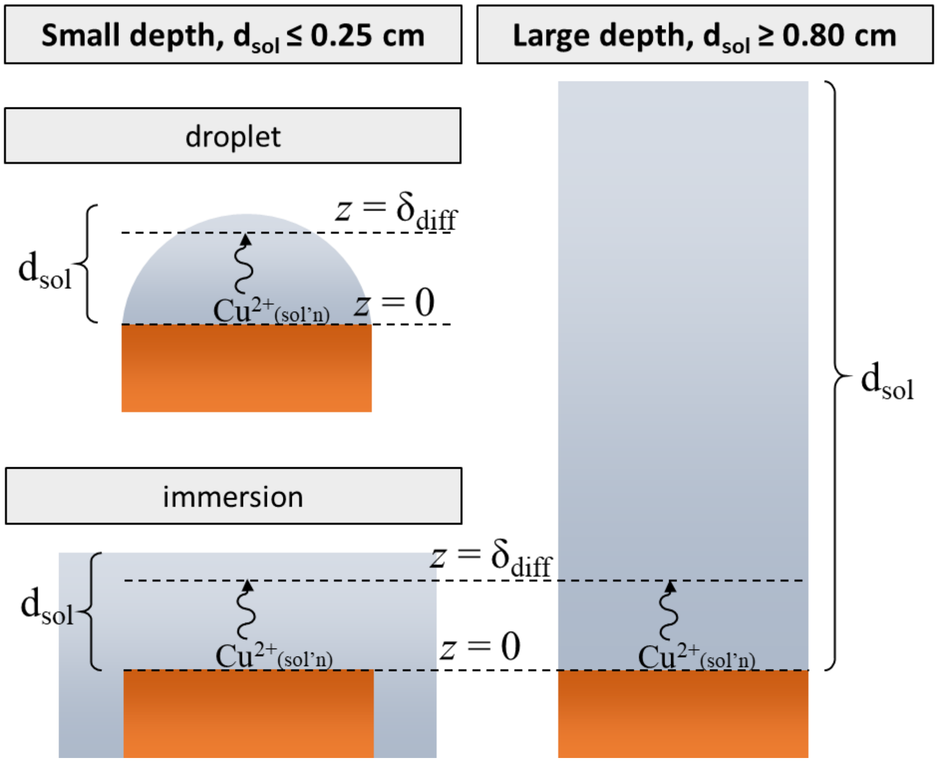

Figure 4.7 Schematic representation of the diffusion length (δ_{diff}) in small (left) and large (right) volumes, where d_{sol} is the solution depth.

The solution used for all values of d_{sol} was pure water with pH_0 near neutral, which is the same solution used in the droplet experiments presented in **Section 4.3.3**. The radiolytic copper corrosion mechanism for droplet solutions (where the maximum d_{sol} is 0.20 cm) was discussed in the previous section. The time-dependent evolution of corrosion products in droplet solutions and all d_{sol} show similar trends, although the length and the corrosion product yield in each stage was dependent on the solution depth. The solution volume used for the smallest d_{sol} (0.25 cm) in **Figure 4.8** (black) was 2.0 mL, which was the same volume used for the largest d_{sol} (2.50 cm, red in **Figure 4.8**) (see experimental set-up information in **Chapter**

8). Despite the same volume, the results with smaller values of d_{sol} are more comparable to those in droplet solutions.

For d_{sol} = 0.25 cm solutions, the depth was similar to the maximum depth of the droplet solutions discussed in the previous section (schematically shown in **Figure 4.7**). $[Cu^{II}_{(sol'n)}]_{max}$ was 2.7 ± 0.3 mM (red dotted line in **Figure 4.8**), which is a much lower concentration than in the droplet solutions, but the same number of moles of $Cu^{II}_{(sol'n)}$ were produced in both solutions (5.0 ± 0.1 μmol). Thus, the pH at which the $[Cu^{II}_{(sol'n)}]_{max}$ is at its saturation value is much higher in this larger volume (5.2, blue dotted line in **Figure 4.8**), than in the droplet solution (4.4 in **Figure 4.6**). Accordingly, the measured pH_t remained high, even with the continuous input of acidic radiolysis products. It is the $Cu(OH)_2$ solubility equilibrium, more so than the radiolysis products, that controls the pH_t in solutions with a small solution depth.

The large d_{sol} ($d_{sol} \geq 0.80$ cm) solution (red, green, and purple in **Figure 4.8**) had a low pH_f of 3.4 ± 0.2. The steady-state pH_t value was lower for larger d_{sol} because the bulk solution reactions contributed more significantly to the overall pH_t. Thus, it is mostly the radiolytic acidic species that contribute to the low pH_f in large d_{sol}, while the corrosion reactions, which are localized in the interfacial solution, contributed more substantially to the pH_t of small solutions. The $[Cu^{II}_{(sol'n)}]_{max}$ values in these solutions were proportional to the solution depth.

In all solutions, Stage 1 involved an increase in $[Cu^{II}_{(sol'n)}]_t$ with time. The length of Stage 1 increased with increasing solution depth, but the rate of $Cu^{II}_{(sol'n)}$ production (in nmol of $Cu/cm^2/h$) was not dependent on solution depth (values given in **Chapter 8**). That is, the rate of corrosion in Stage 1 is not dependent on d_{sol}, but the overall amount of metal loss in Stage 1 increases with increasing d_{sol}. In Stage 2, $[Cu^{II}_{(sol'n)}]$ remained constant with time at a concentration value that was nearly independent of d_{sol}. Thus, the number of moles of $Cu^{2+}_{(sol'n)}$ in solution during $Cu(OH)_2$ hydrogel growth is proportional to d_{sol}. In corrosion stages beyond Stage 2, the overall amount of copper oxidation is proportional to d_{sol}, which is discussed in depth in subsequent chapters.

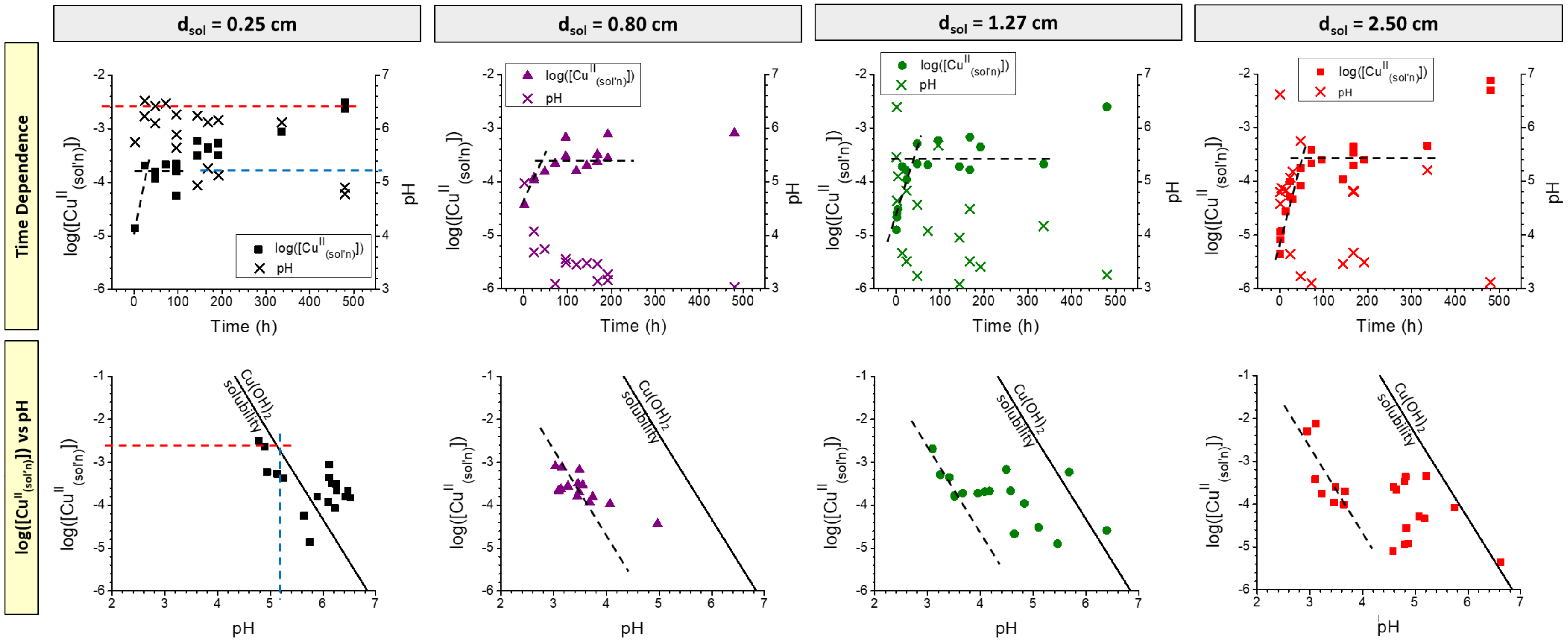

Figure 4.8 Time-dependent behaviour of [Cu^{II}$_{(sol'n)}$] and pH (upper row) and the log([Cu^{II}$_{(sol'n)}$])-pH relationship (bottom row) in solutions of different solution depths (d$_{sol}$) in the presence of radiation. The red dotted line indicates the [Cu^{II}$_{(sol'n)}$]$_{max}$ and the blue dotted line indicate the pH at which the [Cu^{II}$_{(sol'n)}$]$_{max}$ is at its saturation capacity. The black dotted lines show the general trend of the data (not based on regression analysis).

The log([$Cu^{II}_{(sol'n)}$])-pH relationship for d_{sol} = 0.25 cm (black, **Figure 4.8**) shows that the $Cu(OH)_2$ solubility equilibrium was established and maintained despite the changes in pH_t between 4.8 and 6.5. This quick establishment of the $Cu(OH)_2$ solubility equilibrium was also observed in the droplet solutions with a similar d_{sol}, however, the pH_t and [$Cu^{II}_{(sol'n)}$]$_t$ values were lower in the larger volumes. Thus, solutions with similar d_{sol} show a similar log([$Cu^{II}_{(sol'n)}$])-pH relationship but with [$Cu^{II}_{(sol'n)}$]$_{max}$ and pH_f values that depend on the solution conditions.

The log([$Cu^{II}_{(sol'n)}$])-pH relationship when $d_{sol} \geq 0.8$ cm follows the $Cu(OH)_2$ quasi-equilibrium when the pH is between 4.0 and 7.0 (a similar pH range to that of d_{sol} = 0.25 cm). However, as the pH_t decreased past 4.0, the log([$Cu^{II}_{(sol'n)}$])-pH values fell well below those of the solubility equilibrium curve (the entire solution was not saturated with cupric ions). Despite being undersaturated, the [$Cu^{II}_{(sol'n)}$] increase with pH or time is not what was expected for active dissolution. Instead, for pH < 4.0 the increase in log([$Cu^{II}_{(sol'n)}$]) has a similar relationship with pH to that of the $Cu(OH)_2$ solubility curve, with a log([$Cu^{II}_{(sol'n)}$])-pH slope of −2 (indicated by the black dotted line in the bottom row in **Figure 4.8**), albeit at lower log([$Cu^{II}_{(sol'n)}$])-pH values. This suggests that the change in [$Cu^{II}_{(sol'n)}$] with pH remains governed by the $Cu(OH)_2$ solubility equilibrium. This is consistent with the proposed mechanism of the formation of the hydrogel between the metal surface and the bulk solution. However, the measured values of pH_t and [$Cu^{II}_{(sol'n)}$]$_t$ are averaged over the entire solution (*z*-averaged), and the log([$Cu^{II}_{(sol'n)}$])-pH relationship is to the left of the $Cu(OH)_2$ solubility curve.

The log([$Cu^{II}_{(sol'n)}$])-pH relationships in various d_{sol} are shown in **Figure 4.9**. The $Cu(OH)_2$ solubility quasi-equilibrium was maintained for all d_{sol} for pH values between 4.0 and 7.0. Only the largest d_{sol} (≤ 0.80 cm) had pH values lower than this range, at which the solution was under its solubility limit, as discussed above. This again confirms that the values of [$Cu^{II}_{(sol'n)}$] and pH after long-term copper corrosion converge at the Ksp, but the absolute values are based on the initial conditions and the evolution of [$Cu^{II}_{(sol'n)}$]$_t$ and pH_t with time. Thus, to accurately predict the values of [$Cu^{II}_{(sol'n)}$]$_{max}$ and pH_f along the solubility curve, the initial conditions and the time-dependent behaviours of [$Cu^{II}_{(sol'n)}$]$_t$ and pH_t must be known. The findings presented in this section indicate that the solution depth, not volume, determines how the log([$Cu^{II}_{(sol'n)}$])-pH relationship evolves.

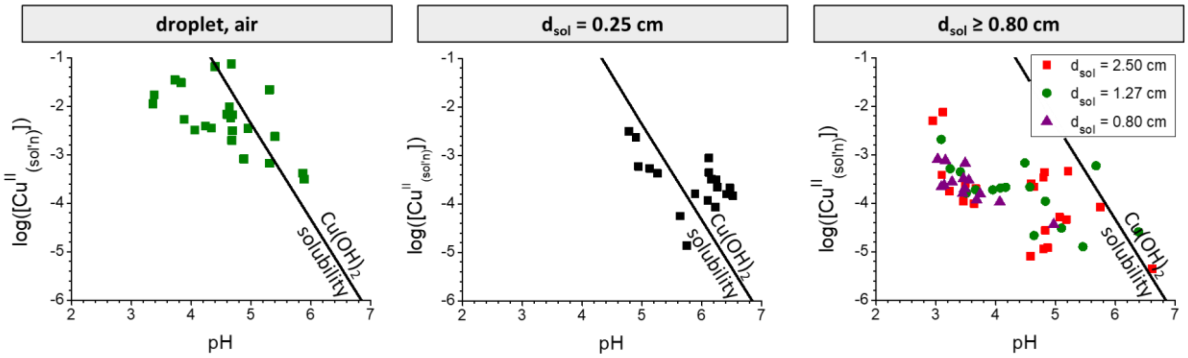

Figure 4.9 The $\log([Cu^{II}_{(sol'n)}])$-pH relationship during radiolytic corrosion in droplet solutions (**Section 4.3.3**), small solution depths (d_{sol} = 0.25 cm), and large solution depths ($d_{sol} \geq 0.8$ cm).

4.4 CONCLUSION

This chapter investigated the relationship between $Cu^{II}_{(sol'n)}$ dissolution and pH during copper corrosion in a wide range of conditions. The time dependences for $[H^+]$ and $[Cu^{II}_{(sol'n)}]$ were established and it was shown that the same elementary rate-determining steps are involved in Stages 1 and 2 in all studied conditions (in a variety of pH_0 and oxidizing environments). The time-dependent values of $[H^+]$ and $[Cu^{II}_{(sol'n)}]$ had outliers and variations, however, the $\log([Cu^{II}_{(sol'n)}])$-pH relationship was consistent across all time points and solution conditions. It was shown that beyond Stage 1, the values of $[Cu^{II}_{(sol'n)}]$ and pH can be determined by the solubility equilibrium of $Cu(OH)_2$ if the initial conditions and the evolution with time are known.

Although the process of developing a quantitative corrosion rate model is still underway, the elementary steps identified through this study can consistently explain the time-dependent behaviours of measured dissolved copper concentration ($[Cu^{II}_{(sol'n)}]_t$) and pH_t, and the effects of pH_0, type and concentration of oxidant, and CO_2/carbonate on the time dependences and the durations of Stages 1 and 2. Furthermore, the fundamental understanding gained from the results presented in this chapter of the thermodynamic limitations for copper concentration values could simplify long-term corrosion modelling.

4.5 REFERENCES

1 Powell, K. J., Brown, P. L., Byrne, R. H., Gajda, T., Hefter, G., Sjöberg, S., Wanner, H. Chemical Speciation of Environmentally Significant Metals with Inorganic Ligands. Part 2: The Cu^{2+}-OH^-, Cl^-, CO_3^{2-}, SO_4^{2-}, and PO_4^{3-} Systems. *Pure Appl. Chem.* **79**, 895-950, (2007).

2 Wren, J. C., Jean, A., Naghizadeh, M., Grandy, L., Morco, R., Joseph, J. M., Behazin, M., Keech, P. G. Radiation Induced Corrosion of Copper in Deep Geological Repositories in *WM2019: 45 Annual Waste Management Conference.* 1-15 (Office of Scientific and Technical Information).

3 Wren, J. C., Guo, D., Shin, Y., Li, M., Morco, R., Joseph, J. M., Behazin, M., Keech, P. G. Corrosion of Carbon Steel Inside Used Nuclear Fuel Containers in *WM2019: 45 Annual Waste Management Conference.* (Office of Scientific and Technical Information).

4 Naghizadeh, M. "Copper Corrosion Dynamics under Deep Geologic Repository Conditions" Doctor of Philosophy, The University of Western Ontario, Electronic Thesis and Dissertation Repository. (2021). 7894.

5 Shin, Y. G. "Nonlinear Dynamics of Carbon Steel Corrosion under Gamma Radiation" Doctor of Philosophy, The University of Western Ontario, Electronic Thesis and Dissertation Repository. (2020). 7339.

6 Wu, L., Guo, D., Li, M., Joseph, J. M., Noël, J. J., Keech, P. G., Wren, J. C. Inverse Crevice Corrosion of Carbon Steel: Effect of Solution Volume to Surface Area. *J. Electrochem. Soc.* **164**, C539-C553, (2017).

7 Turnbull, J., Szukalo, R., Behazin, M., Hall, D., Zagidulin, D., Ramamurthy, S., Wren, J. C., Shoesmith, D. W. The Effects of Cathodic Reagent Concentration and Small Solution Volumes on the Corrosion of Copper in Dilute Nitric Acid Solutions. *Corrosion* **74**, 326-336, (2017).

8 Rustad, J. R., Casey, W. H. A Molecular Dynamics Investigation of Hydrolytic Polymerization in a Metal−Hydroxide Gel. *J. Phys. Chem. B* **110**, 7107-7112, (2006).

9 Baes, C. F., Mesmer, R. E. *The Hydrolysis of Cations*. (Wiley, 1976).

10 Gustafson, R., Martell, A. Formation of Polynuclear Complexes in Aqueous Solution. *Ann. N.Y. Acad. Sci.* **88**, 322-331, (2006).

11 Bessho, K., Oki, Y., Akimune, N., Matsumura, H., Masumoto, K., Sekimoto, S., Osada, N., Kinoshita, N., Monjushiro, H., Shibata, S. Corrosion of Copper in Water and Colloid Formation Under Intense Radiation Field. *J. Radioanal. Nucl. Chem.* **303**, 1117-1121, (2015).

12 Khatouri, J., Mostafavi, M., Amblard, J., Belloni, J. Radiation-Induced Copper Aggregates and Oligomers. *Chem. Phys. Lett.* **191**, 351-356, (1992).

13 Zezin, A. A., Klimov, D. I., Zezina, E. A., Mkrtchyan, K. V., Feldman, V. I. Controlled Radiation-Chemical Synthesis of Metal Polymer Nanocomposites in the Films of Interpolyelectrolyte Complexes: Principles, Prospects and Implications. *Radiat. Phys. Chem.* **169**, 108076, (2020).

14 Pohl, P., Saparov, S. M., Antonenko, Y. N. The Size of the Unstirred Layer as a Function of the Solute Diffusion Coefficient. *Biophys. J.* **75**, 1403-1409, (1998).

CHAPTER 5. CHEMICAL ADDITION OF KEY RADIOLYSIS PRODUCTS

5.1 INTRODUCTION

The copper layer of the UFC and the DGR environment will be exposed to a continuous flux of γ-radiation emitted from decaying radionuclides in the used fuel.[1] The absorbed γ-radiation by copper metal will be dissipated by heat without inducing chemical changes in the metal. However, the absorbed γ-radiation by liquid water and humid air will cause their decomposition into redox active and acidic species. Due to a low linear energy transfer rate from γ-photon (via Compton scattered electron) to water, γ-radiation produces the species homogeneously within the irradiated solution volume and, under a continuous flux of γ-radiation, the radiolysis product concentrations reach steady state. Hence, the effects of γ-radiation on corrosion rate are through the radiolysis products that are distributed homogeneously and at near constant concentrations (even though they may be consumed by corrosion reactions).

The initial products formed from the radiolytic decomposition are referred to as primary radiolysis products and are distributed homogeneously within 100 ns at a concentration that is affected by the total absorbed radiation dose.[2-5] For processes that occur within 100 ns, such as allowed electronic energy state transitions (light absorption/fluorescence), it is critical to follow the rates of production of the primary radiolysis products. However, the primary radiolysis products will react together in solution as well as with other solution species on a micro- to millisecond timescale, from which they are consumed to form secondary species in concentrations that are affected by the radiation dose rate and the concentration of other species in solution (e.g., H^+, O_2, Cl^{--}, and other radical scavengers). For water (**Eq. 5.1**) and humid air (**Eq. 5.2**) exposed to gamma radiation, these species include redox active and acidic products:

$$H_2O_{(l)} \overset{\gamma}{\rightsquigarrow} HO^{\bullet}, H^+, e^-_{(aq)}, H^{\bullet}, H_2, H_2O_2, O_2^{\bullet-} \qquad (5.1)$$

$$H_2O_{(g)}, N_{2(g)}, O_{2(g)} \overset{\gamma}{\rightsquigarrow} NO_x, HNO_3 \qquad (5.2)$$

The steady-state concentrations of these species, not the primary radiolysis species concentration, affect the rates of solid-liquid interfacial mass transfer processes or surface reactions that occur on the timescale of minutes. The steady-state concentrations of these radiolysis products depends on the radiation dose rate, not the total absorbed dose.[3] Calculated concentrations for water and humid air radiolysis products produced at the dose rate used in this thesis is shown in **Figure 5.1**.[1]

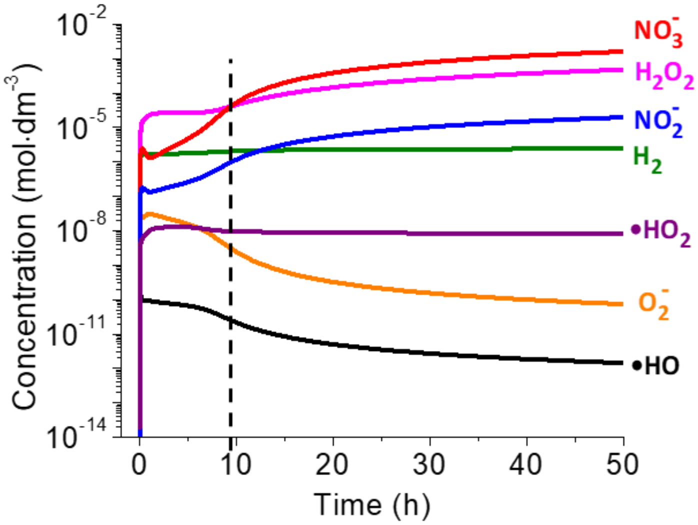

Figure 5.1 Simulated production of water and humid air radiolysis species in the presence of γ-radiation (2 kGy/h) in the absence of Cu corrosion.[1] The dashed vertical line indicates a change in the dominant radiolysis product from H_2O_2 to NO_3^-.

Furthermore, because of the different reaction times of homogeneous solution and surface reactions, the important radiolysis products for corrosion are not the more reactive radical species but the more stable molecular products such as H_2O_2, O_2, H^+, NO_3^-/NO_2^-. (For ground waters that may contain highly saline concentrations, the intermediate chloride radiolysis products such as ClO and Cl_2 may become important.) So while there are many highly oxidizing radiolysis products (e.g., •OH), their lifetime is short and will be consumed in solution before reaching the metal surface to participate in redox reactions that occur at the metal surface.[1] Due to their continual production in a continuous flux of γ-radiation, these radical species can participate in other solution reactions that occur at later stages of corrosion.

The main oxidant species that induces metal oxidation in the presence of radiation is the source of much debate.[6-9] The molecular species, particularly H_2O_2 has been identified as a key radiolysis product for corrosion reactions.[3,6,7,10-12] Nitrate has also been shown to participate in the oxidation of copper.[13,14] However, the main role of radiolytically-produced nitrate has been identified as the complexation and co-precipitation with copper ions in late corrosion stages.[13-16] During late-stage corrosion, both H_2O_2 and NO_3^- are able to reduce $Cu^{II}_{(sol'n)}$, once it accumulates in the solution, accelerating its precipitation as $Cu(OH)_2$ hydrogel and Cu_2O,[7,17-19] which is discussed in detail in **Chapter 6**. Water and humid air radiolytic decomposition also produce acidic species, decreasing the pH of the solution substantially.

Determining the overall effects of the presence of radiation on a corroding system is complicated as both the individual effects of each species and the combined effects must be fully understood. The presence of radiation produces species continuously at a steady-state concentration, so they are not depleted by reactions and can continuously interact with the corroding system. Because of this continuous production, the effects of long-term radiolysis on copper corrosion cannot be extrapolated from the results from a one-time chemical addition of radiolysis products.[3,8] However, how the key radiolysis species affect corrosion at early times can be determined and is the aim of this study.

The effects of the key water and humid air radiolysis products, H_2O_2 and HNO_3, on the copper corrosion dynamics at early corrosion times are studied in this chapter. The initial concentration of oxidant, the addition of nitrate, and a lowered pH are all investigated. The experiments were conducted in the absence of radiation and the corrosion dynamics were followed by analysing the dissolved and solid corrosion products as a function of corrosion duration.

5.2 EXPERIMENTAL

5.2.1 Materials and Solutions

All experiments were performed with high purity copper (99.9% purity) coupons made from wrought copper samples (provided by SKB, the Swedish Nuclear Waste Management Company) with an exposed surface area of 0.785 cm^2. The top surface of the copper coupons was ground using silicon carbide papers with grit sizes 400, 800, and 1200 in succession. The coupons were then washed with deionized water, dried under flowing $Ar_{(g)}$ and placed in a 20 mL vial sealed with an aluminum crimp cap with a polytetrafluoroethylene (PTFE)-coated silicone septum (Thermo Fisher Scientific, Waltham, MA). More information on this procedure is provided in **Section 3.1**. Poly-vinyl chloride heat shrink tubing (Techflex, Sparta, NJ) with an inner diameter of 15.88 mm was used to expose only the top, polished surface, and 2.0 mL of solution was used, as shown in **Figure 5.1**. Samples were left on the benchtop, not exposed to radiation, and covered with aluminium foil to minimize photochemical degradation of H_2O_2. Control experiments were performed in shrink tubing without copper to measure H_2O_2 degradation (not shown).

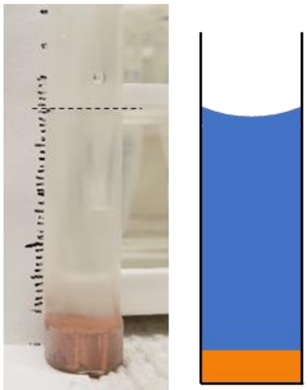

Figure 5.2 Image and schematic of the experimental set up, in which a copper coupon is embedded in a shrink tubing to expose only the top surface to 2.0 mL of solution.

Hydrogen peroxide (H_2O_2) solutions were prepared by dilution of a 3 wt. % stock H_2O_2 solution (Thermo Fisher Scientific, Waltham, MA), using water purified to a resistivity of 18.2 MΩ·cm with a NANOpure Diamond UV ultra-pure water system (Barnstead International, Dubuque, IA) and were stored in a fridge between experiments. If a pH increase was required (i.e., for $pH_0 = 6.5$, 10 mM H_2O_2 solutions), a 1 M sodium hydroxide (≥ 98 %, Sigma Aldrich, St. Louis, MO) solution was added dropwise to achieve the desired pH.

H_2O_2 solutions containing nitrate (NO_3^-) were made using $NaNO_3$ supplied by Sigma-Aldrich. HNO_3 stock solution (70 % Sigma Aldrich, St. Louis, MO) was added dropwise to lower the pH to 4.0 when required, with the pH determined using an Orion 9110DJWP Double Junction Micro-pH Electrode (Thermo Fisher Scientific, Waltham, MA).

Cu^{2+}-saturated solutions were made by dissolving 0.8 mg of technical grade copper (II) hydroxide (Sigma Aldrich, St. Louis, MO) in 20.0 mL of water (purified using a NANOpure

Diamond UV ultra-pure water system (Barnstead International, Dubuque, IA). For qualitative determination of the effect of [H_2O_2] on cupric ion precipitation in **Section 5.3.2**, 0.5 mL of the Cu^{2+}-saturated solution was placed on top of the copper coupon embedded in the shrink tubing, followed by 1.5 mL of water or H_2O_2 solution.

5.2.2 Post-Test Analyses

Experiments were terminated by removing the solution from the coupon surface using a Pasteur pipette. The copper coupon was washed with deionized water and dried using Ar gas. Optical images were obtained using a Leica DVM6A digital microscope, as outlined in **Section 3.3.1**, then the coupon was stored under vacuum. Scanning electron microscopy (SEM) was performed at the Western Nanofabrication Facility using Zeiss LEO 1530 instrument (more information is given in **Section 3.3.2**).

An aliquot of the solution was diluted for ultraviolet visible spectrophotometry (BioLogic Science Instruments) to determine the H_2O_2 concentration using the Ghormley triiodide method, following the procedure outlined in **Section 3.4.3**.[20] A second aliquot of solution was diluted so the dissolved copper concentration could be quantified using inductively coupled plasma optical emission spectroscopy (ICP-OES) (PerkinElmer Avio 200 ICP-OES) following the procedure outlined in **Section 3.4.2**. The remaining solution was used for pH determination performed using a Thermo Scientific Orion 9110DJWP Double Junction Micro-pH Electrode, outlined in **Section 3.4.1**.

5.3 RESULTS & DISCUSSION

5.3.1 Effects of H_2O_2 on Copper Dissolution Kinetics

Radiolysis decomposition products, including H_2O_2, are continuously formed at a low steady-state concentration during radiolytic copper corrosion. However, for copper corrosion in the presence of a chemical solutions containing the species produced via radiolytic decomposition, the radiolysis product concentration is initially high and decreases as it is consumed by corrosion reactions. Thus, in experiments done with chemical addition, only initial corrosion processes can be studied. The advantage of using chemical solutions over exposing solutions to a continuous flux of γ-radiation is the individual effects of radiolysis species can be investigated and decoupled from each other.

In this section, the effects of the initial [H_2O_2] ([H_2O_2]$_0$) on Stages 1 and 2 are investigated by using chemical solutions with various [H_2O_2]$_0$ at an initial pH (pH_0) near neutral (unadjusted for [H_2O_2]$_0$ = 0 M and 0.1 mM at 6.5 and increased to 7.0 for [H_2O_2]$_0$ = 10 mM). The time-dependent behaviours of [$Cu^{II}_{(sol'n)}$], pH, and H_2O_2 consumption ($\% H_2O_2 = \frac{[H_2O_2]_0 - [H_2O_2]_t}{[H_2O_2]_0} \times 100\%$) are shown in **Figure 5.3**.

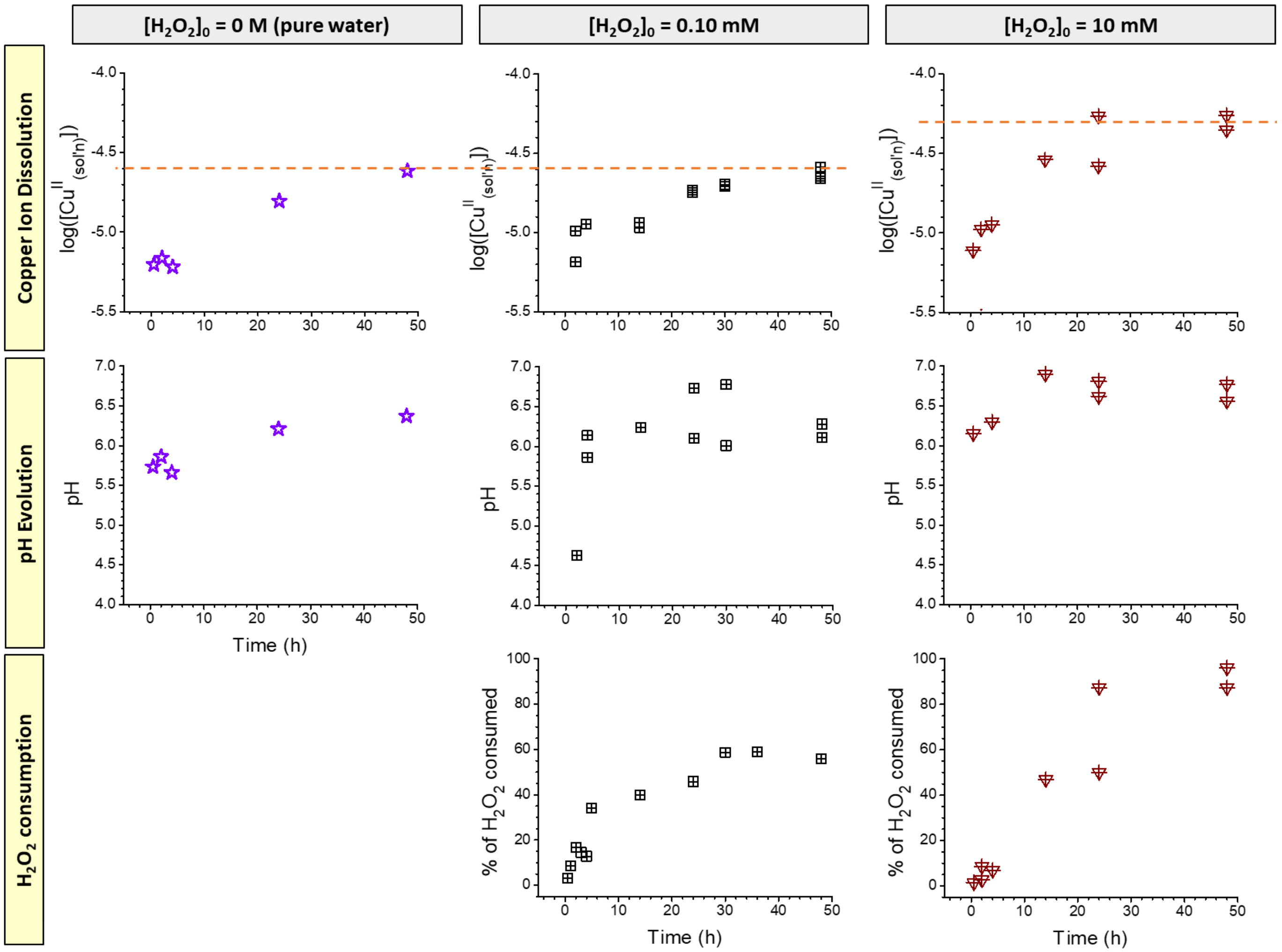

Figure 5.3 Time-dependent behaviour of $[Cu^{II}_{(sol'n)}]$ (top row), pH (middle row), and H_2O_2 consumption (bottom row) in the presence of various $[H_2O_2]_0$ with pH_0 = 6.5 – 7.0. The orange dotted line indicates $[Cu^{II}_{(sol'n)}]_{max}$.

In solutions with a near neutral pH_0, the first measured pH_t (t = 2 h) was lower than pH_0, shown in the middle row in **Figure 5.3**. This indicates that in initial corrosion times, the production of H^+ is faster than the production of OH^- via O_2 reduction at $z = 0$. As discussed in detail in **Chapter 4**, when the pH of a solution is near the equivalence point of water, a small production of OH^- by the oxidant reduction reaction can cause a significant and immediate increase in pH at $z = 0$. The increase in pH pushes the cupric ion hydrolysis reaction towards the formation of $Cu(OH)_3^-$ very quickly. The fast rates of these reactions mean that they can be considered one elementary reaction occurring at $z = 0$ and at very early corrosion times, both $[H^+]_t$ and $[Cu^{II}_{(sol'n)}]$ increase (**Figure 5.3**). This initial pH_t decrease at initial corrosion times was observed when the oxidant was O_2 ($[H_2O_2]_0 = 0$ M) and H_2O_2 ($[H_2O_2]_0 = 0.1$ mM and 10 mM), indicating this elementary step is not dependent on the oxidant type:

$$Cu^0_{(m)} + \tfrac{1}{2}\,O_2 + 2\,H_2O \rightarrow Cu(OH)_3^- + H^+ \qquad \text{in } \underline{\text{Stage 1a}} \qquad (5.3)$$

$$Cu^0_{(m)} + H_2O_2 + H_2O \rightarrow Cu(OH)_3^- + H^+ \qquad \text{in } \underline{\text{Stage 1a}} \qquad (5.4)$$

When $[H_2O_2] > 0.05$ mM, O_2 reduction is too slow to compete with H_2O_2 reduction coupled with $Cu^0_{(m)}$ reduction and can be considered negligible.[21,22]

$Cu(OH)_3^-$ and H^+ diffuse from $z = 0$, where they are produced, into the bulk solution ($z = \delta_{diff}$), which results in the increase in $[Cu^{II}_{(sol'n)}]_t$ and the decrease in pH_t in <u>Stage 1a</u>. The stochiometric ratios in **Eq. 5.3** and **Eq. 5.4** indicate that the increase in $[Cu^{II}_{(sol'n)}]_t$ should be equal to the increase in $[H^+]_t$. This equivalence is observed when no other acid-base equilibria are established in the solution (e.g., unirradiated CO_2-free solutions, shown in **Chapter 6**). However, in naturally aerated solutions, such as those presented in this chapter, the bicarbonate buffering system affects $[H^+]_t$ of solutions near its pKa.

$$H_2CO_3 \rightleftharpoons H^+ + HCO_3^- \qquad pKa = 6.4 \qquad (5.5)$$

Small amounts of H^+ produced at the surface will be consumed via **Eq. 5.5** which makes the increase in $[Cu^{II}_{(sol'n)}]$ by the first measurement larger than the increase in $[H^+]$ for all $[H_2O_2]_0$ (**Figure 5.2** shows the first measurement: $\log([Cu^{II}_{(sol'n)}]) = -5.1$ and pH = 5.4).

The subsequent increase in pH$_t$ for 0.5 h ≤ t ≤ 14 h (**Figure 5.3**) is due to the formation of $Cu(OH)_{2(solv)}$ and $Cu(OH)^+$ as $Cu(OH)_3^-$ and H^+ diffuse into the bulk solution.

$$Cu(OH)_3^- + H^+ \rightarrow Cu(OH)_{2(solv)} + H_2O \rightarrow Cu(OH)^+ + OH^- \quad \text{in } \underline{\text{Stage 1b}} \qquad (5.6)$$

Despite a pH$_t$ increase of more than an order of magnitude during <u>Stage 1b</u>, $[Cu^{II}_{(sol'n)}]$ dissolution throughout <u>Stage 1a</u> and <u>1b</u> is linear with time. Because only dissolved copper species are produced during <u>Stage 1</u>, the corrosion rate is proportional to the dissolution rate, as described in **Chapter 4**. The linear dissolution rate in <u>Stage 1</u> indicates that the corrosion rate does not change with pH$_t$.

$Cu(OH)_{2(solid)}$ will precipitate after the solution reaches the cupric ion solubility limit. Previous studies show that precipitation of $Cu(OH)_2$ will initially be as colloid particles that remain dispersed in solution.[23-25] The formation of the colloidal particles does not change the rate in <u>Stage 1</u> and contribute to the overall $[Cu^{II}_{(sol'n)}]_t$. The final pH$_t$ of 6.4 ± 0.2 (corresponding to the pKa of bicarbonate, **Eq. 5.5**) reached at the end of <u>Stage 1</u> was the same for $[H_2O_2]_0$ of 0 M (purple) and 0.1 mM (black). The highest $[H_2O_2]_0$ (10 mM) reached a slightly higher pH$_t$ of 6.7 ± 0.2, likely due to the slightly higher $[OH^-]_0$.

During <u>Stage 1a</u> and <u>1b</u> (t ≤ 14 h), the increase of $[Cu^{II}_{(sol'n)}]_t$ matched the decrease of $[H_2O_2]_t$ (bottom row in **Figure 5.3**) for solutions with $[H_2O_2]_0 > 0$ M. This equivalence is predicted by the stochiometric ratios in **Eqs. 5.3** and **5.6**, which lends additional confirmation that the metal oxidation is forming mainly dissolved cupric ion species during <u>Stage 1</u>.

$[Cu^{II}_{(sol'n)}]_t$ and pH$_t$ plateau when t > 14 h for all $[H_2O_2]_0$. Furthermore, **Chapter 4** showed that at this time, the solution had reached $Cu(OH)_2$ solubility equilibrium. Thus, the $Cu(OH)_2$ colloid particles agglomerate into a hydrogel network while the solution remains at the saturation limit. That is, the rate of $Cu^0_{(m)}$ oxidation to form $Cu^{2+}_{(sol'n)}$ is as fast as $Cu^{2+}_{(sol'n)}$ precipitation to form the hydrogel network. The equal rates of production and removal of $Cu^{2+}_{(sol'n)}$ result in the overall corrosion rate being controlled by the growth rate of the hydrogel species, as discussed in detail in **Chapter 6**. The plateau in $[Cu^{II}_{(sol'n)}]_t$ was at 24 ± 3 μM for $[H_2O_2]_0$ of 0 M (purple) and 0.1 mM (black). The same $[Cu^{II}_{(sol'n)}]_t$ indicates that a change in oxidant from O_2 (approximately constant at 0.25 mM) to H_2O_2 (initially at 0.10 mM) did not affect the dissolution rate or yield of $Cu^{II}_{(sol'n)}$. The $[Cu^{II}_{(sol'n)}]_t$ plateau for $[H_2O_2]_0$ of 10 mM was at 49 ± 7 μM, which was only two times higher than for $[H_2O_2]_0$ = 0.1 mM and 0 M, not 100 times higher, as one would expect if $Cu^{II}_{(sol'n)}$ dissolution rate was dependent on the initial oxidant concentration.

In all $[H_2O_2]_0$ solutions with pH_0 near neutral, the $Cu^{II}_{(sol'n)}$ dissolution behaviour and pH_t evolution was the same. The dissolution behaviour of $Cu^{II}_{(sol'n)}$ and the final yield of $[Cu^{II}_{(sol'n)}]$ was unaffected by the initial concentration of oxidant (0 – 10 mM) and identity of the oxidant (O_2 or H_2O_2). This finding contradicts the conventional understanding that the corrosion rate increases with increasing concentration of oxidant (usually $[O_2]$[26-28] or in the presence of radiation[8,9,29]). The steady-state $[H_2O_2]$ in the presence of radiation is dependent on the solution conditions and the dose rate, but this study has demonstrated that the identity and concentration of the oxidant do not need to be determined precisely to predict overall copper dissolution. These results indicate that it may be unnecessary to determine the identity of the main oxidant in radiation-induced corrosion of copper when predicting the copper dissolution behaviour. Both these major findings can simplify copper corrosion modelling in the presence of radiation.

5.3.2 Effects of H_2O_2 on Cu_2O Precipitation

The time-dependent surface evolution in solutions of various $[H_2O_2]_0$ is shown in **Figure 5.4** (the corresponding solution evolution is in **Figure 5.3**). In initial corrosion times (t = 2 h in **Figure 5.4**), the surface remains relatively clean of granular oxides. This corresponds with Stage 1, during which the main corrosion product is dissolved cupric species. With increasing time, more oxide deposits were observed on the surface and the proportion of the surface covered by oxides was proportional to $[H_2O_2]_0$. The surface remains relatively clear in the pure water solutions, although faint orange Liesegang bands were observed after 48 h (bottom row in **Figure 5.4**). Localized spots of Cu_2O growth appeared on the surface for $[H_2O_2]_0$ = 0.1 mM, while almost uniform growth was observed for $[H_2O_2]_0$ = 10 mM.

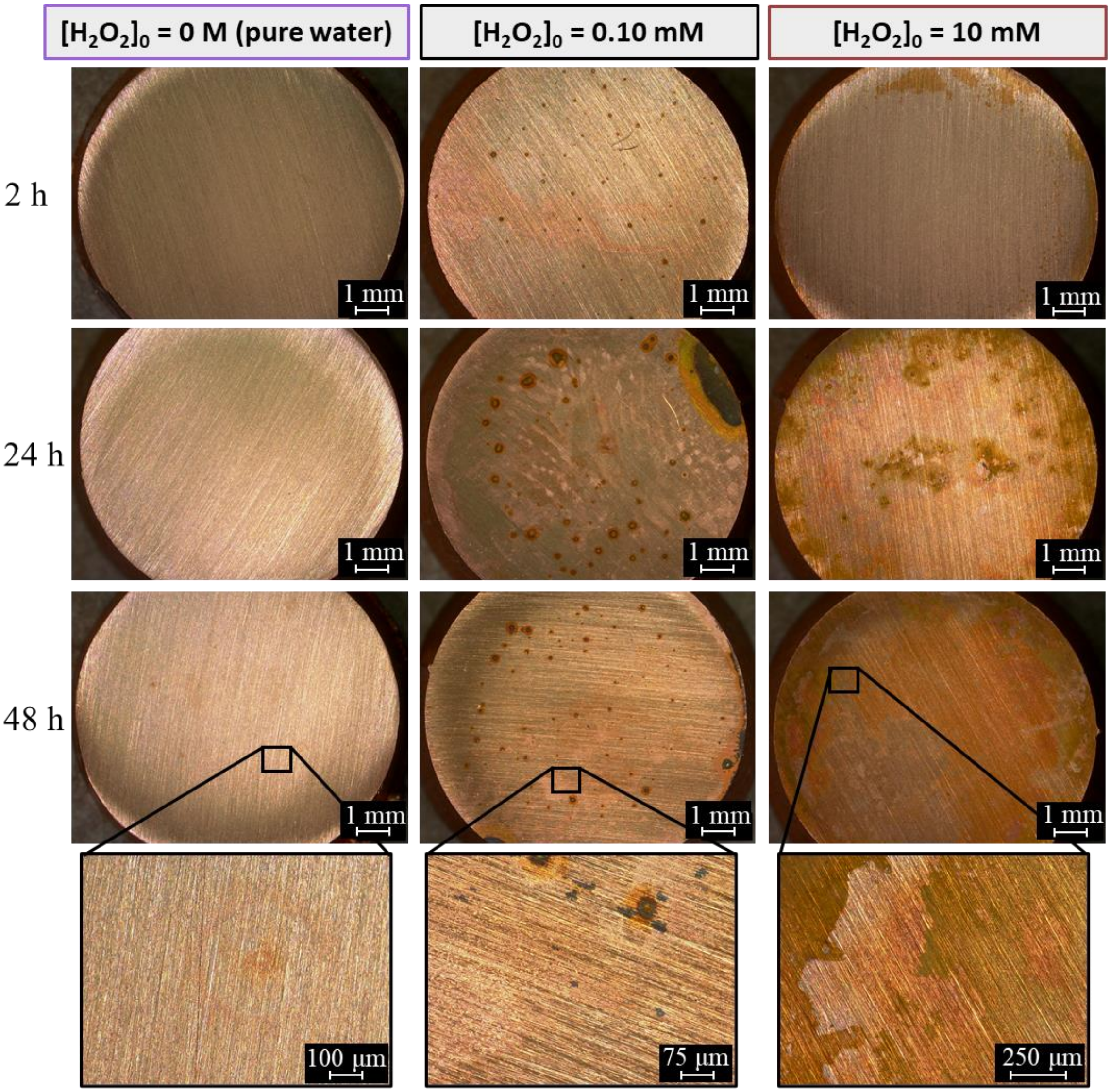

Figure 5.4 Optical images of the surface after exposure to various $[H_2O_2]_0$ ($pH_0 = 6.5 – 7.0$) for 2, 24, and 48 h of corrosion.

As cupric ions accumulate in solution during Stage 2, H_2O_2 can be oxidized coupled with the reduction of cupric ion (**Eq. 5.7a**). The rate of oxidation of H_2O_2 by $Cu^{2+}_{(sol'n)}$ can only compete with its rate of reduction by $Cu^{0}_{(m)}$ when the concentration of $Cu^{2+}_{(sol'n)}$ is high, and thus only occurs at later stages of corrosion (i.e., Stage 2 and 3). The solubility of $Cu^{+}_{(sol'n)}$ is very low, quickly establishing its solubility equilibrium, and CuOH joins the solid hydrogel network (**Eq. 5.7b**). This process is discussed in detail in **Chapter 6**. CuOH is unstable and will dehydrate to form the more stable Cu_2O (**Eq. 5.7c**).

$$2\ Cu^{2+} + H_2O_2 + 2\ OH^- \rightarrow 2\ Cu^+ + O_2 + 2\ H_2O \quad (5.7a)$$

$$Cu^+ + OH^- \rightleftharpoons CuOH_{(solid)} \quad (5.7b)$$

$$2\ CuOH \rightarrow Cu_2O + H_2O \quad (5.7c)$$

The redox activity of the solution is key to the reduction of $Cu(OH)_2$ to CuOH and thus, the growth of Cu_2O particles. The chemical activity of H_2O_2 is directly proportional to the rate of reaction of **Eq. 5.7a**, and thus, the amount of oxide growth at a particular corrosion time is directly proportional to $[H_2O_2]_0$ (**Figure 5.4**).

Note, in pure water ($[H_2O_2]_0$ = 0 M), the reduction of $Cu^{2+}{}_{(sol'n)}$ may be $Cu^0{}_{(m)}$ or H_2O_2, the latter formed from the two step O_2 reduction.[13,14,21,30,31] However, the chemical activity of $Cu^0{}_{(m)}$, as with any solid, is one and thus does not affect the rate of reaction.

For $[H_2O_2]_0 > 0$ M solutions (black and brown in **Figure 5.3**), the consumption of H_2O_2 in Stage 2 was higher than the $Cu^{II}{}_{(sol'n)}$ production at the same corrosion time, despite an expected ratio of 1:1 if all H_2O_2 was used to make $Cu^{II}{}_{(sol'n)}$ (**Eq. 5.4**). In the blank experiments performed in the absence of copper corrosion (data not shown), H_2O_2 decomposition was minimal indicating that the self-decomposition of H_2O_2 without copper is minimal. H_2O_2 decomposition can be catalyzed by $Cu^I{}_{(sol'n)}$ via Fenton-like reactions; however due to the low solubility of $Cu^I{}_{(sol'n)}$, its reaction with H_2O_2 is expected to be low.[7,32,33] The reduction of cupric ions to cuprous ions homogeneously in solution by H_2O_2 is known to occur in irradiated solutions.[21] It is proposed that most of the extra consumption of H_2O_2 is via $Cu(OH)_2$ reduction to CuOH (which precipitates as Cu_2O, **Eq. 5.7**).

For $[H_2O_2]_0$ = 0.10 mM solutions, the pseudo-first order rate constant for H_2O_2 consumption when t > 14 h was found to be $4 \pm 2 \times 10^{-6}\ s^{-1}$ (extracted from **Figure 5.3**). This measured rate constant is similar to that reported for the oxidation of H_2O_2 by Cu^{2+} (**Eq. 5.7a**), $k_{H2O2} \sim 3\times10^{-6}\ s^{-1}$ at pH 6 for 10 μM Cu^{2+} ($\log([Cu^{2+}] = -5.0)$.[7,17] This suggests that the oxidation of H_2O_2 (coupled with $Cu^{2+}{}_{(sol'n)}$ reduction), not just its reduction (coupled with $Cu^0{}_{(m)}$ oxidation), occurs during Stage 2 and beyond, and therefore, is included in the mechanistic description presented in **Chapter 6**, and eventually the modelling of radiation-induced copper corrosion.

To decouple the $Cu^0_{(m)}$ oxidation ($Cu^{II}_{(sol'n)}$ dissolution) and Cu_2O formation, a copper surface was exposed to a Cu^{2+}-saturated solution mixed with pure water, 0.1 mM H_2O_2, and 10 mM H_2O_2 and the optical images of the surfaces after 48 h of exposure are shown in **Figure 5.5**. The surface exposed to pure water showed only a few localized areas of solid corrosion product growth across the surface, but the general area remained clean. Similarly, after exposure to $[H_2O_2]_0$ = 0.1 mM there was some precipitation on the surface, but it remained generally clean. After exposure to $[H_2O_2]_0$ = 10 mM, many oxide islands were observed on the surface and the general surface darkened in colour (indicative of the entire surface covered with small Cu_2O crystals, discussed in depth in **Chapter 6**).

In these solutions, cupric ions were already at their saturation capacity, and thus, $Cu^0_{(m)}$ did not need to be oxidized before Cu_2O precipitation could begin. $[Cu^{II}_{(sol'n)}]$ in all $[H_2O_2]_0$ solutions was the same and no H_2O_2 consumption by $Cu^0_{(m)}$ needed to occur before precipitation. Therefore the effect of $[H_2O_2]_0$ on Cu_2O precipitation from a Cu^{2+}-saturated solution could be determined. In these experiments, pH_t and $[Cu^{II}_{(sol'n)}]_t$ did not change substantially over the 48-h experimental time (**Appendix B**), which means that if precipitation removed $Cu^{II}_{(sol'n)}$, it was replaced via $Cu^0_{(m)}$ oxidation. This is consistent with the interpretation of the corrosion studies that the solution remains at or above Cu^{2+}-saturation while Cu_2O precipitates via $Cu^{II}_{(sol'n)}$ reduction. Furthermore, these findings confirm that the $[H_2O_2]_0$ is directly proportional to the rate of Cu_2O growth.

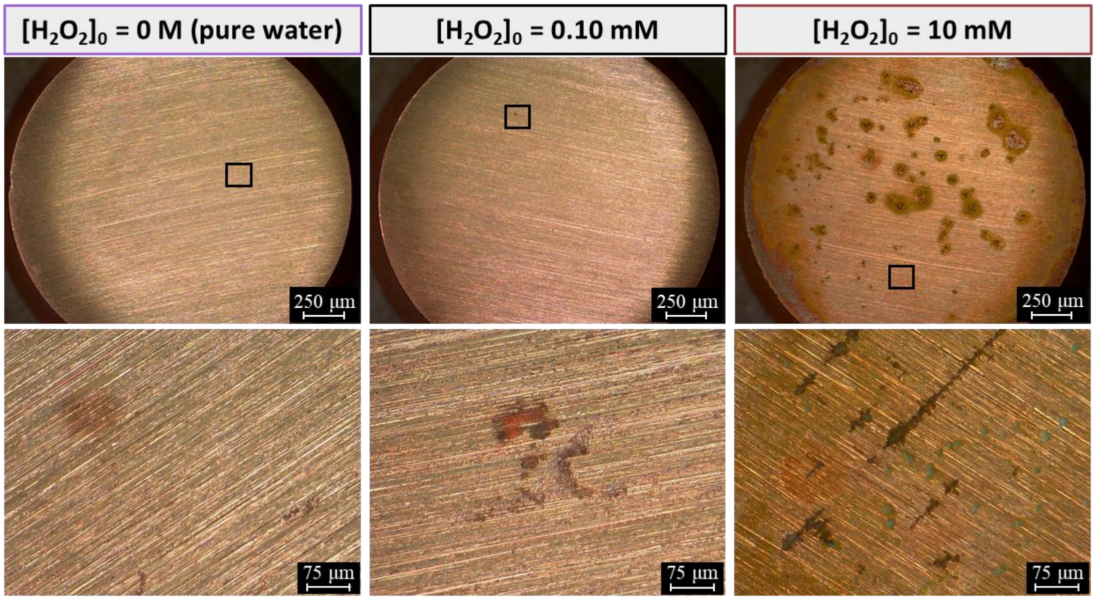

Figure 5.5 Optical images of copper surfaces after exposure to a Cu^{2+}-saturated solution and various $[H_2O_2]_0$ (pH_0 = 6.5) for 48 h corrosion time. The black boxes indicate where the respective higher magnification image was taken.

These findings indeed indicate that the amount of Cu_2O growth is dependent on the $[H_2O_2]_0$ in solutions with the same $[Cu^{II}_{(sol'n)}]_t$ and pH_t, consistent with the corrosion tests that all contained slightly different $[Cu^{II}_{(sol'n)}]_t$ and pH_t. Thus, the main effect of the presence of H_2O_2 during radiolytic copper corrosion is not the oxidation of $Cu^0_{(m)}$ during early corrosion stages (shown in **Section 5.3.1**), but the reduction of $Cu^{2+}_{(sol'n)}$ after their accumulation to cause the precipitation of Cu_2O during later corrosion stages.

5.3.3 Effects of NO_3^- on Copper Dissolution Kinetics and Cu_2O Precipitation

Nitric acid (HNO_3) is formed via humid air radiolytic decomposition and quickly coalesces onto surfaces or dissolves into available solution. Because the dissolution occurs at the air-solution interface, it takes longer for HNO_3 to reach homogeneous distribution and its steady-state concentration than it does for water decomposition products (**Figure 5.1**).[1] The production of HNO_3 can affect the copper corrosion dynamics by decreasing the solution pH and by the formation of nitrate (NO_3^-), which is a redox active species and can complex with copper cations.[1] In this section, the effects of the presence of NO_3^- (near-neutral pH_0) and of HNO_3 in H_2O_2 solutions are investigated. Both solutions contained $[H_2O_2]_0$ = 0.1 mM and

$[NO_3^-]_0$ = 2 mM, and the time-dependent behaviours of $[Cu^{II}_{(sol'n)}]$, pH, and H_2O_2 consumption are shown in **Figure 5.6**.

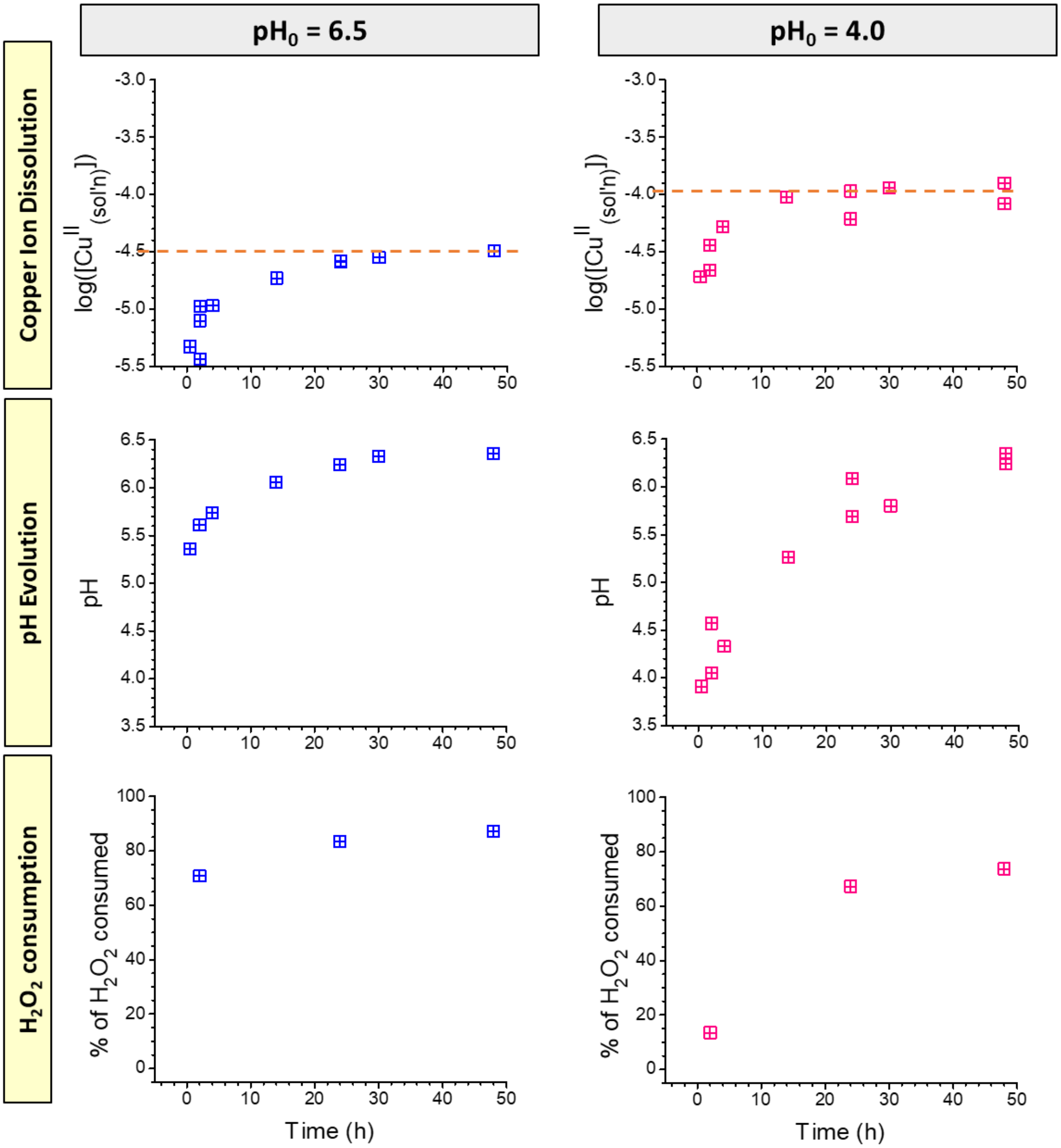

Figure 5.6 Time-dependent behaviours of $[Cu^{II}_{(sol'n)}]$ (top row), pH (middle row), and H_2O_2 consumption (bottom row) in the presence of $[H_2O_2]_0$ = 0.1 mM + $[NO_3^-]_0$ = 2 mM with pH_0 = 6.5 (blue, left) and pH_0 = 4.0 (pink, right). The orange dotted line indicates $[Cu^{II}_{(sol'n)}]_{max}$.

In near neutral pH_0 solutions, Stage 1a includes the production of $Cu(OH)_3^-$ and H^+ in one elementary step (**Eqs. 5.3** and **5.4**). The nitrate containing solution with $pH_0 = 6.5$ (blue in in **Figure 5.6**) showed the decrease in pH_t to 5.5 ± 0.1, associated with Stage 1a. This elementary step is not dependent on the oxidant type, as shown in the previous section. Thus, although nitrate has been reported to contribute to the oxidation of copper,[13,34,35] the mechanism of corrosion is unaffected by the additional oxidizing power. The $[Cu^{II}_{(sol'n)}]$ yield at the end of Stage 1a was 8 μM (blue in **Figure 5.6**), which is comparable to solutions without NO_3^- (10 μM, black in **Figure 5.4**).

In Stage 1b, pH_t increased with the shift in cupric ion hydrolysis from $Cu(OH)_3^-$ to $Cu(OH)^+$ and $Cu(OH)_{2(solv)}$ (**Eq. 5.6**) as $[Cu^{II}_{(sol'n)}]_t$ continued to increase (blue in **Figure 5.6**). When t > 14 h, $[Cu^{II}_{(sol'n)}]_t$ and pH_t plateaued with time as $Cu(OH)_2$ precipitated as a hydrogel, as discussed in **Section 5.3.1**. The plateau in pH_t corresponded to the pKa of bicarbonate (6.3 ± 0.1, **Eq. 5.5**). $[Cu^{II}_{(sol'n)}]_t$ plateaued at 28 ± 3 μM, a similar value to without nitrate 24 ± 3 μM.

Thus, the corrosion mechanism, the dissolution behaviour, and $[Cu^{II}_{(sol'n)}]$ yields in Stages 1 and 2 were unaffected by the presence of nitrate in solutions of $[H_2O_2]_0 = 0.1$ mM with near-neutral pH_0. This is consistent with the finding in **Section 5.3.1** that the oxidant type or concentration does not affect the overall $Cu^{II}_{(sol'n)}$ dissolution behaviour.

Oxide growth on the surface in the nitrate solutions are shown in **Figure 5.7**. Less oxide growth was observed when NO_3^- was present (left in **Figure 5.7**) than in its absence (black in **Figure 5.4**) with the same $[H_2O_2]_0$ of 0.10 mM. Since NO_3^- can couple with the reduction of $Cu(OH)_2$ to Cu_2O, this was a surprising result. This observation indicates that reduction of $Cu(OH)_2$ to Cu_2O was hindered when NO_3^- was present in solution. Although the surface that was exposed to NO_3^- appeared relatively clean, some localized areas of oxides are seen on the surface, such as that presented in the left images in **Figure 5.7**. This area showed localized growth of a small, compact ring of red oxides (Cu_2O).

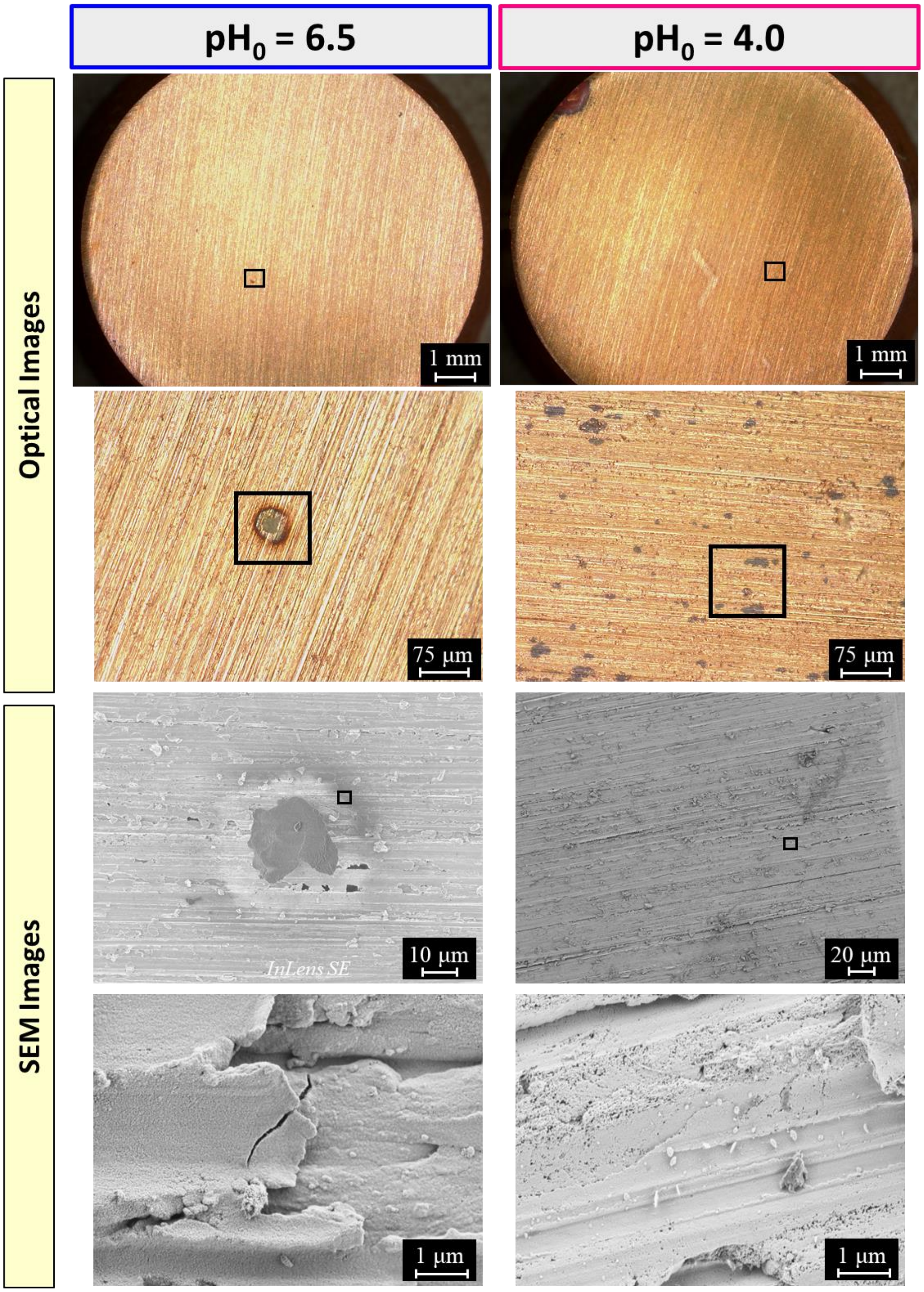

Figure 5.7 Optical (top two rows) and SEM (bottom two rows) images of copper surfaces after exposure to $[H_2O_2]_0$ = 0.1 mM + $[NO_3^-]_0$ = 2 mM with pH_0 = 6.5 (left) and pH_0 4.0 (right) for 48 h. The black boxes indicate where the subsequent image was taken (from top row to bottom row).

With $pH_0 = 4.0$, the pH is no longer close to the equivalence point of water and the production of OH^- via charge transfer at $z = 0$ increases the pH_t throughout all of Stage 1 ($t \leq 14$ h). Accordingly, the pH_t of the first measurement was higher than pH_0. As discussed in depth in **Chapter 4**, the initial charge transfer reaction should result in the $[Cu^{II}_{(sol'n)}]$ production rate twice the $[H^+]$ consumption rate. However, the observed $[Cu^{II}_{(sol'n)}]$ production rate was equal to the $[H^+]$ consumption in Stage 1 (**Figure 5.6**) due to the production of $Cu(OH)^+$ as the main form of dissolved copper.

$$Cu^0_{(m)} + H_2O_2 \rightarrow Cu(OH)^+ + OH^- \qquad \text{in Stage 1} \qquad (5.8)$$

The measured $[H^+]_t$ during Stage 1 was not significantly affected by the bicarbonate buffering system (**Eq. 5.5**) because pH_t remains far from the pKa. During Stage 1, $Cu(OH)^+$ and OH^- formed at $z = 0$, diffused into the bulk solution and consequently $[Cu^{II}_{(sol'n)}]_t$ and pH_t increased.

With the production of OH^- in the interfacial region (via **Eq. 5.8**), the pH at $z = 0$ is much higher than in the bulk solution. The concentrations of $Cu(OH)^+$ and OH^- at $z = 0$ increase, shifting the cupric ion hydrolysis equilibrium more to the right and forming $Cu(OH)_{2(solv)}$.

$$Cu(OH)^+ + OH^- \rightarrow Cu(OH)_{2(solv)} \rightarrow Cu(OH)_{2(colloid)} \qquad (5.9)$$

This shift in hydrolysis equilibrium at $z = 0$ causes the rate of increase in pH_t to slow, observed when $t \geq 14$ h (pink in **Figure 5.6**). However, in the bulk solution, where the pH is higher, the main form of cupric ions continues to be $Cu(OH)^+$ and thus, the increase in pH_t does not cease, as shown in **Figure 5.6**.

With increasing time and concentration of cupric ion species, $Cu(OH)_2$ precipitates as colloids in the interfacial solution. The volume of solution in which colloids are forming is smaller than when they form in the bulk solution (i.e., in pH_0 near neutral solutions), and therefore, the rate of colloid agglomeration into a hydrogel is faster in these solutions. The hydrogel that grows in the interfacial solution also has a higher colloidal density than hydrogels that form in the bulk solution.

The diffusion of $Cu^{2+}_{(sol'n)}$ from $z = 0$ to $z = \delta_{diff}$ is hindered by the thick hydrogel layer that covers the surface at $t \geq 14$ h. However, as described in **Chapter 4**, the transport of OH^- is not affected by the hydrogel layer, and thus, its concentration continues to increase until the solubility equilibrium is achieved. The hydrogel was observed as blue patches in the optical images (right in **Figure 5.7**) that were invisible in SEM because they are very thin and conform to the metal grinding lines. Stage 2 was observed for $t \geq 14$ h, when $[Cu^{II}_{(sol'n)}]$ plateaued at 94 ± 13 μM. This plateau in copper concentration was higher than that in near neutral pH_0 (28 ± 3 μM, blue in **Figure 5.6**) and in solutions with 100 times larger $[H_2O_2]_0$ (49 ± 7 μM, brown in **Figure 5.3**).

In $pH_0 = 4.0$ solutions, the H_2O_2 consumption was initially faster but the final percent of H_2O_2 consumed was lower than in $pH_0 = 6.5$ solutions. This is the opposite for what would be expected if the H_2O_2 consumption corresponds exactly to $[Cu^{II}_{(sol'n)}]$ dissolution. In both nitrate solutions, the amount of H_2O_2 consumption is higher than $Cu^{II}_{(sol'n)}$ production (opposed to 1:1 ratio required if all the H_2O_2 was consumed to produce $Cu^{II}_{(sol'n)}$, **Eq. 5.4**), indicating another H_2O_2 removal path (e.g., $Cu(OH)_2$ reduction to Cu_2O). Moreover, the extent of H_2O_2 consumption is higher than in the absence of nitrate than without nitrate. It is possible that H_2O_2 is oxidized by NO_3^- in the bulk solution via **Eq. 5.9**, which is faster at a higher pH because OH^- is a reactant.

$$NO_3^- + H_2O_2 \rightarrow NO_2^- + H_2O \qquad (5.9)$$

The consumption of NO_3^- and H_2O_2 via **Eq. 5.9** is in a 1:1 molar ratio, and so the maximum amount of NO_3^- that could be consumed is 0.08 mM, with 80 % consumption of H_2O_2 (**Figure 5.6**), leaving 1.92 mM of NO_3^- in solution. Thus, even if all H_2O_2 consumption occurred via **Eq. 5.9**, the effects of NO_3^- on $Cu^{II}_{(sol'n)}$ dissolution can still be investigated in this section.

Regardless of pH_0, a comparison of the optical images with (**Figure 5.7**) and without nitrate (**Figure 5.4**) indicate that the presence of nitrate hindered the rate of precipitation of Cu_2O. That is, less oxide growth was observed when the solution contained nitrate. This is attributed, not to the presence of NO_3^-, but the removal of H_2O_2 via **Eq. 5.9**. The consequence of this H_2O_2 removal is that less H_2O_2 is available to reduce $Cu(OH)_2$. However, in the presence of a continuous flux of γ-radiation, H_2O_2 is produced at a constant concentration allowing it to be available at later corrosion stages when $Cu^{2+}_{(sol'n)}$ accumulates to a concentration that can couple with H_2O_2 oxidation. The results in this section show that the presence of NO_3^- has no effect on the copper dissolution rate or yield. However, the production of HNO_3 via radiolytic humid air decomposition lowers the pH, which was observed to have a large effect on the overall copper corrosion.

5.3.4 Effects of Acidic Initial pH on Copper Dissolution Kinetics and Cu_2O Precipitation

The time-dependent behaviour during copper corrosion in solutions of $[H_2O_2]_0 = 10$ mM with an unadjusted pH_0 of 4.0 is shown in **Figure 5.8**. This experiment was originally performed to compare with solutions with varying $[H_2O_2]_0$ (i.e., in **Section 5.3.1**), but it was found that it was more comparable to other solutions with $pH_0 = 4.0$ (pink in **Section 5.3.3**), regardless of the oxidant concentration. Thus, this section investigates the effects of the lowered pH_0 on $Cu^{II}_{(sol'n)}$ dissolution.

In solutions of $[H_2O_2]_0 = 10$ mM and $pH_0 = 4.0$ (**Figure 5.8**), the first measured pH_t was higher than pH_0, indicating the first elementary step was **Eq. 5.8**, not **Eq. 5.4**. Stage 1 was observed when $t < 14$ h, during which the increases in $[Cu^{II}_{(sol'n)}]_t$ and pH_t are approximately equal and the main form of dissolved copper is $Cu(OH)^+$. The accumulation of cupric and hydroxide ions in the interfacial region, causes the shift in hydrolysis equilibrium and precipitation of $Cu(OH)_2$ colloid particles (**Eq. 5.9**). Stage 2 begins when the $Cu(OH)_2$ hydrogel forms in the interfacial solution, during which $[Cu^{II}_{(sol'n)}]_t$ is constant with time, observed when $t \geq 14$ h (**Figure 5.8**). The $[Cu^{II}_{(sol'n)}]_t$ plateau was at 120 ± 20 μM, which was a more comparable value to the solutions containing 0.1 mM H_2O_2 and 2 mM NO_3^- with $pH_0 = 4.0$ (94 ± 13 μM, pink in **Figure 5.6**) than the value with the same concentration of $[H_2O_2]_0$ (10 mM) and higher pH_0 (49 ± 7 μM, brown in **Figure 5.3**). This clearly demonstrates that the pH_0, not $[H_2O_2]_0$, has a large impact on the copper concentration yield.

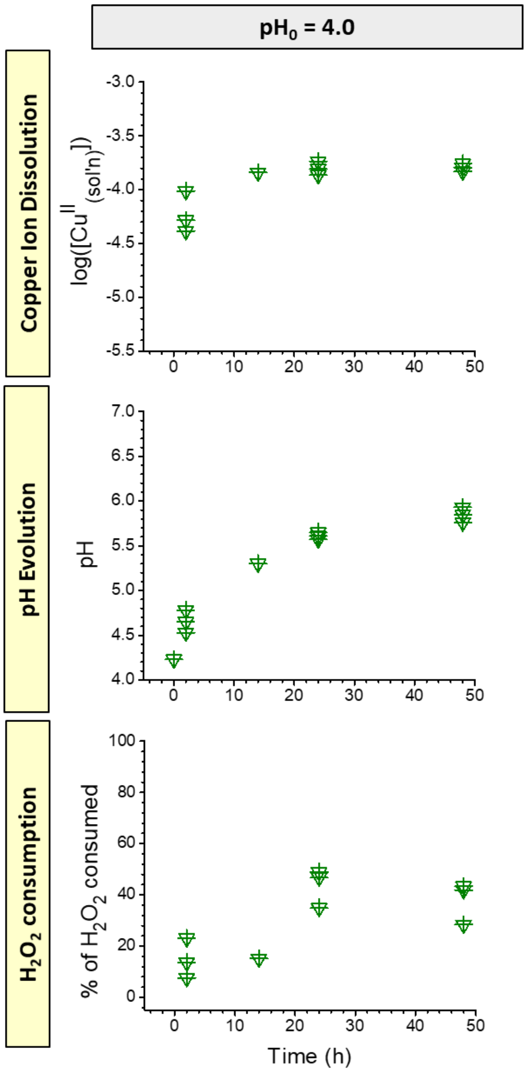

Figure 5.8 Time-dependent behaviours of [$Cu^{II}_{(sol'n)}$] (top row), pH (middle row), and H_2O_2 consumption (bottom row) in [H_2O_2]$_0$ = 10 mM solutions with pH$_0$ = 4.0.

The optical images of the surface during corrosion in pH$_0$ = 4.0 is shown in **Figure 5.9**. The general surface remains relatively clean, with oxide growth appearing on the edges of the coupon. The surface after exposure to pH$_0$ = 4.0 solutions (**Figure 5.9**) show less oxide growth than after exposure to pH$_0$ = 6.5 solutions (**Figure 5.4**). This is consistent with oxidation of H_2O_2 producing Cu_2O, as it is a pH dependent reaction and is faster in high pH (high [OH^-]) solutions. Furthermore, the H_2O_2 consumption in solutions with pH$_0$ = 4.0 (bottom row in **Figure 5.8**) increases slower and the total amount of H_2O_2 consumed is lower relative to that in pH$_0$ = 6.5. These observations of H_2O_2 consumption are consistent with a lower amount of $Cu(OH)_2$ reduction to produce Cu_2O (**Eq. 5.7**).

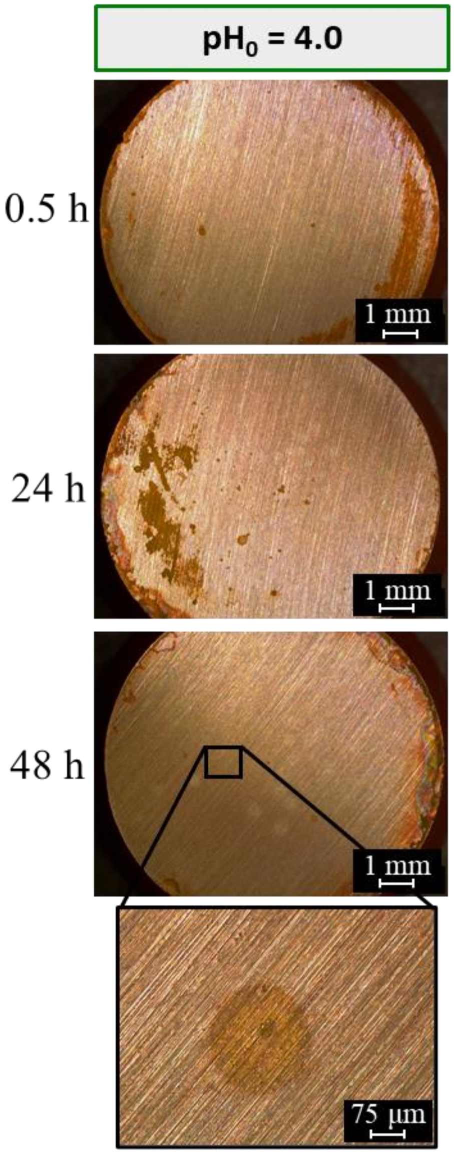

Figure 5.9 Optical images of the copper surfaces after exposure to $[H_2O_2]_0$ = 10 mM with pH_0 = 4.0 at 0.5, 24, and 48 h of corrosion.

The results presented in this section showed that the decrease in pH_0, not $[H_2O_2]_0$ determines the time-dependent $[Cu^{II}_{(sol'n)}]$ behaviour, and thus the overall corrosion behaviour. It was also shown that the lower pH during precipitation will slow the H_2O_2 reduction reaction and hinder the growth of Cu_2O. These results decouple the effects of radiolytically produced acidic products and H_2O_2 and will help in the analysis of corrosion in the presence of radiation.

5.4 CONCLUSIONS

The effects of the presence of continuous radiation are more complicated than can be studied with the one-time addition of molecular radiolysis products. However, this study served to decouple the effects of the main radiolysis oxidants, H_2O_2 and NO_3^-, and the decrease in pH due to radiation on the cupric ion dissolution behaviour at initial corrosion times.

This chapter has shown that for a given pH_0, the oxidant type and concentration do not affect copper dissolution behaviour during corrosion. The oxidants investigated were O_2, H_2O_2, and NO_3^- – all molecular oxidants are produced via water and humid air radiolysis. The precipitation of Cu_2O is dependent on $[H_2O_2]_0$, where a higher initial concentration of H_2O_2 leads to more Cu_2O growth due more redox coupling between the species. Less Cu_2O growth was observed in the nitrate-containing solutions, due to H_2O_2 consumption by nitrate, leaving less in solution to reduce cupric ions. As H_2O_2 reduction is faster at higher pH values, more Cu_2O growth was observed in the higher pH solutions, confirming that the Cu_2O growth occurs via $Cu(OH)_2$ reduction. Finally, it was shown that the pH_0 had a much greater effect on the initial copper dissolution than the oxidizing power of the solution. The results in this chapter will contribute to the understanding of the effect of radiolysis products on the copper dissolution behaviour when determining the corrosion mechanism.

5.5 REFERENCES

1 Morco, R. P., Joseph, J. M., Hall, D. S., Medri, C., Shoesmith, D. W., Wren, J. C. Modelling of Radiolytic Production of HNO_3 Relevant to Corrosion of a Used Fuel Container in Deep Geologic Repository Environments. *Corros. Eng. Sci. Technol.* **52**, 141-147, (2017).

2 Bobrowski, K. *Radiation Chemistry of Liquid Systems* in *Applications of Ionizing Radiation in Materials Processing* Vol. 1 (eds Yongxia Sun & Andrzej G. Chmielewski) Ch. 4, 81 - 116 (Institute of Nuclear Chemistry and Technology, 2017).

3 Joseph, J. M., Choi, B. S., Yakabuskie, P., Wren, J. C. A Combined Experimental and Model Analysis on the Effect of pH and $O_{2(aq)}$ on Gamma-Radiolytically Produced H_2 and H_2O_2. *Radiat. Phys. Chem.* **77**, 1009-1020, (2008).

4 Yakabuskie, P., Joseph, J., Wren, J. The Effect of Interfacial Mass Transfer on Steady-State Water Radiolysis. *Radiat. Phys. Chem.* **79**, 777-785, (2010).

5 Spinks, J. W. T., Woods, R. J. *An Introduction to Radiation Chemistry*. 2nd edn, (Wiley, 1976).

6 Daub, K., Zhang, X., Noël, J. J., Wren, J. C. Effects of γ-Radiation Versus H_2O_2 on Carbon Steel Corrosion. *Electrochim. Acta* **55**, 2767-2776, (2010).

7 Björkbacka, Å., Yang, M., Gasparrini, C., Leygraf, C., Jonsson, M. Kinetics and Mechanisms of Reactions Between H_2O_2 and Copper and Copper Oxides. *Dalton Trans.* **44**, 16045-16051, (2015).

8 Björkbacka, Å., Hosseinpour, S., Johnson, M., Leygraf, C., Jonsson, M. Radiation Induced Corrosion of Copper for Spent Nuclear Fuel Storage. *Radiat. Phys. Chem.* **92**, 80-86, (2013).

9 Soroka, I., Chae, N., Jonsson, M. On the Mechanism of γ-Radiation-Induced Corrosion of Copper in Water. *Corros. Sci.* **182**, 109279, (2021).

10 Knapp, Q. W., Wren, J. C. Film Formation on Type-316L Stainless Steel as a Function of Potential: Probing the Role of Gamma-Radiation. *Electrochim. Acta* **80**, 90-99, (2012).

11 Behazin, M., Noël, J. J., Wren, J. C. Combined Effects of pH and γ-Irradiation on the Corrosion of Co-Cr Alloy Stellite-6. *Electrochim. Acta* **134**, 399-410, (2014).

12 Bessho, K., Oki, Y., Akimune, N., Matsumura, H., Masumoto, K., Sekimoto, S., Osada, N., Kinoshita, N., Monjushiro, H., Shibata, S. Corrosion of Copper in Water and Colloid Formation Under Intense Radiation Field. *J. Radioanal. Nucl. Chem.* **303**, 1117-1121, (2015).

13 Turnbull, J., Szukalo, R., Behazin, M., Hall, D., Zagidulin, D., Ramamurthy, S., Wren, J. C., Shoesmith, D. W. The Effects of Cathodic Reagent Concentration and Small Solution Volumes on the Corrosion of Copper in Dilute Nitric Acid Solutions. *Corrosion* **74**, 326-336, (2017).

14 Naghizadeh, M. "Copper Corrosion Dynamics under Deep Geologic Repository Conditions" Doctor of Philosophy, The University of Western Ontario, Electronic Thesis and Dissertation Repository. (2021). 7894.

15 Magaino, S. Corrosion Rate of Copper Rotating-Disk-Electrode in Simulated Acid Rain. *Electrochim. Acta* **42**, 377-382, (1997).

16 Broo, A. E., Berghult, B., Hedberg, T. Copper Corrosion in Drinking Water Distribution Systems — The Influence of Water Quality. *Corros. Sci.* **39**, 1119-1132, (1997).

17 Lee, H.-J., Lee, H., Lee, C. Degradation of Diclofenac and Carbamazepine by the Copper(II)-Catalyzed Dark and Photo-Assisted Fenton-Like Systems. *Chem. Eng. J.* **245**, 258-264, (2014).

18 Moffett, J. W., Zika, R. G. Reaction Kinetics of Hydrogen Peroxide with Copper and Iron in Seawater. *Environ. Sci. Technol.* **21**, 804-810, (1987).

19 Xing, G. "Reactions of Cu(I) and Cu(II) with H_2O_2 in Natural Waters: Kinetics, Mechanism and the Generation of Reactive Oxidizing Intermediates" Masters by Research of Environmental Engineering, The University of New South Wales Australia. (2012).

20 Ghormley, J. A., Stewart, A. C. Effects of γ-Radiation on Ice. *J. Am. Chem. Soc.* **78**, 2934-2939, (1956).

21 Pham, A. N., Xing, G., Miller, C. J., Waite, T. D. Fenton-Like Copper Redox Chemistry Revisited: Hydrogen Peroxide and Superoxide Mediation of Copper-Catalyzed Oxidant Production. *J. Catal.* **301**, 54-64, (2013).

22 Sharma, V. K., Millero, F. J. The Oxidation of Cu(I) with H_2O_2 in Natural Waters. *Geochim. Cosmochim. Acta* **53**, 2269-2276, (1989).

23 Gustafson, R., Martell, A. Formation of Polynuclear Complexes in Aqueous Solution. *Ann. N.Y. Acad. Sci.* **88**, 322-331, (2006).

24 Powell, K. J., Brown, P. L., Byrne, R. H., Gajda, T., Hefter, G., Sjöberg, S., Wanner, H. Chemical Speciation of Environmentally Significant Metals with Inorganic Ligands. Part 2: The Cu^{2+}-OH^-, Cl^-, CO_3^{2-}, SO_4^{2-}, and PO_4^{3-} Systems. *Pure Appl. Chem.* **79**, 895-950, (2007).

25 Tegenaw, A., Sorial, G. A., Sahle-Demessie, E., Han, C. Influence of Water Chemistry on Colloid-Size Cu-Based Pesticides Particles: A Case of $Cu(OH)_2$ Commercial Fungicide/Bactericide. *Chemosphere* **239**, 124699, (2020).

26 King, F., Lilja, C., Vähänen, M. Progress in the Understanding of the Long-Term Corrosion Behaviour of Copper Canisters. *J. Nucl. Mater.* **438**, 228-237, (2013).

27 King, F., Lilja, C., Pedersen, K., Pitkänen, P., Vähänen, M. *An Update of the State-of-the-Art Report on the Corrosion of Copper Under Expected Conditions in a Deep Geologic Repository* (SKB, 2010).

28 Power, G. P., Ritchie, I. M. Mixed Potential Measurements in the Elucidation of Corrosion Mechanisms— 1. Introductory Theory. *Electrochim. Acta* **26**, 1073-1078, (1981).

29 Ekeroth, E., Roth, O., Jonsson, M. The Relative Impact of Radiolysis Products in Radiation Induced Oxidative Dissolution of UO_2. *J. Nucl. Mater.* **355**, 38-46, (2006).

30 Björkbacka, Å., Johnson, C. M., Leygraf, C., Jonsson, M. Radiation Induced Corrosion of Copper in Humid Air and Argon Atmospheres. *J. Electrochem. Soc.* **164**, C201-C206, (2017).

31 Baes, C. F., Mesmer, R. E. *The Hydrolysis of Cations*. (Wiley, 1976).

32 Salem, I. A., El-Maazawi, M., Zaki, A. B. Kinetics and Mechanisms of Decomposition Reaction of Hydrogen Peroxide in Presence of Metal Complexes. *Int. J. Chem. Kinet.* **32**, 643-666, (2000).

33 Perez-Benito, J. F. Reaction Pathways in the Decomposition of Hydrogen Peroxide Catalyzed by Copper(II). *J. Inorg. Biochem.* **98**, 430-438, (2004).

34 Dima, G. E., de Vooys, A. C. A., Koper, M. T. M. Electrocatalytic Reduction of Nitrate at Low Concentration on Coinage and Transition-Metal Electrodes in Acid Solutions. *J. Electroanal. Chem.* **554-555**, 15-23, (2003).

35 Pérez-Gallent, E., Figueiredo, M. C., Katsounaros, I., Koper, M. T. M. Electrocatalytic Reduction of Nitrate on Copper Single Crystals in Acidic and Alkaline Solutions. *Electrochim. Acta* **227**, 77-84, (2017).

CHAPTER 6. EFFECTS OF RADIATION ON THE COPPER CORROSION PROGRESSION

6.1 INTRODUCTION

Corrosion (the loss of metal from the solid metal phase) is an interfacial charge and mass transfer process. It occurs through the oxidation of solid metal (e.g., $Cu^0_{(m)}$) to the soluble metal cation (e.g., Cu^{2+}), coupled with the reduction of oxidant (e.g., O_2 to OH^-), at the metal-solution interface ($z = 0$) (**Eq. 6.1**) and the transport of species between the interface ($z = 0$) and the bulk solution ($z = \delta_{diff}$) (**Eq. 6.2**).

Interfacial charge and mass transfer reactions at *z* = 0:

Ox. half-reaction:	$Cu^0_{(m)} \rightleftarrows Cu^{2+} + 2\ e^-$	(6.1a)
Red. half-reaction:	$O_2 + 2\ H_2O + 4\ e^- \rightleftarrows 4\ OH^-$	(6.1b)
Overall reaction:	$2\ Cu^0_{(m)} + O_2 + 2\ H_2O \rightleftarrows 2\ Cu^{2+} + 4\ OH^-$	(6.1c)

The subscript (m) represents the metal phase and the species without phase designations are all solvated species.

Transport of reactants and products through the diffusion layer (0 < *z* < δ_{diff}):

$$Cu^{2+}|_{z=0} \rightsquigarrow Cu^{2+}|_{z=\delta_{diff}} \quad (6.2a)$$

$$O_2|_{z=\delta_{diff}} \rightsquigarrow O_2|_{z=0} \quad (6.2b)$$

$$OH^-|_{z=0} \rightsquigarrow OH^-|_{z=\delta_{diff}} \quad (6.2c)$$

where δ_{diff} is the diffusion length. The solution from $z = 0$ to $z = \delta_{diff}$ will be referred to as the interfacial solution. The bulk solution phase begins where the redox species (O_2, OH^- and Cu^{2+}) can be treated as homogeneously distributed, i.e., the bulk solution begins at $z = \delta_{diff}$.

Because the overall process of corrosion involves interfacial electron and mass transfer reactions and mass transport through the solution phase, the rate of corrosion depends strongly on the redox and transport conditions of the solution in contact with the metal.

Previous studies on corrosion dynamics without radiation present,[1-6] including the studies presented in **Chapters 4** and **5**, have shown that under certain redox and transport conditions the dissolved metal cation can accumulate quickly and reach its saturation or supersaturation level and subsequently precipitate as colloid particles. As the colloid concentration increases, they can aggregate and grow a hydrogel network. If the hydrogel layer growth is in the interfacial region, it can significantly alter the metal cation transport (**Eq. 6.2a**) rate which, in turn, affects the interfacial charge transfer (**Eq. 6.1**) rate and, hence, the overall rate of metal loss.

The metal cation in the interfacial solution, either in the dissolved or colloidal state, can oxidize or reduce to less soluble species (e.g., oxidation of soluble ferrous to nearly insoluble ferric species during carbon steel corrosion,[3] reduction of soluble cupric to insoluble cuprous species during copper corrosion[4,5]). The production of less soluble species accelerates the growth of the hydrogel network, i.e., it accelerates the increase in colloid particle concentration and cuprous content (ferric content during carbon steel corrosion) in the hydrogel layer. With time, the mixed metal hydroxides in the hydrogel layer can convert to thermodynamically more stable metal oxide crystals.

Thus, if dissolved metal cations (the initial metal oxidation product) can accumulate and grow as metal hydroxide hydrogel in the interfacial region, the overall corrosion dynamics (the time-dependence of metal loss) can change as corrosion progresses. The previous studies referred to above found that, due to cyclic feedback between the initial oxidation of metal to soluble metal cation and later chemical and electrochemical reactions of the initial and intermediate metal oxidation products, corrosion of transition metal progresses through distinct periods having characteristic (quasi-) steady-state rates. These quasi-steady states are referred to as dynamic stages, with the transition between one dynamic stage to another occurring over a much shorter duration than the durations of the individual dynamic stages themselves. These studies found that the duration of each stage and the overall corrosion rate within it depend strongly on the solution redox and transport parameters.

As described earlier, water and humid air exposed to γ-radiation decompose into redox-active (mainly H_2O_2) and acidic species (mainly HNO_3) that can affect the rates of individual elementary steps, including those that determine the overall rate of corrosion in each stage (the rate determining step). Their continual production means they can affect all dynamic stages – even those at that occur after long times – and may affect the rates of each stage differently. The effects of H_2O_2, NO_3^-, and H^+ on the initial corrosion dynamics were decoupled in **Chapter 5**. Comparison of the time-dependent behaviours of corrosion products in the presence and absence of radiation will provide insight into the underlying processes that are affected by the presence of γ-radiation and how the overall corrosion rates in all dynamic stages are affected.

This chapter presents a study on the effects of γ-radiation on the corrosion dynamics of copper under stagnant water droplets. Corrosion experiments were performed using droplets of pure water with an unadjusted initial pH (7.0), previously purged with CO_2-free air to prevent bicarbonate/carbonate pH buffering and complexation with the metal cation from affecting the corrosion behaviour. (The study on the effects of CO_2 on copper corrosion is presented in **Chapter 7**). The experiments were conducted in the absence and presence of a continuous flux of γ-radiation at a dose rate of 2.0 kGy/h. The corrosion dynamics were followed by analysing both dissolved and solid corrosion products as a function of corrosion duration. The post-test analyses include surface morphology and chemical/elemental composition of oxide deposits using optical microscopy, SEM, EDX, and Raman spectroscopy, and measurement of the dissolved (and dispersed) metal concentration using ICP-OES, and the pH change using a micro-pH meter.

6.2 EXPERIMENTAL

6.2.1 Materials and Solutions

All experiments were performed with high purity copper (99.9% purity) coupons made from wrought copper samples (provided by SKB, the Swedish Nuclear Waste Management Company) with an exposed surface area of 0.785 cm^2. The top surface of the copper coupons was ground using silicon carbide papers (Buehler, Inc., Wooster, OH) with grit size 400, 800, and 1200 in succession. Diamond polished coupons (data presented in **Section 6.3.6**) were not ground; after fabrication they were polished using a 1 μm MetaDi diamond suspension

(Buehler, Inc., Wooster, OH). The coupons were then washed with deionized water, dried under flowing $Ar_{(g)}$ and placed in a 20 mL vial sealed with an aluminum crimp cap with a polytetrafluoroethylene (PTFE)-coated silicone septum (Thermo Fisher Scientific, Waltham, MA). More information on this procedure is outlined in **Section 3.1**. All solutions used in this study were prepared using water purified with a NANOpure Diamond UV ultra-pure water system (Barnstead International, Dubuque, IA) to give a resistivity of 18.2 MΩ·cm.

The coupon vial and solutions were purged with zero air (i.e., air with 0 ppm CO_2) (Praxair, Danbury, CT) via the procedure in **Section 3.1.2**. 100 µL of the sample solution was placed on the copper surface by injection into the sealed vial through the silicon septum using a syringe. Radiation experiments were performed using a MDS Nordion (Ottawa, ON) Gamma Cell 220 Excel ^{60}Co irradiator, as described in **Section 3.2**, and non-radiation experiments were done by leaving the vials on the benchtop, in otherwise the same conditions.

6.2.2 Post-Test Analyses

Experiments were terminated by removing the solution from the coupon surface using a Pasteur pipette. The copper coupon was washed and dried using $Ar_{(g)}$. Optical images were taken using a Leica DVM6A digital microscope, then the coupon was stored under vacuum. Scanning electron microscopy (SEM), energy-dispersive X-ray spectroscopy (EDX), and focused ion beam (FIB) milling were performed at the Western Nanofabrication Facility using Zeiss LEO 1530 and 1540XB instruments. Raman spectroscopy was performed at Surface Science Western using a Renishaw (Wotton-under-Edge, UK) Model 2000 Raman spectrometer equipped with a MellesGriot (Carlsbad, CA) 35 mW HeNe laser with a wavelength of 633 nm. More information on the surface analysis can be found in **Section 3.3**.

The pH of the solution was determined using a Thermo Scientific (Waltham, MA) Orion 9110DJWP Double Junction Micro-pH Electrode. The solution was then diluted to quantify the dissolved copper concentration using inductively coupled plasma optical emission spectroscopy (ICP-OES) (PerkinElmer Avio 200 ICP-OES) to determine the dissolved/dispersed copper concentration. More information on the procedure for solution analysis can be found in **Section 3.4**.

6.3 RESULTS AND DISCUSSION

This chapter investigates the effects of a continuous flux of γ-radiation on copper corrosion in small water droplets without CO_2. The corrosion dynamics and mechanism without radiation are first discussed, then γ-radiation is introduced into the system. To determine the kinetics of copper corrosion in the presence of absence of radiation, the evolution of dissolved species concentration, including cupric and hydroxide ions, and solid species quantity and identity are followed as a function of time. Optical microscopy is used in this thesis to investigate the formation of solid products because the colour of the solid corrosion product provides information about the copper oxidation state and anion in the complex. It also is an efficient tool to determine the spatial distribution of the corrosion products across the entire surface. An analysis of the species that create common colours observed during corrosion is provided.

6.3.1 Analysis of Solid Corrosion Product Colour

Copper species have distinct colours depending on its oxidation state and the counter-anion: pure Cu^0 is an orange-red colour, pure Cu_2O is red-pink, pure CuO is black, pure $Cu(OH)_2$ is blue (**Figure 6.1**), and various Cu^{2+}-OH-X complexes (where X represents other anions, such as CO_3^-, NO_3^-) are green to blueish green. The copper species formed during corrosion are unlikely to be in a pure chemical phase and/or are likely to be highly hydrated, which can change the intensity and tint of the species colour. However, the hue (i.e., the observed colour) of each species remains the same and hence, the colour of the corroded surface can be used to characterize the main species present on the surface.

The presence of nanometer thick layers of copper hydroxides and/or oxides on a corroded copper metal surface is difficult to detect by SEM and spectroscopic analyses such as EDX and Raman. However, due to their high light reflectance, the growth of even very thin layers of copper hydroxides and/or oxides causes a colour change.[7] Thus, in this study, the colour of the copper surface observed via optical microscopy was used to characterize the hydroxides and/or oxides that grow or dissolve with time, and their spatial distribution across the surface. An additional advantage of optical microscopy over SEM is that it can easily and quickly image large sections of the surface to allow for the determination of general corrosion trends across the surface. This section provides characterization of copper hydroxide and oxide species grown during corrosion using optical images, corroborated using SEM, EDX, and Raman spectroscopic analyses.

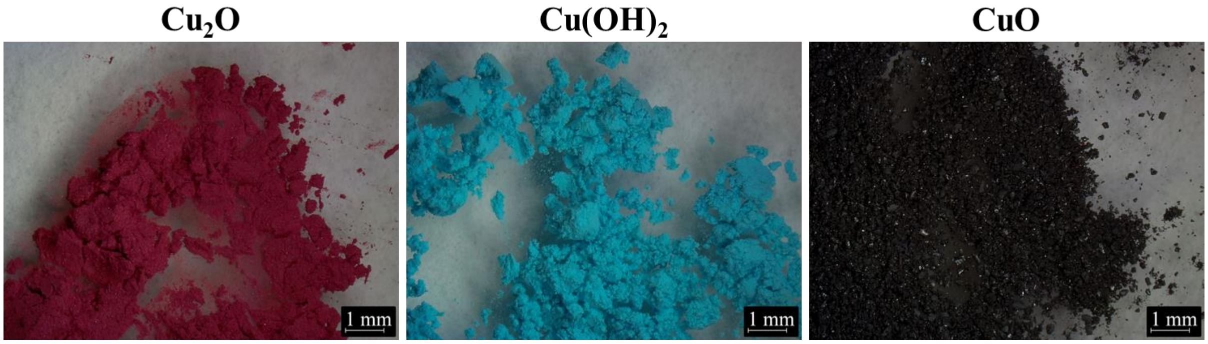

Figure 6.1 Optical images of Cu_2O, $Cu(OH)_2$ and CuO powders.

The main colours seen throughout radiolytic corrosion are purple and pink. The SEM images of the surfaces of both colours show extensive coverage by large (micron sized) oxide crystals, as shown in **Figure 6.2**. The optical and SEM images of uncorroded copper surface are also presented in **Figure 6.2** to illustrate the colour and morphological differences of the surface after corrosion. The EDX analysis gave a Cu:O atomic ratio of 2.1 for the pink-coloured surface and 0.9 for the purple-coloured surface. The atomic ratios obtained using EDX analysis include all species on the surface up to a depth of 1 – 2 μm, which may include all solid corrosion products as well as contribution from the underlying $Cu^0_{(m)}$. With a pure Cu_2O sample, the Cu:O atomic ratio would be 2.0, and thus, EDX analysis indicates the pink-coloured surface is mostly Cu_2O. A mixture of equal parts Cu_2O and $Cu(OH)_2$ would give a Cu:O ratio of 1.0, and thus the EDX analysis suggests the purple-coloured surface is a combination of these species.

$Cu(OH)_2$ and Cu_2O have similar Raman shifts, and thus, the relative intensities of the characteristic peaks can be used to determine the contribution of the species. Pure Cu_2O has a sharp peak at 218 cm^{-1} and peaks at 523 cm^{-1} and 623 cm^{-1}, where the latter is more intense than the former. Pure $Cu(OH)_2$ has a weak (negligible) 218 cm^{-1} peak, and a 523 cm^{-1} peak that is more intense than the 623 cm^{-1} peak (the opposite of the peak intensities in the Cu_2O

Raman spectrum). Pure $Cu^0_{(m)}$ has no Raman peaks because metals do not show the required polarizability change.[8] Thus, a combination of $Cu(OH)_2$ and Cu_2O will have peaks at 218 cm^{-1}, 523 cm^{-1}, and 623 cm^{-1}, but with 523 cm^{-1} and 623 cm^{-1} peaks of similar intensities. The Raman spectra of the pink and purple-coloured surfaces in **Figure 6.2** both contain peaks at 218, 523 and 623 cm^{-1}. The Raman spectrum of the pink-colour surface has an intense 218 cm^{-1} peak and the peak at 623 cm^{-1} is more intense than the one at 523 cm^{-1}, characteristic of Cu_2O. The Raman spectrum of the purple-coloured surface has a small peak at 218 cm^{-1} and peaks of equal intensity at 523 cm^{-1} and 623 cm^{-1}, indicative of a combination of $Cu(OH)_2$ and Cu_2O. The Raman analysis is consistent with the results from the EDX analysis and the colour of the surface.

The EDX and Raman analyses presented in **Figure 6.2** indicate that the pink oxide crystals mostly consist of Cu_2O, consistent with the expectation from the pink colour. On the other hand, the lower Cu:O atomic ratio, equal 523 cm^{-1} and 623 cm^{-1} peak intensities, and weak 218 cm^{-1} peak indicate that the purple colour results from pink Cu_2O crystals covered by a gel-like layer of blue $Cu(OH)_2$. However, despite the two distinct colours, the morphologies observed in the SEM images of the pink and purple surfaces are the same as that of Cu_2O crystals. SEM could not detect any morphological change due to the deposition of $Cu(OH)_2$ hydrogel onto the Cu_2O crystals because the hydrogel layer was thin and conformed to the Cu_2O crystal shape, which is discussed in detail in this chapter.

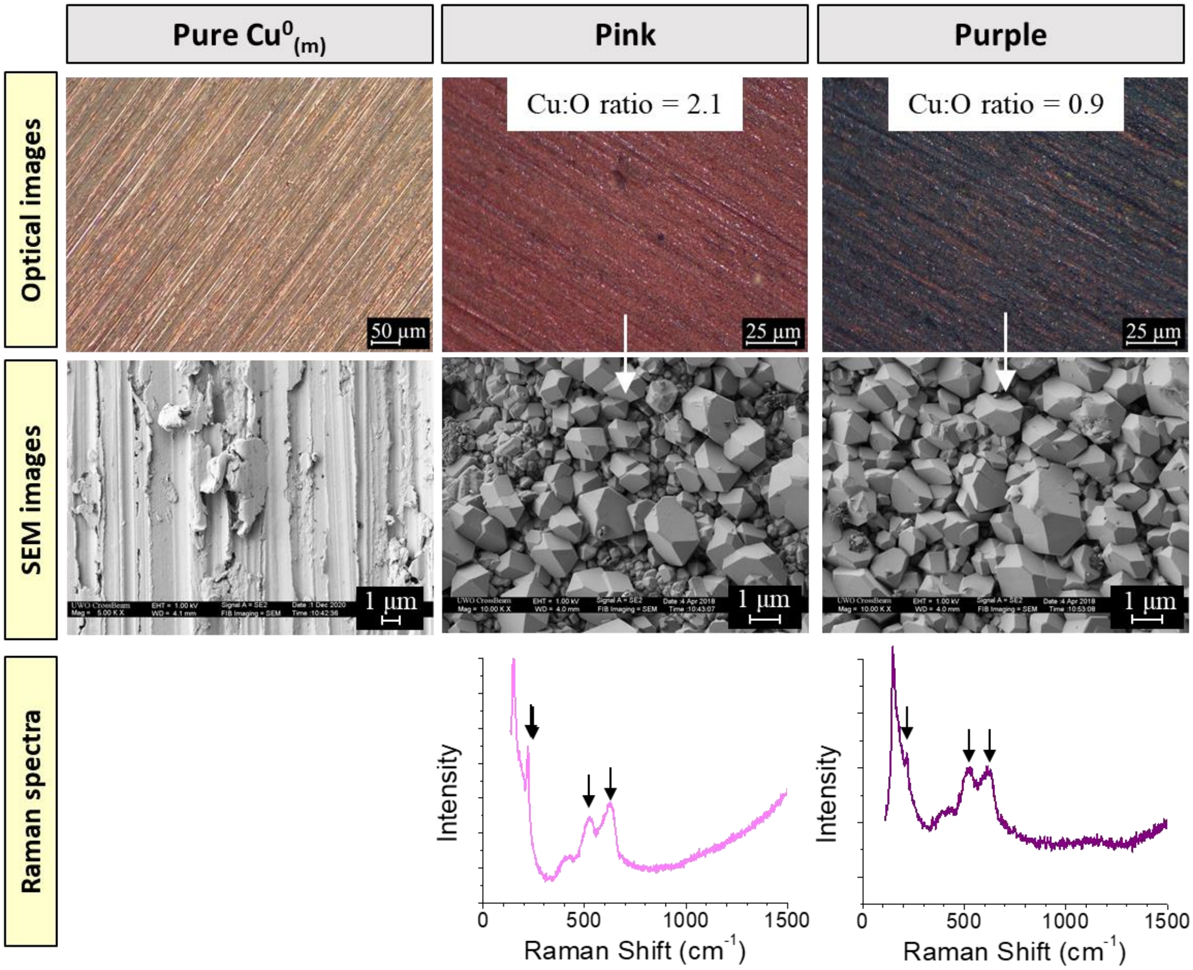

Figure 6.2 Optical images (with Cu:O ratio from EDX analysis) (top row), SEM images (middle row), and Raman spectra (bottom row) of the pure Cu$^0_{(m)}$ surface (before corrosion, left column), and pink- (middle column) and purple-coloured surfaces (right column) observed during copper corrosion.

Other oxide colours observed on the surface during corrosion are blue and yellow, shown in **Figure 6.3**. The yellow colour was seen on top of the metallic surface at early corrosion times (left in **Figure 6.3**) or next to blue and purple oxides at late corrosion times (right in **Figure 6.3**). As Cu_2O crystals decrease in size, their bandgap increases due to quantum confinement shifting their colour from red to yellow and thus, the yellow colour indicates this area is covered in seed Cu_2O crystals. Indeed, small Cu_2O crystals are often reported as yellow.[9-12] The SEM images (left two SEM images in **Figure 6.3**) confirm that the yellow oxides are smaller (hundreds of nm) than the pink/purple crystals and the Raman spectrum of the yellow crystals show the Cu_2O characteristic peaks (intense 218 cm^{-1} peak, and intense 623 cm^{-1} peak compared to the 523 cm^{-1} peak). Thus, the yellow crystals growth during copper corrosion are small, seed Cu_2O crystals.

A bright blue colour is also commonly observed on the copper surface during corrosion (**Figure 6.3**). SEM images show the blue surface is smooth without crystalline oxides; however, underneath the smooth surface, there are large Cu_2O crystals. The Cu:O atomic ratio (of 1.5) and Raman spectrum (with a weak 218 cm^{-1} peak, and equal intensity peaks at 523 and 623 cm^{-1}) both indicate that the blue surface is a combination of Cu_2O and $Cu(OH)_2$. The blue colour is indicative of $Cu(OH)_2$ and the smooth surface is due to the spread of the hydrogel.[13] Thus, the blue surface is a thick layer of $Cu(OH)_2$ covering Cu_2O crystals. Furthermore, the $Cu(OH)_2$-covered Cu_2O crystals can range from bright blue – when the $Cu(OH)_2$ layer is thick and is the main species contributing to the observed colour – to purple – when the Cu_2O crystals are large and blue $Cu(OH)_2$ and red Cu_2O both contribute to the observed colour.

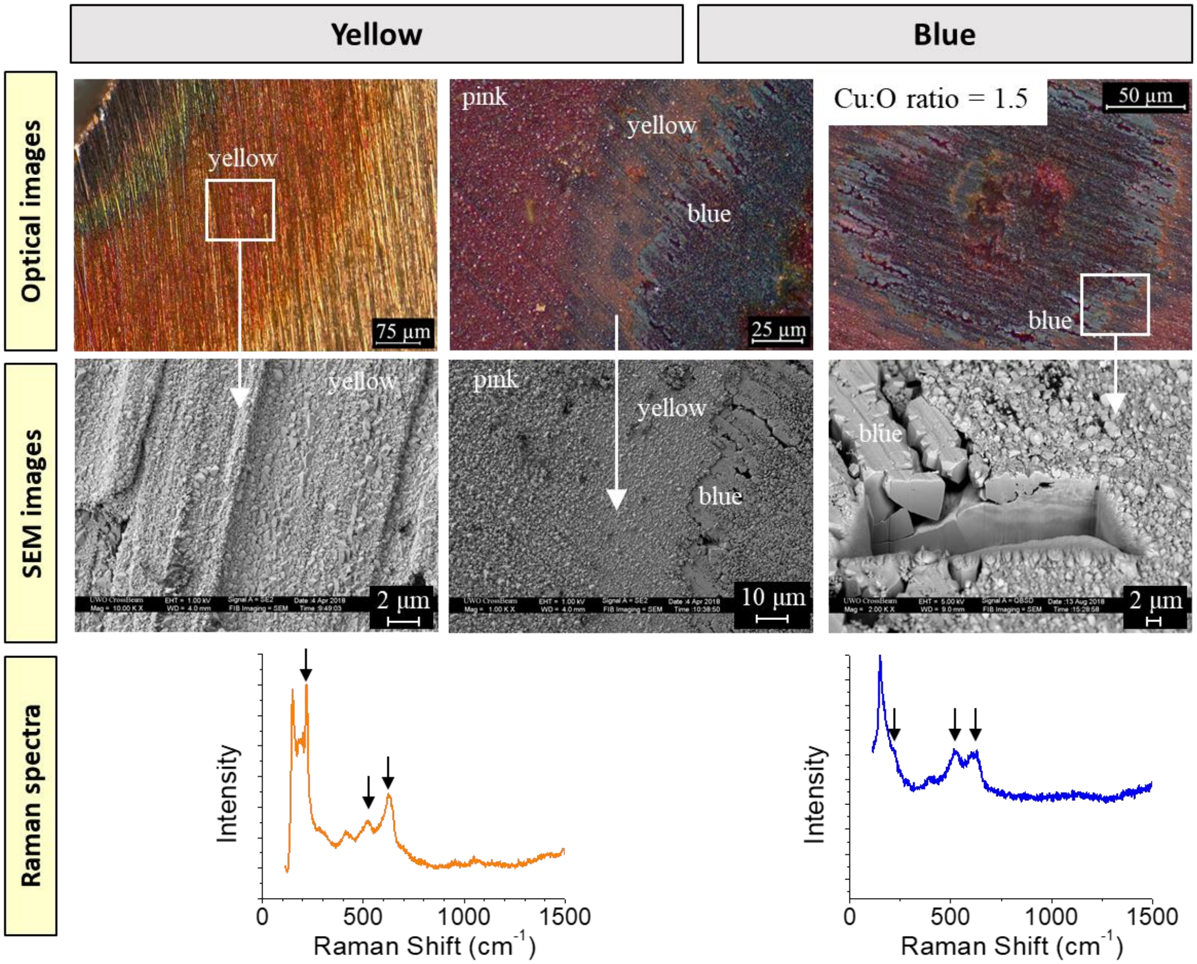

Figure 6.3 Optical images (with Cu:O ratio from EDX analysis) (top row), SEM images (middle row), and Raman spectra (bottom row) of the yellow- (left column) and blue-coloured (right column) surfaces during copper corrosion. The colour of the surface is labelled in the optical and SEM images.

The qualitative characterizations of the coloured areas on the corroded copper surfaces are summarized in **Table 6.1**. The yellow and pink-coloured areas represent those covered mainly with Cu_2O crystals of small, seed (submicron sized) crystals and large (micron sized) crystals, respectively. The purple and blue-coloured areas are those with $Cu(OH)_2$ hydrogel-covered Cu_2O crystals. A thin hydrogel layer on top of the Cu_2O crystals results in a purple-coloured surface, and the thicker the hydrogel layer is on top of the Cu_2O crystal, the bluer the surface appears. From this analysis, the colours in optical images were used in this thesis to determine the time progression and spatial distribution of oxides during corrosion.

Table 6.1 The identity of coloured surfaces observed during copper corrosion.

Colour of Film	Identity based on colour, SEM images, EDX, and Raman spectroscopy.
Yellow	Small Cu_2O crystals.
Pink	Cu_2O crystals.
Purple	Thin $Cu(OH)_2$ hydrogel layer covering Cu_2O crystals.
Blue	Thick $Cu(OH)_2$ hydrogel layer covering Cu_2O crystals.

6.3.2 Corrosion Progression Without Radiation

The changes in the time-dependence of corrosion products ([OH^-], [$Cu^{II}_{(sol'n)}$], and the amount of oxide deposits) indicate that the elementary steps that affect the overall rate of metal oxidation change as time progresses. Thus, the time-averaged behaviour of these species (i.e., pH, [$Cu^{II}_{(sol'n)}$], and solid corrosion products) can be used to describe the general corrosion mechanism. A dynamic stage represents a period over which the overall metal loss process occurs through the same rate-determining steps (RDS).[4,5] A robust chemical dynamic model should have a same reaction mechanism (i.e., same RDS), irrespective of reaction conditions. The same RDS in a given stage does not mean that the actual values of the overall rate and yield in the stage do not vary with initial solution redox and transport conditions, but they will vary according to the kinetics of the elementary steps.

The time-dependent behaviours of log([$Cu^{II}_{(sol'n)}$]), pH, and the surface morphology and colour observed during copper corrosion in stagnant droplet solutions free of CO_2/carbonate are presented in **Figure 6.4**. The results show that copper corrosion in CO_2-free-air saturated solutions without radiation present progresses through the same dynamic stages as observed in previous studies,[4,5] including those presented in **Chapters 4** and **5**, (up to Stage 3 by 480 h) although the duration of each stage, and the rates and the yields of corrosion products (dissolved ions and hydroxide/oxide deposits) in each stage are different. The key observations of the time-dependent behaviour of corrosion products are presented below, as well as their stage designation, which will be discussed in depth in this chapter.

Stage 1a: By the first measurement (t = 16 h), log([$Cu^{II}_{(sol'n)}$]) increased to -4.5 ± 0.1 and pH_t decreased from a pH_0 of 7.0 to 4.7 ± 0.1. The corresponding increases in [$Cu^{II}_{(sol'n)}$] and [H^+] were 0.03 ± 0.01 mM and 0.02 ± 0.01 mM, respectively. That is, the production rates of $Cu^{II}_{(sol'n)}$ and H^+ were nearly the same, and $[H^+]_t$ was significantly higher than $[H^+]_0$. No significant granular oxide deposits were observed on the surface. The metal grinding lines increased in roughness.

Stage 1b: For 16 h < t ≤ 40 h, both $[Cu^{II}_{(sol'n)}]_t$ and pH_t increased with time. The pH_t increased to a steady-state value of 8.4 ± 0.1, corresponding to the pKa of $Cu(OH)^+$. The concentration product, $[Cu^{II}_{(sol'n)}]_t \times [OH^-]_t^2$, was higher than the K_{sp} of $Cu(OH)_2$, i.e., the solution was supersaturated in this time period. Nevertheless, the surface remained clean, with no colour change or granular oxide deposits, but the metal grinding lines appeared smoother due to metal loss.

Stage 2: For 48 h ≤ t < 200 h, log($[Cu^{II}_{(sol'n)}]_t$) and pH_t fluctuated with time around average values. The time-averaged values were nearly constant with time: –3.6 for log($[Cu^{II}_{(sol'n)}]_t$) and 8.4 for pH_t, and the corresponding $[Cu^{II}_{(sol'n)}]_t$ was 0.3 ± 0.2 mM and $[OH^-]_t$ was 2.8 ± 0.4 μM. The concentration product remained higher than the K_{sp} of $Cu(OH)_2$. The surface became smoother while remaining free of granular oxide deposits. Images of these surfaces show a few small patches of dried hydrogel.

Stage 3: At the longest time (480 h), the colour of the surface became orange-yellow, indicating uniform growth of small Cu_2O crystals across the surface. $[Cu^{II}_{(sol'n)}]_t$ remained close to the average value in Stage 2 (0.5 mM) while the pH_t decreased to 6.6 ± 0.1, and the solution approached the $Cu(OH)_2$ solubility equilibrium.

Each corrosion test was conducted using a freshly polished copper coupon and freshly prepared solution (free of corrosion products) and the presented results are from *ex situ* analyses. That is, the individual data points in each graph in the figure (**Figure 6.4** as well as others presented in this thesis) are from different copper coupons. The durations of the stages given above are based on averaged surface and solution behaviour. However, different regions of a particular coupon may progress through the same stages at slightly different rates, due to variations in surface energy and solution conditions adjacent to the surface. While the difference in rates may be small (e.g., a factor of two) at early times when the reactions of the initial products are not significant, the variance in the overall rate will increase as the reactions of the intial and intermediate products become rate-controlling and may result in large variances in concentrations of dissolved species or surface phenomena after long corrosion times. The variances in rate may widen due to systemic feedback (i.e., cyclic feedback loops established between elementary steps).[3,4,14] As a result, a particular quantity measured after a specific corrosion time in different corrosion tests may have a large distribution around an average value, but the magnitude of this distribution does not necessarily reflect the magnitude of the initial spatial variations on copper surface or in solution parameters. Furthermore, there may be variations in the time at which the transition from one corrosion stage to another occurs. However, a corroding system is a macroscopic chemical system (even for localized corrosion) and thus, the general corrosion mechanism presented in this thesis represents the time-dependent corrosion behaviour. The time-dependent outliers presented in this data are a result of the systemic feedback causing large variations in the data, not due to the general corrosion behaviour. This was confirmed in **Chapter 4**, where despite time variations, the log([$\mathrm{Cu}^{\mathrm{II}}_{(\mathrm{sol'n})}$])-pH relationship was consistent.

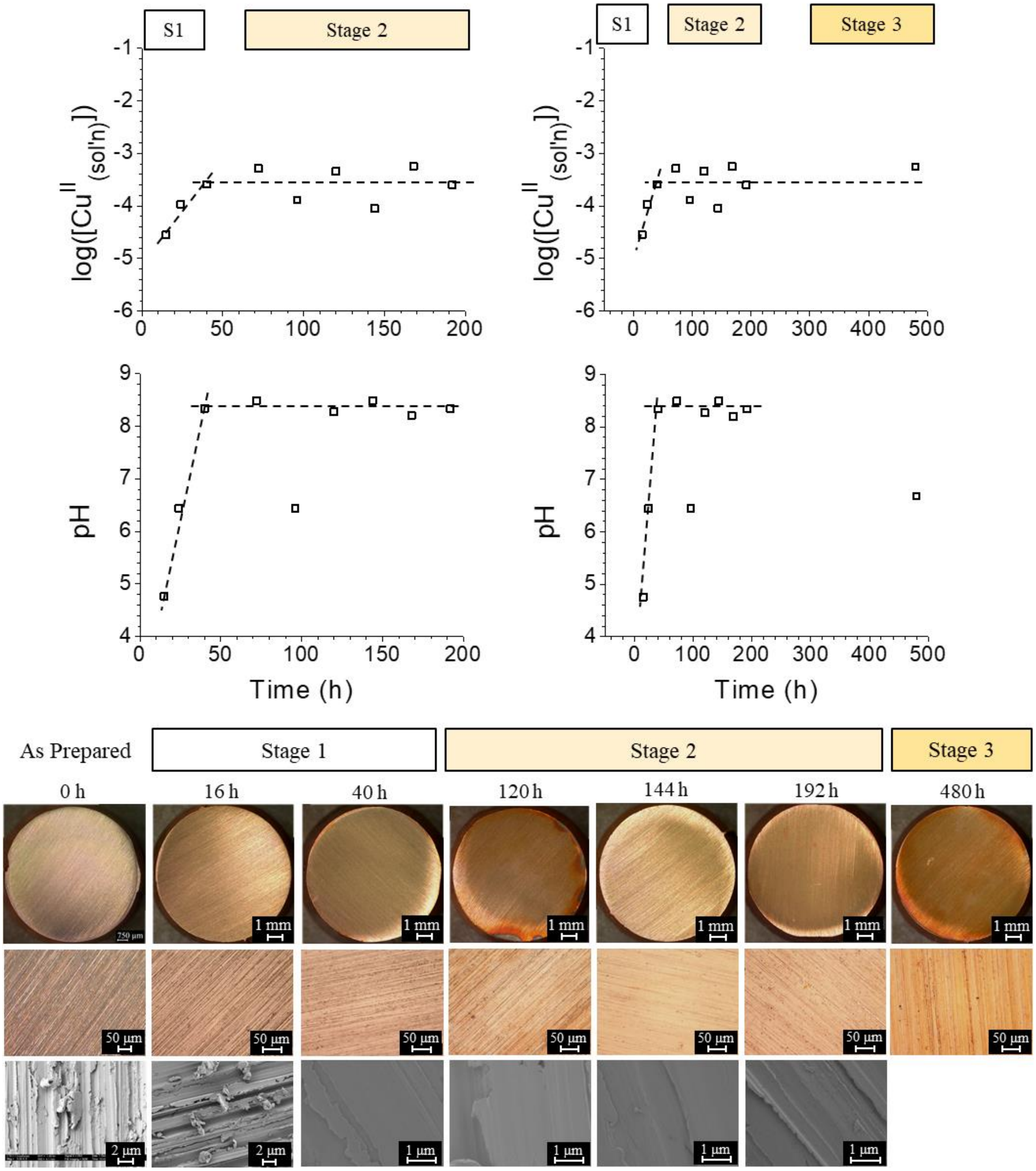

Figure 6.4 Time-dependent behaviour of [Cu^{II}$_{(sol'n)}$] (top row), pH (middle row), and the exposed surface (optical and SEM images) during copper corrosion after exposure to a 100 µL droplet of pure water (purged of CO$_2$, pH$_0$ = 7.0) in the absence of γ-radiation. The black dotted lines indicate the general trends of the solution species.

Based on the observed time-dependent behaviours of corrosion products and durations of individual stages as a function of solution redox and transport parameters we have proposed a copper corrosion mechanism in which the RDS evolves as corrosion progresses, as schematically presented in **Figure 6.5**. The elementary reactions and transport processes that control the overall metal loss rate in each stage, and how the transition from one stage to the next occurs are described below. For convenience, mass transport through the solution phase is treated as a 1-D process in the following discussion.

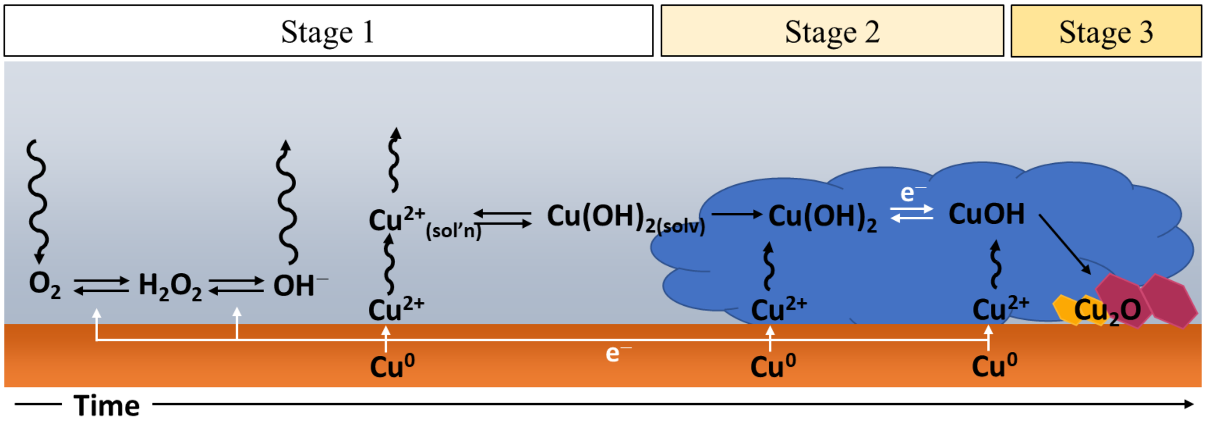

Figure 6.5 Copper corrosion mechanism in the absence of ionizing radiation, where the white arrows indicate electron transfer reactions.

In Stage 1, the main corrosion product was the dissolved cupric ion formed via interfacial charge transfer at $z = 0$ (**Eq. 6.1**).[4] The charge transfer step may involve intermediate steps. For example, the reduction of O_2 to OH^- at $z = 0$ (**Eq. 6.1b**) is known to occur in two 2-e transfer steps, where the first step is the reduction of O_2 to H_2O_2, and is followed by the reduction of H_2O_2 to OH^-.[15,16]

1st 2-e transfer: $O_2 + 2\,H_2O + 2\,e^- \rightleftarrows H_2O_2 + 2\,OH^-$ (6.3a)

2st 2-e transfer: $H_2O_2 + 2\,e^- \rightleftarrows 2\,OH^-$ (6.3b)

Overall e-transfer: $O_2 + 2\,H_2O + 4\,e^- \rightleftarrows 4\,OH^-$ (6.3c)

During corrosion in solutions initially free of H_2O_2 and Cu^{2+}, the transport of the intermediate product, H_2O_2, from $z = 0$ to $z = \delta_{diff}$ is significantly slower than its reduction to OH^- at $z = 0$

(**Eq. 6.3b**). Thus, under these conditions, it is not necessary to determine the amount of H_2O_2 in the solution phase and the transport step of H_2O_2 through the interfacial solution does not need to be included in the corrosion mechanism.

On *inert* metal surfaces, the RDS of the overall process of O_2 reduction to OH^- can change from the 1st 2-e transfer step (**Eq. 6.3a**), to transport of O_2 from the bulk solution to the interface (**Eq. 6.2b**), to the 2nd 2-e transfer step (**Eq. 6.3b**), depending on the polarization potential applied to the metal electrode.[15] In corrosion, O_2 reduction is coupled with metal oxidation, and mass and charge conservation during natural corrosion dictate that the rates of the half-reactions must be the same. However, that does not mean that the two half reactions contribute equally to the rate of the overall reaction. Although there is a prevailing assumption that the O_2 reduction half-reaction is rate limiting in all corrosion systems,[2,5,6,17,18] the metal oxidation half-reaction involves interfacial transfer of mass as well as of electrons, therefore it is generally slower than O_2 reduction. Hence, the RDS of the full corrosion reaction in Stage 1 is typically the metal oxidation half-reaction. To model the overall corrosion rate in Stage 1 as a function of solution parameters in the absence of radiation, O_2 reduction to OH^- can be treated as a single 4-e transfer step.

The other half-reaction involved in the interfacial charge transfer at $z = 0$ is the transfer of metal atom from the solid metal phase to the solution phase (**Eq. 6.1a**). The metal oxidation half-reaction may also occur through two 1-e transfer steps: the oxidation of $Cu^0_{(m)}$ to Cu^I adsorbed on the metal surface (indicated by the subscript "(ads)"), followed by the oxidation of $Cu^I_{(ads)}$ to $Cu^{II}_{(ads)}$ and the subsequent desorption and solvation of $Cu^{II}_{(ads)}$ to Cu^{2+} at the metal surface:

1st 1-e transfer: $Cu^0_{(m)} \rightleftarrows Cu^I_{(ads)} + e^-$ (6.4a)
2nd 1-e transfer: $Cu^I_{(ads)} \rightleftarrows Cu^{II}_{(ads)} + e^-$ (6.4b)
Desorption/solvation: $Cu^{II}_{(ads)} \rightleftarrows Cu^{2+}|_{z = 0}$ (6.4c)
Overall charge transfer: $Cu^0_{(m)} \rightleftarrows Cu^{2+}|_{z = 0} + 2\,e^-$ (6.4d)

Because the desorption/solvation of nearly insoluble $Cu^I_{(ads)}$ is negligible compared to the electron-transfer steps (**Eqs. 6.4a** and **6.4b**), it is not considered to be a RDS of the overall oxidation of $Cu^0_{(m)}$ to Cu^{2+}. The desorption/solvation of $Cu^{II}_{(ads)}$ (**Eq. 6.4c**) is an interfacial mass transfer process and hence, it is much slower than the preceding two electron transfer steps (**Eqs. 6.4a** and **6.4b**). Hence, the overall interfacial charge transfer step at $z = 0$ (**Eq. 6.4**) can be represented as a single elementary step when determining the oxidation rate of $Cu^0_{(m)}$ to Cu^{2+} at $z = 0$ in Stage 1, when the solution is not saturated with cupric ions.

Thus, it is sufficient to assume that the metal oxidation half-reaction (**Eq. 6.3**) and the O_2 reduction half-reaction (**Eq. 6.4**) at $z = 0$ occur in one elementary step for determination of the overall corrosion damage in air-saturated solutions without radiation present in Stage 1.

In the absence of any other reactions involving Cu^{2+} and OH^- in the interfacial solution region ($0 \leq z \leq \delta_{diff}$), the overall metal oxidation to Cu^{2+} dissolved in solution occurs in two sequential steps: the interfacial charge transfer step to inject Cu^{2+} at $z = 0$ (**Eq. 6.3** coupled with **Eq. 6.4**, i.e., **Eq. 6.1**), followed by diffusion of Cu^{2+} from the interface to the bulk solution (**Eq. 6.2a**). As discussed in **Chapter 4**, this two-step metal oxidation occurs in small solutions with $pH_0 \leq 2.0$. However, in solutions with $pH_0 > 2.0$, the hydrolysis equilibrium reactions (**Eq. 6.5**) are not negligible in the interfacial solution ($0 \leq z \leq \delta_{diff}$):

$$Cu^{2+} + 2\ OH^- \rightleftharpoons Cu(OH)^+ + OH^- \rightleftharpoons Cu(OH)_{2(solv)} + H_2O \rightleftharpoons Cu(OH)_3^- + H^+ \qquad (6.5)$$

where all of the cupric species in this chemical equation are solvated species, but the phase designation (solv) is given only to the neutral species $Cu(OH)_2$ to distinguish it from its solid form. The forward and reverse reactions of acid-base equilibria are very fast. Hence, once in solution, the dissolved cupric ion exists in various chemical forms and all the hydrolyzed species will be collectively referred to as $Cu^{2+}_{(sol'n)}$.

$$Cu^{2+}_{(sol'n)} \equiv Cu^{2+} + Cu(OH)^+ + Cu(OH)_{2(solv)} + Cu(OH)_3^- \qquad (6.6)$$

The relative amounts of the different chemical forms of $Cu^{2+}_{(sol'n)}$ are determined by the pKa values of the hydrolysis equilibria (**Eq. 6.5**) and hence, are a function of the total dissolved cupric ion concentration ($[Cu^{2+}_{(sol'n)}]$) and $[OH^-]$. During corrosion, these concentrations change with time (t) and with distance from the interface (z). The experimentally determined values for $[H^+]_t$ (based on pH_t) and $[Cu^{II}_{(sol'n)}]_t$ (which includes both dissolved ($Cu^{2+}_{(sol'n)}$) and dispersed copper species) are values that are averaged across z within the entire solution volume, as discussed in **Section 4.3.1**.

The hydrolysis equilibrium (**Eq. 6.5**) can change the $[H^+]_t$ (or $[OH^-]_t$) in the interfacial solution. In $pH_0 > 2.0$ solutions, the change in $[H^+]_t$ ($\Delta[H^+]_t$) is significant enough that $[H^+]_t$ cannot be approximated as constant, remaining at the initial value $[H^+]_0$. For $2.0 < pH_0 \leq 4.0$, pH_t increases ($[H^+]_t$ decreases) with time (but pH_t along the diffusion path still remains in the acidic range), which causes a shift in the hydrolysis equilibrium (**Eq. 6.5**) towards the formation of $Cu(OH)^+$. Accordingly, the measured metal concentration in solution at time t ($[Cu^{II}_{(sol'n)}]_t$) (in solutions initially free of dissolved copper) was observed to be the same as $-\Delta[H^+]_t$ (not $-[H^+]_t$). That is, in <u>Stage 1</u> the metal dissolution rate (υ_{diss}) is the same as the proton consumption rate (υ_{-H^+}) and they are both constant with time.

$$\Delta[Cu^{II}_{(sol'n)}]_t \ (= [Cu^{II}_{(sol'n)}]_t) \approx -\Delta[H^+]_t \ (\neq -[H^+]_t) \qquad \text{in } \underline{\text{Stage 1}} \text{ for } 2.0 < pH_0 \leq 4.0 \tag{6.7a}$$

$$\upsilon_{diss} \approx \upsilon_{-H^+} \approx \text{constant with } t \tag{6.7b}$$

$$\text{where } \upsilon_{diss} = \frac{V_{sol}}{A_{int}} \cdot \frac{d[Cu^{II}_{(sol)}]_t}{dt} \quad \text{and} \quad \upsilon_{-H^+} = \frac{V_{sol}}{A_{int}} \cdot \frac{d[H^+]_t}{dt} \tag{6.7c}$$

When pH_0 is near neutral, a small addition of OH^- can change $[H^+]_t$ or $[OH^-]_t$ substantially. Thus, initial metal oxidation coupled with oxidant reduction at $z = 0$ (**Eq. 6.1**) can increase $[OH^-]_t$ in the interfacial solution substantially, which shifts the hydrolysis equilibrium far to the right nearly immediately. Hence, the main chemical species being transported into the solution are $Cu(OH)_3^-$ and H^+, rather than Cu^{2+} and OH^-. Because these reactions occur very quickly, they can be considered as one elementary step occurring at $z = 0$ (**Eq. 6.8**).

$$Cu^0_{(m)} + \tfrac{1}{2} O_2 + 2\, H_2O \rightarrow Cu(OH)_3^- + H^+ \qquad \text{in } \underline{\text{Stage 1a}} \text{ for } 6.0 \leq pH_0 \leq 9.0 \tag{6.8}$$

Following their production, $Cu(OH)_3^-$ and H^+ diffuse away from the metal surface through the interfacial solution.

$$Cu(OH)_3^-|_{z=0} \rightsquigarrow Cu(OH)_3^-|_{z=\delta_{diff}} \tag{6.9a}$$

$$H^+|_{z=0} \rightsquigarrow H^+|_{z=\delta_{diff}} \tag{6.9b}$$

Thus, while $[Cu^{II}{}_{(sol'n)}]_t$ increases with time, $\Delta[H^+]_t$ ($\approx [H^+]_t$) does not decrease, but increases with time initially (Stage 1a), the opposite trend to that observed at lower pH_0.

$$\frac{d[Cu^{II}{}_{(sol)}]_t}{dt} \approx \frac{d[H^+]_t}{dt} \quad \text{in Stage 1a for } 6.0 \leq pH_0 \leq 9.0 \tag{6.10a}$$

$$\upsilon_{diss} \neq \upsilon_{-H^+}, \text{ but } \upsilon_{diss} \approx -\upsilon_{-H^+} \tag{6.10b}$$

In small volume solution droplets free of CO_2, the pH_t of the first measurement (t = 16 h) had decreased from pH_0 (7.0) to 4.7 ± 0.1 (middle row in **Figure 6.4**). With no other acid-base equilibria in solution (such as equilibria of carbonate species, discussed in **Chapter 7**), the average concentration of $Cu^{II}{}_{(sol'n)}$ and H^+ increased by the same amount (**Eq. 6.10b**). In Stage 1a, the increase in $[Cu^{II}{}_{(sol'n)}]_t$ was equal to the increase in $[H^+]_t$ and $-\log([Cu^{II}{}_{(sol'n)}]_t)$ was equal to the pH_t.

The increase in $[H^+]_t$ ($\approx \Delta[H^+]_t$) shifts the hydrolysis equilibrium more and more to the left with time, and the dominant chemical form of $Cu^{2+}{}_{(sol'n)}$ switches from $Cu(OH)_3^-$ to $Cu(OH)_{2(solv)}$ and to $Cu(OH)^+$, while consuming H^+.

$$Cu(OH)_3^- + H^+ \rightarrow Cu(OH)_{2(solv)} + H_2O \rightarrow Cu(OH)^+ + OH^- + H_2O$$
$$\text{in Stage 1b for } 6.0 \leq pH_0 \leq 9.0 \tag{6.11}$$

With the production of $Cu(OH)_2$ at the start of Stage 1b, $[H^+]_t$ reaches a maximum (or pH_t reaches a minimum, the value of which is based on the solution conditions) then subsequently $[H^+]_t$ decreases (pH_t increases) with time as $Cu(OH)^+$ forms. Hence, although the rate of increase of $[Cu^{2+}{}_{(sol'n)}]_t$ remains nearly constant (only the dominant chemical form changes with time), the rate of change of $[H^+]_t$ decreases to zero (with the formation of $Cu(OH)_2$) then increases (with the formation of $Cu(OH)^+$). The rates of increase of $[Cu^{2+}{}_{(sol'n)}]_t$ and $[H^+]_t$ in Stage 1b are not equal.

$$\frac{d[Cu^{II}{}_{(sol)}]_t}{dt} \neq \frac{d[H^+]_t}{dt} \quad \text{in Stage 1b when } 6.0 \leq pH_0 \leq 9.0 \tag{6.12a}$$

$$\upsilon_{diss} \neq \upsilon_{-H^+} \text{ and } \upsilon_{diss} \neq -\upsilon_{-H^+} \qquad (6.12b)$$

Because pH$_t$ increases over a large range during Stage 1b, the solubility of cupric ions decreases substantially (the solubility diagram is shown in **Chapter 4**, **Figure 4.1**). However, this change in solubility did not influence the copper dissolution rate, which was constant with time (9.4 μM/h in **Figure 6.4**). In fact, in all solutions with pH$_0$ > 2.0, the rate of increase of $[\mathrm{Cu^{II}}_{(\mathrm{sol'n})}]_t$ is constant throughout Stage 1 (at different rates depending on solution conditions) despite large changes in pH$_t$ ($\Delta[\mathrm{H^+}]_t$) with corrosion time, as discussed in depth in **Chapter 4**:

$$\upsilon_{diss} \approx \text{constant with } t \qquad \text{in Stage 1 for pH}_0 > 2.0 \qquad (6.13)$$

When a corrosion measurement is taken after one timepoint in different solution pH values, the observed corrosion product yield leads to the assumption that the solution pH affects the rate of metal oxidation.[19-21] However, our time-dependent studies consistently show that the pH does not affect the *rate* of metal oxidation, but that the pH affects the maximum amount of metal cation that can be dissolved in the solution (i.e., the solubility of $\mathrm{Cu(OH)_{2(solid)}}$). For pH$_0$ > 2.0, $[\mathrm{H^+}]_t$ is a not a simple function of $[\mathrm{H^+}]_0$ but also depends on $-\Delta[\mathrm{H^+}]_t$, while $-\Delta[\mathrm{H^+}]_t$ is determined by the rate of metal dissolution as well as the acid-base equilibria. Hence, although metal dissolution continues until $[\mathrm{Cu^{2+}}_{(\mathrm{sol'n})}]_t$ reaches the solubility of $\mathrm{Cu(OH)_{2(solid)}}$, the increase of $[\mathrm{Cu^{2+}}_{(\mathrm{sol'n})}]_t$ with time induces different changes in $[\mathrm{H^+}]_t$ depending on pH$_0$. This further induces a change in the $\mathrm{Cu^{2+}}_{(\mathrm{sol'n})}$ saturation capacity of the solution with time.

In solutions with a pH$_0$ near neutral, the bulk solution has a lower pH than at the metal surface during Stage 1b and as $\mathrm{Cu^{2+}}_{(\mathrm{sol'n})}$ transports through the diffusion layer, its solubility decreases with *z*. Thus, precipitation of $\mathrm{Cu(OH)_2}$ as solid colloid particles ($\mathrm{Cu(OH)_{2(colloid)}}$) occurs in the bulk solution (away from the metal surface) and the colloid particles remain dispersed in the bulk solution, as discussed in **Chapter 4**. The measured concentration of copper, then, includes these dispersed particles in Stage 1b.

$$[\mathrm{Cu^{II}}_{(\mathrm{sol'n})}]_t \approx [\mathrm{Cu(OH)^+} + \mathrm{Cu(OH)_{2(solv)}} + \mathrm{Cu(OH)_{2(colloid)}}]_t$$

$$\text{in Stage 1b for } 6.0 \leq \text{pH} \leq 9.0 \qquad (6.14)$$

The formation of colloid particles has a negligible effect on the preceding corrosion reactions (i.e., initial overall redox reaction at $z = 0$ via **Eq. 6.1**, the diffusion of products away from the surface, **Eq. 6.2**, and cupric ion hydrolysis, **Eq. 6.5**) thus, despite a change in the main dissolved cupric ion species, the rate determining step does not change between Stage 1a and 1b (i.e., cupric ion diffusion from $z = 0$) and both stages are considered to be part of Stage 1.

Throughout Stage 1b, $[\mathrm{Cu^{II}}_{(sol'n)}]$ and $[\mathrm{OH^-}]$ continue to increase until the bulk pH reaches the pKa of $\mathrm{Cu(OH)^+}$ (**Figure 6.4**).[22]

$$\mathrm{Cu(OH)^+ + H_2O \rightleftharpoons Cu(OH)_{2(solv)} + H^+} \qquad \mathrm{pKa} = 8.3 \tag{6.15}$$

That is, when a sufficient amount of $\mathrm{Cu^{2+}}_{(sol'n)}$ and $\mathrm{OH^-}$ have dissolved into the solution to establish the acid-base equilibrium, the pKa of the weak acid $\mathrm{Cu(OH)^+}$ regulates the pH of the bulk solution. This further confirms that $\mathrm{Cu(OH)^+}$ and $\mathrm{Cu(OH)_{2(solv)}}$ are the main cupric ion forms in solution.

In Stage 1b, the overall flux of metal atoms is from the solid (metal) phase to the solution phase then to the solid (colloid) phase (**Eq. 6.16**).

$$\mathrm{Cu^0}_{(m)} \rightarrow\rightarrow \mathrm{Cu^{2+}}_{(sol'n)} \rightarrow\rightarrow \mathrm{Cu(OH)_{2(colloid)}} \tag{6.16}$$

At the end of Stage 1, there was no significant quantity of solid granular products on the surface, but the grinding lines had become smoother (bottom row SEM images in **Figure 6.4**) as $\mathrm{Cu^0}_{(m)}$ had been lost via oxidation and dissolution.

As the concentration of $\mathrm{Cu(OH)_{2(colloid)}}$ particles in the bulk solution increases, the frequency of their collisions increases and they agglomerate together in the bulk solution. The colloid particles will accumulate water molecules during aggregation due to strong hydrogen bonds between the colloid molecules and the surrounding water molecules.[23,24] Colloid agglomeration results in the formation of a hydrogel, which consists of a network of loosely connected $\mathrm{Cu(OH)_2}$ colloid (solid) particles with a mobile phase of $\mathrm{Cu^{II}}_{(sol'n)}$-saturated solution in the interstices.[3,25,26] The precipitation of this $\mathrm{Cu(OH)_2}$ hydrogel marks the beginning of Stage 2.

As discussed in **Chapter 4**, in solutions with $pH_0 \leq 2.0$, the pH_t remains low ($\approx pH_0$) for the duration of Stage 1, and thus the solubility of cupric ions remains very high. Under these conditions, reaching Stage 2 would take a very long time. In flowing solutions, cupric ions may never accumulate enough that they begin to precipitate in Stage 2. In solutions with $2.0 < pH_0 \leq 4.0$, the accumulation of $Cu^{2+}_{(sol'n)}$ occurs in the interfacial solution and the hydrogel is, consequently, dense and grows next to the metal surface. With the formation of a Cu^{2+}-selective layer at the metal surface, OH^- continues to transport into the bulk solution until the solution pH increases sufficiently for the $Cu^{2+}_{(sol'n)}$ to attain saturation capacity. With a near neutral pH_0, the evolution of $[H^+]_t$ results in the formation of hydrogel in the bulk solution, not between the metal and the solution. Thus, Cu^{2+} and OH^- can both continue to transport from the metal surface until reaching the (quasi-)solubility limit. Furthermore, hydrogel growth occurs within the entire solution, not just the interfacial volume of solution, and thus, the hydrogel contains a low density of colloid particles.

The hydrogel grows as the colloids dispersed in the bulk solution join the solid network (i.e., the colloid density increases within the hydrogel). This agglomeration of colloid particles does not affect the pH_t, which, with no other acid-base equilibria in solution, is buffered at the pKa of $Cu(OH)^+$ (**Eq. 6.12**) and thus $[H^+]_t$ does not change with time (**Figure 6.4**).

$$\upsilon_{diss}, \upsilon_{-H^+} \approx 0 \qquad \text{in Stage 2 for } pH_0 > 2.0 \qquad (6.17)$$

When the pH is equal to the pKa of $Cu(OH)^+$, the concentrations of $Cu(OH)_{2(solv)}$ and $Cu(OH)^+$ are equal and the solubility of cupric ions is around its minimum. The time-averaged pH during Stage 2 (48 h ≤ t < 200 h) was 8.4 ± 0.1 (**Figure 6.4**).

As the hydrogel layer grows, the concentration copper dissolved and dispersed in solution remains at an approximately constant value (due to the constant pH_t). The time-averaged $[Cu^{II}_{(sol'n)}]$ value during Stage 2 was 0.38 mM ($\log([Cu^{II}_{(sol'n)}]) = -3.4$) (**Figure 6.4**), which is above the solubility limit at pH_t (8.4 ± 0.1 in Stage 2), due to the inclusion of colloid particles in the measurement.

The transport of cupric ions through the hydrogel network is slow and slows further as the colloid concentration in the hydrogel increases.[27] When cupric ions (as dissolved or dispersed colloidal species) get trapped next to the metal surface, they can more easily reduce to Cu^+ species, coupled with the oxidation of $Cu^0_{(m)}$ to $Cu^{2+}_{(sol'n)}$.[28]

Ox half-reaction: $Cu^0_{(m)} \rightleftarrows Cu^{2+}_{(sol'n)} + 2\ e^-$ (6.18a)

Red half-reaction: $2\ Cu^{2+}_{(sol'n)} + 2\ e^- \rightleftarrows 2\ Cu^+_{(sol'n)}$ (6.18b)

Overall reaction: $Cu^0_{(m)} + Cu^{2+}_{(sol'n)} \rightleftarrows 2\ Cu^+_{(sol'n)}$ (6.18c)

As $Cu^+_{(sol'n)}$ dissolves into the solution next to the metal surface, it establishes fast hydrolysis equilibria in the mobile phase of the hydrogel (**Eq. 6.19**) and is incorporated into the hydrogel as a solid species (**Eq. 6.20**). Similar to the cupric ion, dissolved $Cu^+_{(sol'n)}$ is the sum of all hydrolysis species (i.e., Cu^+, $Cu(OH)_{(solv)}$, $Cu(OH)_2^-$).

$$Cu^+ + 2\ OH^- \rightleftharpoons CuOH_{(solv)} + OH^- \rightleftharpoons Cu(OH)_2^- \quad (6.19)$$

$$Cu^+_{(sol'n)} + x\ OH^- \rightleftharpoons CuOH_{(solid)} \quad (6.20)$$

The hydrogel now contains both Cu^I and Cu^{II} hydroxide species.

$$Cu^+_{(sol'n)}/CuOH_{(solid)} + Cu^{2+}_{(sol'n)}/Cu(OH)_{2(solid)} + OH^- \rightarrow \text{mixed } Cu^I/Cu^{II} \text{ hydroxide hydrogel} \quad (6.21)$$

The reduction of $Cu^{2+}_{(sol'n)}/Cu(OH)_2$ to $Cu^+_{(sol'n)}/CuOH$ via **Eq. 6.21** accelerates further precipitation of $Cu(OH)_2$ colloid particles. The faster growth of hydrogel, in turn, increases the rate of Cu^I formation. That is, a cyclic feedback loop between the formation of $Cu(OH)_2$ hydrogel (**Eq. 6.18**) and its reduction to $Cu^+_{(sol'n)}$ (**Eq. 6.21**) is established.

The formation of the mixed Cu^I/Cu^{II} hydrogel during Stage 2 did not affect the pH_t, which was buffered at the pKa of $Cu(OH)^+$. This indicates that the cupric ion hydrolysis and $Cu(OH)_2$ solubility equilibrium are maintained throughout this stage. That is, the initial metal oxidation coupled with solution reduction (**Eq. 6.1**), diffusion of cupric ions (**Eq. 6.2**), cupric ion hydrolysis (**Eq. 6.5**), and the precipitation of colloid particles are all in a steady state, while the growth of the hydrogel (including agglomeration of colloid particles and $Cu(OH)_2$ reduction to CuOH) is controlling the overall rate of metal loss.

In the absence of radiation, the low $[Cu^{2+}_{(sol'n)}]$ results in a low colloid density in the hydrogel during <u>Stage 2</u>, and thus, the hydrogel does not easily stick to the surface to be observed by post-test analysis (but is included in the solution analysis). Nevertheless, some local observations of the hydrogel are shown in **Figure 6.6**. The optical images show that the hydrogel appears as an amorphous, clear growth on the surface. Although $Cu(OH)_2$ is blue, the hydrogel that grows under these conditions is highly hydrated with a low colloid concentration, thus the colour is diluted. The Raman spectrum (right in **Figure 6.6**) has peaks at 523 and 623 cm^{-1}, with the former slightly more intense, confirming that the clear crystals containing mostly $Cu(OH)_2$.

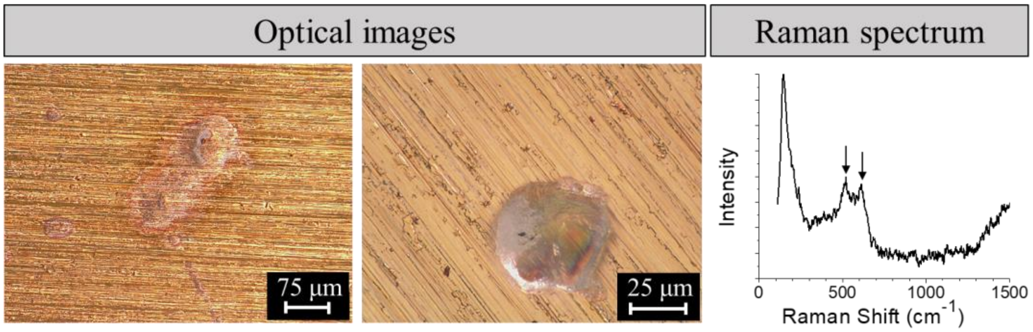
Optical images

Raman spectrum

Figure 6.6 Optical images and Raman spectrum of the amorphous, clear hydrogel formed during <u>Stage 2</u> in the absence of radiation. The arrows in the Raman spectrum (right) indicate the 523 cm^{-1} and 623 cm^{-1} peaks, the intensities of which confirm the species in the optical images (left) contain $Cu(OH)_2$.

In <u>Stage 2</u>, the overall flux of metal atoms is from the metal phase to the solution phase to the hydrogel:

$$Cu^0_{(m)} \rightarrow\rightarrow Cu^{2+}_{(sol'n)}/Cu(OH)_{2(hydrogel)} \rightarrow\rightarrow \text{mixed } Cu^{I}/Cu^{II} \text{ hydroxide hydrogel} \quad (6.22)$$

<u>Stage 2</u> ends when CuOH reaches supersaturation and begins to precipitate as Cu_2O. Thus, the duration of this stage is dependent on the redox activity of the solution and the dissolved cupric ion concentration at the end of <u>Stage 1</u> and during <u>Stage 2</u>. In CO_2-free pure water without

radiation, the reduction of $Cu(OH)_2$ to CuOH is slow and $[Cu^{II}_{(sol'n)}]$ is low, and accordingly, the duration of Stage 2 is longer than in the presence of radiation (shown in the following sections).

The elementary steps to consider in determining the overall corrosion rate in Stage 2 are those listed in **Eqs. 6.3**, **6.4**, **6.5**, **6.18**, and **6.21**. The rate of the underlying metal oxidation to soluble $Cu^{2+}_{(sol'n)}$ is determined by the rate at which $Cu^{2+}_{(sol'n)}$ can be removed from the saturated solution (i.e., as fast as the $Cu(OH)_2$ colloid particles join the hydrogel network). The amount of $Cu(OH)_2$ hydrogel that grows during Stage 2 and its rate of growth is proportional to $[Cu^{2+}_{(sol'n)}]$ at the end of Stage 1, which was very low in the studied conditions. The rate of hydrogel growth is also dependent on the redox conditions of the solution (due to **Eq. 6.18**), and thus, the rate of hydrogel growth in solutions without radiation is low. However, the fact that the corrosion process is able to progress past Stage 2 indicates that the corrosion rate in this stage is not zero.

CuOH is thermodynamically unstable and dehydrates in the hydrogel in Stage 3 to form more stable Cu_2O crystals.[29,30]

$$2\ Cu^{+}_{(sol'n)} + x\ OH^{-} \rightleftharpoons 2\ CuOH_{(solid)} \rightarrow Cu_2O + H_2O \qquad (6.23)$$

The rate of precipitation of Cu_2O crystals is dependent on the supersaturation concentration of CuOH within the hydrogel. $[Cu^{II}_{(sol'n)}]$ at the end of Stage 2 was low and the rate of $Cu(OH)_2$ reduction to CuOH was low, which suggests the precipitation rate of Cu_2O crystals was also low in these conditions. Nevertheless, after 480 h, the entire surface was a deep yellow colour (optical images in **Figure 6.5**), indicating that small Cu_2O crystals covered the surface (see colour analysis in **Section 6.3.1**). $[Cu^{II}_{(sol'n)}]_t$ continued to fluctuate around its time-dependent average, while the pH_t decreased to 6.7 to satisfy the $Cu(OH)_2$ solubility equilibrium with copper dissolved in solution (shown in **Chapter 4**). The previous corrosion reactions are in a steady-state and the main corrosion product is Cu_2O (**Eq. 6.24**).

$$Cu^{0}_{(m)} \rightarrow\rightarrow \text{mixed } Cu^{I}/Cu^{II} \text{ hydroxide hydrogel} \rightarrow\rightarrow Cu_2O \qquad (6.24)$$

6.3.3 Corrosion Progression in the Presence of γ-Radiation

As described in **Chapter 5**, the energy of γ-radiation transferred to a metal quickly dissipates as heat and does not induce any chemical change. However, water and humid air exposed to γ-radiation decompose into redox-active (mainly H_2O_2) and acidic species (mainly HNO_3). Under a continuous flux of γ-radiation, the radiolysis products reach steady-state concentrations and become homogeneously distributed in solution. Hence, the effects of γ-radiation on the corrosion rate are through the radiolysis products that are distributed homogeneously and at near constant concentrations (even though they may be consumed by corrosion reactions).

The steady-state concentrations of radiolysis products depend on not only the radiation dose rate but also on solution pH, and the concentration of radical scavengers such as O_2 and Cl^-.[31-34] The radiolysis species reach steady-state concentrations homogeneously in solution in a short period of time (on a micro- to millisecond timescale) compared to the timescale of interfacial mass transfer processes and surface reactions (minutes). Thus, the surface reactions of radiolysis products are much slower than their formation reactions in the solution phase. The implication of these different reaction rates is that corrosion reactions typically do not contribute to the determination of the steady-state concentrations of radiolysis products; however, the radiolysis product concentrations may control the corrosion reactions. Hence, the radiolysis kinetics that determine the steady-state concentrations do not require a detailed kinetic description in terms of their effect on the corrosion process, i.e., there is no cyclic feedback between radiolysis and corrosion reactions, as shown schematically in **Figure 6.9**.

Because of the different reaction timescales for homogeneous solution and surface reactions, the important radiolysis products for corrosion are not the more reactive radical species but the more stable molecular products such as H_2O_2, O_2, H^+, NO_3^-/NO_2^-. (For ground waters that may be highly saline, intermediate chloride radiolysis products such as ClO and Cl_2 may become important.)

In the absence of radiation, we have shown that regardless of the particular redox and transport condition, copper corrosion progresses through different dynamic stages as the initial and intermediate corrosion products accumulate significantly and undergo their own reactions. Solution redox ([H_2O_2] and [O_2]), pH, and transport conditions affect the rates of different elementary steps differently, and thus affect the overall rate of metal loss (through metal oxidation) in more complicated ways than would be expected based on linear dynamics. Hence, to evaluate the overall effect of radiation on corrosion dynamics, the effects of steady-state concentrations of radiolysis products (H_2O_2 and H^+ in particular) on the kinetics of the elementary steps must be examined.

The time-dependent behaviours of log([$Cu^{II}_{(sol'n)}$]), pH, and the surface morphology and colours during radiolytic copper corrosion in stagnant droplet solutions free of CO_2/carbonate are presented in **Figure 6.7**. Further analysis of the solid deposits is presented in **Figure 6.8**. Despite faster rates of increase of [$Cu^{II}_{(sol'n)}$] and oxide deposits than observed without radiation, copper corrosion in the presence of radiation progresses through similar dynamic stages. As discussed earlier, the rate of progression is expected to vary across the metal surface and this variance is expected to increase with time. The spatial variance increased faster with radiation than without radiation present due to the faster rates of reactions. Hence, there were also considerable overlaps of the different dynamic stages that were defined based on the average chemical behaviours. The key observations during radiolytic copper corrosion are:

Stage 1: When $t \leq 40$ h, [$Cu^{II}_{(sol'n)}$]$_t$ increased while minimal oxide growth was observed on the surface. The [$Cu^{II}_{(sol'n)}$] yield at the end of this stage was much higher than observed in the absence of radiation. The largest difference observed in the presence of radiation in this stage was the time-dependent behaviour of pH_t, which decreased with time and found a near constant value of about 4.6, instead of increasing at later times of Stage 1.

Stage 2: For $48 \text{ h} \leq t \leq 96$ h, pH_t fluctuated around a near constant value of 4.6 and [$Cu^{II}_{(sol'n)}$] fluctuated around 6.0 mM. The metal surface in general became smoother with time and remained relatively free of granular oxides. The differences due to radiation were the near steady-state values of pH_t and [$Cu^{II}_{(sol'n)}$]$_t$; pH_t was lower while [$Cu^{II}_{(sol'n)}$] was higher in irradiated solutions than in unirradiated solutions. The duration of this stage was also shorter with than in the absence of radiation and the colloid density within the hydrogel was higher.

Stage 3: For 120 h ≤ t ≤ 200 h, $[Cu^{II}_{(sol'n)}]_t$ continued to increase with time but at a much slower rate than observed at earlier stages, while pH_t continued fluctuating around a value of 4.6. Pink to purple-coloured granular oxides also began to grow on the surface. As discussed in **Section 6.3.1**, these colours indicate the presence of Cu_2O crystals covered with various thicknesses of $Cu(OH)_2$ hydrogel. The average Cu_2O crystal size at the start of Stage 3 was small (< 200 nm) with a narrow size distribution, but with increasing time the crystal size distribution became bimodal indicating Ostwald ripening of Cu_2O crystals.

Stage 4: After the longest time duration of the experiment (t = 480 h), $[Cu^{II}_{(sol'n)}]_t$ had decreased, but the pH_t remained at the same steady-state value. The surface was covered with large Cu_2O crystals, with a thick layer of blue hydrogel that contained adsorbed nitrate.

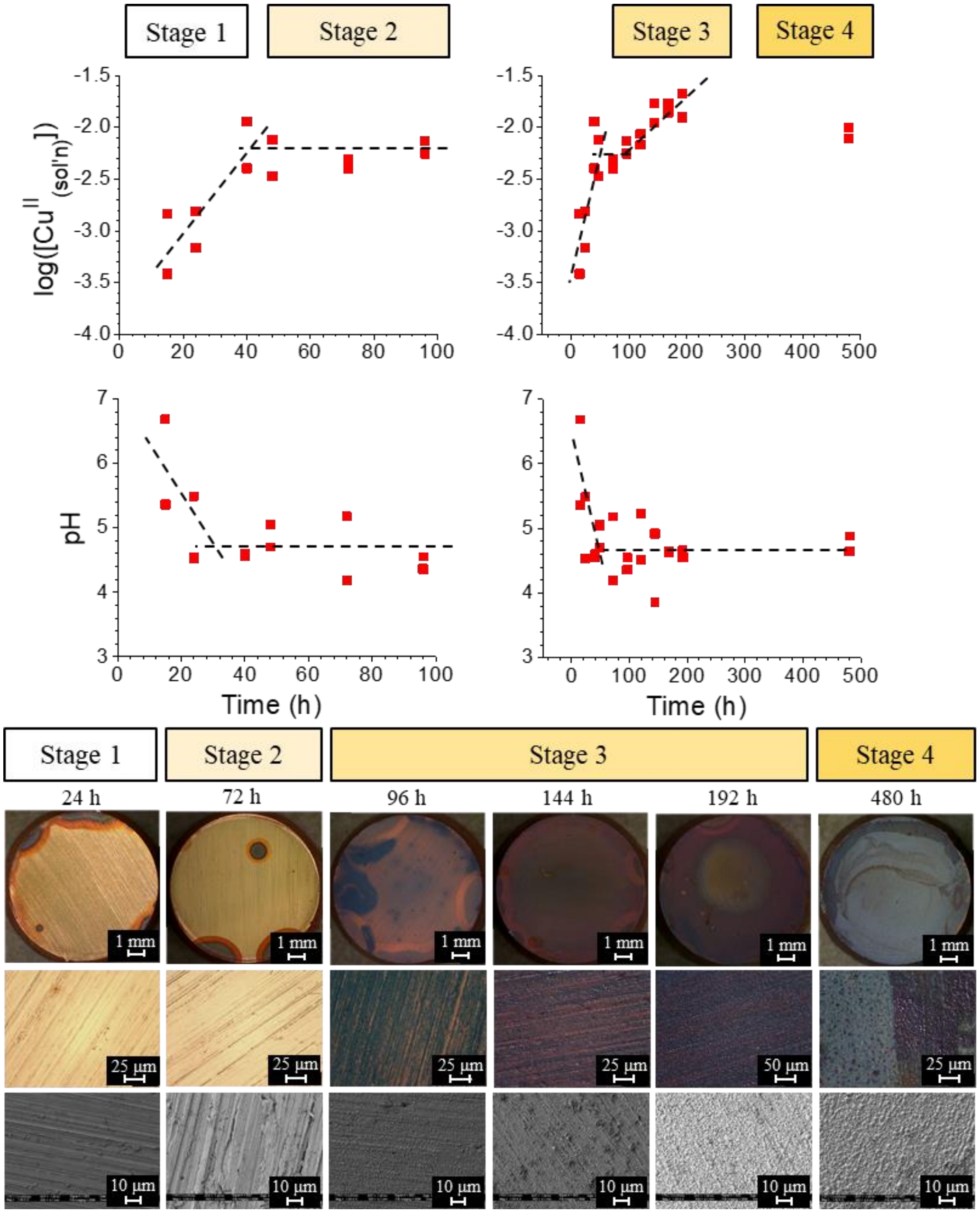

Figure 6.7 Time-dependent behaviours of [$Cu^{II}_{(sol'n)}$] (top row), pH (middle row), and the exposed surface (optical and SEM images, bottom three rows) during copper corrosion after exposure to a 100 µL droplet of pure water (purged of CO_2, $pH_0 = 7.0$) in the presence of γ-radiation. The black dotted lines show the general trend of the data (not based on regression analysis).

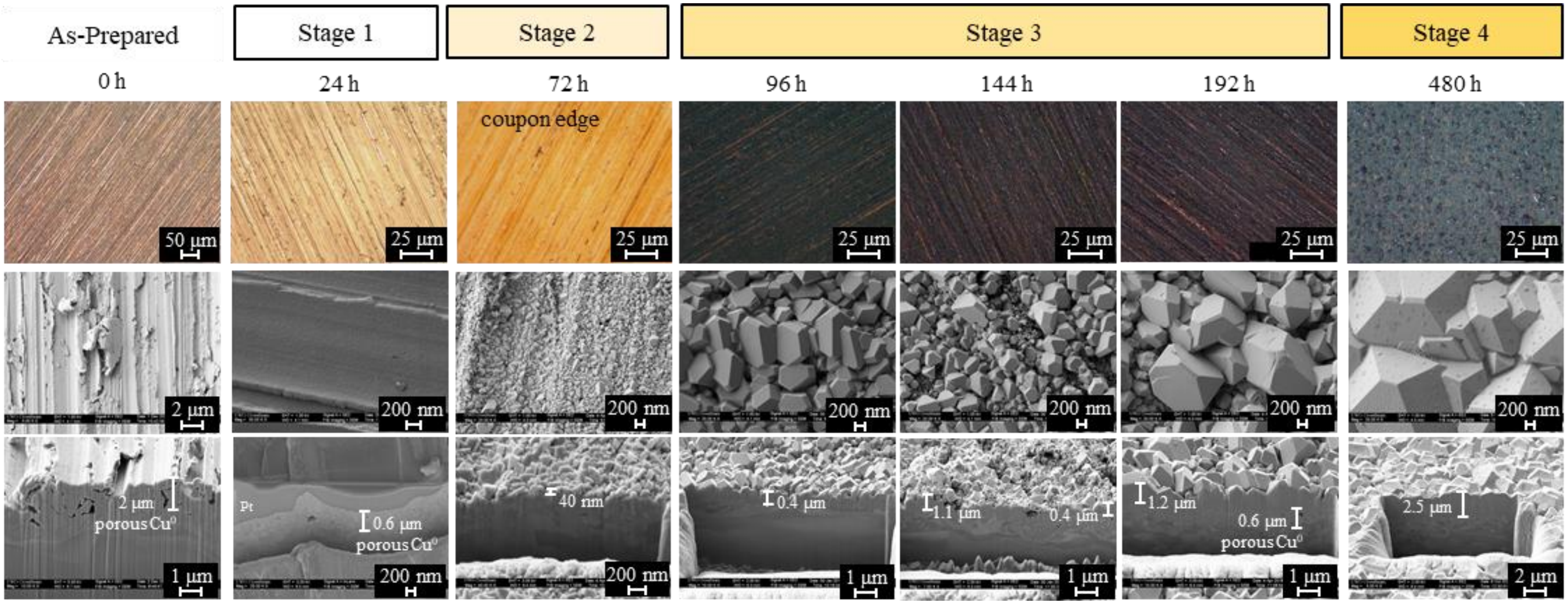

Figure 6.8 Optical (top row) and SEM images of the surface (middle row) and the metal-oxide cross section (bottom row, cut using focused Ga-ion beam) in each stage of corrosion in the presence of radiation.

As discussed for the unirradiated samples, the durations of the corrosion stages given above are based on averaged solution and surface behaviour, while different areas of the same coupon may progress through the same stages at slightly different rates. The differences in rate may initially be small but can increase with time, especially after the establishment of cyclic feedback loops within the system. Thus, a quantity measured after specific corrosion time in different corrosion tests may have a large distribution around an average value and variations in the time at which the transition from one corrosion stage to another occurs. These large variations due to these corrosion processes are more significant than the instrumental error for each measurement. Thus, by presenting the data for each trial (shown in **Figure 6.7**), opposed to their average with error bars, the general corrosion behaviour can be determined. The time-dependent behaviour of the corrosion products (i.e., $[\mathrm{Cu^{II}}_{(sol'n)}]$, pH, and solid corrosion product amount) are used in this thesis to determine how the corrosion progression is affected by the studied solution parameter (which, in this section, is the presence of γ-radiation). The corrosion mechanism in the presence of radiation is schematically illustrated in **Figure 6.9** and described in detail below.

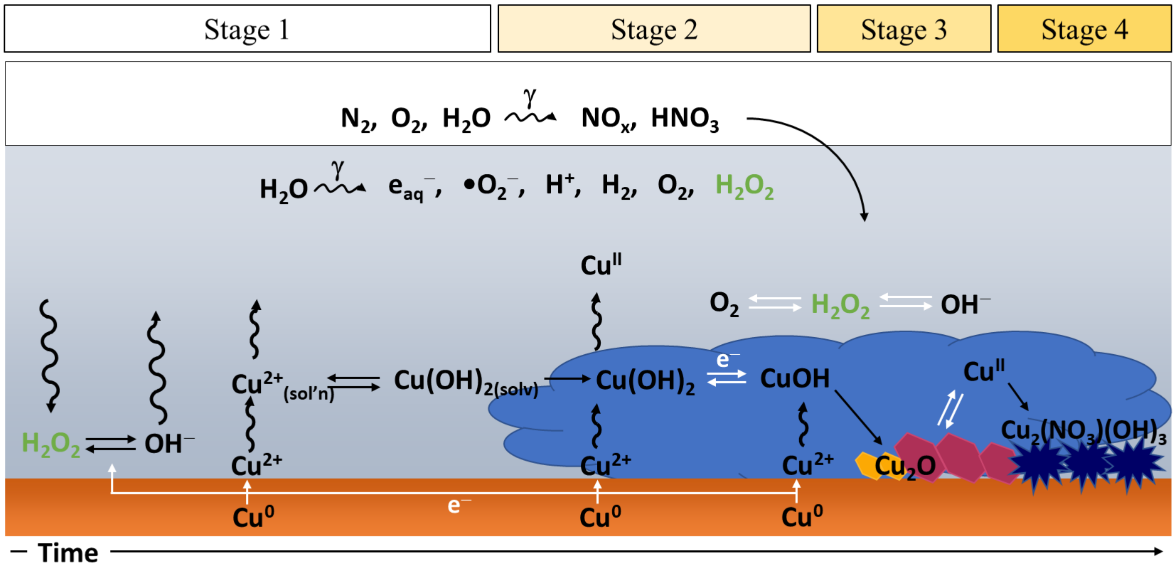

Figure 6.9 Copper corrosion mechanism in the presence of ionizing radiation, where the white arrows indicate an electron transfer process.

6.3.3.1 Corrosion Stage 1

The oxidation of $Cu^0_{(m)}$ to Cu^{2+} is coupled mainly with H_2O_2 reduction in irradiated solutions.[34,35] The reduction of H_2O_2 occurs through one 2-e elementary step (**Eq. 6.3b**), although the oxidation of H_2O_2 becomes increasingly important as cupric ions accumulate in solution (discussed in Stage 3). Other species, such as nitrate (NO_3^-) produced via humid air radiolysis, may also contribute to the overall oxidation of $Cu^0_{(m)}$ (**Eq. 6.26**), to a lesser extent.[4,6,36-39] However, the studies presented in **Chapter 5** indicated that the initial oxidant had less of an effect on the overall corrosion process than pH_0. Thus, the initial corrosion steps are the same regardless of the presence of radiation.

In Stage 1a, the charge transfer process produces Cu^{2+} and OH^- followed by the quick establishment of the hydrolysis equilibrium that results in the main form of $Cu^{2+}_{(sol'n)}$ being $Cu(OH)_3^-$. These processes are quick and can be considered to be a single elementary process.

$$Cu^0_{(m)} + H_2O_2 + H_2O \rightarrow Cu(OH)_3^- + H^+ \qquad (6.25)$$

Following their production, $Cu(OH)_3^-$ and H^+ diffuse from $z = 0$ to $z = \delta_{diff}$ (**Eq. 6.9**). $Cu^{2+}_{(sol'n)}$ and H^+ will remain in hydrolysis equilibrium as they diffuse along z.

As the pH_t increases, the hydrolysis equilibrium will shift more and more to the right (**Eq. 6.11**), forming $Cu(OH)_2$ and $Cu(OH)^+$. In the presence of a continuous flux of γ-radiation, HNO_3 produced by humid-air radiolysis dissolves into the droplet solution and is the main radiolytically-produced pH-affecting species. Hence, in addition to oxidant reduction and metal cation hydrolysis, humid-air-radiolysis-induced proton production in solution contributes to the change in pH_t. Because of systemic feedback between electrochemical redox reactions, cupric ion hydrolysis, and acid-base equilibria, the production of H^+ in the bulk solution and the relative contribution of each reaction in determining the pH_t changes with time. Initially, the rate of production of $Cu(OH)_3^-$ and H^+ via **Eq. 6.25** is faster than the rate of production and dissolution of HNO_3 into the droplet. In sum, the bulk pH_t decreases faster in the presence of radiation (due to this production and dissolution of HNO_3) than without radiation (and the pH_t remains at a low pH_t value, discussed later) and thus, the diffusing

$Cu(OH)_3^-$ experiences a lower pH_t that shifts the hydrolysis equilibrium earlier in irradiated solutions. That is, Stage 1b starts earlier in the presence of radiation.

The consumption of $Cu(OH)_3^-$ and H^+ to form $Cu(OH)_2$ and $Cu(OH)^+$ (**Eq. 6.11**) causes $[H^+]_t$ to decrease but the rate of input of $[H^+]_t$ via radiation is approximately equal to its rate of consumption through cupric ion hydrolysis reactions. This is shown by the first measured pH_t (t = 16 h) which was higher in the presence of radiation (6.0, shown in **Figure 6.7**) than in its absence (4.5 in Stage 1a, shown in **Figure 6.4**), and thus Stage 1a ended before 16 h.

Without radiation in Stage 1b, it was shown that the rate of change of $[Cu^{II}_{(sol'n)}]$ was not equal to the rate of change of $[H^+]$, but the cupric ion dissolution rate was constant with time. The same is true in the presence of radiation, however, $[H^+]_t$ increases throughout Stage 1b (pH_t decreases, **Figure 6.7**). The increase of $[H^+]_t$ in the presence, but not in the absence, of radiation indicates that the rate of production of $[H^+]_t$ via radiolytic decomposition is faster than the rate of consumption of $[H^+]_t$ via cupric ion hydrolysis or the production of $[OH^-]_t$ via oxidant reduction. The low and decreasing pH_t in the presence of radiation allowed more copper to dissolve during Stage 1b than without radiation. The $[Cu^{II}_{(sol'n)}]$ yield at the end of Stage 1b in the presence of radiation was 6.0 ± 2.8 mM, compared to 0.3 ± 0.2 mM in its absence. The effects of the higher $[Cu^{II}_{(sol'n)}]$ will be discussed in the next section. The metal oxidation rate in Stage 1 is equal to the cupric ion dissolution rate, as discussed in depth in **Chapter 4**, which was 0.18 ± 0.02 mM/h and the rate of metal loss was 11.6 ± 1.2 nmol $Cu/cm^2/h$.

Due to the homogeneous production of acidic radiolysis species, the bulk pH is lower than at $z = 0$ (the opposite is true without radiation). Thus, the cupric ion solubility limit is reached in the interfacial solution before the bulk solution, and $Cu(OH)_2$ colloid particles form first at $z = 0$ (as opposed to homogeneously in solution without radiation). The agglomeration of colloid particles into a hydrogel is accelerated in the presence of radiation due to the presence of reactive radiolysis products (e.g., $\bullet O_2^-$), which lower the zeta potential of the colloid particles (increasing their intermolecular attraction),[40-42] and due to the increase in rate of reduction to CuOH, discussed later.[43,44] The absence of these products when the solution is not exposed to radiation allows for the colloid particles to remain suspended in solution in a metastable manner throughout Stage 2.

6.3.3.2 Corrosion Stage 2

In Stage 2, the colloid particles begin to aggregate and grow as a hydrogel network. **Chapter 4** showed that the solution conditions (specifically, the pH_t evolution during Stage 1) can determine where the hydrogel growth occurs. Without radiation, the pH in the interfacial solution is low enough that the cupric ions remain in the dissolved state, but as they diffuse away from the surface, the pH increases, resulting in $Cu(OH)_2$ colloid precipitation in the bulk solution. In the presence of radiation, the decreasing bulk solution pH_t results in the colloidal precipitation in the interfacial solution, where the pH is higher. Furthermore, the aggregation of these colloid particles is quick in the presence of radiation, as discussed previously. The aggregation and growth of colloid particles in a hydrogel network marks the start of Stage 2.

As the hydrogel grows, it spreads laterally along the surface and conforms to its shape. As a result, the "grinding lines" are seen even after the underlying metal has become extensively corroded (although they are not the metallic grinding lines, but the $Cu(OH)_2$ hydrogel in the shape of the grinding lines, **Figure 6.8**). As the concentration of $Cu(OH)_{2(colloid)}$ in the solid network increases, the structure becomes more rigid.

Dried hydrogel was observed in localized areas of the surface during Stage 2, as shown in **Figure 6.10**. In **Figure 6.10a**, the hydrogel appears as blue patches on the surface, unobservable in SEM. The optical and SEM images are taken in the exact same location, with the centre of the feature visible in both cases, but the outside blue patches appear only in the optical images. Without radiation, the hydrogel was clear due to a high degree of hydration (low colloidal concentration) which diluted the blue colour associated with Cu^{2+} complexes. In the presence of radiation, the high concentration of dissolved copper means the colloid concentration is high and the blue colour is observable.

Figure 6.10b shows a location on the surface imaged with a secondary electron (SE) detector and an in-lens detector. The in-lens detector in an instrument is located in the column above the sample, which allows it to efficiently collect SEs emitted from the surface. Thus, the in-lens detector is more sensitive to surface features than the SE detector, which is located at an angle from the surface.[45,46] That the feature can be observed using the in-lens detector and not the SE detector indicates it is very thin (< 30 nm). This area shows no indication of a defined crystal structure, and hence, must be the growth of a thin layer of hydrogel. **Figure 6.10c** shows the solid $Cu(OH)_2$ network, indicating an advanced stage of hydrogel growth (high colloid density in the solid phase), located within a crevice in the metal surface (white circles).

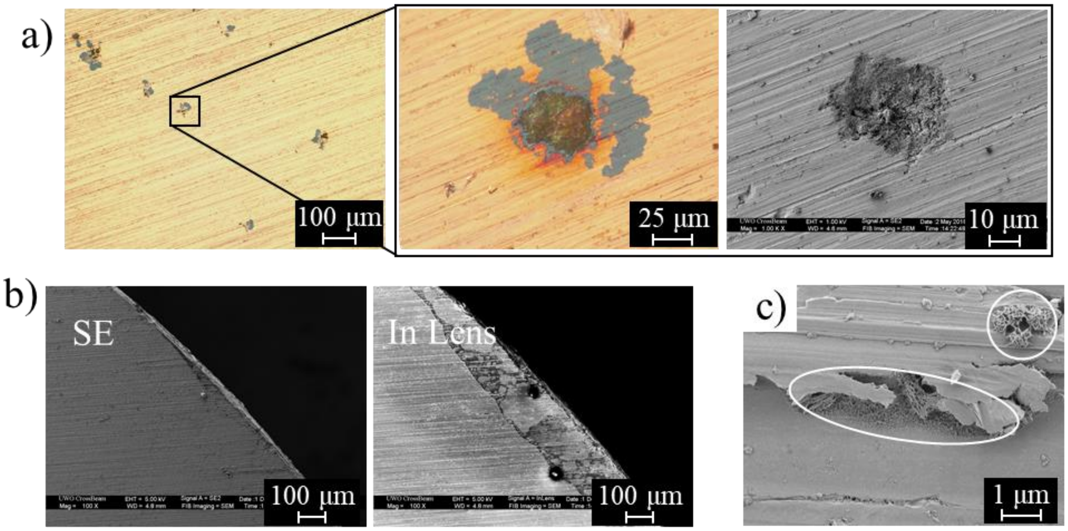

Figure 6.10 Images of dried $Cu(OH)_2$ hydrogel after corrosion in the presence of radiation. a) Optical and SEM images of the same location on the surface. b) SEM images of the same location taken with a secondary electron (SE) detector and an in-lens detector. c) SEM image of the solid $Cu(OH)_2$ framework under a metal crevice, indicated by the white circles.

The formation of a polymeric, amorphous, hydrated $Cu(OH)_2$ species in the presence of radiation has been reported.[11,17,24,44,47-49] It has also been shown to be a precursor to copper salts in contexts other than corrosion.[48,49] However, its impact on the copper corrosion mechanism has not been established in the presence of radiation. Our mechanism bridges the gap between knowledge of this species and how it impacts the corrosion progression of copper.

During Stage 2, both $[Cu^{II}_{(sol'n)}]_t$ and pH_t are constant with time (**Eq. 6.17**). The steady-state pH_t value was not controlled by the pKa of $Cu(OH)^+$, as it was in the absence of radiation, but influenced by the production of acidic radiolysis species and found to be 4.6 ± 0.4 (**Figure 6.7**). In large solutions, where the volume of solution that the solid hydrogel network occupies is only a small fraction of the whole solution, the steady-state pH value is determined almost exclusively by the production of acidic species via radiolysis (see discussion in **Chapter 8**). However, in these small droplet solutions, in which the solid hydrogel network occupies a significant proportion of the total volume, the solubility equilibrium (**Eq. 6.26**) results in a higher steady-state pH_t value than would be expected from the radiolytically-produced acidic species (the pH evolution in water droplets without a corroding system is shown in **Appendix A**). The $Cu(OH)_2$ solubility equilibrium is established quickly in the presence of radiation due to the accelerated growth of the hydrogel.

$$Cu^{2+}_{(sol'n)}\ (\equiv Cu^{2+} + Cu(OH)^{+} + Cu(OH)_{2(solv)}) \rightleftharpoons Cu(OH)_{2(solid)} \qquad (6.26)$$

The copper concentration in solution remained approximately constant with time. The steady-state $[Cu^{II}_{(sol'n)}]$ value was 6.0 ± 2.8 mM, which, due to the lowered pH_t, was much higher than in unirradiated solutions. Because the amount of $Cu(OH)_2$ precipitation is proportional to the concentration of cupric ions in solution, the hydrogel layer has a higher density of colloid particles in the presence of radiation.

As $Cu^{2+}_{(sol'n)}$ and colloid particles accumulate, H_2O_2 can be oxidized coupled with the reduction of cupric ion (**Eq. 6.27**). The rate of oxidation of H_2O_2 by $Cu^{2+}_{(sol'n)}$ can only compete with its rate of reduction by $Cu^0_{(m)}$ when the concentration of $Cu^{2+}_{(sol'n)}$ is high. Because H_2O_2 is produced via radiolytic decomposition, it is distributed homogeneously in solution, and thus, cupric ion reduction coupled with H_2O_2 oxidation can occur anywhere there is a high enough $[Cu^{2+}_{(sol'n)}]$. Initially, the accumulation of cupric ions is in the interfacial solution, and thus cuprous ion formation only occurs in the interfacial solution. However, the cuprous content can increase as this saturated volume (and hydrogel layer) expands into the bulk solution.

$$\text{Ox half-reaction:}\quad H_2O_2 + 2\,OH^- \rightarrow O_2 + 2\,H_2O + 2\,e^- \qquad (6.27a)$$

$$\underline{\text{Red half-reaction:}\quad 2\,Cu^{2+} + 2\,e^- \rightarrow 2\,Cu^+ \qquad (6.27b)}$$

Overall reaction: $2\ Cu^{2+} + H_2O_2 + 2\ OH^- \rightarrow 2\ Cu^+ + O_2 + 2\ H_2O$ (6.27c)

As $Cu^+_{(sol'n)}$ dissolves into the solution adjacent to the metal surface, it establishes fast hydrolysis equilibria in the mobile phase of the hydrogel (**Eq. 6.19**) and is incorporated into the hydrogel as a solid species (**Eq. 6.20**), forming a mixed Cu^I/Cu^{II} hydroxide hydrogel.

The presence of H_2O_2 in irradiated solutions accelerates the reduction of $Cu(OH)_2$ to CuOH. The cyclic feedback loop between the formation of $Cu(OH)_2$ hydrogel (**Eq. 6.18**) and its reduction to $Cu^+_{(sol'n)}$ (**Eq. 6.27**) is similarly accelerated. Thus, the formation of CuOH is quick, resulting in a shorter Stage 2 in the presence of radiation (48 h, shown in **Figure 6.7**) than in its absence (120 h, shown in **Figure 6.4**). In this stage in the presence of radiation, both the reduction of H_2O_2 to OH^- (coupled with $Cu^0_{(m)}$ oxidation to $Cu^{2+}_{(sol'n)}$) and the oxidation of H_2O_2 to O_2 (**Eq. 6.27b**) are occurring simultaneously.

The oxides observed on the edges of the copper surface in the first 96 h (with an average thickness of 175 ± 46.1 nm, shown in **Figure 6.9**) were a result of the slight variations in rate across the surface, as discussed previously. Due to the hemispherical shape of the droplet, at the edge of the droplet the solution depth is smaller and $Cu^{2+}_{(sol'n)}$ diffusion is hindered relative to at the centre. The edges of the solution will therefore reach saturation concentration before the center of the droplet does and thus, precipitation will begin at the edges first. Oxide formation initiates as a blue ($Cu(OH)_2$) internal semicircle with an outside ring of orange (Cu_2O), which will be discussed later. The edges of the droplet enter Stage 3 before the centre due to variations in solution chemistry (i.e., $[Cu^{II}_{(sol'n)}]$ compared to its solubility) across the surface, and not due to metallurgical differences. Thus, the whole surface is not necessarily at the exact same stage of corrosion, especially in small solution depths.[4] However, the general surface remains clean and the thin oxides that grow on the edges have a negligible effect on the averaged rate across the surface.

In unirradiated solutions, pH_t was low throughout Stage 1 before reaching the steady-state value of 8.4 in Stage 2. Accordingly, by the time Stage 2 was reached, the accumulated $[Cu^{II}_{(sol'n)}]_t$ was above its saturation limit at the pH_t reached in Stage 2, and

$Cu^{2+}_{(sol'n)}$ had begun to precipitate as $Cu(OH)_2$ colloid particles. The overall consequence is that $[Cu^{II}_{(sol'n)}]_t$ is higher than the solubility of $Cu(OH)_{2(solid)}$ at the pH_t reached.

In irradiated solutions, the bulk pH_t remained low (pH 4.6 ± 0.4) in Stage 2 due to the homogeneous radiolytic production of H^+. The lower pH in the interfacial and bulk solution in Stages 1 and 2 in the presence of radiation results in high concentrations of accumulated $Cu^{2+}_{(sol'n)}$ and $Cu(OH)_{2(solid)}$ colloids in the interfacial hydrogel layer. The presence of radiolytically-produced H_2O_2 at a low but steady-state concentration also accelerates the reduction of the Cu^{2+} species to Cu^+ species, which further accelerates the growth of hydrogel. The overall effect of radiation on corrosion dynamics in Stage 2 is to grow a thicker hydrogel layer with a higher density of colloid aggregates and over a shorter duration.

6.3.3.3 Corrosion Stage 3

Stage 3 begins after CuOH reaches a supersaturation concentration within the hydrogel and precipitates as more stable Cu_2O crystals (**Eq. 6.23**). The supersaturation concentration of CuOH that is achieved before precipitation as Cu_2O is dependent on the solution redox and chemical conditions. In the presence of radiation, the amount of copper that dissolves into solution in Stage 1 is much higher (**Figure 6.7**) than without radiation (**Figure 6.4**). Accordingly, in Stage 2, the steady-state concentration is much higher, the hydrogel can grow thicker, and the supersaturation concentration of CuOH at the start of Stage 3 is higher. As a result, the rate of Cu_2O precipitation is faster in the presence of radiation. Precipitation of crystals is stochastic, but preferential at high surface energy locations, such as grain boundaries and peaks of grinding lines,[4,50] and preferential oxide growth along grinding lines was observed (**Figure 6.8**).

In Stage 3, the net production and removal rates of the mixed hydroxide hydrogel are equal (i.e., the system is close to its steady state). At the start of the stage, the metal layer is covered with a layer of hydrogel and the full redox reaction (consisting of oxidation of $Cu^0_{(m)}$ to $Cu^{2+}_{(sol'n)}$ coupled with reduction of oxidant to OH^-) can now couple with the reduction of $Cu^{2+}_{(sol'n)}/Cu(OH)_2$ to Cu_2O (schematically represented in **Figure 6.9**). Thus, the concentration of Cu^{2+} species in the interfacial solution is important in determining the size of Cu_2O crystals and the rate of their production. In the presence of radiation, the decreasing pH_t during Stage 1 and the low steady-state pH_t in Stage 2 result in a high $[Cu^{II}_{(sol'n)}]$ during Stage 3 and Cu_2O crystals can grow large (**Figure 6.8**). Furthermore, H_2O_2 produced in the presence of radiation can accelerate both the metal oxidation and the reduction of Cu^{2+} to Cu_2O, thereby increasing the rate of Cu_2O growth. Once the surface is covered by Cu_2O, any further Cu_2O growth must occur via electron transfer through the semiconducting oxide film, which continues throughout Stage 3.

The surface during Stage 3 was purple and/or pink coloured, with large spatial variations in colour (**Figure 6.8**) indicating the coverage of $Cu(OH)_2$ was not uniform (see discussion on colour in **Section 6.3.1**). SEM images of the FIB milled cross-section between the oxide layer and metal is shown in the bottom row of **Figure 6.8**. The solid oxide layer can be assumed to be entirely Cu_2O, as the thin $Cu(OH)_2$ layer covering the oxide crystals is a negligible fraction of the thickness. The Cu_2O film was not porous and thus, the density can be used to determine the amount of copper in the oxide layer based on its thickness. The film thickness and the amount of copper in the oxide film were reported in **Table 6.2**.

Determining the rate of oxide precipitation is challenging, due to large variations in film thickness across the surface. Most of the film thickness variations are a result of uneven dissolution across the surface, making the pre-treatment grinding lines become even more pronounced, particularly after long corrosion times. These variations lead to a large standard error in the measured film thickness (**Table 6.2**). More substantial variations result from localized areas with a much thicker oxide film due to deeper penetration into the metal, which is discussed in **Section 6.3.4**. The depth of these localized attacks can be regarded as an upper bound for the oxide formation rate. While the average thickness is not strictly representative due to the effect of these localized deep attacks, it is helpful for establishing a lower bound for the oxidation rate. The film thicknesses as a function of corrosion time were used to determine the average rate of Cu_2O precipitation in Stage 3, calculated to be 62 ± 28 nmol $Cu/cm^2/h$.

Table 6.2 Amount of copper in solution (from **Figure 6.7**) compared to that in the oxide layer (from cross-sections in **Figure 6.8**) in all corrosion stages during radiolytic corrosion in droplet solutions scrubbed of CO_2.

Stage	Corrosion time (h)	n_{Cu} in solution (µmol)	n_{Cu} in oxide (µmol)
1	24	0.11 ± 0.05	0.22 ± 0.06 (edge of coupon)
2	72	0.24 ± 0.03	0.13 ± 0.10 (edge of coupon)
3	96	0.42 ± 0.17	3.66 ± 0.76
	144	1.08 ± 0.68	5.64 ± 2.74
	192	0.90 ± 0.24	8.19 ± 3.74
4	480	0.45 ± 0.08	14.7 ± 3.21

During Stage 3, pH_t remains at its low steady-state value of 4.6. However, variations about the average value ranged from 3.9 – 5.2, which is equal to a cupric ion solubility range of approximately three orders of magnitude. When the pH is low, the solution is slightly undersaturated allowing cupric ion dissolution. When the pH is high, the solution is saturated with cupric ions and dissolution stopped. Continuous pH fluctuations around the average value, result in an overall increase in $[Cu^{II}_{(sol'n)}]$ with time but with large variations in the measured $[Cu^{II}_{(sol'n)}]$ at specific time points. The average dissolution rate throughout Stage 3 was 0.11 ± 0.02 mM/h or a metal loss rate of 6.8 ± 1.3 $nmol/cm^2/h$ (negligible compared to the oxide growth rate).

Once formed on the surface, Cu_2O crystals undergo redox-assisted Ostwald ripening. Ostwald ripening is a thermodynamically driven process in which ionic salt crystals dissolve and reprecipitate depending on their size, to lower the overall surface energy in a system. The salt ions in the interfacial region at the crystal surface are in adsorption/desorption quasi-equilibrium with the dissolved salt ions. Small crystals will have net desorption and larger crystals will have a net adsorption of their constituents on the surface, as described in depth in **Section 2.4.1**.[51]

With Cu_2O crystals, the solubility of Cu^+ is low and oxidation followed by dissolution as Cu^{2+} is favoured over Cu^+ dissolution.[52] Thus, the Ostwald ripening of Cu_2O crystals is assisted by redox reactions between the copper species. Cu_2O first oxidizes to $Cu^{2+}_{(sol'n)}$ (**Eq. 6.29a**) then dissolves into and diffuses through the solution. The net reduction and reprecipitation of Cu_2O constituents will occur on a different, larger crystal of lower average free energy (indicated by a * in **Eq. 6.29b**). In the presence of radiation, the redox reactions between copper species easily couple with H_2O_2 redox reactions.

$$Cu_2O + H_2O_2 + H_2O \rightarrow 2\ Cu^{2+}_{(sol'n)} + 4\ OH^- \tag{6.29a}$$

$$2\ Cu^{2+}_{(sol'n)} + H_2O_2 \rightarrow Cu_2O^* + O_2 + 3\ H_2O \tag{6.29b}$$

In closed systems, Ostwald ripening leads to the growth of large crystals at the expense of small crystals.[53] During corrosion, however, small Cu_2O crystals will continue to form due to continuous metal oxidation injecting $Cu^{2+}_{(sol'n)}$ into the solution. Instead of the average size of crystals increasing with time, the older crystals will ripen while small crystals continue to precipitate (then ripen), which results in a bimodal crystal size distribution.

This bimodal distribution of Cu_2O particle size was observed during Stage 3 (**Figures 6.7** and **6.8**). Early in Stage 3, the average particle size is small (< 200 nm), then with increasing time the average size increases to 500 – 800 nm. Later in Stage 3, crystals are either < 100 nm or ~ 300 nm (bimodal distribution) and, as the ripening process continues, the distribution widens such that the particle sizes are either ~ 300 nm or ~ 1 μm. The redox-assisted Ostwald ripening of Cu_2O does not affect the corrosion rate of Stage 3, nor the overall amount of copper that dissolves into solution. However, the continuous dissolution as $Cu^{2+}_{(sol'n)}$ (resulting in a blue and purple-coloured surface) and reprecipitation of Cu_2O (resulting in a yellow and pink-coloured surface) causes large spatial variations in the colour of the oxide film.

6.3.3.4 Liesegang Band Formation during Stage 3

If there is a directional preference for the diffusion of solution species while particles undergo Ostwald ripening, the crystals may form in Liesegang band patterns.[51] Liesegang band patterns can only form if the diffusion rate and precipitation rate are comparable, and thus, they form when diffusion is through a slow transport medium, such as porous rocks or gel layers.[54-57] During copper corrosion, the diffusion of $Cu^{2+}_{(sol'n)}$ during Cu_2O Ostwald ripening is slow through the $Cu(OH)_2$ hydrogel layer that covers the surface, which results in Liesegang band patterns appearing in the oxide layer (**Figure 6.11**).

The Liesegang bands observed during copper corrosion are circular or semicircular (**Figure 6.11**), and do not correspond to the underlying grain structure. Instead, this shape is a result of the diffusion of $Cu^{2+}_{(sol'n)}$ through the mobile phase of the hydrogel, which occurs equally in all directions from the initiation point. If the initiation point is at the edge of the coupon, from where $Cu^{2+}_{(sol'n)}$ can only diffuse towards the centre of the coupon, the resulting shape is semicircular. Each Liesegang band that grow throughout corrosion contains bands of Cu_2O (pink-coloured band), bands of $Cu(OH)_2$ (blue-coloured band), and bands containing a combination of Cu_2O and $Cu(OH)_2$ (purple-coloured band), as illustrated in **Figure 6.11** (see solid corrosion product colour analysis in **Section 6.3.1**).

After a Cu_2O crystal dissolves as $Cu^{2+}_{(sol'n)}$ and OH^- (**Eq. 6.29a**), the solution species diffuse through the $Cu(OH)_2$ hydrogel layer. The diffusion of $Cu^{2+}_{(sol'n)}$ is slow due to its continuous adsorption and desorption on $Cu(OH)_{2(solid)}$. This slows the rate of $Cu^{2+}_{(sol'n)}$ diffusion through the interfacial solution and allows the coupling of diffusion and precipitation to occur. When a Cu_2O crystal precipitates from the hydrogel network, it leaves an area deficient of the constituent ions, creating a concentration gradient for cupric ions within the hydrogel. Additionally, the entire solution is saturated with cupric ions and thus diffusing cupric ions remain in the interfacial solution and diffuse laterally across the surface. This directional diffusion for $Cu^{2+}_{(sol'n)}$ and the similar diffusion and precipitation rates results in $Cu(OH)_2$ and Cu_2O precipitating in Liesegang bands. With increasing corrosion time, bands will become more defined as large Cu_2O crystals absorb $Cu^{+}_{(sol'n)}$ within a certain volume around them, thickening each band (shown in **Figure 6.11**).[58]

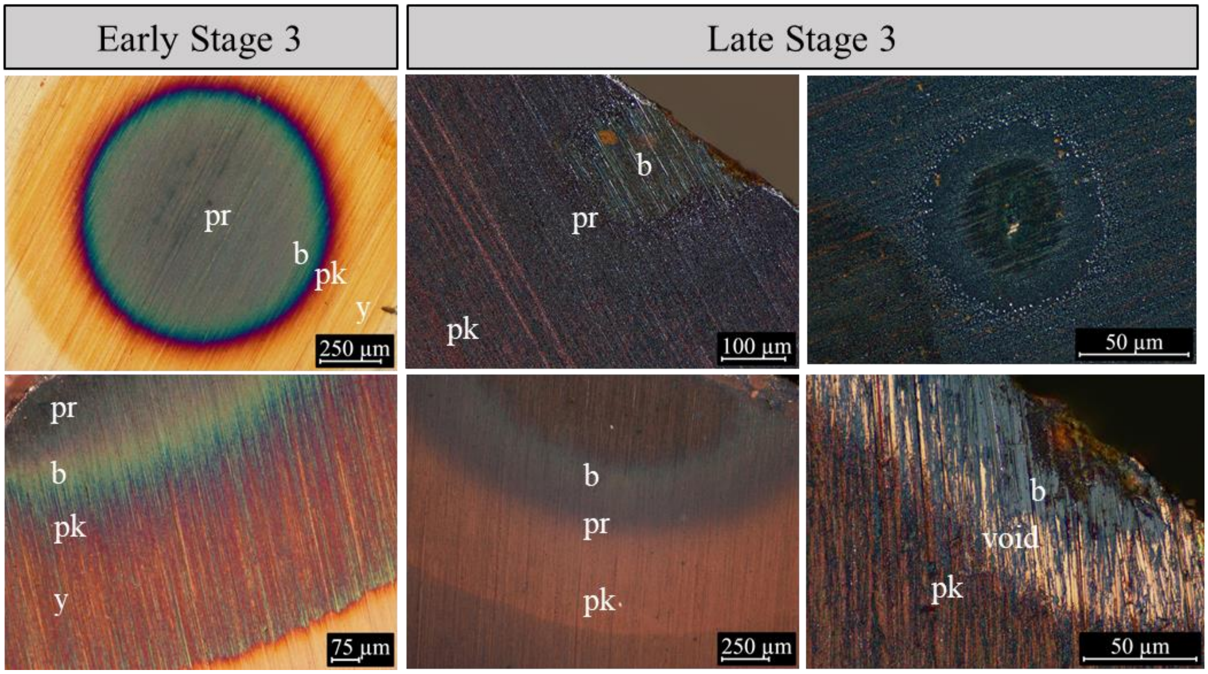

Figure 6.11 Liesegang band patterns formed in early (left) and late (right) Stage 3 of copper corrosion. The colours of the bands are labelled with ‘pr’ for purple, ‘b’ for blue, ‘pk’ for pink, and ‘y’ for yellow.

With increasing corrosion time, Cu_2O crystals cover the entire surface, and the hydrogel layer grows thicker. As the hydrogel volume expands into the bulk solution, Liesegang rings are observed perpendicular to the surface, as well as across the surface. The cross-section of an area traversing the boundary between the blue and purple films in late Stage 3 (middle images in **Figure 6.11**) is shown in **Figure 6.12**. The blue film is a 6.1 µm thick layer of compact oxide crystals (crystals shown by the white circle) covered by a thick layer of hydrogel (invisible in SEM, as shown earlier). The surface of the crystals in this area are smooth due to their extensive dissolution and their coverage by the hydrogel. On the right side of the image, the film that looks purple from the surface is a thin layer of small Cu_2O crystals. Under this layer is void space (where $Cu(OH)_2$ hydrogel existed before drying), then the compact Cu_2O oxide film. These alternating bands of precipitate and void space (Cu_2O-void space-Cu_2O) reflect a typical Liesegang band structure.

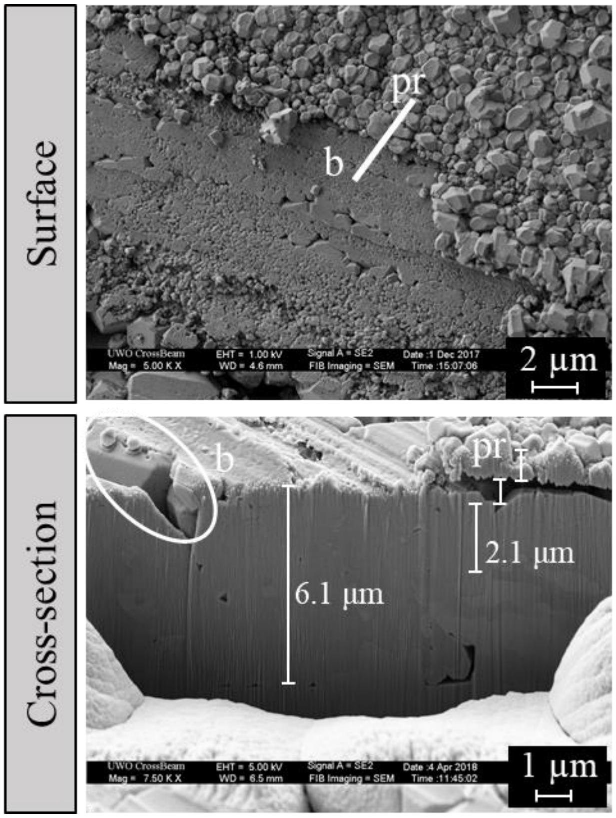

Figure 6.12 SEM images of the surface (top row) and the cross-section of the metal-oxide interface (bottom row) of the blue (labelled with ‘b’) and purple (labelled with ‘pr’) oxide films.

Neither Ostwald ripening of Cu_2O crystals nor the Liesegang band formation affects the rate of <u>Stage 3</u>. However, they create phenomenon in the oxide layer that has been observed during copper corrosion in this and other studies.[4,57,59,60] They also provide further evidence for the existence of non-linear dynamics and feedback processes in this system.

6.3.3.5 Corrosion Stage 4

As Cu_2O crystals grow in number and size, mass and charge transport through the oxide layer are suppressed. No metal oxidation takes place during <u>Stage 4</u> and thus, neither $Cu^{2+}_{(sol'n)}$ nor OH^- are produced at the surface. However, the solution will continue to evolve until an equilibrium is reached. As Cu_2O particles undergo redox-assisted Ostwald ripening, the reprecipitation of copper can include solution anions to balance charge due to a lack of OH^-

production at the surface (**Eq. 6.29 – 6.30**). Consequently, the Cu_2O crystal size decreases as they dissolve and convert to the more thermodynamically stable cuprous-hydroxide-anion crystals. In CO_2-free solutions, complexing anions only exist in the presence of radiation, where humid air radiolysis leads to the production of NO_3^-.

After 480 h, the surface was covered with a thick layer of blue hydrogel (the colour of both $Cu(OH)_2$ and gerhardtite, $Cu_2(NO_3)(OH)_3$) (**Figure 6.8**).[61,62] The Raman spectra of the surfaces during Stage 3 and Stage 4 are presented in **Figure 6.13**. In Stage 3 (pink in **Figure 6.13**), the 523 and 623 cm^{-1} peaks with equal intensities indicate a combination of Cu_2O and $Cu(OH)_2$, as expected based on the colour of the surface. In Stage 4 (blue in **Figure 6.13**), the 623 cm^{-1} peak was much more intense than the 523 cm^{-1} peak, indicating the surface was mostly Cu_2O. However, the emergence of peaks at 530 cm^{-1} and 1070 cm^{-1} (indicated by the blue arrows in **Figure 6.13**), suggest the presence of a nitrate species. These nitrate peaks are blue shifted from the literature values[63,64] and are weak and broad, which are all attributes of an amorphous species. Furthermore, the spectrum at large wavenumbers (not shown) had two very broad peaks centered at approximately 2500 cm^{-1} and 3300 cm^{-1}, indicative of OH^- stretching from the hydroxide hydrogel.

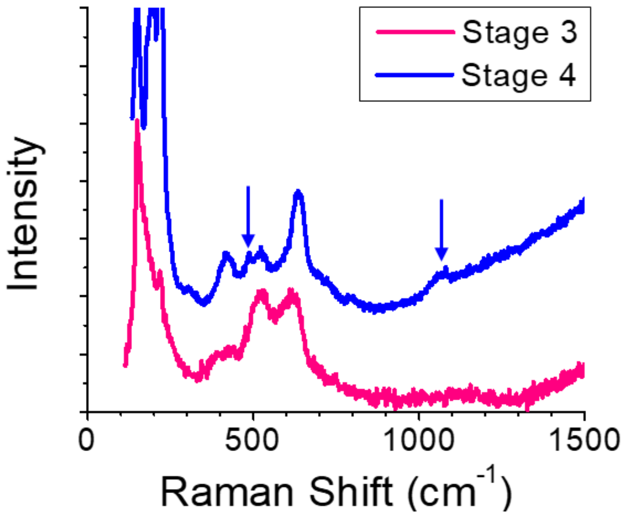

Figure 6.13 Raman spectra of the solid particles on the copper surface formed during Stage 2 (red) and Stage 3 (blue) of corrosion in the presence of radiation. The blue arrows point to Raman peaks that indicate adsorbed nitrate in the blue spectrum.

Despite the presence of nitrate in the Raman spectrum, the crystals observed in the SEM images in **Figure 6.8** after 480 h were not the characteristic shape for cupric-hydroxide-nitrate crystals (hexagonal thin plates). However, the optical and SEM images both show a substantial amount of hydrogel on the surface (**Figures 6.7** and **6.8**). From the Raman spectrum indicating adsorbed NO_3^- on the surface, the blue colour in the optical images (**Figure 6.8**), and a lack of cupric-hydroxide-nitrate crystals in the SEM images (**Figure 6.13**), it can be concluded that nitrate was incorporated into the hydrogel network (**Eq. 6.30**). This incorporation occurs as Cu_2O undergoes Ostwald ripening, as nitrate co-precipitates with $Cu^{2+}_{(sol'n)}$.

The formation of crystals from a gel and the co-precipitation of copper and nitrate are commonly reported.[48,49,62,65] Thus, it is proposed that with increasing corrosion time, cupric-hydroxide-nitrate crystals (likely gerhardtite, $Cu_2(NO_3)(OH)_3$) precipitate from the nitrate-containing $Cu(OH)_2$ hydrogel (**Eq. 6.30**, where the nitrate containing hydrogel is expressed as $Cu_2(NO_3)(OH)_{3(hydrogel)}$ for simplicity).

$$2\ Cu^{2+}_{(sol'n)} + 3\ OH^- + NO_3^- \rightarrow Cu_2(NO_3)(OH)_{3(hydrogel)} \rightarrow Cu_2(NO_3)(OH)_{3(crys)} \quad (6.30)$$

$Cu^{2+}_{(sol'n)}$ is consumed at the surface as it precipitates as Cu_2O (and later cupric-hydroxide-nitrate crystals) but is not produced via metal oxidation in Stage 4. This creates a cupric ion concentration gradient and $Cu^{2+}_{(sol'n)}$ in the bulk solution diffuses towards the surface, where it is subsequently consumed via precipitation. Thus, $[Cu^{II}_{(sol'n)}]$ decreased with time after 480 h to 8.9 ± 1.6 mM. The Cu_2O crystals that remained on the surface were present at a thickness of 2.2 ± 0.5 μm, corresponding to 14.7 ± 3.2 μmol of Cu in the oxide film. The rate of oxide precipitation had also slowed from Stage 3 to Stage 4 (**Figure 6.14**) due to Cu_2O dissolution and nitrate-containing hydrogel growth. These observations are a result of a metal oxidation rate that is below detection limit, and approaching zero.

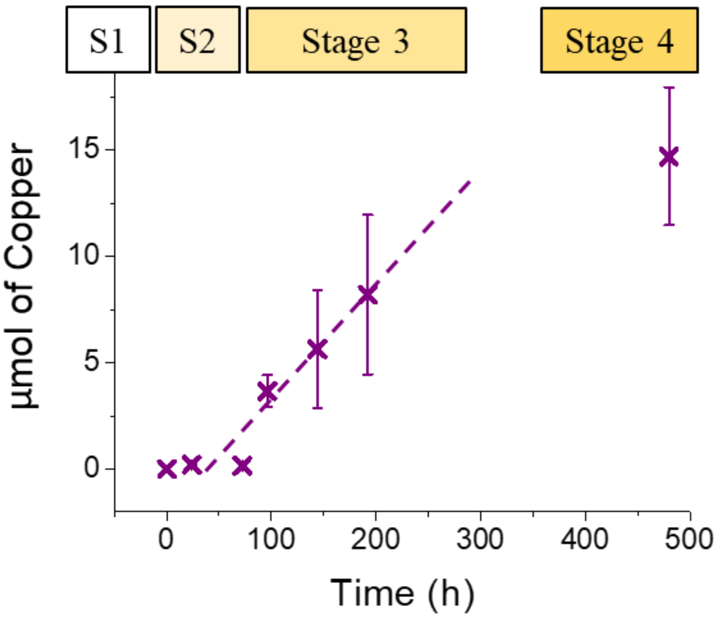

Figure 6.14 Amount of copper in Cu_2O as a function of corrosion time in CO_2-free solutions.

6.3.4 Surface Variations

The general corrosion mechanism describes the corrosion processes based on bulk properties (i.e., pH_t, $[Cu^{II}_{(sol'n)}]_t$, and solid oxide growth across the surface). As discussed earlier, different areas of the same coupon may progress through the same stages at slightly different rates, due to variations in surface energy and solution conditions adjacent to the surface. These variations in time progression and spatial distribution increase as corrosion progresses and more elementary steps are added. This can vary the observed corrosion product concentration or amount, especially after long corrosion times. An example of this variation was observed during Stages 1 and 2 when the droplet edges reached saturation before the center of the droplet, leading to oxide growth on the edge of the coupon. At longer corrosion times, holes filled with solid corrosion products were observed to have grown deeper than the average oxide depth. Thus, the average oxide thickness is helpful to establish a lower bound on the oxidation rate, while the depth of these localized attacks, analyzed in depth in this section, can be regarded as an upper bound on the oxide formation rate.

Investigations of the cross-sections presented in **Figure 6.8** revealed a porous metal layer just below the surface that is present at all corrosion times. Shear stress during the preexperimental grinding step is known to create cracks in the metal as a result of the heating and rearrangement of the metal grain under the wear surface.[66] This grain rearrangement within the metal decreases the surface grain size from 100 μm in the bulk to 100 nm at the surface (which can be seen in the SEM images, where different shades of grey indicate different grain faces). Thus, even before the metal corrodes, small cracks and voids exist ~ 2 μm under the metal surface (and can be seen in the as-prepared sample in **Figure 6.15**). In previous studies that used solutions with $pH_0 \leq 2.0$, the porous metal layer was observed at early corrosion times but disappeared at later times due to its active dissolution in Stage 1.[4] In this study, the porous metal layer was observed at all corrosion times (**Figure 6.8**) because the active dissolution stage was short and precipitation of $Cu(OH)_2$ hydrogel started quickly, which stopped the porous metal layer from dissolving completely.

The cracks formed during pre-treatment allow for the formation of deep holes during corrosion. The mechanism of formation of these holes is not different than the general mechanism proposed above, where metal oxidation and dissolution is a result of contact with a Cu^{2+}-unsaturated solution. The atoms on the surface of the metal oxidize and dissolve into solution, exposing metal atoms that are deeper within the bulk metal. If the metal was free of voids and preferential dissolution areas, such as a perfect single crystal, the metal loss would occur atomically layer-by-layer with no large variation across the surface (on a macroscopic timescale). However, preferential dissolution at grain boundaries and on certain grain faces can cause certain areas to dissolve faster than others and the solution can propagate deep in that area.[67,68] Furthermore, the voids formed deep under the surface layer during pre-treatment can be exposed to the solution, which allows for even deeper solution propagation, i.e., deep metal dissolution, in that area. That is, metal exposed to solution will continue to dissolve, which can lead to deep holes. Once the penetrating solution becomes saturated with $Cu^{2+}_{(sol'n)}$, $Cu(OH)_2$ and Cu_2O precipitate (according to the corrosion mechanism). All holes imaged were filled with solid corrosion products (**Figure 6.15**). Holes formed in this way can be seen in the top row in **Figure 6.15**, where their depth is 2 – 40 times deeper than the average oxide thickness at the same corrosion time.

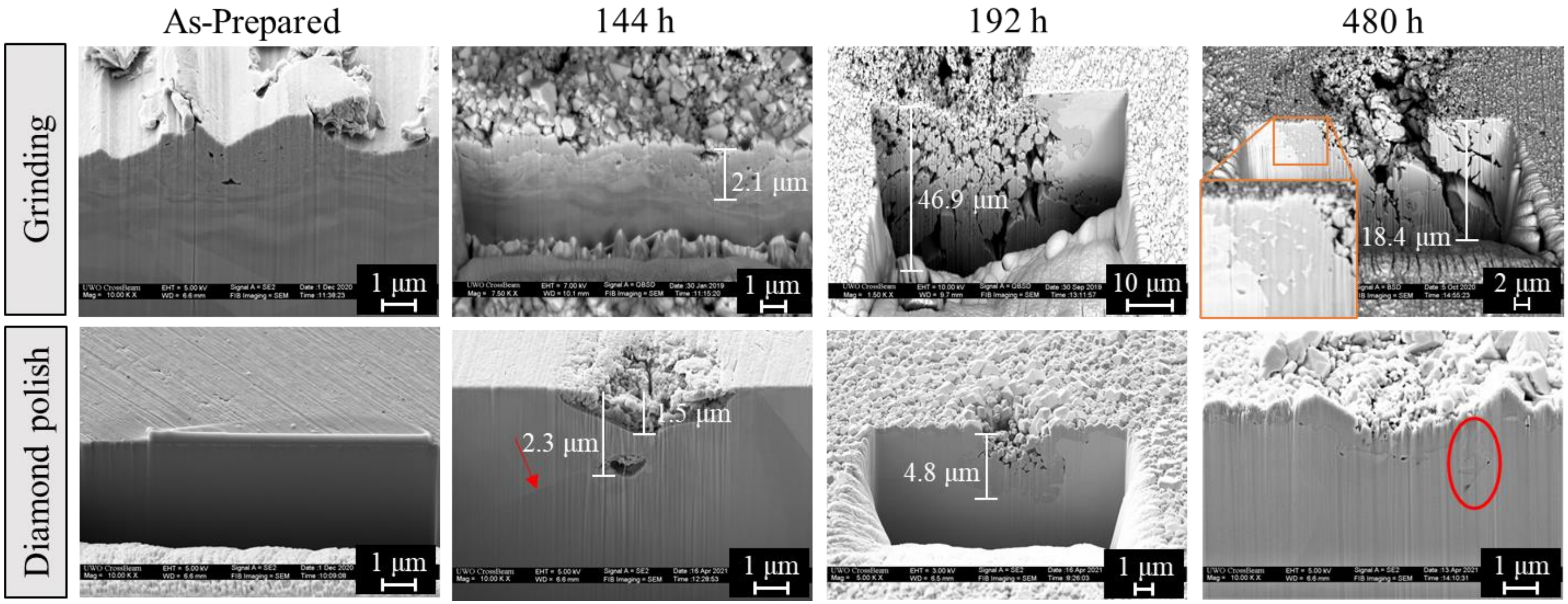

Figure 6.15 Focused Ga-ion beam cross-sections of copper before and during corrosion with pre-treatment grinding (top row) and diamond polish (bottom row). The red arrow shows a grain boundary, and the red circle shows oxide growth within grain

Pitting corrosion is the conventional explanation for these types of features, but it is not a plausible explanation in the studied conditions, as a passivating film is not initially formed and the types of aggressive ions required for pitting attacks (e.g. chloride, bicarbonate) are not present.[69-71] It is well known that different $Cu^0_{(m)}$ grains have different electrochemical properties, and thus, when exposed to unsaturated solution, some grains will dissolve fast while others remain intact.[67,72] This preferential grain dissolution is illustrated in the inset (in orange box) in **Figure 6.15** after 480 h corrosion time, where $Cu^0_{(m)}$ (white areas) is fully surrounded by oxide (dark areas).

Using diamond polishing opposed to grinding as a pre-treatment does not lead to cracks within the metal (bottom row in **Figure 6.15**) due to less friction on the metal surface.[66] Some holes were observed during corrosion after diamond polishing, however they are not as deep, which supports the theory that the pre-treatment cracks propagate as large holes. However, there are still areas on the metal surface which preferentially dissolve leading to deep localized damage. Preferential grain dissolution was observed after 144 h corrosion time, where a hole formed on the surface to a depth of 1.5 μm into the metal with a second hole 2.3 μm beneath the metal surface. The deeper hole is at the apex of a grain, the grain boundary of which is highlighted by the red arrow in **Figure 6.15**. The deeper hole does not appear to be connected to the surface hole, but they are likely connected by a water channel elsewhere. The undissolved metal in between the two holes is likely a lower energy grain and thus is less dissolved by the solution. Both holes had corrosion product growth (the deeper one less so) that is amorphous, hypothesized to be $Cu(OH)_2$ hydrogel or very small Cu_2O particles.

Another high energy area is between grains, where the metal oxidation rate may be slightly faster than the average rate, allowing solution to propagate in a localized area.[73,74] This intergranular corrosion was imaged after 480 h corrosion time following diamond polishing pre-treatment (red circle in **Figure 6.15**). Propagation in this area was 2.5 μm into the metal while the average oxide depth was < 1.0 μm. This damage would be exacerbated if there were cracks and voids that already existed within the metal due to pre-treatment grinding or if the surface grains were smaller. However, it is not being suggested here that diamond polishing or any other pre-treatment for the metal surface will decrease the depth of metal dissolution. The metal dissolution is solely a result of the solution saturation properties. The holes formed after grinding are similar to those formed after diamond polishing, which confirms the understanding outlined above of their formation.

Holes penetrating deep into copper (and other metals) are of particular concern for the application of nuclear waste disposal. The hole growth is consistent with our corrosion mechanism, which means their propagation can be included in a corrosion model, allowing the process to be predicted confidently and the hole depth can be included when refining the maximum copper corrosion allowance of the UFC. The depth of metal loss at these localized sites provides an upper bound for the metal loss and oxide formation rate, as previously discussed. However, the metal loss does not continue linearly, but will stop in Stage 4, as described in the mechanism.

6.4 CONCLUSION

In this chapter, the corrosion mechanism of copper in small water droplets (scrubbed of CO_2) was investigated. To elucidate the effects of the presence of γ-radiation, experiments were performed in the presence and absence of radiation. The time-dependent behaviour of pH_t, $[Cu^{II}_{(sol'n)}]$, and the surface oxides allowed for the identification of the stages of corrosion behaviour and how they are influenced by γ-radiation.

Stage 1 involves metal oxidation coupled with solution oxidant reduction, forming soluble cupric ions at the metal-solution interface. In small droplet solutions with a near neutral pH_0, Stage 1 proceeds in two steps, initially with the formation of $Cu(OH)_3^-$ (Stage 1a) which, after diffusing to the bulk solution, produces $Cu(OH)_2$ colloid particles (Stage 1b). In the absence of radiation, the pH is controlled by the cupric ion hydrolysis equilibrium, and thus initially decreases, then increases with time. $[Cu^{II}_{(sol'n)}]$ increased linearly with time throughout both steps of Stage 1, reaching a low yield at the end of the stage due to the low cupric ion solubility.

In the presence of radiation, Stage 1a is short due to the production of acidic radiolysis products that decrease the pH very quickly and cause Stage 1b to start before the first measurement. The radiolytic production of acidic species caused the pH to decrease throughout Stage 1, and $[Cu^{II}_{(sol'n)}]$ increased to a higher concentration than in the absence of radiation. The corrosion rate in Stage 1 in CO_2-free irradiated solutions was 11.6 ± 1.2 nmol $Cu/cm^2/h$.

During Stage 2, the $Cu(OH)_2$ colloid particles formed in Stage 1b aggregated and grew as a hydrogel network, while pH_t and $[Cu^{II}_{(sol'n)}]_t$ remained constant regardless of the presence of radiation. Radiation in this stage affects the values at which pH_t and $[Cu^{II}_{(sol'n)}]_t$ plateau and the colloid density in the hydrogel network. Without radiation, the pH_t was buffered at the pKa value for $Cu(OH)^+$ (8.4 ± 0.1), and $[Cu^{II}_{(sol'n)}]_t$ remained low, at 0.3 ± 0.2 mM. This low concentration of dissolved copper resulted in a highly hydrated hydrogel network (low colloid density). The hydrogel network slowed the transport of $Cu^{2+}_{(sol'n)}$ away from the surface, allowing redox coupling between the metal surface and the cupric ions to occur, resulting in the incorporation of cuprous species into the hydrogel.

In the presence of radiation, the steady-state pH value was 4.6 ± 0.4, and the higher pH_t allowed more copper to dissolve. The $[Cu^{II}_{(sol'n)}]_t$ plateau was 6.0 ± 2.8 mM, and this higher concentration of cupric ions in solution allowed for the growth of a hydrogel with a higher concentration of colloid particles (as seen in the optical and SEM images). Furthermore, the reduction of $Cu^{2+}_{(sol'n)}$ to form a mixed Cu^I/Cu^{II} hydroxide hydrogel was accelerated due to redox coupling with H_2O_2, which was continuously produced via water radiolysis. Both the higher concentration of colloid particles in the hydrogel and the accelerated reduction of $Cu(OH)_2$ to CuOH resulted in a shortened Stage 2 in the presence of radiation.

Stage 3 involves the precipitation of Cu_2O from the mixed Cu^I/Cu^{II} hydroxide hydrogel. Without radiation, this stage was observed after 480 h when the surface had turned a deep yellow, indicating uniform growth of small Cu_2O particles. However, the amount of Cu_2O formed on the surface was too low to be meaningfully quantified. $[Cu^{II}_{(sol'n)}]_t$ continued to fluctuate around the value established in Stage 2, but the pH_t had decreased to satisfy the $Cu(OH)_2$ solubility equilibrium.

In Stage 3 in the presence of radiation, the pH_t continued to fluctuate around the low steady-state value. The effect of these large fluctuations with time is the overall dissolution of

$[Cu^{II}_{(sol'n)}]$ at a rate of 6.8 ± 1.3 nmol Cu/cm^2/h. However, the main corrosion product in this stage was Cu_2O, which grew at an average rate of 62 ± 28 nmol Cu/cm^2/h, although large surface variations resulted in significant corrosion depth differences across the surface. Very deep holes (up to 50 μm) were observed during corrosion because unsaturated solution can penetrate deeply into the metal at locations of faster dissolution (e.g., grain boundaries). The metal pre-treatment method selected can exacerbate the formation of deep holes with the formation of cracks and void under the metal surface before the onset of corrosion. The formation of holes and their propagation is consistent with the proposed corrosion mechanism and their depth can provide an upper bound on the metal loss.

The large concentration of cupric ions that can dissolve in Stages 1 and 2 in the presence of radiation result in the formation of large Cu_2O crystals that cover the entire metal surface during Stage 3. The Cu_2O crystal size had a bimodal distribution in the later times of Stage 3, after undergoing redox-assisted Ostwald ripening. The thick hydrogel covering the surface slowed $Cu^{2+}_{(sol'n)}$ diffusion, allowing the diffusion and precipitation processes to couple. As a result, Liesegang bands in the oxide layer were observed on the surface during this stage. However, Ostwald ripening of Cu_2O crystals and Liesegang band formation did not affect the overall corrosion rate in this stage.

Stage 4 was only observed in the presence of radiation. Metal oxidation ceases due to a thick oxide film that hinders the transfer of charge. This stage was observed after 480 h, when $[Cu^{II}_{(sol'n)}]_t$ had decreased, and the oxide growth had slowed. However, Ostwald ripening of Cu_2O crystals continued, and solution anions participated in the reprecipitation of cupric ions. Raman analysis indicated that nitrate was incorporated into the hydrogel network and, after longer corrosion times, it is hypothesized that Cu^{II}-OH-NO_3 crystals will precipitate from the hydrogel.

Although the process of developing a quantitative corrosion rate model is still underway, the results in this chapter provide important insights into how the presence of a continuous flux of γ-radiation affects the rates of the elementary steps that are important during corrosion. It shows that the same rate determining elementary steps can consistently explain the time-dependent behaviours of measured dissolved copper concentration ($[Cu^{II}_{(sol'n)}]_t$) and

pH_t in the presence and absence of radiation, indicative of the same RDS in both conditions. These results will be critical for the development of a robust dynamic copper corrosion model that can be used to accurately determine the copper corrosion allowance of the UFC in the presence of radiation.

6.5 REFERENCES

1 Wang, L., Daub, K., Qin, Z., Wren, J. C. Effect of Dissolved Ferrous Iron on Oxide Film Formation on Carbon Steel. *Electrochim. Acta* **76**, 208-217, (2012).

2 Wu, L., Guo, D., Li, M., Joseph, J. M., Noël, J. J., Keech, P. G., Wren, J. C. Inverse Crevice Corrosion of Carbon Steel: Effect of Solution Volume to Surface Area. *J. Electrochem. Soc.* **164**, C539-C553, (2017).

3 Shin, Y. G. "Nonlinear Dynamics of Carbon Steel Corrosion under Gamma Radiation" Doctor of Philosophy, The University of Western Ontario, Electronic Thesis and Dissertation Repository. (2020). 7339.

4 Naghizadeh, M. "Copper Corrosion Dynamics under Deep Geologic Repository Conditions" Doctor of Philosophy, The University of Western Ontario, Electronic Thesis and Dissertation Repository. (2021). 7894.

5 Wren, J. C., Jean, A., Naghizadeh, M., Grandy, L., Morco, R., Joseph, J. M., Behazin, M., Keech, P. G. Radiation Induced Corrosion of Copper in Deep Geological Repositories in *WM2019: 45 Annual Waste Management Conference.* 1-15 (Office of Scientific and Technical Information).

6 Turnbull, J., Szukalo, R., Behazin, M., Hall, D., Zagidulin, D., Ramamurthy, S., Wren, J. C., Shoesmith, D. W. The Effects of Cathodic Reagent Concentration and Small Solution Volumes on the Corrosion of Copper in Dilute Nitric Acid Solutions. *Corrosion* **74**, 326-336, (2017).

7 Krätschmer, A., Odnevall Wallinder, I., Leygraf, C. The Evolution of Outdoor Copper Patina. *Corros. Sci.* **44**, 425-450, (2002).

8 Deng, Y., Handoko, A. D., Du, Y., Xi, S., Yeo, B. S. *In Situ* Raman Spectroscopy of Copper and Copper Oxide Surfaces during Electrochemical Oxygen Evolution

Reaction: Identification of Cu^{III} Oxides as Catalytically Active Species. *ACS Catal.* **6**, 2473-2481, (2016).

9 Rogers, A. F. A Review of the Amorphous Minerals. *J. Geol.* **25**, 515-541, (1917).

10 Soroka, I. L., Shchukarev, A., Jonsson, M., Tarakina, N. V., Korzhavyi, P. A. Cuprous Hydroxide in a Solid Form: Does It Exist? *Dalton Trans.* **42**, 9585-9594, (2013).

11 Khatouri, J., Mostafavi, M., Amblard, J., Belloni, J. Radiation-Induced Copper Aggregates and Oligomers. *Chem. Phys. Lett.* **191**, 351-356, (1992).

12 Cotton, F. A., Wilkinson, G. *Advanced Inorganic Chemistry: A Comprehensive Text*. Fourth edn, (John Wiley & Sons, 1980).

13 Greenwood, N. N., Earnshaw, A. *Chemistry of the Elements*. 2nd edn, (Butterworth-Heinemann, 1997).

14 Orlik, M. Self-Organization in Nonlinear Dynamical Systems and Its Relation to the Materials Science. *J. Solid State Electrochem.* **13**, 245-261, (2009).

15 Bard, A. J., Faulkner, L. R. *Electrochemical Methods: Fundamentals and Applications*. 2nd edn, (John Wiley, 2001).

16 Delahay, P. A Polarographic Method for the Indirect Determination of Polarization Curves for Oxygen Reduction on Various Metals. *J. Electrochem. Soc.* **97**, 198, (1950).

17 Ibrahim, B., Zagidulin, D., Behazin, M., Ramamurthy, S., Wren, J. C., Shoesmith, D. W. The Corrosion of Copper in Irradiated and Unirradiated Humid Air. *Corros. Sci.* **141**, 53-62, (2018).

18 Wren, J. C., Guo, D., Shin, Y., Li, M., Morco, R., Joseph, J. M., Behazin, M., Keech, P. G. Corrosion of Carbon Steel Inside Used Nuclear Fuel Containers in *WM2019: 45 Annual Waste Management Conference.* (Office of Scientific and Technical Information).

19 Feng, Y., Tan, K. L., Hsieh, A. K., Teo, W. K., Siow, K. S. Corrosion Mechanisms and Products of Copper in Aqueous Solutions at Various pH Values. *Corros. Sci.* **53**, 389-398, (1997).

20 Feng, Y., Teo, W. K., Siow, K. S., Hsieh, A. K. The Corrosion Behaviour of Copper in Neutral Tap Water. Part II: Determination of Corrosion Rates. *Corros. Sci.* **38**, 387-395, (1996).

21 Brusic, V., Frisch, M. A., Eldridge, B. N., Novak, F. P., Kaufman, F. B., Rush, B. M., Frankel, G. S. Copper Corrosion With and Without Inhibitors. *J. Electrochem. Soc.* **138**, 2253-2259, (1991).

22 Cuppett, J. D., Duncan, S. E., Dietrich, A. M. Evaluation of Copper Speciation and Water Quality Factors That Affect Aqueous Copper Tasting Response. *Chem. Senses* **31**, 689-697, (2006).

23 Rustad, J. R., Casey, W. H. A Molecular Dynamics Investigation of Hydrolytic Polymerization in a Metal−Hydroxide Gel. *J. Phys. Chem. B* **110**, 7107-7112, (2006).

24 Gustafson, R., Martell, A. Formation of Polynuclear Complexes in Aqueous Solution. *Ann. N.Y. Acad. Sci.* **88**, 322-331, (2006).

25 Holmes, H. N. The Formation of Crystals in Gels. *J. Franklin Inst.* **184**, 743-773, (1917).

26 Durand-Keklikian, L., Matijević, E. Needle-Type Colloidal Copper (II) Hydroxide Particles. *Colloid. Polym. Sci.* **268**, 1151-1158, (1990).

27 Naghizadeh, M., Joseph, J. M., Behazin, M., Keech, P. G., Wren, J. C. Development of a Mechanism for Copper Corrosion Under Gamma Radiation. *ECS Meeting Abstracts* **MA2020-01**, 1006-1006, (2020).

28 Baes, C. F., Mesmer, R. E. *The Hydrolysis of Cations*. (Wiley, 1976).

29 Nakayama, S., Kaji, T., Notoya, T., Osakai, T. Mechanistic Study of the Reduction of Copper Oxides in Alkaline Solutions by Electrochemical Impedance Spectroscopy. *Electrochim. Acta* **53**, 3493-3499, (2008).

30 Chen, Q., Shen, X., Gao, H. Formation of Solid and Hollow Cuprous Oxide Nanocubes in Water-In-Oil Microemulsions Controlled by the Yield of Hydrated Electrons. *J. Colloid Interface Sci.* **312**, 272-278, (2007).

31 Joseph, J. M., Choi, B. S., Yakabuskie, P., Wren, J. C. A Combined Experimental and Model Analysis on the Effect of pH and $O_{2(aq)}$ on Gamma-Radiolytically Produced H_2 and H_2O_2. *Radiat. Phys. Chem.* **77**, 1009-1020, (2008).

32 Yakabuskie, P., Joseph, J., Wren, J. The Effect of Interfacial Mass Transfer on Steady-State Water Radiolysis. *Radiat. Phys. Chem.* **79**, 777-785, (2010).

33 Yakabuskie, P. A., Joseph, J. M., Stuart, C. R., Wren, J. C. Long-Term γ-Radiolysis Kinetics of NO_3^- and NO_2^- Solutions. *J. Phys. Chem. A* **115**, 4270-4278, (2011).

34 Morco, R. P., Joseph, J. M., Hall, D. S., Medri, C., Shoesmith, D. W., Wren, J. C. Modelling of Radiolytic Production of HNO_3 Relevant to Corrosion of a Used Fuel Container in Deep Geologic Repository Environments. *Corros. Eng. Sci. Technol.* **52**, 141-147, (2017).

35 Sharma, V. K., Millero, F. J. The Oxidation of Cu(I) with H_2O_2 in Natural Waters. *Geochim. Cosmochim. Acta* **53**, 2269-2276, (1989).

36 Turnbull, J. P. "The Influence of Radiolytically Produced Nitric Acid on the Corrosion Resistance of Copper-Coated Used Nuclear Fuel Containers" Doctor of Philosophy, The University of Western Ontario, Electronic Thesis and Dissertation Repository. (2020).

37 King, F., Lilja, C., Vähänen, M. Progress in the Understanding of the Long-Term Corrosion Behaviour of Copper Canisters. *J. Nucl. Mater.* **438**, 228-237, (2013).

38 Keech, P. G., Behazin, M., Binns, W. J., Briggs, S. An Update on the Copper Corrosion Program for the Long-Term Management of Used Nuclear Fuel in Canada. *Mater. Corros.* **72**, 25-31, (2020).

39 Turnbull, J., Szukalo, R., Zagidulin, D., Biesinger, M., Shoesmith, D. The Kinetics of Copper Corrosion in Nitric Acid. *Mater. Corros.* **72**, 1-13, (2020).

40 Galante, R., Rediguieri, C. F., Kikuchi, I. S., Vasquez, P. A. S., Colaço, R., Serro, A. P., Pinto, T. J. A. About the Sterilization of Chitosan Hydrogel Nanoparticles. *PLOS ONE* **11**, e0168862, (2016).

41 Zheng, J., Clogston, J. D., Patri, A. K., Dobrovolskaia, M. A., McNeil, S. E. Sterilization of Silver Nanoparticles Using Standard Gamma Irradiation Procedure Affects Particle Integrity and Biocompatibility. *J. Nanomed. Nanotechnol.* **2011**, 001, (2011).

42 Ulanski, P., Rosiak, J. M. The Use of Radiation Technique in the Synthesis of Polymeric Nanogels. *Nucl. Instrum. Methods Phys. Res. B* **151**, 356-360, (1999).

43 Wren, J. C. *Steady-State Radiolysis: Effects of Dissolved Additives* in *Nuclear Energy and the Environment* Vol. 1046 *ACS Symposium Series* (eds C. M. Wai & B. J. Mincher) 271-295 (2010).

44 Bessho, K., Oki, Y., Akimune, N., Matsumura, H., Masumoto, K., Sekimoto, S., Osada, N., Kinoshita, N., Monjushiro, H., Shibata, S. Corrosion of Copper in Water and Colloid Formation Under Intense Radiation Field. *J. Radioanal. Nucl. Chem.* **303**, 1117-1121, (2015).

45 Goldstein, J., Newbury, D. E., Joy, D. C., Lyman, C. E., Echlin, P., Lifshin, E., Sawyer, L., Michael, J. R. *Scanning Electron Microscopy and X-Ray Microanalysis*. Third edn, (Springer US, 2003).

46 Kumagai, K., Sekiguchi, T. Sharing of Secondary Electrons by In-Lens and Out-Lens Detector in Low-Voltage Scanning Electron Microscope Equipped with Immersion Lens. *Ultramicroscopy* **109**, 368-372, (2009).

47 Powell, K. J., Brown, P. L., Byrne, R. H., Gajda, T., Hefter, G., Sjöberg, S., Wanner, H. Chemical Speciation of Environmentally Significant Metals with Inorganic Ligands. Part 2: The Cu^{2+}-OH^-, Cl^-, CO_3^{2-}, SO_4^{2-}, and PO_4^{3-} Systems. *Pure Appl. Chem.* **79**, 895-950, (2007).

48 Spark, K. M., Johnson, B. B., Wells, J. D. Is Copper(II) Hydroxide an Intermediate in the Formation of the Hydroxide Chloride and Hydroxide Nitrate of Copper(II)? *Aust. J. Chem.* **43**, 749-754, (1990).

49 Candal, R. J., Regazzoni, A. E., Blesa, M. A. Precipitation of Copper(II) Hydrous Oxides and Copper(II) Basic Salts. *J. Mater. Chem.* **2**, 657-661, (1992).

50 Jarvenin, G. Precipitation and Crystallization Processes. (2008).

51 Lifshitz, I. M., Slyozov, V. V. The Kinetics of Precipitation From Supersaturated Solid Solutions. *J. Phys. Chem. Solids* **19**, 35-50, (1961).

52 Chen, K., Song, S., Xue, D. Chemical Reaction Controlled Synthesis of Cu_2O Hollow Octahedra and Core–Shell Structures. *CrystEngComm* **15**, 10028-10033, (2013).

53 Kahlweit, M. Ostwald Ripening of Precipitates. *Adv. Colloid Interface Sci.* **5**, 1-35, (1975).

54 Epstein, I. R., Pojman, J. A. *An Introduction to Nonlinear Chemical Dynamics: Oscillations, Waves, Patterns, and Chaos* (Oxford University Press, 1998).

55 Scott, D. A. Periodic Corrosion Phenomena in Bronze Antiquities. *Studies in Conservation* **30**, 49-57, (1985).

56 Ricketts, V. L., Culbertson, J. L. Diffusion in Alkaline Copper Systems. *J. Am. Chem. Soc.* **53**, 4002-4008, (1931).

57 Emami, M. A., Bigham, M. Mechanism of Corrosion Due to Unalloyed Copper Inclusion in Ancient Bronzes. *Surf. Eng.* **29**, 128-133, (2013).

58 Kai, S., Müller, S. C., Ross, J. Measurements of Temporal and Spatial Sequences of Events in Periodic Precipitation Processes. *J. Chem. Phys.* **76**, 1392-1406, (1982).

59 Jean, A. M. "Evolution of Cu_2O Morphology During Copper Corrosion in the Presence of Gamma-Radiation" M.Sc., The University of Western Ontario, Electronic Thesis and Dissertation Repository. (2017). 4593.

60 Björkbacka, Å., Hosseinpour, S., Johnson, M., Leygraf, C., Jonsson, M. Radiation Induced Corrosion of Copper for Spent Nuclear Fuel Storage. *Radiat. Phys. Chem.* **92**, 80-86, (2013).

61 Yoder, C., Bushong, E., Liu, X., Weidner, V., McWilliams, P., Martin, K., Lorgunpai, J., Haller, J., Schaeffer, R. The Synthesis and Solubility of the Copper Hydroxyl Nitrates: Gerhardtite, Rouaite and Likasite. *Mineral. Mag.* **74**, 433-440, (2010).

62 Davidson, J., Sefiane, K., Wood, T. Fast Diffusion Reaction in the Composition and Morphology of Coprecipitated Carbonates and Nitrates of Copper(II), Magnesium(II), and Zinc(II). *Ind. Eng. Chem. Res.* **54**, 1555-1563, (2015).

63 Frost, R. L., Leverett, P., Williams, P. A., Weier, M. L., Erickson, K. L. Raman Spectroscopy of Gerhardtite at 298 and 77 K. *J. Raman Spectrosc.* **35**, 991-996, (2004).

64 Pereira, D., Faria, D., Constantino, V. Cu^{II} Hydroxy Salts: Characterization of Layered Compounds by Vibrational Spectroscopy. *J. Braz. Chem. Soc.* **17**, (2006).

65 Dörner, L., Cancellieri, C., Rheingans, B., Walter, M., Kägi, R., Schmutz, P., Kovalenko, M. V., Jeurgens, L. P. H. Cost-Effective Sol-Gel Synthesis of Porous CuO Nanoparticle Aggregates with Tunable Specific Surface Area. *Sci. Rep.* **9**, 11758, (2019).

66 Xiong, S., Sun, J. Sliding Wear-Induced Nano-Tribofilm Formation from EP/AW Agent on Copper Foil Against Ferroalloy Counterparts Under High Load. *Surf. Interface Anal.* **50**, 1255-1264, (2018).

67 Martinez-Lombardia, E., Gonzalez-Garcia, Y., Lapeire, L., De Graeve, I., Verbeken, K., Kestens, L., Mol, J. M. C., Terryn, H. Scanning Electrochemical Microscopy to Study the Effect of Crystallographic Orientation on the Electrochemical Activity of Pure Copper. *Electrochim. Acta* **116**, 89-96, (2014).

68 Marsh, G. A., Schaschl, E. The Difference Effect and the Chunk Effect. *J. Electrochem. Soc.* **107**, 960, (1960).

69 King, F., Lilja, C. Localised Corrosion of Copper Canisters. *Corros. Eng. Sci. Technol.* **49**, 420-424, (2014).

70 Ives, M. B. Metallography of Pitting Corrosion. *Mater. Charact.* **28**, 257-270, (1992).

71 Sequeria, C. A. C. *Copper and Copper Alloys* in *Uhlig's Corrosion Handbook* Vol. 3 (ed R. Winston Revie) Ch. 56, 757-785 (John Wiley & Sons, Inc, 2011).

72 Kruger, J. The Oxide Films Formed on Copper Single Crystal Surfaces in Pure Water. *J. Electrochem. Soc.* **106**, 847, (1959).

73 Martinez-Lombardia, E., Lapeire, L., Maurice, V., De Graeve, I., Verbeken, K., Klein, L. H., Kestens, L. A. I., Marcus, P., Terryn, H. In Situ Scanning Tunneling Microscopy Study of the Intergranular Corrosion of Copper. *Electrochem. Commun.* **41**, 1-4, (2014).

74 Yuan, Y., Jiang, Y., Zhou, J., Liu, G., Ren, X. Influence of Grain Boundary Character Distribution and Random High Angle Grain Boundaries Networks on Intergranular Corrosion in High Purity Copper. *Mater. Lett.* **253**, 424-426, (2019).

CHAPTER 7. EFFECTS OF COVER GAS COMPOSITION ON COPPER CORROSION DYNAMICS

7.1 INTRODUCTION

Corrosion involves a series of elementary processes which include electrochemical redox reactions, solutions reactions, transport processes, and oxide particle nucleation and growth. To develop a mechanistic model that can predict the evolution of copper corrosion in different solution environments, it is critical to be able to decouple the elementary processes involved. In previous chapters, it was shown that the elementary reactions that determine the overall rate of corrosion evolve with corrosion time. Initially, the oxidation of solid copper ($Cu^0_{(m)}$) to the soluble cupric cation is coupled with the reduction of oxidant (e.g., O_2 to OH^-), at the metal-solution interface ($z = 0$, where z is the distance from the metal surface) (**Eq. 7.1**, the initial charge transfer), and the subsequent transport of the oxidant and the metal cation between the interface ($z = 0$) and the bulk solution ($z = \delta_{diff}$). While diffusing, these products can participate in other (electro)chemical reactions, including the quick establishment of the cupric ion hydrolysis equilibrium (**Eq. 7.2**), which can affect both the main form of cupric ions and the pH of the solution.

$$Cu^0_{(m)} + \tfrac{1}{2}\, O_2 + H_2O \rightleftarrows Cu^{2+} + 2\, OH^- \tag{7.1}$$

$$Cu^{2+} + 2\, OH^- \rightleftharpoons Cu(OH)^+ + OH^- \rightleftharpoons Cu(OH)_{2(solv)} + H_2O \rightleftharpoons Cu(OH)_3^- + H^+ \tag{7.2}$$

Because corrosion involves both charge and mass transfer, the rates of the elementary reactions are dependent on the solution redox and/or transport conditions.

In **Chapter 6**, the copper corrosion progression in small stagnant CO_2-free water droplets was investigated in the presence and absence of radiation. From this analysis, a copper corrosion mechanism was proposed. In Stage 1, copper corrosion rate can be determined by the dissolution rate of cupric ions, as they are the main corrosion product. After cupric ions accumulate in the interfacial solution, systemic feedback loops between multiple elementary reactions can be established that affect the overall metal loss (corrosion) rate. The concentration of cupric ions that accumulate, determined by their solubility, can affect the rate of metal loss in Stages 2 and 3 when the main corrosion products are a mixed Cu^I/Cu^{II}

hydroxide hydrogel and Cu_2O, respectively. The continuous production of radiolysis products in the presence of radiation can affect rate determining elementary reactions in each corrosion stage, changing the rate and duration of the stage.

The effects of solution parameters on the rates of the elementary reactions are not necessarily linearly additive to the effects of γ-radiation. The effects of γ-radiation in CO_2-free solutions were determined in **Chapter 6**. This chapter will investigate the combined effects of radiation and cover gas composition. The cover gas environments examined are aerated (with CO_2), 21% O_2 (balance Ar), and deaerated, and the results are compared to those from the CO_2-free air environment analyzed in **Chapter 6**. Each cover gas composition was chosen because it adds or removes a key redox active or pH-affecting species from solution thereby affecting the redox or transport conditions of the solution. They are also atmospheres relevant to the conditions that the copper layer of the UFC may experience during its lifetime.[1,2] The corrosion dynamics in the absence and presence of γ-radiation in each cover gas composition are determined by following the bulk concentration of cupric ions, pH, and morphology and composition of the surface oxides as a function of time.

7.2 EXPERIMENTAL

7.2.1 Materials and Solutions

All experiments were performed with copper coupons (99.9% purity) made from wrought copper samples (provided by SKB, the Swedish Nuclear Waste Management Company) with an exposed surface area of 0.785 cm^2. The top surface of the copper coupons was ground using silicon carbide papers (Buehler, Inc., Wooster, OH) with grit size 400, 800, and 1200 in succession. The coupons were then washed with deionized water, dried under flowing $Ar_{(g)}$, and placed in a 20 mL vial sealed with an aluminum crimp cap with a polytetrafluoroethylene (PTFE)-coated silicone septum (Thermo Fisher Scientific, Waltham, MA). More information on this procedure is provided in **Section 3.1**. All solutions used in this study were prepared using water purified with a NANOpure Diamond UV ultra-pure water system (Barnstead International, Dubuque, IA) to give a resistivity of 18.2 MΩ·cm.

The coupon vial and solution were purged with 21% O_2 balance Ar (Praxair, Danbury, CT), or ultra-high purity $Ar_{(g)}$ (Praxair, Danbury, CT) via the procedure in **Section 3.1.2**.

Aerated solutions were not purged. Experiments done in cover gas compositions containing 21% O_2 (i.e., CO_2-free air in **Chapter 6** and 21% O_2 balance Ar and aerated in this chapter) are collectively referred to as oxygenated solutions/environments, while experiments done after purging with $Ar_{(g)}$ are referred to as deaerated solutions/environments. 100 μL of the sample solution was placed on the copper surface by injection into the sealed vial using a syringe. Radiation experiments were performed using a MDS Nordion (Ottawa, ON) Gamma Cell 220 Excel ^{60}Co irradiator, as described in **Section 3.2**, and non-radiation experiments were done by leaving the vials on the benchtop, in otherwise the same conditions.

7.2.2 Post-Test Analyses

Experiments were terminated by removing the solution from the coupon surface using a Pasteur pipette. The copper coupon was washed and dried using $Ar_{(g)}$. Optical images were taken using a Leica DVM6A digital microscope, then the coupon was stored under vacuum. Scanning electron microscopy (SEM), energy-dispersive X-ray spectroscopy (EDX), and focused ion beam (FIB) milling were performed at the Western Nanofabrication Facility using Zeiss LEO 1530 and 1540XB instruments. Raman spectroscopy was performed at Surface Science Western using a Renishaw (Wotton-under-Edge, UK) Model 2000 Raman spectrometer equipped with a MellesGriot (Carlsbad, CA) 35 mW HeNe laser with a wavelength of 633 nm. More information on the surface analysis can be found in **Section 3.3**.

The pH of the solution was determined using a Thermo Scientific (Waltham, MA) Orion 9110DJWP Double Junction Micro-pH Electrode. The solution was then diluted to quantify the dissolved copper concentration using inductively coupled plasma optical emission spectroscopy (ICP-OES) (PerkinElmer Avio 200 ICP-OES) to determine the dissolved/dispersed copper concentration. More information on the procedure for solution analysis can be found in **Section 3.4**.

7.3 RESULTS AND DISCUSSION

7.3.1 Corrosion Dynamics in the Presence of Atmospheric CO_2

In an aerated environment, $CO_{2(g)}$ dissolves into solution (with an approximate concentration of 12.7 μM or 280 ppm by volume) and reacts with water to produce H_2CO_3.[3]

This weak acid can lower the initial pH (pH_0) of the solution to 6.0 – 6.5, and thus a corroding copper surface is exposed to a slightly lower pH_0 when solutions are naturally aerated. H_2CO_3 has two pKa values at 6.4 and 10.3 (**Eq. 7.3**), and thus, when near one of these values, the pH can become buffered.

$$H_2CO_3 \rightleftharpoons HCO_3^- + H^+ \quad pKa = 6.4 \tag{7.3a}$$

$$HCO_3^- \rightleftharpoons CO_3^{2-} + H^+ \quad pKa = 10.3 \tag{7.3b}$$

7.3.1.1 In the Absence of Radiation

The time-dependent behaviours of $\log([Cu^{II}_{(sol'n)}])$, pH, and the surface morphology and colour observed during copper corrosion in aerated droplet solutions are presented in **Figure 7.1**. The key observations for the three observed stages are outlined below and discussions on these observations will follow.

Stage 1: For t ≤ 48 h, $[Cu^{II}_{(sol'n)}]_t$ increased with time and the general surface remained clean. The pH_t increased from its initial value then was buffered at a value of 8.8 ± 0.1, corresponding to the pKa of $Cu(OH)^+$. The general surface did not show a significant amount of oxide growth.

Stage 2: For 72 h ≤ t ≤ 200 h, $[Cu^{II}_{(sol'n)}]_t$ remained at a steady-state value of 0.79 ± 0.50 mM. Throughout this stage, the pH_t fluctuated between the pKa of $Cu(OH)^+$ and the pKa of HCO_3^-. Many patches of dried hydrogel were observed across the general surface. Although the edges showed some oxide growth, the amount did not appear to increase from Stage 1.

Stage 3: When t = 240 h, the entire surface was a deep yellow, indicative of uniform growth of small Cu_2O particles across the surface. $[Cu^{II}_{(sol'n)}]_t$ and pH_t both decreased, causing the solution to approach the $Cu(OH)_2$ solubility equilibrium.

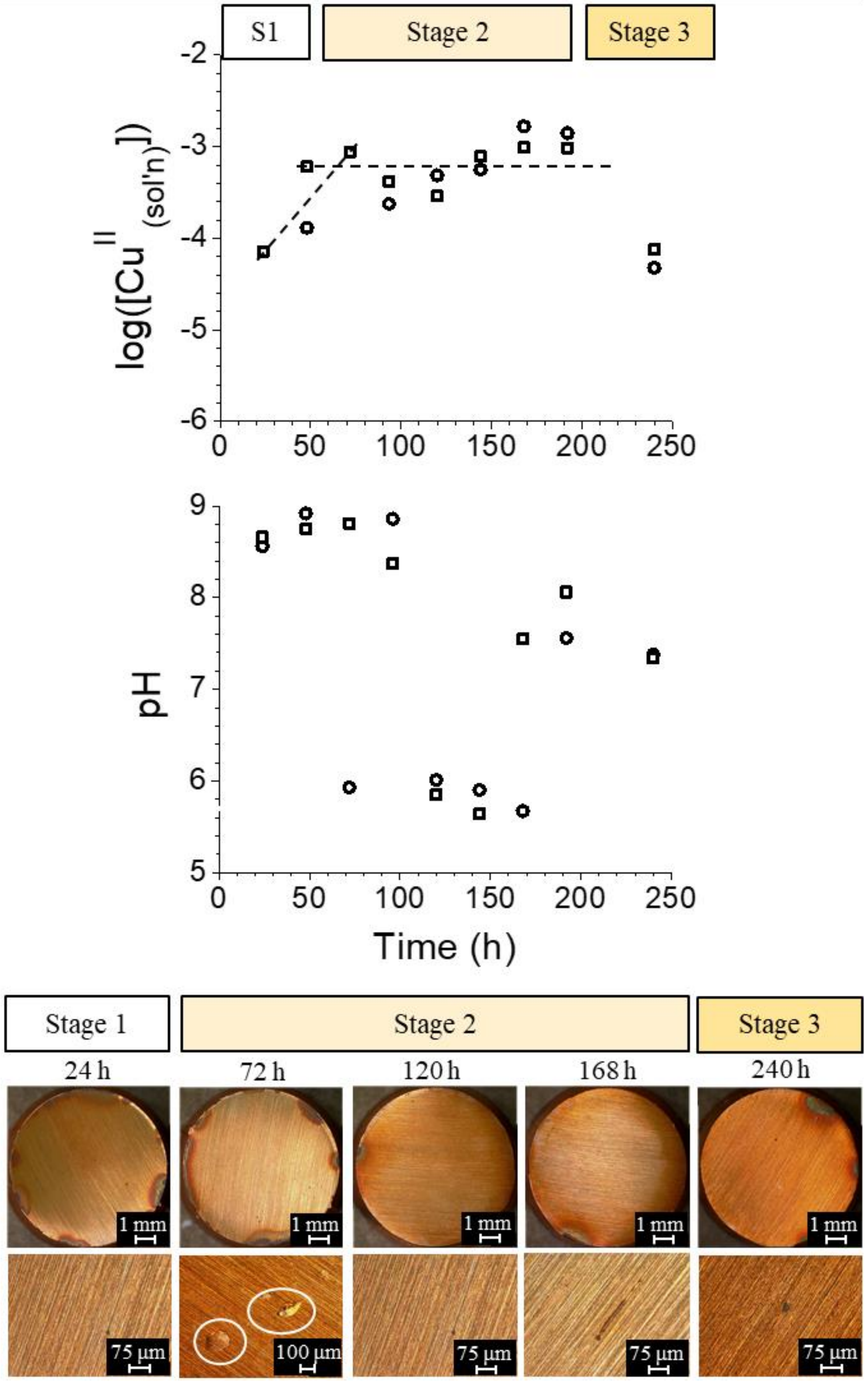

Figure 7.1 Time-dependent behaviour of $[\mathrm{Cu}^{\mathrm{II}}_{(\mathrm{sol'n})}]$ (top row), pH (middle row), and the exposed surface (optical images, bottom row) during copper corrosion after exposure to a 100 µL droplet of aerated water ($\mathrm{pH}_0 = 6.0$) in the absence of γ-radiation. The black dotted lines show the general trend of the data (not based on regression analysis).

Figure 7.1 shows that the pH initially increased, the opposite observation to in Stage 1a in CO_2-free solutions. In naturally aerated solutions, pH_0 is lower than in CO_2-free solutions and buffered at the bicarbonate pKa (**Eq. 7.3a**). Thus, unlike in CO_2-free solutions (**Chapter 6**), the production of OH^- via the initial charge transfer does not substantially change the pH, and instead, the pH initially remains buffered around 6.4. At this pH, the main form of cupric ion due to the hydrolysis equilibrium (**Eq. 7.2**) is $Cu(OH)^+$ and the initial corrosion reaction can be considered:

$$Cu^0_{(m)} + \tfrac{1}{2} O_2 + H_2O \rightarrow Cu(OH)^+ + OH^- \qquad (7.4)$$

Thus, the concentrations of $Cu(OH)^+$ and OH^- increase, and by 24 h (**Figure 7.1**), $[OH^-]$ produced via **Eq. 7.4** was more than the buffering capacity of HCO_3^-. The first measured pH_t (**Figure 7.1**) was at the pKa of $Cu(OH)^+$ (**Eq. 7.5**), indicating $Cu(OH)^+$ and $Cu(OH)_{2(solv)}$ had been formed in a high enough concentration to reach its buffering capacity and overcome that of HCO_3^-.

$$Cu(OH)^+ + H_2O \rightleftharpoons Cu(OH)_{2(solv)} + H^+ \qquad pKa = 8.3 \qquad (7.5)$$

The acid-base equilibrium of $Cu(OH)^+$ buffered the pH for the entirety of Stage 1, while $[Cu^{II}_{(sol'n)}]_t$ increased. When the solution pH is at the pKa of $Cu(OH)^+$, $Cu(OH)^+$ and $Cu(OH)_{2(solv)}$ are present in equal amounts. As the concentration of cupric ions continues to increase, $Cu(OH)_2$ precipitates as colloid particles that remain dispersed in solution and contribute to the $[Cu^{II}_{(sol'n)}]_t$.

Thus, Stage 1 in aerated solutions does not occur in two observable steps (i.e., Stage 1a, producing $Cu(OH)_3^-$ and H^+, and Stage 1b, producing $Cu(OH)^+$ and $Cu(OH)_2$ colloid particles). The duration of Stage 1, defined by the length of linear increase in $[Cu^{II}_{(sol'n)}]$ with time, was nearly the same in both CO_2-free and aerated solutions. However, the rate of $[Cu^{II}_{(sol'n)}]$ dissolution was slightly higher in aerated solutions. This results in a higher dissolved copper yield at the end of Stage 1 (0.63 mM, **Figure 7.1**) than in CO_2-free solutions (0.25 mM in **Chapter 6**).

Stage 2 begins when the $Cu(OH)_2$ colloid particles begin to agglomerate and precipitate as a hydrogel, which was seen in the optical images starting at 72 h. During this stage, the production of $Cu^{2+}{}_{(sol'n)}$ via metal oxidation is equal to their consumption via precipitation, and therefore, $[Cu^{II}{}_{(sol'n)}]_t$ is constant with time. Stage 2 was observed for $72\ h \leq t \leq 200\ h$ (**Figure 7.1**), during which $[Cu^{II}{}_{(sol'n)}]_t$ fluctuated with time around an average value of 0.79 ± 0.50 mM. In Stage 2, the plateau in $[Cu^{II}{}_{(sol'n)}]_t$ in aerated solutions was higher than in CO_2-free solutions (0.38 ± 0.15 mM, **Chapter 6**) due to more dissolution during Stage 1.

Patches of dried hydrogel are shown in the optical images (bottom row) in **Figure 7.1** (indicated by the white circles). More of these dried hydrogel patches were observed after corrosion in aerated solutions compared to in CO_2-free solutions. With a higher $[Cu^{II}{}_{(sol'n)}]$ at the start of Stage 2, the hydrogel precipitation rate is faster in aerated solutions. This also means the colloid concentration within the hydrogel that grows in aerated solutions is higher than in CO_2-free solutions. However, the hydrogel was clear and colourless (on top of the orange metal surface, **Figure 7.1**), indicating the colloid concentration was still too low to produce the characteristic blue colour of $Cu(OH)_2$.

As discussed in detail in **Chapter 6**, the dynamics of the hydrogel precipitation and growth are complicated and involve systemic feedback. As the colloid concentration increases within the hydrogel, cupric ion transport becomes limited and $Cu^{2+}{}_{(sol'n)}$ gets trapped next to the metal surface. As Cu^{2+} accumulates, the rate of its reduction to $Cu^{+}{}_{(sol'n)}$, coupled with $Cu^{0}{}_{(m)}$ oxidation, increases. Cuprous ions have a low solubility thereby reaching its solubility equilibrium quickly. $CuOH_{(solid)}$ gets incorporated into the solid hydrogel network, resulting in the formation of a Cu^{I}/Cu^{II} mixed hydrogel.

$$Cu^{0}{}_{(m)} + Cu^{2+}{}_{(sol'n)} \rightarrow 2\ Cu^{+}{}_{(sol'n)} \tag{7.6a}$$

$$Cu^{+}{}_{(sol'n)} + x\ OH^{-} \rightleftharpoons CuOH_{(solid)} \tag{7.6b}$$

$$Cu^{+}{}_{(sol'n)}/CuOH_{(solid)} + Cu^{2+}{}_{(sol'n)}/Cu(OH)_{2(solid)} + OH^{-} \rightarrow \text{mixed } Cu^{I}/Cu^{II} \text{ hydroxide hydrogel} \tag{7.6c}$$

Figure 7.1 showed that in Stage 2 in aerated solutions, pH_t was initially buffered at the $Cu(OH)^{+}$ pKa, but then decreased. The decrease in pH was not observed in CO_2-free air (**Chapter 6**). In solutions that contain CO_2, cupric ion hydrolysis equilibria and bicarbonate acid-base equilibrium compete. That is, the pH is initially buffered at the $Cu(OH)^{+}$ pKa until t = 96 h, but as a small amount of OH^{-} is consumed via **Eq. 7.6c**, the pH decreased enough that the pH became buffered at the HCO_3^- pKa (**Eq. 7.1a**). Later in Stage 2, pH_t increased again to close to the $Cu(OH)^+$ pKa. These large changes in pH_t result in large changes in cupric ion solubility, and the fluctuations around the average $[Cu^{II}_{(sol'n)}]_t$ are large.

The rate of CuOH formation within the hydrogel network is proportional to the concentration of $[Cu^{II}_{(sol'n)}]$ (**Eq. 7.6**). With a higher $[Cu^{II}_{(sol'n)}]_t$ in aerated solutions compared to in CO_2-free solutions, more CuOH is formed in a shorter period and therefore, Stage 3 starts earlier (**Figure 7.1**). Stage 3 begins after CuOH reaches supersaturation and precipitates as Cu_2O.

$$2\ Cu^{+}_{(sol'n)} + x\ OH^{-} \rightleftharpoons 2\ CuOH_{(solid)} \rightarrow Cu_2O + H_2O \qquad (7.7)$$

The entire surface was a deep yellow colour at t = 240 h seen in optical images in **Figure 7.1**, indicating it was covered with small Cu_2O crystals. At this time, $[Cu^{II}_{(sol'n)}]_t$ and pH_t decreased to satisfy the $Cu(OH)_2$ solubility equilibrium. Stage 3 started earlier in aerated solutions than in CO_2-free solutions because of a higher $[Cu^{II}_{(sol'n)}]_t$ in Stages 1 and 2. Thus, the colloid concentration in the hydrogel was higher and it took less time for CuOH to reach the supersaturation concentration.

Overall, the presence of CO_2 did not change the progression through corrosion stages but affected the duration and product yields in each stage. Stage 1 had a higher corrosion rate that resulted in a higher $[Cu^{II}_{(sol'n)}]$ yield. Thus, when Stage 2 started, $[Cu^{II}_{(sol'n)}]$ was higher and more hydrogel formed. The rate of CuOH formation was higher due to the higher concentration of $Cu(OH)_2/Cu^{2+}_{(sol'n)}$ during Stage 2 and Stage 2 was shortened. Stage 3 was observed at an earlier time.

7.3.1.2 In the Presence of Radiation

Water and humid air exposed to γ-radiation decompose into redox-active (mainly H_2O_2) and acidic species (mainly HNO_3). Under a continuous flux of γ-radiation, the radiolysis products reach steady-state concentrations and become homogeneously distributed in solution. Hence, the effects of γ-radiation on the corrosion rate are through the radiolysis products that are distributed homogeneously and at near constant concentrations (even though they may be consumed by corrosion reactions).

The time-dependent behaviours of log([$Cu^{II}_{(sol'n)}$]), pH, and the surface morphology and colour observed during radiolytic copper corrosion in aerated droplet solutions are presented in **Figure 7.2** and **7.3**. The observations that led to the identification and assignment of the stages are:

Stage 1: When $t \leq 24$ h, $[Cu^{II}_{(sol'n)}]_t$ increased, and minimal oxide growth was observed on the surface. During this time, pH_t remained constant at 5.4. While the rate of increase in [$Cu^{II}_{(sol'n)}$] was not different than in CO_2-free solutions, the time duration was shorter.

Stage 2: For $48 \text{ h} \leq t \leq 96$ h, $[Cu^{II}_{(sol'n)}]_t$ and pH_t are constant at 4.2 ± 2.1 mM and 4.3 ± 0.4, respectively. A large amount of dried hydrogel was observed on the surface by SEM and optical imaging. Raman analysis indicated the incorporation of carbonate into the top layer of the hydrogel and both cupric and cuprous ions in the bottom layer.

Stage 3: For $120 \text{ h} \leq t \leq 192$ h, $[Cu^{II}_{(sol'n)}]_t$ increased while pH_t continued fluctuating around a value of 4.3. The surface was entirely pink and purple-coloured, indicating Cu_2O crystals covered with various thicknesses of $Cu(OH)_2$ hydrogel had grown. The precipitation rate of Cu_2O crystals in this stage was much higher than in CO_2-free solutions.

Stage 4: After 480 h, [$Cu^{II}_{(sol'n)}$] decreased to 6.3 ± 3.2 mM while pH_t remained at the same value as in Stage 3. Thick layers of hydrogel remained covering the surface, and large, green malachite ($Cu_2(CO_3)(OH)_2$) crystals had grown on top of the Cu_2O on the surface.

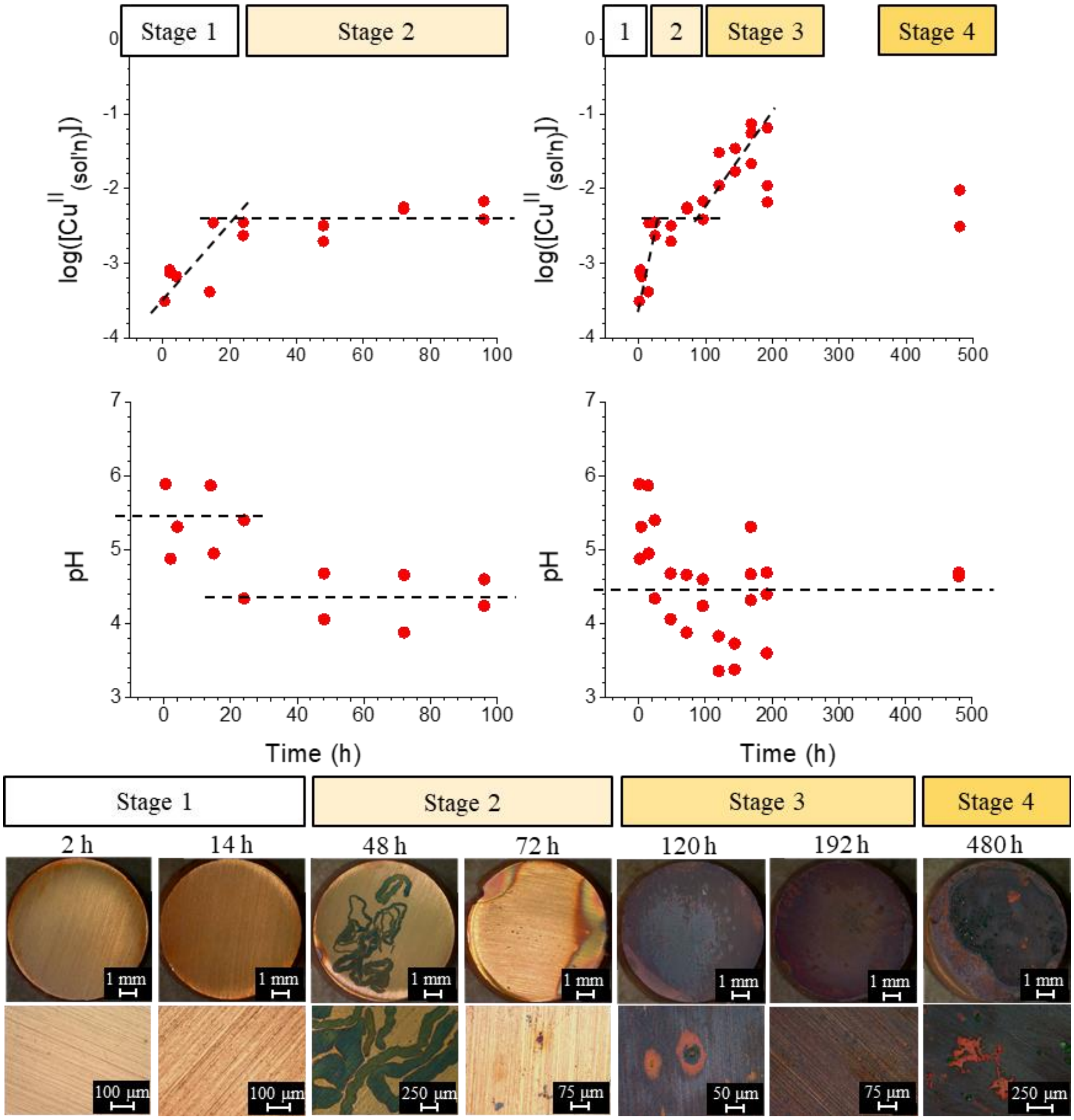

Figure 7.2 Time-dependent behaviours of [Cu^{II}$_{(sol'n)}$] (top row), pH (middle row), and the exposed surface (optical, bottom two rows) during copper corrosion after exposure to a 100 µL droplet of aerated pure water (pH$_0$ = 6.5) in the presence of γ-radiation. The black dotted lines show the general trend of the data (not based on regression analysis).

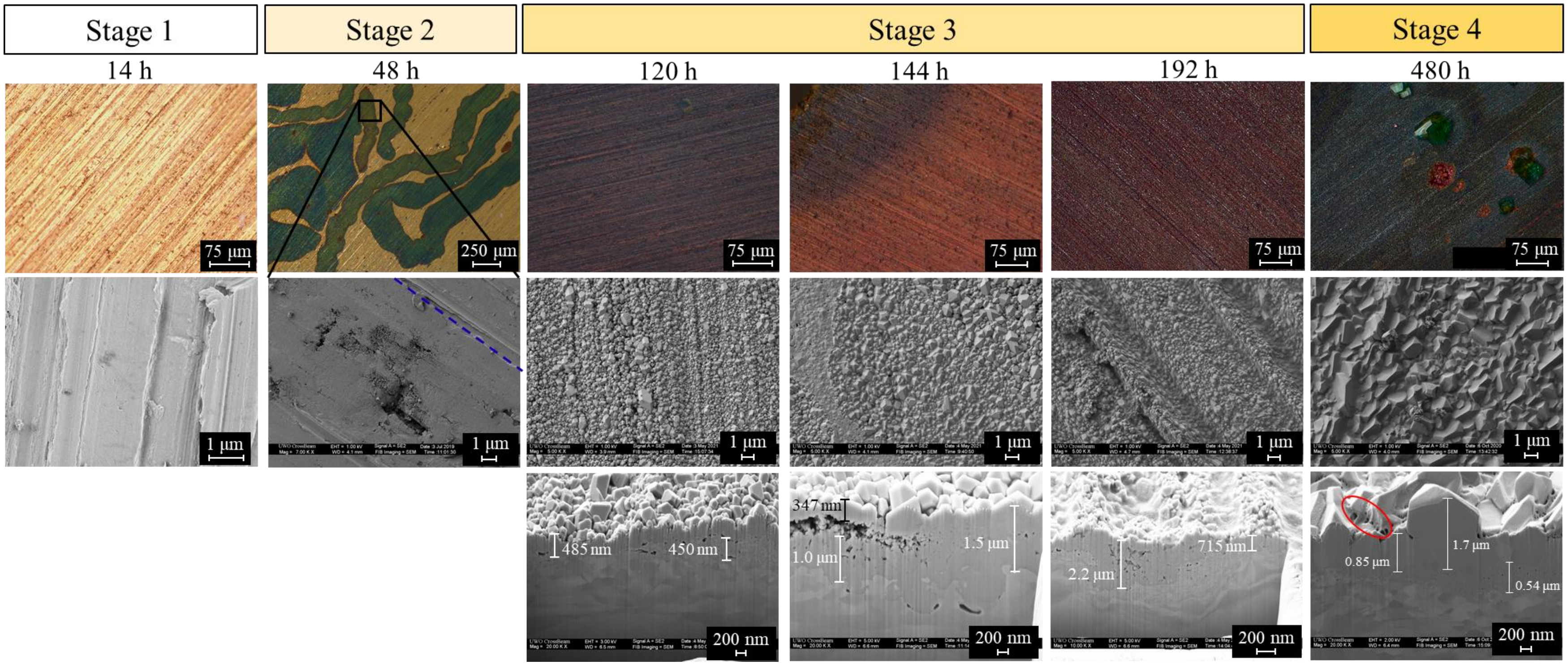

Figure 7.3 Optical (top row) and SEM images of the surface (middle row) and the metal-oxide cross section (bottom row) (cut using focused Ga-ion beam) in each stage of corrosion in aerated solutions in the presence of radiation. The blue dotted line indicates the intersection between the metal surface and the blue species in the optical image. The red circle shows hydrogel growth.

The pH during the first 24 h of radiolytic corrosion (**Figure 7.2**) was constant with time, indicating that the rate of production of $[OH^-]$ via the initial corrosion reactions (**Eq. 7.8**) was approximately equal to the rate of production of $[H^+]$ via radiolytic decomposition. As discussed in **Chapter 5** and **6**, in the presence of radiation, water and humid air decompose to produce H_2O_2, which becomes the main oxidant for $Cu^0{}_{(m)}$:

$$Cu^0{}_{(m)} + H_2O_2 \rightarrow Cu(OH)^+ + OH^- \qquad (7.8)$$

While pH_t was constant, $[Cu^{II}{}_{(sol'n)}]$ increased linearly with time and no significant oxides were observed on the surface (**Figures 7.2** and **7.3**). These were the same observations in Stage 1 in CO_2-free solutions (**Chapter 6**). The rate of copper dissolution in Stage 1 in aerated solutions was 0.20 ± 0.06 mM/h (**Figure 7.2**). In Stage 1, when metal oxidation produces mainly dissolved metal species, the overall rate of metal loss (corrosion) is the same as the overall increase in dissolved metal cation with time, as discussed in depth in **Chapter 4**, and thus can be approximated to the metal dissolution rate. In aerated droplet solutions, the corrosion rate in Stage 1 was 12.6 ± 4.0 nmol $Cu/cm^2/h$. This rate was unaffected by the presence of CO_2 (the rates and yields for all cover gas compositions are summarized in **Table 7.4**), consistent with it being determined by the $Cu^{2+}{}_{(sol'n)}$ transport rate.

In aerated solutions, Stage 1, indicated by the linear increase in $[Cu^{II}{}_{(sol'n)}]$ with time, was shorter than in CO_2-free solutions (24 h in **Figure 7.2** compared to 40 h in **Chapter 6**). It was shown in **Chapter 6** that the presence of radiation accelerates the transition between Stages 1 and 2 with the production of reactive species accelerate the rate of agglomeration of colloid particles into a hydrogel network. In aerated solutions, this agglomeration is further accelerated due to the complexation of $Cu^{2+}{}_{(sol'n)}$ with HCO_3^- which stabilizes the solid network, which is discussed in detail later in this section. Thus, Stage 2 started after 24 h in aerated solutions (**Figure 7.2**).

During Stage 2, the colloid concentration within the hydrogel increases which slows the transport of $Cu^{2+}{}_{(sol'n)}$ causing their accumulation at the metal surface. The accumulation of cupric ions increases the rate of oxidation of H_2O_2 by $Cu^{2+}{}_{(sol'n)}$ to form $Cu^+{}_{(sol'n)}$ (**Eq. 7.9a**). With a low solubility, $Cu^+{}_{(sol'n)}$ is quickly in its solubility equilibrium (**Eq. 7.9b**), and CuOH incorporates into the hydrogel network (**Eq. 7.9c**). The incorporation of cuprous species into the hydrogel network is confirmed later in this section.

$$2\ Cu^{2+} + H_2O_2 + 2\ OH^- \rightarrow 2\ Cu^+ + O_2 + 2\ H_2O \qquad (7.9a)$$

$$Cu^+_{(sol'n)} + x\ OH^- \rightleftharpoons CuOH_{(solid)} \qquad (7.9b)$$

$$Cu^+_{(sol'n)}/CuOH_{(solid)} + Cu^{2+}_{(sol'n)}/Cu(OH)_{2(solid)} + OH^- \rightarrow \text{mixed } Cu^I/Cu^{II} \text{ hydroxide hydrogel} \qquad (7.9c)$$

Stage 2 was observed for 48 h ≤ t ≤ 96 h, during which $[Cu^{II}_{(sol'n)}]_t$ and pH_t were constant at 4.2 ± 2.1 mM and 4.3 ± 0.4, respectively. While the amount of copper that remained dissolved in solution was lower in aerated solutions (summarized in **Table 7.4**), more hydrogel was observed on the surface compared to in CO_2-free solutions. This is a result of the incorporation of HCO_3^- into the hydrogel solid network, which decreases the extent of hydration causing more solid precipitate. Studies on the stability of gels in the presence of salts, sometimes referred to as Hofmeister ions, confirm that CO_3^{2-} increases the rate of their precipitation and extent of agglomeration.[4-6] A higher extent of precipitation is also the reason the $[Cu^{II}_{(sol'n)}]$ plateau value is lower in aerated solutions and Stage 1 was shorter compared to in CO_2-free solutions.

Large patches of dried hydrogel were observed during Stage 2. After 48 h, a filiform-type growth of the blue hydrogel was observed (**Figures 7.2** and **7.3**). The SEM image of the blue area is smooth with cracks, while the metal surface beside it still has its grinding lines (**Figure 7.3**). In one case (after 192 h), the hydrogel had covered the entire surface, which is shown in **Figure 7.4** and **7.5**. The hydrogel is a translucent blue colour and appears as a cracked sheet on top of pink/purple Cu_2O crystals (top row in **Figure 7.4**). The SEM images (bottom row in **Figure 7.4**) show that there are two layers of the dried hydrogel structure: the underlying layer is a typical gel structure with large pores of > 2 μm and the top layer is a smooth thin sheet with pores ~20 nm in diameter (red circle in last image in **Figure 7.4**). Previous studies have synthesized copper hydroxide hydrogels with a similar pore sizes.[7,8]

The term hydrogel refers to a gel in which the mobile phase solvent is water, and when hydrogels are dried (i.e., the mobile solution phase removed via evaporation) the solid network that is left is referred to as a xerogel. Xerogels retain the shape of hydrogels, but often crack due to shrinkage (~ 90 % shrinkage).[9,10] Thus, *ex situ* imaging shows the xerogel (**Figure 7.4**). The chemical characterization of the xerogel can be directly related to the hydrogel, but pore sizes are considerably larger when hydrated.

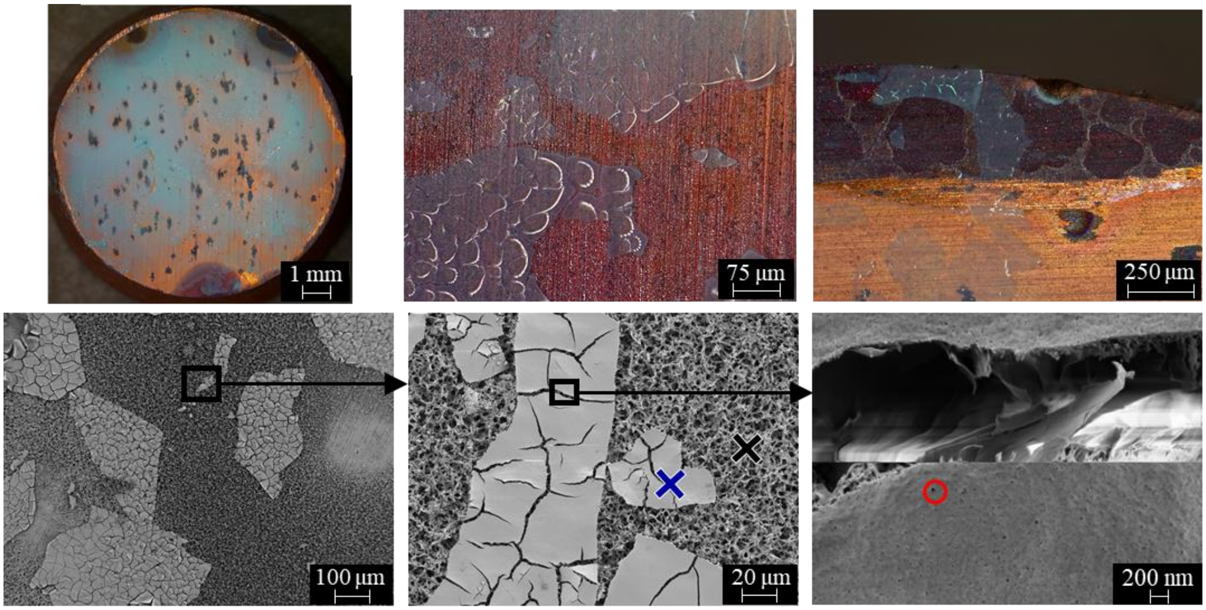

Figure 7.4 Optical (top row) and SEM (bottom row) images of dehydrated $Cu(OH)_2$ hydrogel formed after exposure to a 100 µL droplet of aerated water in the presence of γ-radiation for 192 h. The Raman spectra in **Figure 7.5b** were taken in the areas indicated with the blue and black 'x'. The red circle indicates a pore in the top layer of the xerogel.

Cross sections of the xerogel (**Figure 7.5a**) confirm the pore size in the top and bottom layer and show that these layers are connected and continuous. The thin top layer is approximately 522 nm thick and dense with small pores. To obtain the Raman spectrum of the top layer (blue trace, **Figure 7.5b**), the depth of penetration was restricted to the top ~ 1 µm of the surface and was taken in the area indicated in a blue 'x' in **Figure 7.4** and **7.5a**. The peak at 523 cm^{-1} – without the 623 cm^{-1} peak – indicates that $Cu(OH)_2$ is present without Cu_2O. There were also peaks at 1064 cm^{-1}, 1347 cm^{-1}, and 2935 cm^{-1} which indicate the incorporation of a carbonate group. This is further confirmed at later corrosion stages when large copper-carbonate crystals are observed on the surface. While nitrate is present in solution and could complex with copper ions, there is no indication of its presence in the Raman spectra. Thus, from the optical images, SEM images, and the Raman spectrum, it can be concluded that this top xerogel layer consists of copper hydroxide and carbonate.

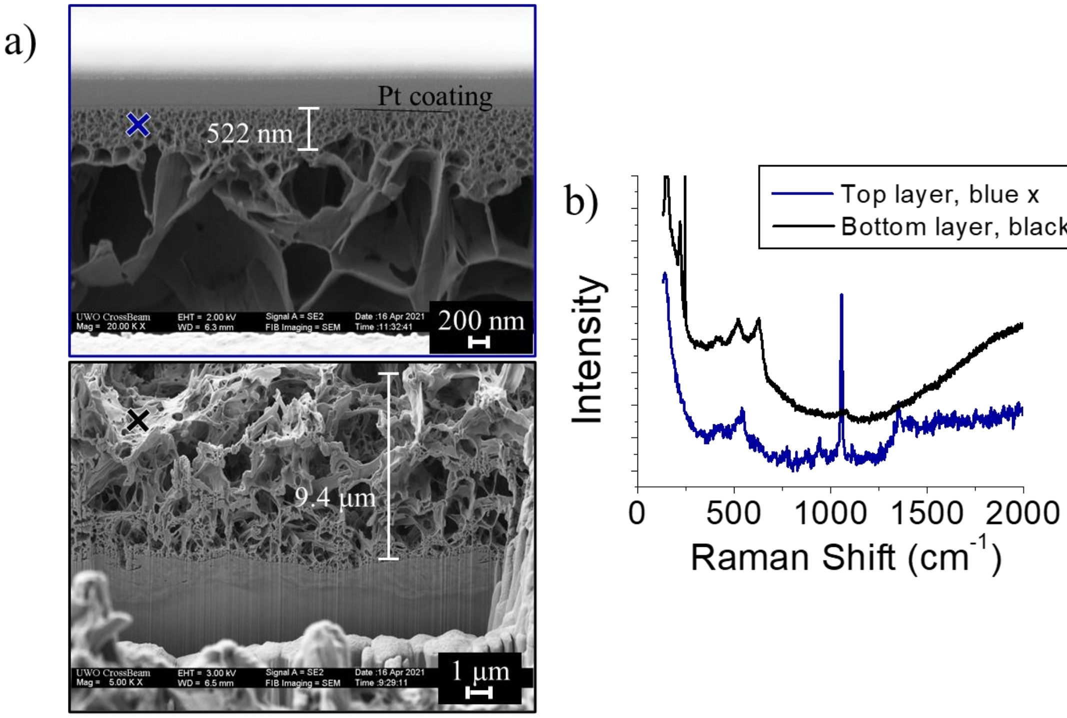

Figure 7.5 a) SEM images of the metal-gel interface and b) Raman spectra of $Cu(OH)_2$ xerogel formed after exposure to a 100 µL droplet of aerated water in the presence of γ-radiation for 192 h. The locations of Raman spectra are indicated by the blue and black 'x' in **a** and in **Figure 7.4**.

The bottom layer is approximately 9.4 µm thick and void size decreases closer to the metal surface. The increase in xerogel density by the metal surface where Cu^{2+} and OH^{-} are being produced was expected. The Raman spectrum of the bottom layer (**Figure 7.5b**) has equal intensity peaks at 523 and 623 cm^{-1}, indicating a combination of $Cu(OH)_2$ and Cu_2O. However, the SEM images did not show crystalline Cu_2O crystals. Instead, the 632 cm^{-1} peak in the Raman spectrum may be a result of the incorporation of cuprous ions into the hydrogel network, which supports the theory of the formation of a mixed Cu^{I}/Cu^{II} hydroxide hydrogel during Stage 2. Furthermore, there is also a large broad peak at 2200 cm^{-1} (the start of which can be seen in **Figure 7.5b**), which is from the OH stretching in the hydrogel.

The analysis of the xerogel formed in large quantities showed that there are two distinct layers. The bottom layer is composed of a mixed Cu^{I}/Cu^{II} hydroxide hydrogel (**Eq. 7.9c**) and has large pores, while the top layer is thin, dense, and composed of copper hydroxide and carbonate. The incorporation of carbonate into only the outer layer of the hydrogel may be due to the lower concentration of OH^- at the gel-bulk interface, so that HCO_3^- must satisfy the charge balance in the hydrogel. It is not obvious whether the two layers were formed in parallel, are a result of diffusion and the beginning of Stage 4, or if they are an artifact of *ex situ* drying.

Thus, in aerated solutions, a thick layer of hydrogel is formed during Stage 2. While the $[Cu^{II}_{(sol'n)}]$ plateau was lower than in CO_2-free solutions (**Table 7.4**), the concentration of cuprous ions in the hydrogel is higher when Stage 3 begins.

For 120 h ≤ t ≤ 192 h, the surface was entirely covered with purple and pink oxides (**Figures 7.2** and **7.3**), indicative of Stage 3. In Stage 3, the concentration of CuOH within the hydrogel is supersaturated and precipitates as Cu_2O.

$$2\ Cu^+_{(sol'n)} + x\ OH^- \rightleftharpoons 2\ CuOH_{(solid)} \rightarrow Cu_2O + H_2O \tag{7.10}$$

The film thickness and the amount of copper in the oxide film were quantified (**Table 7.1**) using the SEM images of the FIB milled cross-sections of the oxide-metal interface. The film was assumed to be composed of entirely Cu_2O, as the very thin hydrated $Cu(OH)_2$ layer should be a negligible fraction of the thickness. The average rate of Cu_2O precipitation in Stage 3 was 99 ± 52 nmol Cu/cm^2/h, which is shown in **Figure 7.6**. This precipitation rate is much higher than in CO_2-free solutions (62 ± 28 nmol Cu/cm^2/h, **Chapter 6**), consistent with a higher concentration of CuOH in the hydrogel.

Table 7.1 Amount of copper in the solution and in the surface oxides during corrosion in the presence of radiation in a naturally aerated atmosphere.

Stage	**Time (h)**	**n_{Cu} in solution (μmol)**	**n_{Cu} in oxide (μmol)**
3	120	0.27 ± 0.10	3.35 ± 1.27
	144	2.04 ± 1.70	7.56 ± 3.34
	192	5.50 ± 4.86	9.81 ± 6.78
4	480	0.43 ± 0.22	7.69 ± 2.73

During Stage 3, the pH fluctuated significantly around its steady-state value from 3.3 to 4.7 (**Figure 7.2**). When at low pH values, the cupric ion solubility is high which allows further dissolution. When at the higher values, dissolution ceases as the solution is saturated or slightly supersaturated. The result of these large solubility fluctuations is an overall increase of [$Cu^{II}_{(sol'n)}$] with time. The average $Cu^{II}_{(sol'n)}$ dissolution rate in this stage was 0.56 ± 0.01 mM/h, which corresponds to a metal loss rate of 35.8 ± 9.1 nmol $Cu/cm^2/h$.

Stage 4 was observed at t = 480 h, when [$Cu^{II}_{(sol'n)}$] had decreased (**Figure 7.2**) and the precipitation rate slowed (**Figure 7.6**). Stage 4 starts when the oxide layer grows thick enough that the charge transfer required for metal oxidation is hindered. Because cupric ions were not being produced in this stage at the metal surface, but were continuously consumed via precipitation, [$Cu^{II}_{(sol'n)}$] decreased. Without the production of OH^-, the reprecipitation of cupric ions during redox-assisted Ostwald ripening of Cu_2O crystals included carbonate anions to balance charge, which is shown later.

$$Cu_2O + H_2O_2 + H_2O \rightarrow 2\ Cu^{2+}_{(sol'n)} + 4\ OH^- \qquad (7.11a)$$

$$2\ Cu^{2+}_{(sol'n)} + 2\ OH^- + CO_3^{2-} \rightarrow Cu_2(CO_3)(OH)_{2(hydrogel)} \rightarrow Cu_2(CO_3)(OH)_{2(solid)} \qquad (7.11b)$$

The general oxide surface was purple (**Figure 7.3** and left column in **Figure 7.7**), indicating large Cu_2O crystals were covered by a thin layer of hydrogel. The thickness of the Cu_2O layer was 1.2 ± 0.3 μm (**Figure 7.3**), which corresponds to 7.72 ± 2.43 μmol of copper (summarized in **Table 7.1**). **Figure 7.6** shows the precipitation rate of Cu_2O had substantially decreased in Stage 4. However, the amount of copper in Cu_2O does not account for the total amount of precipitated copper due to the growth of large carbonate crystals, as discussed later.

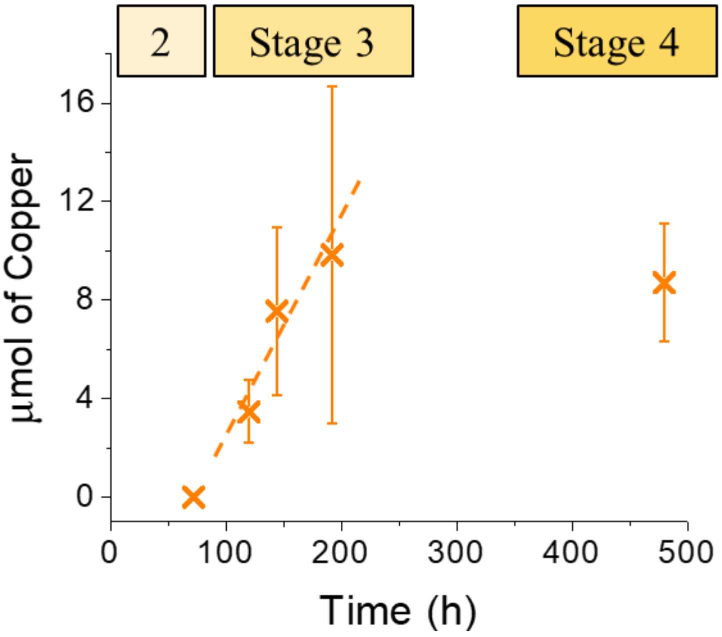

Figure 7.6 Amount of copper in Cu_2O during radiolytic copper corrosion in aerated solutions.

Figure 7.7 show that the Cu_2O crystals grown after 480 h are hoppered (also called “skeletal”), that is, the edges of the cube are fully developed but the faces are not. Hoppered Cu_2O crystals are formed in a kinetically controlled system with a particular balance between the rate of complexation, precipitation, and redox reactions.[11] This balance is struck either when the driving force for crystallization is high, e.g. high supersaturation, or when the diffusion around the crystal is limited, e.g. when precipitation is occurring in a gel.[11-15] Both of these criteria are met in this system, due to the thick hydrogel layer through which cupric ions must diffuse. Hoppered Cu_2O crystals were not observed in the absence of CO_2 as less hydrogel was present without its complexation with HCO_3^-.

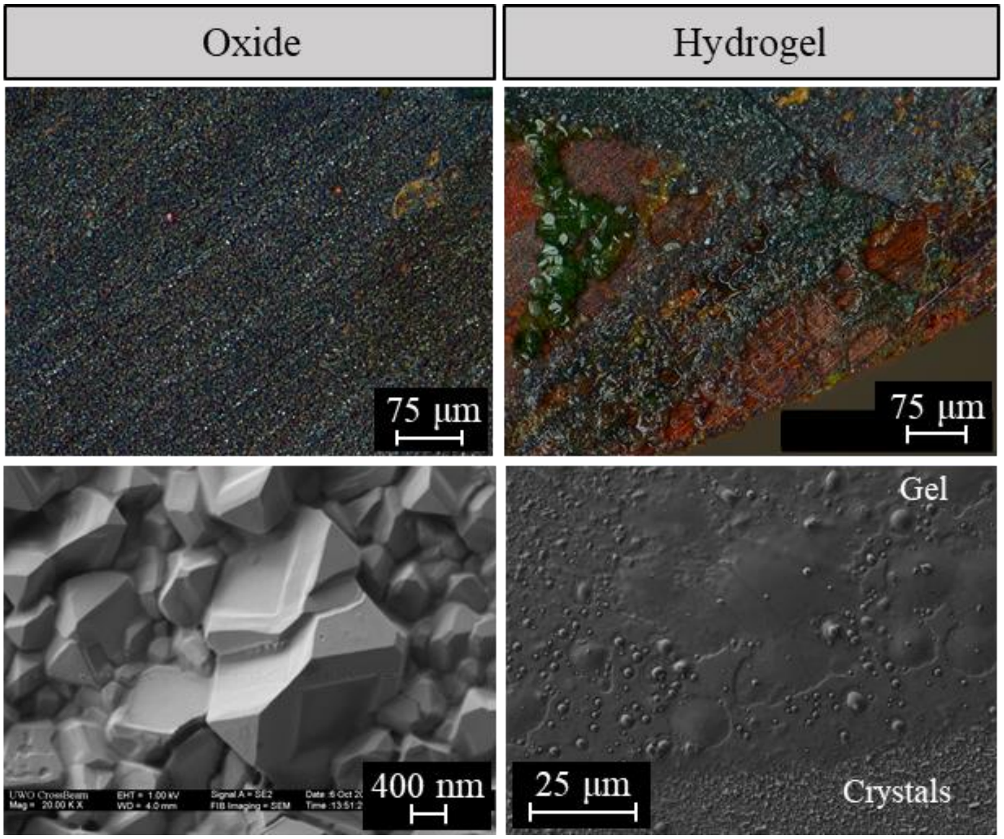

Figure 7.7 Optical (top row) and SEM (bottom row) images of the oxides (left) and hydrogel (right) on the copper surface after 480 h in aerated solution in the presence of γ-radiation.

The hydrogel is present in large quantities during Stage 4 and can be seen in the images on the right in **Figure 7.7**. The hydrogel in the optical image in **Figure 7.7** is amorphous and clear and appears as a coating across the surface. The SEM image in **Figure 7.7** shows a smooth layer of hydrogel on the surface. Hydrogel covered Cu_2O crystals are also observed in the top of the image. Some Cu_2O crystals are not covered by the hydrogel (bottom of the image), showing the hydrogel does not cover the entire surface equally (also indicated by the variations between pink and purple colours across the surface). The red circle in **Figure 7.3** also shows the hydrogel growth between Cu_2O crystals during this stage.

Large green crystals cover the surface after 480 h (**Figure 7.3**) which are further investigated in **Figure 7.8**. The Raman spectrum of the large green crystal is shown in **Figure 7.8b**, compared to that of the purple Cu_2O crystals. The green crystal is characterized as malachite, $Cu_2(CO_3)(OH)_2$, based on the CO stretching peaks at 1064, 1347, 1565 and 2935 cm^{-1}, and the hydroxyl stretching peak at 3573 cm^{-1} (not shown).[16] Interestingly, many of these peaks overlap with peaks seen in the Raman spectrum of the xerogel species in **Figure 7.5b** (blue trace). The formation of malachite crystals from a Cu-carbonate-hydroxide gel precursor is a very common synthesis method for malachite.[17,18] These findings validate the proposed corrosion mechanism for Stages 3 and 4.

Growth of a carbonate species is more thermodynamically favoured than that of a basic copper nitrate complex ($Cu_2(CO_3)(OH)_2$ $\Delta G_f = -903.3$ kJ/mol; $Cu_2(NO_3)(OH)_3$ $\Delta G_f = -653.2$ kJ/mol).[19,20] Thus, despite the presence of nitrate in this solution, $Cu_2(CO_3)(OH)_2$ formation is energetically favoured during Stage 4. The malachite crystals are large but widely dispersed and only account for 1.0 ± 0.5 nmol of copper (compared to the 7.69 ± 2.73 μmol of copper present in Cu_2O). Although the main 'corrosion' product in this stage is malachite, most copper is still in the form of Cu_2O after the longest measured timeframe.

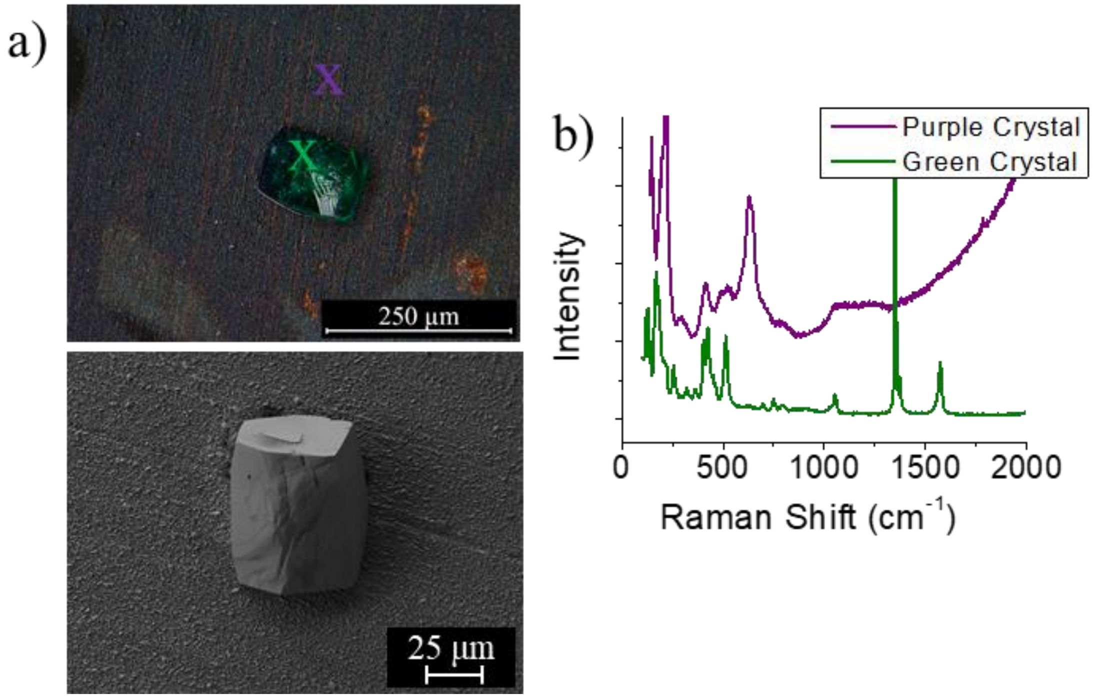

Figure 7.8 a) Images (optical in top row and SEM in bottom row) and b) Raman spectra of the purple and green crystals on a copper surface corroded for 480 h in the presence of 100 μL of aerated pure water in the presence of γ-radiation.

Overall, the time-dependent behaviours of the copper corrosion products in aerated and CO_2-free solutions are the same. However, the yields in and durations of each stage vary slightly. The presence of HCO_3^- in solution has been reported to passivate the copper surface.[21,22] The results presented in this chapter show the surface did not passivate, however, Stage 4, when the metal oxidation rate was zero, began earlier in aerated solutions. The rates, durations, and yields in each corrosion stage in all cover gas compositions are outlined in **Table 7.4**.

7.3.2 Corrosion Dynamics in the Presence of Radiolytically-Produced HNO_3

Purging the atmosphere and solution with 21% O_2 (balance Ar) removes the N_2 from the air and thus, prevents production of HNO_3 in the presence of radiation. Water radiolysis still produces acidic products (i.e., H^+) that cause the pH to decrease with time (see the pH evolution in Ar-purged solutions without a corroding system in **Appendix A**). The results presented in this chapter show that the impurity concentration of CO_2 was not negligible at 1 ppm by volume. The time-dependent behaviours of $\log([Cu^{II}_{(sol'n)}])$, pH, and the surface morphology and colour observed during copper corrosion in the absence of radiation were similar to that in aerated solutions and are presented in **Appendix C**. The time-dependent behaviours of $\log([Cu^{II}_{(sol'n)}])$, pH, and the surface morphology and colour observed during radiolytic copper corrosion are presented in **Figures 7.9** and **7.10**. The following are the key observations.

Stage 1: When $t \leq 24$ h, $[Cu^{II}_{(sol'n)}]$ increased quickly while the surface generally remained clean from granular oxides. The rate of increase in $[Cu^{II}_{(sol'n)}]$ was the same as in aerated and CO_2-free solutions.

Stage 2: For $48 \text{ h} \leq t \leq 120$ h, $[Cu^{II}_{(sol'n)}]_t$ remained constant at 3.4 ± 0.2 mM, a lower value than in aerated solutions. Unlike in other solution compositions, pH_t continued to decrease throughout this stage, with a final value of 4.9 ± 0.5. The surface remained generally clean of oxides and only a few patches of clear, dried hydrogel were observed.

Stage 3: For $144 \text{ h} \leq t \leq 240$ h, $[Cu^{II}_{(sol'n)}]_t$ increased at a rate slower than in Stage 1. The surface was mainly purple in colour, but some pink oxides were observed. Spirals on the faces of Cu_2O crystals indicate a screw-dislocation-driven growth, a requirement for which is a low supersaturation concentration of the crystal constituents.

<u>Stage 4:</u> By t = 480 h, $[Cu^{II}_{(sol'n)}]_t$ decreased slightly to 6.4 ± 4.0 mM, while pH_t did not change from the steady-state value reached in <u>Stage 3</u>. The surface was covered in a thick layer of pink and purple-coloured crystals.

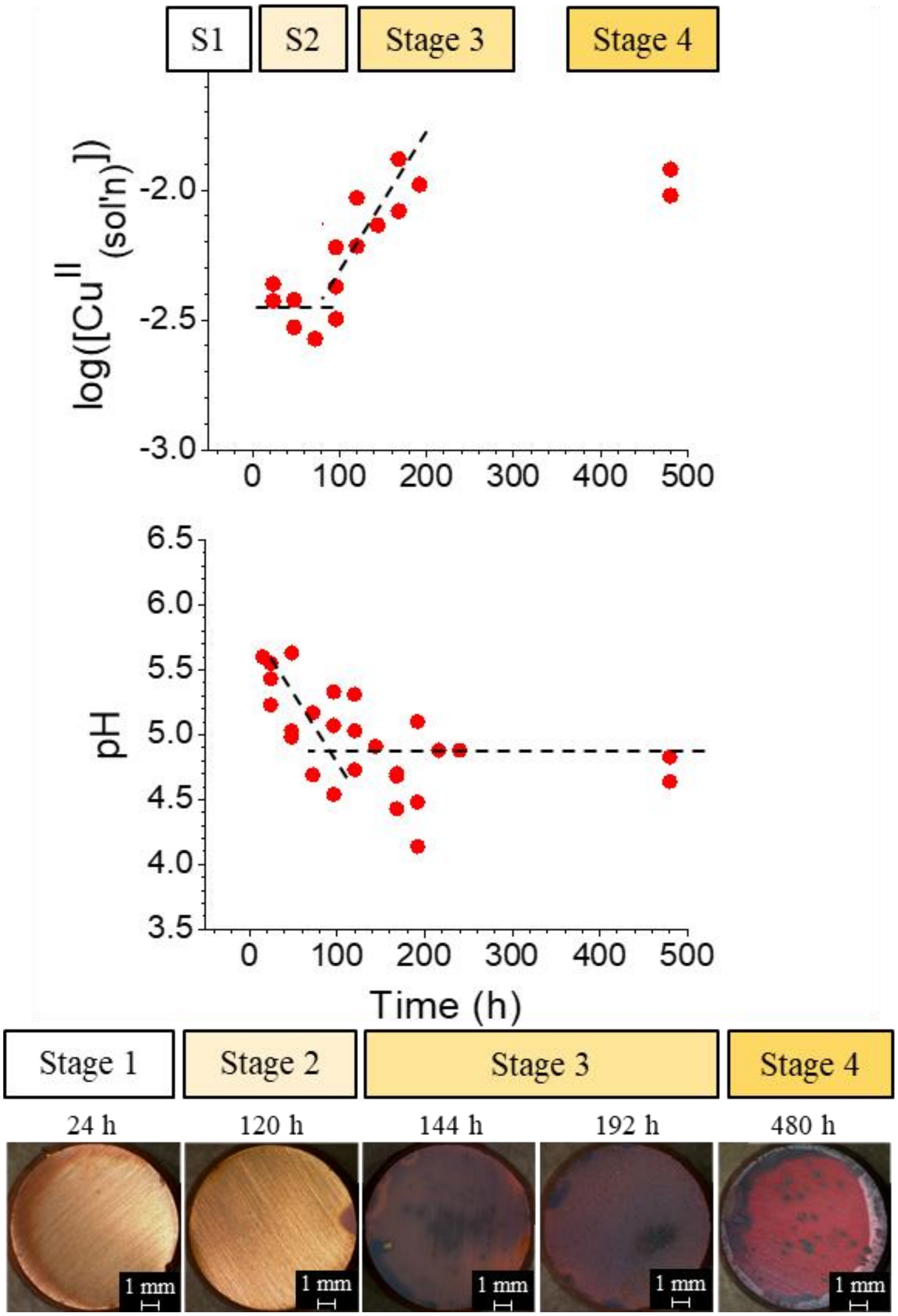

Figure 7.9 Time-dependent behaviour of $[\mathrm{Cu^{II}}_{(\mathrm{sol'n})}]$ (top row), pH (middle row), and the exposed surface (optical images, bottom row) during copper corrosion after exposure to a 100 µL droplet of water previously purged with 21% O_2 (balance Ar) (pH_0 = 7.0) in the presence of γ-radiation. The black dotted lines show the general trend of the data (not based on regression analysis).

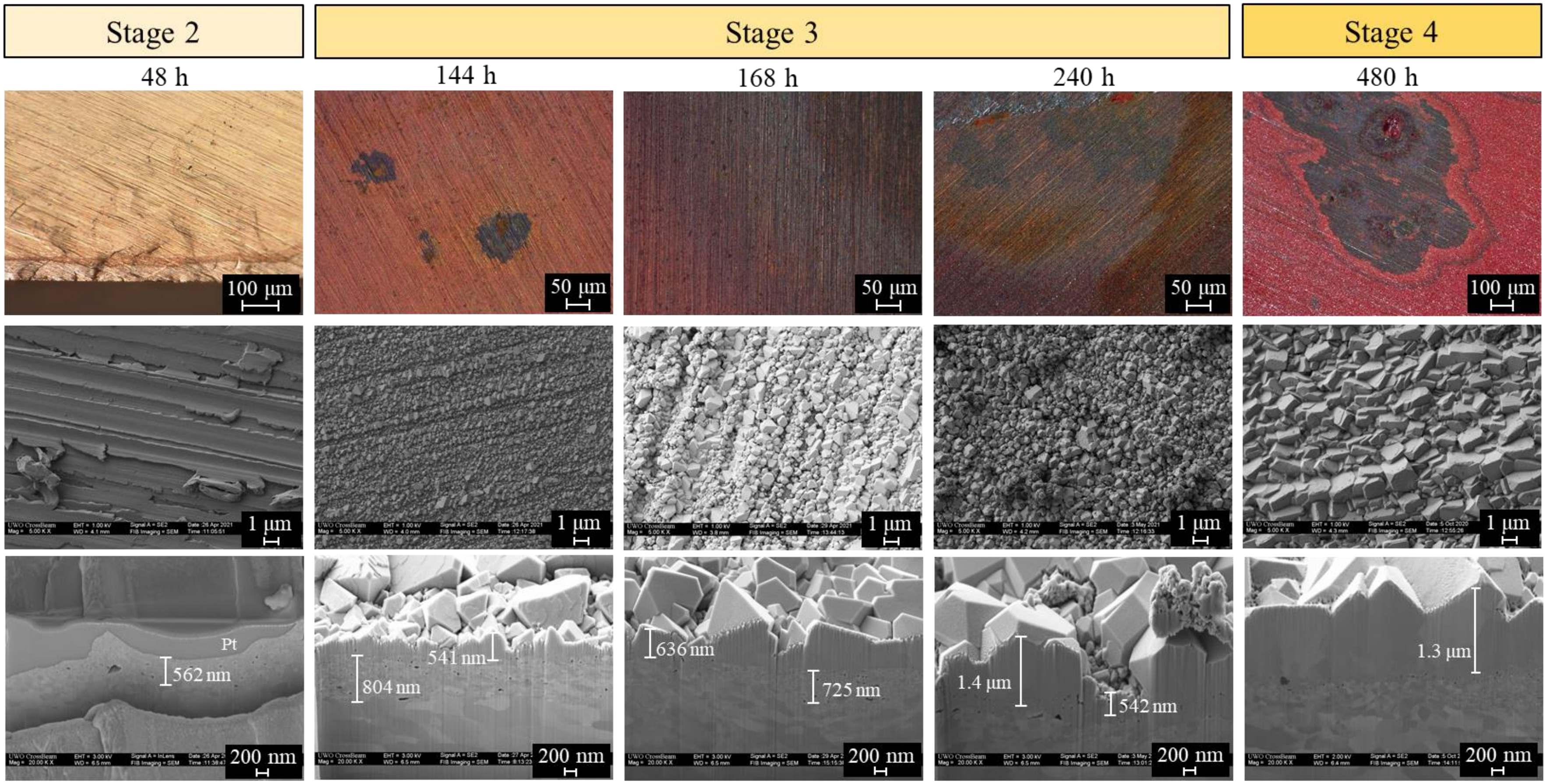

Figure 7.10 Optical (top row) and SEM images of the surface (middle row) and the metal-oxide cross section (bottom row) (cut using focused Ga-ion beam) in each stage of corrosion in solutions previously purged with 21% O_2 (balance Ar) in the presence of radiation.

The first measured pH_t (t = 24 h, **Figure 7.9**) was the same as that in aerated solutions (5.6). Because the bicarbonate buffer system existed in this solution, the same corrosion steps are followed in both aerated and HNO_3-free solutions (**Eq. 7.8**). Thus, Stage 1 was observed in the first 24 h, when $[Cu^{II}_{(sol'n)}]$ increased, pH_t was constant, and the surface showed no oxide growth (**Figure 7.9**). The dissolution rate in Stage 1 was 0.19 ± 0.03 mM/h, corresponding to a metal oxidation rate of 11.9 ± 2.2 nmol $Cu/cm^2/h$, which was the same rate as observed in Stage 1 in the presence of radiation in other cover gas compositions (**Table 7.4**). Because the metal oxidation rate is determined by the diffusion rate of cupric ions, it is unaffected by the absence of NO_3^- in Stage 1. The duration of Stage 1 in HNO_3-free solutions was the same as in aerated solutions, indicating that even the trace concentration of HCO_3^- in solution can accelerate the agglomeration and precipitation of $Cu(OH)_2$ colloid particles.

For $48\ h \leq t \leq 120\ h$, $[Cu^{II}_{(sol'n)}]$ was constant (**Figure 7.9**) and dried patches of hydrogel were observed on the surface (**Figure 7.10**), characteristic of Stage 2. Stage 2 starts after $Cu(OH)_2$ is supersaturated and precipitates first as colloid particles then as a hydrogel network. Some patches of dried hydrogel were observed in the optical images after 48 h (**Figure 7.10**), appearing clear and colourless with no blue colour indicative of a low colloid density. Without the production of HNO_3 in these solutions, the pH decreases slowly throughout Stage 2 reaching a steady-state value only at the end of the stage (**Figure 7.9**). Because the pH remained higher in HNO_3-free solutions, the solubility of cupric ions was lower than in other solutions. Accordingly, the plateau in $[Cu^{II}_{(sol'n)}]$ was lower at 3.4 ± 0.2 mM (**Figure 7.9**), which is also consistent with the low colloid density observed in the hydrogel.

In HNO_3-free solutions, Stage 2 was longer than in aerated and CO_2-free solutions (summarized in **Table 7.4**). When nitrate is present in irradiated solutions, it reacts with radicals (mainly $e^-_{(aq)}$ and •OH) that decompose H_2O_2, thereby increasing the steady-state concentration of H_2O_2.[23] Thus, in HNO_3-free solutions, the steady-state concentration of H_2O_2 is lower. With a low H_2O_2 concentration, the rate of reduction of $Cu(OH)_2$ to CuOH (**Eq. 7.9**) is low, and it takes a long time to reach CuOH supersaturation. Therefore, in HNO_3-free solutions, Stage 2 is elongated.

Stage 3 begins when CuOH reaches a supersaturation concentration and precipitates as Cu_2O, observed in nitrate solutions for $144\ h \leq t \leq 240\ h$ when the surface is completely covered with purple and pink oxides (**Figures 7.9** and **7.10**). The film thickness and the amount of copper in the oxide layer was quantified and summarized in **Table 7.2**, by using the SEM images of the oxide-metal interface in **Figure 7.10**. The average precipitation rate, assuming the film was entirely Cu_2O, was determined to be 50 ± 11 nmol $Cu/cm^2/h$. This is a slower precipitation rate than in CO_2-free and aerated solutions (all rates are summarized in **Table 7.4**) due to the lower supersaturation concentration of CuOH in the HNO_3-free solution, indicated by lower $[Cu^{II}{}_{(sol'n)}]_t$ and less hydrogel growth. The lower supersaturation concentration of CuOH is also confirmed by the shape of the Cu_2O crystals, as shown and discussed next.

Table 7.2 Amount of copper in the solution and in the surface oxides during corrosion in the presence of radiation in an atmosphere of 21% O_2 (balance Ar).

Stage	**Time (h)**	**n_{Cu} in solution (μmol)**	**n_{Cu} in oxide (μmol)**
2	48	0.13 ± 0.02	~ 0
3	144	0.39 ± 0.12	1.91 ± 1.20
	168	0.53 ± 0.17	3.71 ± 1.59
	240	2.25 ± 0.32	7.56 ± 2.47
4	480	0.30 ± 0.15	10.20 ± 3.09

High magnification SEM images of the Cu_2O crystals during Stage 3 (t = 144 h) are shown in **Figure 7.11**. Spirals on the {100} faces on the Cu_2O crystals are characteristic of a screw dislocation growth mechanism. Screw-dislocation-driven crystal growth requires the reactants to be at a low supersaturation concentration, so that the crystal growth is faster at the dislocation spirals along the z-direction than the radial (xy-direction, across the crystal face).[24,25] This mechanism of crystal growth validates the proposed corrosion mechanism in Stage 3 and the effects of the HNO_3-free solution.

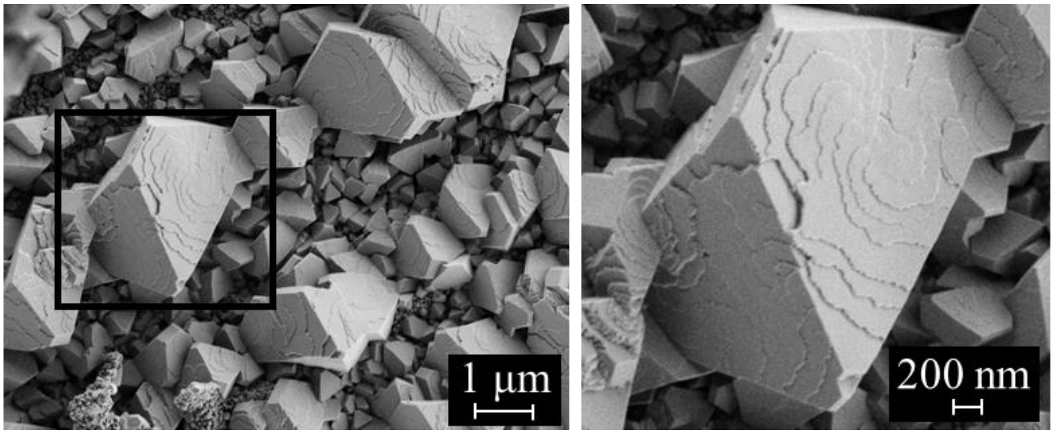

Figure 7.11 Screw dislocations on the Cu_2O crystals after 144 h of radiolytic corrosion HNO_3-free solutions.

Once the oxide layer had grown thick enough to hinder electron transport, Stage 4 begins. Without its production via metal oxidation, $[Cu^{II}_{(sol'n)}]$ decreases to 6.0 ± 3.0 mM (**Figure 7.9**) and the precipitation rate of Cu_2O slows (**Figure 7.12**). The metal oxidation rate in this stage is zero, but precipitation and the redox-assisted Ostwald ripening of crystals continues. When anions are present in solution, they can participate in the reprecipitation of cupric ions during redox-assisted Ostwald ripening, which converts Cu_2O into cupric-hydroxy-anion crystals. Nitrate was incorporated into the hydrogel network in CO_2-free solutions, and large copper-hydroxy-carbonate (malachite) crystals were observed in aerated solutions. Despite it being present in trace amounts, there was no indication of carbonate incorporation into the hydrogel or as crystals in HNO_3-free solutions.

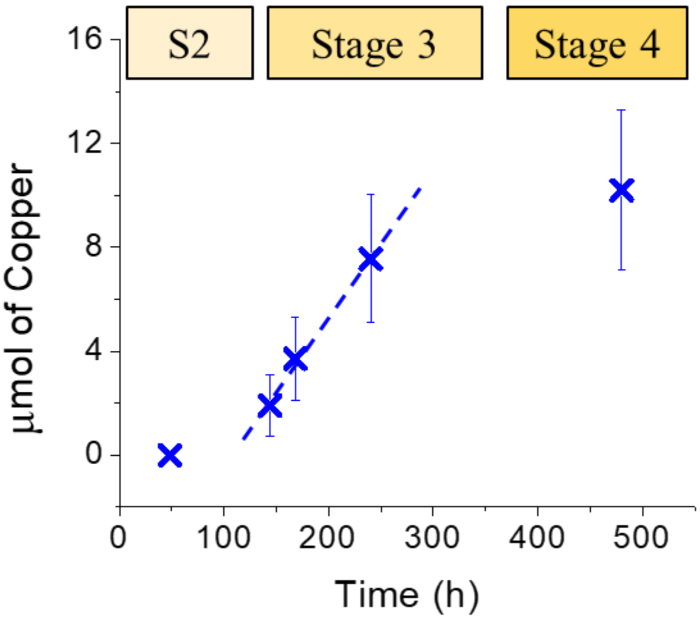

Figure 7.12 Amount of copper in Cu_2O during radiolytic corrosion as a function of corrosion time in solutions previously purged with 21% O_2 (balance Ar).

This section investigated radiolytic copper corrosion in the absence of radiolytically-produced HNO_3. Without the production of HNO_3, the pH decreased slowly throughout Stages 1 and 2 and reached a relatively high steady-state value. The rate of Stage 1 was unaffected, but the $[Cu^{II}_{(sol'n)}]$ yield at the end of the stage was lower. Lower $[Cu^{II}_{(sol'n)}]$ during Stage 2 results in a lower concentration of cupric and cuprous ions within the hydrogel. Without nitrate, the concentration of H_2O_2 was lower, which contributed to the elongation of Stage 2 and lower [CuOH] within the hydrogel. The lower supersaturation concentration of CuOH was confirmed by the screw-dislocations observed on the Cu_2O crystals during this stage. With less CuOH, the precipitation rate in Stage 3 was lower. The rates and durations of each stage are summarized in **Table 7.4**.

7.3.3 Corrosion Dynamics in Deaerated Solutions

Solutions and vials used in this section were purged with $Ar_{(g)}$ before the onset of corrosion. Copper's high reduction potential renders its oxidation by water impossible.[26] In deaerated solutions in the absence of radiation, the oxidant for copper corrosion can only be the trace amount of O_2 trapped in solution (2 ppm by volume). In the presence of radiation, water will decompose into redox active and acidic species that are always produced, however, the steady-state concentrations are different than those in aerated solutions, discussed in detail later.

7.3.3.1 In the Absence of Radiation

The time-dependent behaviours of log([$Cu^{II}_{(sol'n)}$]), pH, and the surface morphology and colour observed during copper corrosion in deaerated solutions in the absence of radiation are shown in **Figure 7.13**. The key observations are listed below, and an in-depth discussion follows.

Stage 1: When t ≤ 48 h, [$Cu^{II}_{(sol'n)}$] increased with time. The concentration of cupric ions in solution is approximately the same as was seen in oxygenated solutions. The surface was a yellow colour indicating the coverage by a thin layer of small Cu_2O crystals. The pH remained constant at the initial pH (7.0).

Stage 2: For 48 h ≤ t ≤ 72 h, [$Cu^{II}_{(sol'n)}$]$_t$ remains constant with time which is characteristic of this stage, during which the hydrogel growth is controlling the overall rate of corrosion. The pH_t decreased at the start of the stage but remained constant at 6.5 ± 0.4. This stage was very short in these highly reducing conditions, and the hydrogel was not directly observed.

Stage 3: When t ≥ 96 h, a large proportion of the surface is covered with pink and purple oxides. The pH remains constant at the value from Stage 2. [$Cu^{II}_{(sol'n)}$] at all *t* is equal to or higher than that in oxygenated solutions.

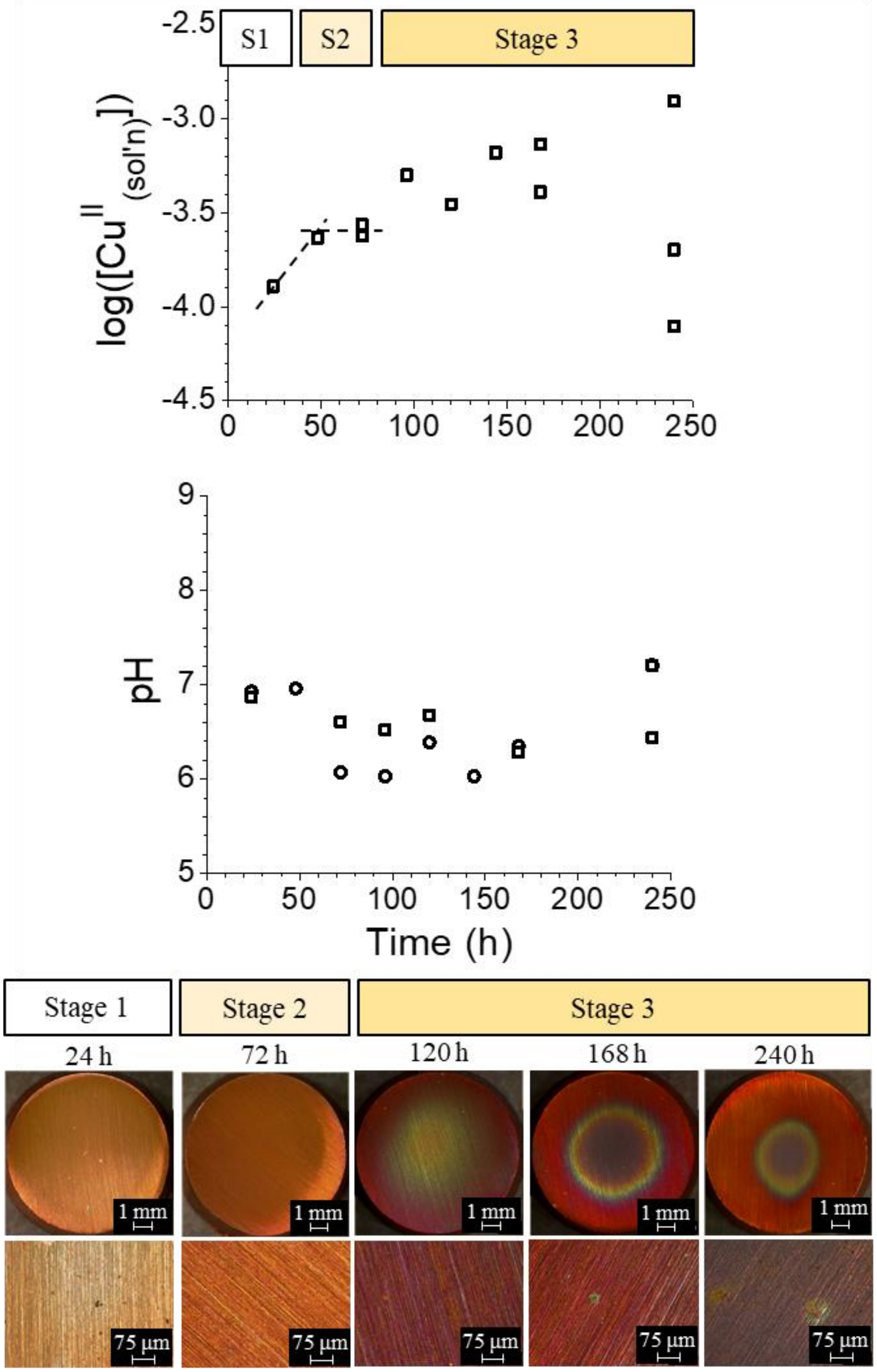

Figure 7.13 Time-dependent behaviour of [$Cu^{II}_{(sol'n)}$] (top row), pH (middle row), and the exposed surface (optical images, bottom row) during copper corrosion after exposure to a 100 µL droplet of Ar-purged water ($pH_0 = 7.0$) in the absence of γ-radiation. The black dotted lines show the general trend of the data (not based on regression analysis).

In the first 48 h, the pH does not change significantly from its initial value of 7.0, shown in **Figure 7.13**. This indicates that the production of OH^- via the initial charge transfer reactions, and the consumption of OH^- via cupric ion hydrolysis are stoichiometrically equal. Thus, in deaerated solutions the overall corrosion reaction in Stage 1 is:

$$Cu^0_{(m)} + ½\, O_2 + H_2O \rightarrow Cu(OH)_{2(solv)} \qquad (7.12)$$

As the concentration of $Cu(OH)_{2(solv)}$ increases, it will precipitate as colloid species. Because there are no significant variations in $[OH^-]$ from $z = 0$ to the bulk solution, the precipitation will happen approximately homogeneously in the interfacial and bulk solution. Like in oxygenated solution, $[Cu^{II}{}_{(sol'n)}]$ during Stage 1 increases linearly shown in **Figure 7.13**, due to the continuous production of dissolved/dispersed cupric species. However, the surface during this stage is yellow (**Figure 7.13**), indicating that the surface is covered with small Cu_2O crystals.

The colloid particles begin to agglomerate and grow as a hydrogel network in Stage 2, observed in **Figure 7.13** for 48 h ≤ t ≤ 72 h, when $[Cu^{II}{}_{(sol'n)}]$ is constant with time. The $[Cu^{II}{}_{(sol'n)}]$ plateau was at 0.25 ± 0.02 mM, which is the same as in CO_2-free solutions. That is, despite significantly less O_2 in solution, the amount of metal loss (copper dissolution) in deaerated solutions is approximately equal to that in oxygenated solutions (without CO_2), demonstrating that the oxidant concentration does not affect the overall metal oxidation yield.

As shown in previous chapters and previous sections in this chapter, the hydrogel growth includes the precipitation of $Cu(OH)_2$ colloid particles that join the solid network, as well as redox coupling that produces a mixed Cu^I/Cu^{II} hydroxide hydrogel (**Eq. 7.6**). These reactions create a cyclic feedback loop in the hydrogel growth. Deaerated solutions are more reducing than oxygenated solutions, and therefore the reduction of $Cu^{2+}{}_{(sol'n)}$ is more efficient. Accordingly, Stage 2 in deaerated solutions is short (24 h, compared to 152 h in CO_2-free solutions, summarized in **Table 7.4**) and the complete coverage of the surface by oxides begins early. When t ≥ 96 h, the surface is pink and purple (optical images in **Figure 7.13**), indicating large Cu_2O crystals had grown on the entire surface with various thicknesses of a $Cu(OH)_2$ layer over the crystals.

Despite the significantly lower O_2 concentration, the measured $[Cu^{II}_{(aq)}]$ within the experimental timeframe is within the range seen in the presence of other cover gases (0.1 to 1.6 mM). This is consistent with the results presented in **Chapter 5** which showed that the oxidant concentration had little effect on copper dissolution rate or yield. It is also consistent with our proposed mechanism, in which the metal cation transport rate determines the overall metal oxidation rate, and the $Cu(OH)_2$ solubility determines maximum yield of dissolved cupric ions. The same $[Cu^{II}_{(sol'n)}]$ and more oxide growth in Stage 3 indicates more overall $Cu^0_{(m)}$ loss in deaerated solutions than in oxygenated solutions.

The time-dependent results from deaerated solutions show that copper dissolves to the same extent regardless of $[O_2]$. The results presented in this section also show that direct oxidation of $Cu^0_{(m)}$ to Cu_2O is unlikely even in solutions with a very low concentration of O_2. Deaerated solutions are more reducing which allows the concentration of cuprous ions within the hydrogel to increase faster than in oxygenated solutions. Thus, Stage 3 begins early and large Cu_2O crystals can grow.

7.3.3.2 In the Presence of Radiation

In deaerated solutions, only water, not humid air, will undergo radiolytic decomposition. Thus, HNO_3 is not produced in these solutions. Many key water radiolysis species, including H_2O_2 and O_2, are produced in a much lower steady-state concentration in deaerated solutions due to a low initial O_2 concentration. Other species, including •OH and $e^-_{(aq)}$, are produced in higher concentrations.[27] Thus, deaerated solutions are less oxidizing than aerated solutions.

The time-dependent behaviours of $\log([Cu^{II}_{(sol'n)}])$, pH, and the surface morphology and colour observed during radiolytic copper corrosion in deaerated solutions are shown in **Figures 7.14** and **7.15**. The observations described below allowed for the identification of the stages.

Stage 2: By the first measurement (24 h), $[Cu^{II}_{(sol'n)}]$ had increased to 1.8 ± 0.2 mM and the pH decreased to its steady-state value of 4.3 ± 0.4, which was lower than in oxygenated solutions. A large proportion of the surface is blue, indicating $Cu(OH)_2$ hydrogel growth.

Stage 3: For $t \geq 48$ h, $[Cu^{II}_{(sol'n)}]$ increased linearly with time for the length of the experiment, while pH_t remained constant. The surface is covered with mostly purple granular oxides, with variations in size of oxides between the middle and the edge of the coupon. The Cu_2O precipitation rate was constant.

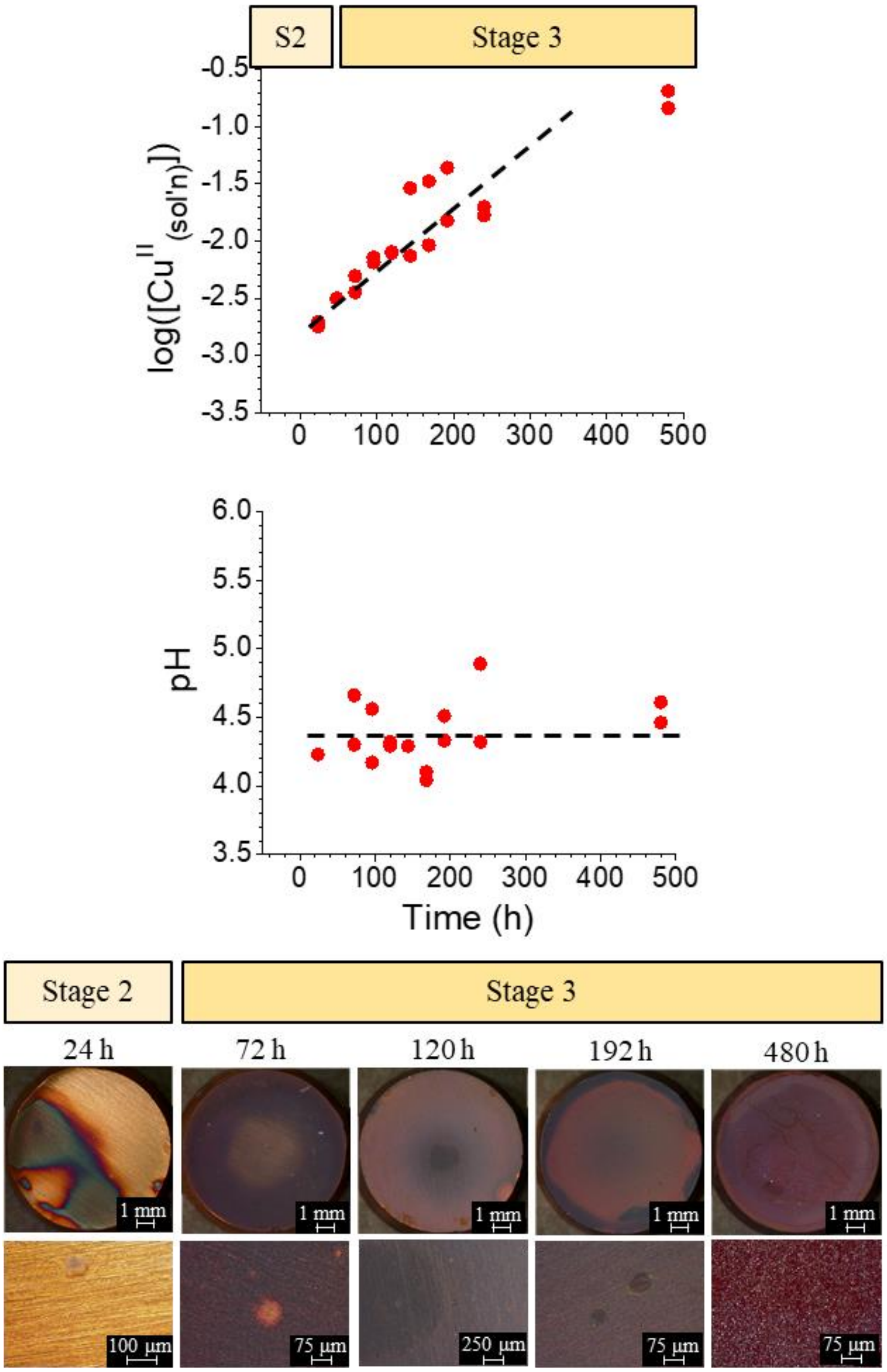

Figure 7.14 Time-dependent behaviour of [$Cu^{II}_{(sol'n)}$] (top row), pH (middle row), and the exposed surface (optical images, bottom row) during copper corrosion after exposure to a 100 µL droplet of Ar-purged water ($pH_0 = 7.0$) in the presence of γ-radiation. The black dotted lines show the general trend of the data (not based on regression analysis).

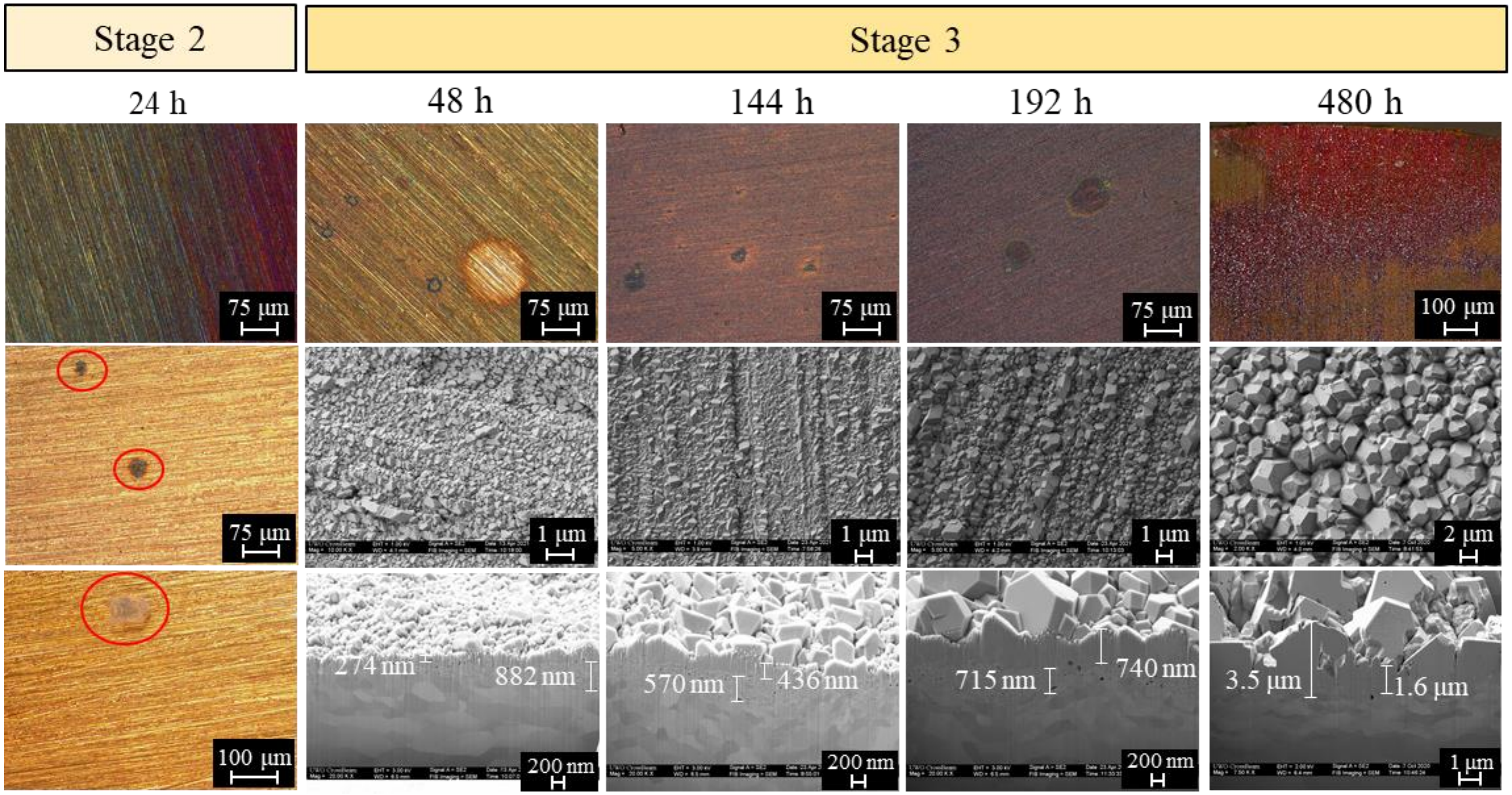

Figure 7.15 Optical and SEM images of the surface and the metal-oxide cross section (cut using focused Ga-ion beam) in each stage of corrosion in Ar-purged solutions in the presence of radiation. The red circles indicate patches of dried hydrogel.

By the first measurement (24 h), the surface was partially covered in a blue species (optical images in **Figures 7.14** and **7.15**), indicating hydrogel growth. Localized areas of hydrogel growth were also observed in **Figure 7.15**, indicated by the red circles. Some patches appeared as blue circles surrounded by a yellow ring (middle row in Stage 2 in **Figure 7.15**), some had a lower colloid density and were transparent and colourless (bottom row in Stage 2 in **Figure 7.15**). $[Cu^{II}_{(sol'n)}]_t$ had increased to 1.8 ± 0.2 mM and pH_t decreased from 7.0 to 4.3. These observations suggest the main corrosion process at this time is hydrogel growth. Thus, the progression through Stages 1 and 2 is very quick in irradiated deaerated solutions (24 h, compared to 100 h in CO_2-free solutions in **Chapter 6**).

In unirradiated solutions, it was shown that the main form of cupric ions in Stage 1 is $Cu(OH)_{2(solv)}$ and the net production of $[OH^{-}]$ (or $[H^{+}]$) is zero. Thus, the radiolytic production of acidic species (mostly H^{+}) causes pH to decrease quicker than it does in oxygenated solutions. Accordingly, **Figure 7.14** shows that within 24 h, pH was at its low steady-state value of 4.3 ± 0.4. As the concentration of cupric ions increases $Cu(OH)_2$ precipitates as colloid particles and a hydrogel network on the surface. In the more reducing solution, the reduction of cupric ions in the hydrogel to cuprous ions (**Eq. 7.9**) starts almost immediately after precipitation), and thus, Stage 2 is shorter in deaerated compared to oxygenated solutions (also observed in unirradiated solutions).

For the remainder of the experimental timeframe (48 – 480 h), pH remained at a low steady-state value of 4.3 ± 0.4, $[Cu^{II}_{(sol'n)}]$ increased with time, and the surface was completely covered with purple and pink-coloured oxides (**Figure 7.14** and **7.15**). The complete coverage by Cu_2O particles is characteristic of Stage 3. Stage 3 begins after CuOH within the hydrogel reaches supersaturation and because the reduction of cupric ions begins early in deaerated solutions, Stage 3 was observed to start early compared to in oxygenated solutions. The rate of precipitation was quantified by the Cu_2O layer thickness obtained from the SEM images of the metal-oxide interface (bottom row in **Figure 7.15**). The amount of copper in the oxide layer compared to in solution is shown in **Table 7.3**, and the precipitation rate is illustrated in **Figure 7.16**. The precipitation rate in deaerated solutions was 47 ± 4.5 nmol $Cu/cm^2/h$, a slower rate than in oxygenated solutions (all rates are summarized in **Table 7.4**). The slower precipitation rate is consistent with the results presented in **Chapter 5** that showed that the amount of Cu_2O

precipitation is directly proportional to [H_2O_2]. That is, although Cu_2O growth starts earlier in the deaerated solutions compared to oxygenated solutions, its formation is slower because of the lower [H_2O_2].

Table 7.3 Amount of copper in the solution and in the surface oxides during corrosion in the presence of radiation in a deaerated atmosphere.

Stage	Time (h)	n_{Cu} in solution (µmol)	n_{Cu} in oxide (µmol)
3	48	0.16 ± 0.05	1.80 ± 0.87
	144	0.91 ± 0.76	2.87 ± 1.35
	192	1.47 ± 1.01	4.87 ± 1.75
	240	0.91 ± 0.11	7.30 ± 1.84
	480	8.76 ± 2.14	15.4 ± 3.95

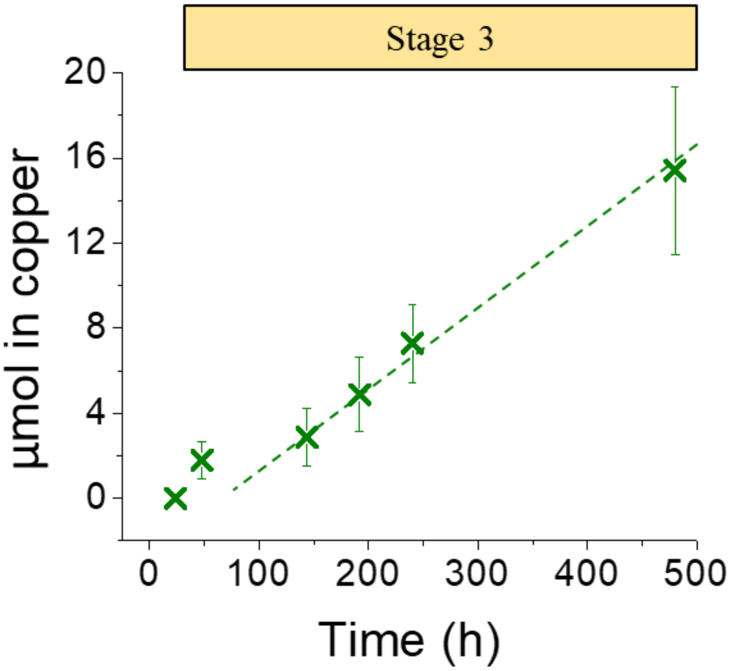

Figure 7.16 Amount of copper in Cu_2O as a function of radiolytic corrosion time in deaerated (Ar-purged) solutions.

In deaerated solutions, Stage 4 was not observed even after 480 h, indicated by the continuous increase in both [$Cu^{II}_{(sol'n)}$] (**Figure 7.14**) and oxide film thickness (**Figure 7.16**) that show that metal oxidation is not zero. That is, despite the oxide thickness being comparable to that in other solutions (**Table 7.4**), metal oxidation through it is not impeded. This is attributed to two characteristics of the oxide film that were unique to that grown in deaerated solutions and discussed below.

The metal-oxide interfaces after 480 h in deaerated and oxygenated solutions are shown in **Figure 7.17**. The interface in all oxygenated solutions is smooth and the oxide layer is approximately uniform across the surface. However, in deaerated solutions, crystals grew individually and large, as opposed to growing a compact film. The growth of individual particles as opposed to in a compact film is a result of the slower precipitation. Slow precipitation allows the crystal constituents to precipitate in the most favourable location (on other crystals), as opposed to forming many small seed crystals which grow uniformly on the surface.[28] Thus, although the entire surface is covered with oxides, some areas are covered by only a thin layer of oxides (indicated by the red circle in **Figure 7.17**) and charge transfer (metal oxidation) can continue in these areas.

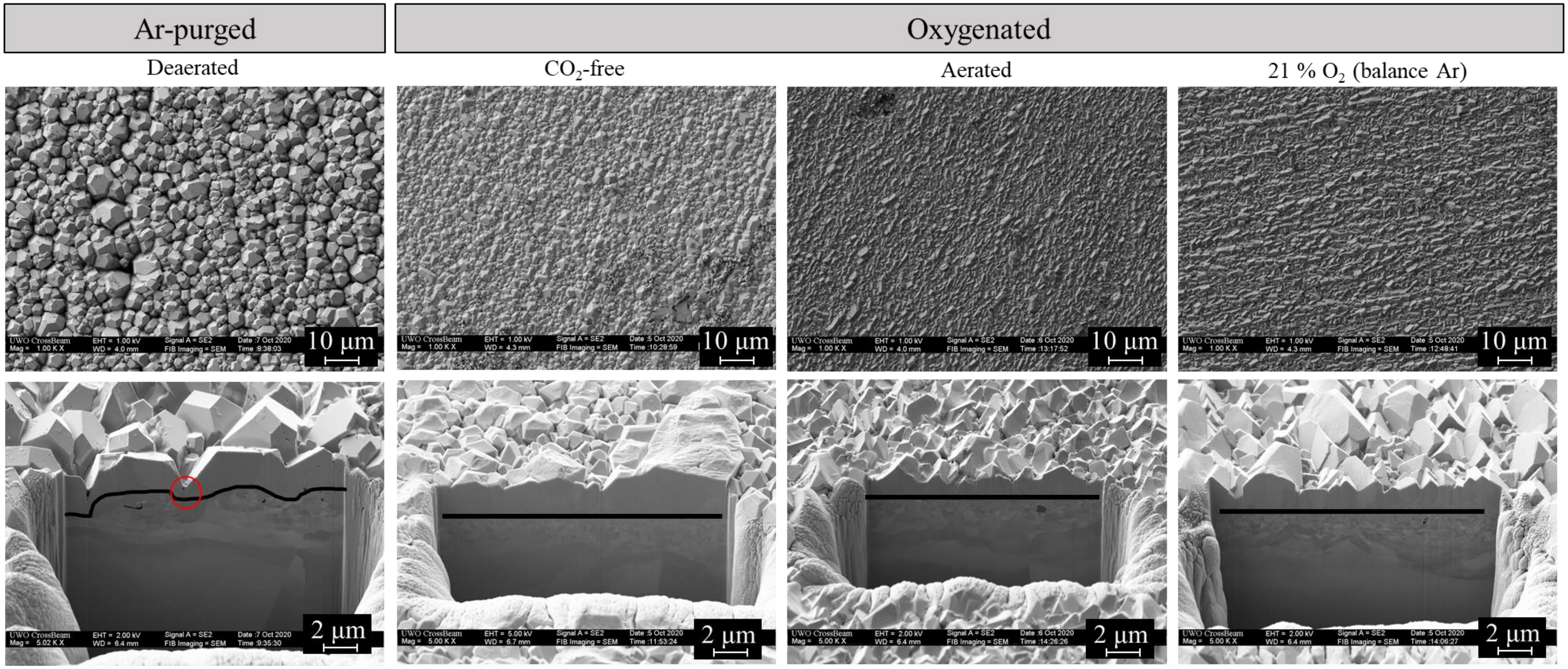

Figure 7.17 SEM images of the surface (top row) and cross-section (bottom row) of the oxides grown after 480 h of corrosion time in the presence of radiation in Ar-purged and oxygenated solutions. The black line indicates the metal-oxide interface.

Another observation that was unique to deaerated solutions was that there was a significant difference in colour and Cu_2O crystal size throughout Stage 3 (**Figure 7.14**). **Figure 7.18** shows optical and SEM images from the middle and the edge of the coupon after 480 h of radiolytic copper corrosion in deaerated solutions. Cu_2O crystals at the edges of the coupon show substantially more signs of dissolution than those in the centre. Dissolution of the oxides on the edges occurred indiscriminately on all faces, although some of the more intact oxides had collapsed {100} facets (indicated with red arrow in **Figure 7.18**, the same facet that was hoppered in aerated solutions). Thus, metal surface is more exposed to the solution on the edges of the coupon allowing continuous metal oxidation in this area. In sum, the oxide film thickness has significant variations on a small scale (shown in **Figure 7.17**) and on a larger scale (across the entire surface, shown in **Figure 7.18**).

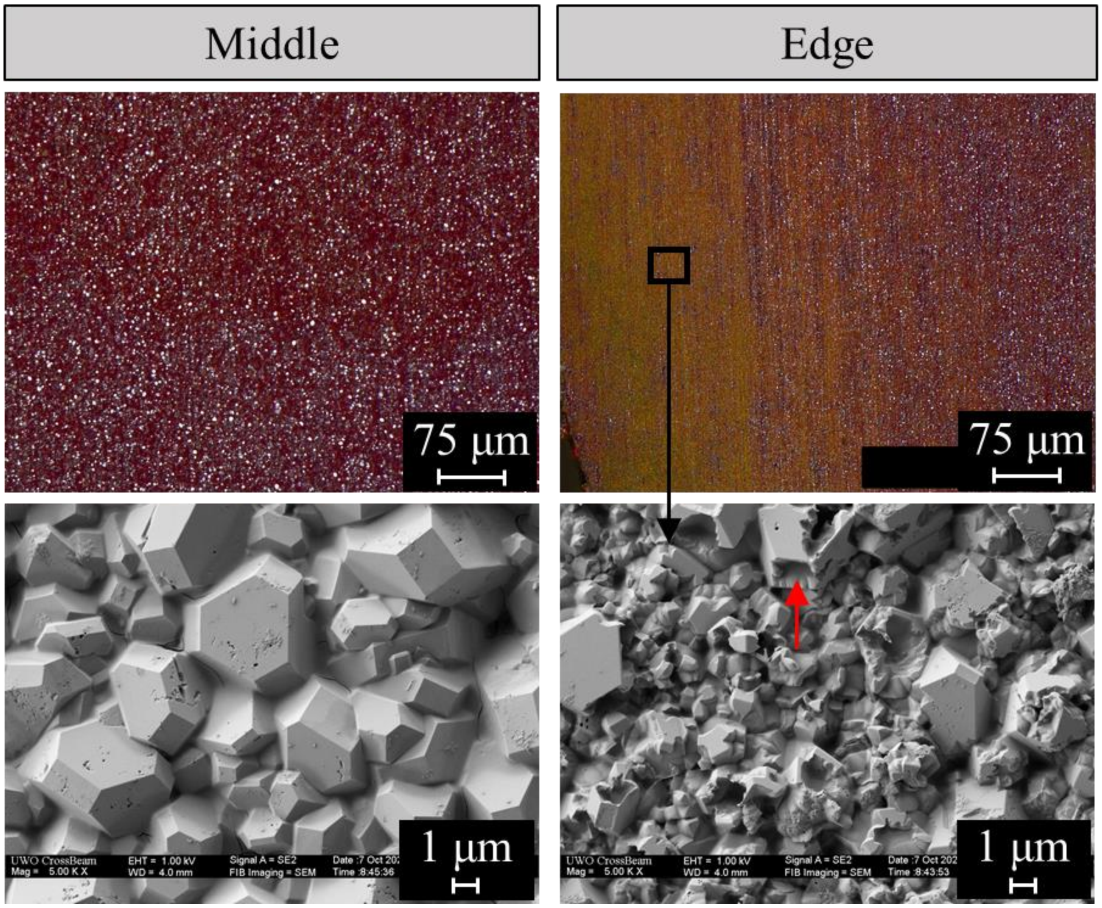

Figure 7.18 Optical (top row) and SEM (bottom row) images of the middle and edge of the coupon after 480 h of corrosion time in deaerated solutions in the presence of γ-radiation. The red arrow indicates the sunken-in {100} facet.

Recently, a paper was published[29] that proposed that the main oxidant in the presence of radiation is O_2, not H_2O_2. These experiments clearly show that this cannot be the case. In the presence of radiation two orders of magnitude less O_2 is produced in the deaerated environment than in aerated conditions, yet both solutions result in same measured $[Cu^{II}_{(sol'n)}]$ and similar oxide growth (when t ≤ 192, but more oxide growth in deaerated solution at t = 480 h). The authors reached this conclusion based on experiments done in N_2-purged solutions compared to aerated solutions without purging, but in this case, it is not the removal of O_2 that causes less oxide growth (in N_2-purged solutions), it is the physical removal of $Cu^{2+}_{(sol'n)}$ from the surface by the fluid convection caused by purging. This physical removal of $Cu^{2+}_{(sol'n)}$ from the surface prolongs its accumulation, and thus, reaching stages beyond Stage 1 is difficult.

This section showed that the elementary reactions that control the corrosion rate as a function of time are the same in deaerated and oxygenated solutions. Because deaerated solutions are more reducing, $Cu(OH)_2$ reduction to CuOH (which precipitates as Cu_2O) is more efficient and Stage 2 is short. Oxide growth started earlier but the rate of its formation was slower due to a lower $[H_2O_2]$, resulting in the individual particles growing in size, rather than the formation of a compact layer. Charge transport through the oxide (Stage 4) was not observed in the experimental timeframe, as it was for oxygenated solutions, thus the $[Cu^{II}_{(sol'n)}]$ yield at the end of Stage 3 was higher than that in oxygenated solutions (**Table 7.4**). This suggests that there is more material loss in deaerated solutions than in oxygenated solutions.

7.4 CONCLUSIONS

The effects of cover gas composition on copper corrosion dynamics were investigated. The cover gas environments chosen all add or remove a key pH-affecting or redox active species from solution and are all atmospheres the copper layer of the UFC may be exposed to. Aerated solutions contain CO_2/HCO_3, 21% O_2 (balance Ar) solutions do not produce HNO_3 via radiolysis, and deaerated solutions have only trace amounts of O_2 in solution. Regardless of this wide range of solution/cover gas compositions, the corrosion stages were consistent, however, the rates, durations, and/or yields in each corrosion stage change with solution composition and are summarized in **Table 7.4**.

Table 7.4 Summary of duration, rates, and yields in each stage during radiolytic copper corrosion after exposure to a 100 μL droplet of CO_2-free, aerated, 21% O_2 (balance Ar), and deaerated solution.

Cover gas:	**CO_2-free**	**Aerated**	**21% O_2**	**Deaerated**
Stage 1				
Duration (h)	40	24	24	--
$Cu^{II}_{(sol'n)}$ dissolution rate (nmol Cu/cm^2/h)	11.6 ± 1.2	12.6 ± 4.0	11.9 ± 2.2	--
Stage 2				
Duration (h)	48	48	72	24
[$Cu^{II}_{(sol'n)}$] plateau (mM)	6.0 ± 2.8	4.2 ± 2.1	3.4 ± 0.2	1.8 ± 0.2
Steady-state pH	4.6 ± 0.4	4.3 ± 0.4	4.9 ± 0.5	4.3 ± 0.4
Stage 3				
Duration (h)	72	72	96	48 <
Precipitation rate of Cu_2O (nmol Cu/cm^2/h)	62 ± 28	99 ± 52	50 ± 11	47 ± 4.5
$Cu^{II}_{(sol'n)}$ dissolution rate (nmol Cu/cm^2/h)	6.8 ± 1.3	35.8 ± 9.1	4.4 ± 0.5	13.6 ± 6.3
Stage 4				Stage 3
Observed after (h)	480	480	480	480
Amount of Copper in Oxides (μmol)	14.7 ± 3.2	7.7 ± 2.4 + 1.0 ± 0.5	10.2 ± 3.1	15.4 ± 3.9
Amount of Copper in Solution (μmol)	0.45 ± 0.08	0.43 ± 0.22	0.30 ± 0.15	8.8 ± 2.1
Total amount of Copper Oxidized (μmol)	15.2 ± 3.3	8.2 ± 3.3	10.5 ± 3.2	24.2 ± 6.0
Depth of Copper Oxidation (μm)	1.4 ± 0.30	0.74 ± 0.30	0.95 ± 0.29	2.2 ± 0.54

The rate of Stage 1 was not affected by any of the studied cover gas compositions. However, the presence of CO_2/HCO_3^- and O_2 prolonged Stage 1. Stage 2 was prolonged when HNO_3 is not present and in oxygenated solutions. The presence of CO_2/HCO_3^- resulted in a fast Cu_2O precipitation rate in Stage 3, while in deaerated solutions, it was slower. Stage 3 was much longer in deaerated solutions compared to oxygenated solutions due to large variations in oxide thickness across the surface allowing for continuous charge transfer.

The results in this chapter show that the proposed mechanism explains phenomena in all studied conditions. Regardless of the solution conditions, the elementary reactions that control the corrosion rate do not change. Similarly, the stepwise evolution of the elementary reactions with corrosion time (corrosion stages and their order) are unaffected by solution conditions. However, the rate of the individual elementary reactions can be dependent on solution conditions and the duration of the individual stages. In sum, this chapter established the combined effects of cover gas composition and the presence of γ-radiation on the corrosion dynamics. The results in this chapter contribute to the database required for the development of a robust copper corrosion model and thus, is a key step towards this future goal.

7.5 REFERENCES

1 King, F., Lilja, C., Pedersen, K., Pitkänen, P., Vähänen, M. *An Update of the State-of-the-Art Report on the Corrosion of Copper Under Expected Conditions in a Deep Geologic Repository* (SKB, 2010).

2 Morco, R. P., Joseph, J. M., Hall, D. S., Medri, C., Shoesmith, D. W., Wren, J. C. Modelling of Radiolytic Production of HNO_3 Relevant to Corrosion of a Used Fuel Container in Deep Geologic Repository Environments. *Corros. Eng. Sci. Technol.* **52**, 141-147, (2017).

3 Metz, B., Davidson, O., Coninck, H. d., Loos, M., Meyer, L. *Carbon Dioxide Capture and Storage*. (Cambridge University Press, 2005).

4 Wu, S., Hua, M., Alsaid, Y., Du, Y., Ma, Y., Zhao, Y., Lo, C.-Y., Wang, C., Wu, D., Yao, B., Strzalka, J., Zhou, H., Zhu, X., He, X. Poly(vinyl alcohol) Hydrogels with Broad-Range Tunable Mechanical Properties via the Hofmeister Effect. *Adv. Mater.* **33**, 2007829, (2021).

5 Xu, Y., Wang, C., Tam, K. C., Li, L. Salt-Assisted and Salt-Suppressed Sol−Gel Transitions of Methylcellulose in Water. *Langmuir* **20**, 646-652, (2004).

6 Sadeghi, R., Jahani, F. Salting-In and Salting-Out of Water-Soluble Polymers in Aqueous Salt Solutions. *J. Phys. Chem. B* **116**, 5234-5241, (2012).

7 Fukumoto, S., Nakanishi, K., Kanamori, K. Direct Preparation and Conversion of Copper Hydroxide-Based Monolithic Xerogels with Hierarchical Pores. *New J. Chem.* **39**, 6771-6777, (2015).

8 Henry, M., Bonhomme, C., Livage, J. Synthesis and Characterisation of Copper(II) Hydroxide Gels. *J. Sol-Gel Sci. Technol.* **6**, 155-167, (1996).

9 Saravanan, K., Tyagi, B., Bajaj, H. C. Nano-Crystalline, Mesoporous Aerogel Sulfated Zirconia as an Efficient Catalyst for Esterification of Stearic Acid with Methanol. *Applied Catalysis B: Environmental* **192**, 161-170, (2016).

10 Zanto, E. J., Al-Muhtaseb, S. A., Ritter, J. A. Sol−Gel-Derived Carbon Aerogels and Xerogels: Design of Experiments Approach to Materials Synthesis. *Ind. Eng. Chem. Res.* **41**, 3151-3162, (2002).

11 Chen, K., Sun, C., Song, S., Xue, D. Polymorphic Crystallization of Cu_2O Compound. *CrystEngComm* **16**, 5257-5267, (2014).

12 Desarnaud, J., Derluyn, H., Carmeliet, J., Bonn, D., Shahidzadeh, N. Hopper Growth of Salt Crystals. *J. Phys. Chem. Lett.* **9**, 2961-2966, (2018).

13 Chen, K., Song, S., Xue, D. Hopper-Like Framework Growth Evolution in a Cubic System: A Case Study of Cu_2O. *J. Appl. Crystallogr.* **46**, (2013).

14 Oaki, Y., Imai, H. Experimental Demonstration for the Morphological Evolution of Crystals Grown in Gel Media. *Cryst. Growth Des.* **3**, 711-716, (2003).

15 Giga, Y., Rybka, P. Berg's Effect. *Adv. Math. Sci. Appl.* **13**, 625-637, (2002).

16 Frost, R. L., Martens, W. N., Rintoul, L., Mahmutagic, E., Kloprogge, J. T. Raman Spectroscopic Study of Azurite and Malachite at 298 and 77 K. *J. Raman Spectrosc.* **33**, 252-259, (2002).

17 Dörner, L., Cancellieri, C., Rheingans, B., Walter, M., Kägi, R., Schmutz, P., Kovalenko, M. V., Jeurgens, L. P. H. Cost-Effective Sol-Gel Synthesis of Porous CuO Nanoparticle Aggregates with Tunable Specific Surface Area. *Sci. Rep.* **9**, 11758, (2019).

18 Kondrat, S., Smith, P., Wells, P., Chater, P., Carter, J., Morgan, D., Fiordaliso, E. M., Wagner, J., Davies, T., Lu, L., Bartley, J., Taylor, S., Spencer, M., Kiely, C., Kelly, G., Park, C., Rosseinsky, M., Hutchings, G. Stable Amorphous Georgeite as a Precursor to a High-Activity Catalyst. *Nature* **531**, (2016).

19 Preis, W., Gamsjäger, H. Thermodynamic Investigation of Phase Equilibria in Metal Carbonate–Water–Carbon Dioxide Systems. *Monatsh. Chem.* **132**, 1327-1346, (2001).

20 Davidson, J., Sefiane, K., Wood, T. Fast Diffusion Reaction in the Composition and Morphology of Coprecipitated Carbonates and Nitrates of Copper(II), Magnesium(II), and Zinc(II). *Ind. Eng. Chem. Res.* **54**, 1555-1563, (2015).

21 González, S., Pérez, M., Barrera, M., González Elipe, A. R., Souto, R. M. Mechanism of Copper Passivation in Aqueous Sodium Carbonate−Bicarbonate Solution Derived from Combined X-ray Photoelectron Spectroscopic and Electrochemical Data. *J. Phys. Chem. B* **102**, 5483-5489, (1998).

22 Nishikata, A., Itagaki, M., Tsuru, T., Haruyama, S. Passivation and Its Stability on Copper in Alkaline Solutions Containing Carbonate and Chloride Ions. *Corros. Sci.* **31**, 287-292, (1990).

23 Yakabuskie, P. A., Joseph, J. M., Stuart, C. R., Wren, J. C. Long-Term γ-Radiolysis Kinetics of NO_3^- and NO_2^- Solutions. *J. Phys. Chem. A* **115**, 4270-4278, (2011).

24 Meng, F., Morin, S. A., Jin, S. *Growth of Nanomaterials by Screw Dislocation* in *Springer Handbook of Nanomaterials* (ed Robert Vajtai) 639-664 (Springer Berlin Heidelberg, 2013).

25 Hacialioglu, S., Meng, F., Jin, S. Facile and Mild Solution Synthesis of Cu_2O Nanowires and Nanotubes Driven by Screw Dislocations. *Chem. Commun.* **48**, 1174-1176, (2012).

26 Zoubov, N. D., Vanleugenhaghe, C., Pourbaix, M. *Copper* in *Atlas of Electrochemical Equilibria in Aqueous Solutions* Ch. 14.1, 384-392 (NACE International Cebelcor, 1974).

27 Joseph, J. M., Choi, B. S., Yakabuskie, P., Wren, J. C. A Combined Experimental and Model Analysis on the Effect of pH and $O_{2(aq)}$ on Gamma-Radiolytically Produced H_2 and H_2O_2. *Radiat. Phys. Chem.* **77**, 1009-1020, (2008).

28 Das, N. P., Zahorán, R., Janovák, L., Deák, Á., Tóth, Á., Horváth, D., Schuszter, G. Kinetic Characterization of Precipitation Reactions: Possible Link between a

Phenomenological Equation and Reaction Pathway. *Cryst. Growth Des.* **20**, 7392-7398, (2020).

29 Soroka, I., Chae, N., Jonsson, M. On the Mechanism of γ-Radiation-Induced Corrosion of Copper in Water. *Corros. Sci.* **182**, 109279, (2021).

CHAPTER 8. EFFECTS OF INITIAL SOLUTION pH AND DEPTH ON THE COPPER CORROSION DYNAMICS

8.1 INTRODUCTION

The copper layer of the UFC will be exposed to a variety of conditions that change throughout its lifetime. It will be exposed to humid air, condensed water droplets, and water films which could provide the aqueous medium required for corrosion to occur.[1] The solution volumes that the copper layer will be exposed to will be small (small water volume per unit copper surface area) and limited by the gap between the UFC and the bentonite clay buffer. Furthermore, the aqueous solution in contact with the copper layer could be condensed humid air or ground water with an expected pH range of 6 – 9.[2] To accurately predict the extent of copper corrosion after long time periods, the effect of these changing parameters on the corrosion rate must be understood.

Chapter 6 showed that the elementary reactions involved in the overall corrosion process evolve with time in a stepwise manner. Solution conditions affect the relative rates of the elementary reactions and thus, the rates and duration of each corrosion stage. The corrosion rate in Stage 1 is determined by the rate of cupric ion diffusion and the duration is determined by the concentration of cupric ions that can be in solution according to the solubility. The corrosion yield at the end of Stage 1 has a large impact on the corrosion rate in the subsequent stages. Thus, the overall corrosion dynamics can be significantly affected in solution conditions that change the mass transport of cupric ions.

If cupric ions can accumulate in solution (e.g., in stagnant solutions, small volumes), their solution reactions and transport processes can become increasingly important with time. Solution reactions involving the initial metal oxidation product, $Cu^{2+}_{(sol'n)}$, can establish cyclic feedback loops with preceding processes (including charge transfer at the metal surface) and in **Chapter 6**, it was demonstrated that these feedback loops are enhanced in the presence of radiation. The solution reactions and transport processes of metal cations are significantly affected by solution parameters, including pH, ionic strength, temperature, and presence of anions. However, if cupric ions are not able to accumulate, corrosion cannot proceed past the initial corrosion steps, and active metal loss can occur for a very long time.

Copper corrosion occurs through the oxidation of solid metal (e.g., $Cu^{0}_{(m)}$) to the soluble metal cation (e.g., Cu^{2+}), coupled with the reduction of oxidant (e.g., O_2 to OH^-), at the metal-solution interface ($z = 0$, where z is the distance from the metal surface) (**Eq. 8.1**).

$$Cu^{0}_{(m)} + \frac{1}{2} O_2 + H_2O \rightleftarrows Cu^{2+} + 2\ OH^- \qquad (8.1)$$

The initial corrosion products subsequently transport between the interface ($z = 0$) and the bulk solution ($z = \delta_{diff}$) (**Eq. 8.2**).

$$Cu^{2+}|_{z=0} \rightsquigarrow Cu^{2+}|_{z=\delta_{diff}} \qquad (8.2a)$$

$$OH^-|_{z=0} \rightsquigarrow OH^-|_{z=\delta_{diff}} \qquad (8.2b)$$

Because the overall process of corrosion involves interfacial electron and mass transfer reactions and mass transport through the solution phase, the rate of corrosion depends strongly on the redox and transport conditions of the solution in contact with the metal.

In this chapter, the corrosion dynamics in conditions that affect the mass transport of cupric ions are investigated by using an initial pH of 9.0 and various solution volumes/depths in the presence of radiation. These conditions are also directly related to the conditions the copper layer will experience in the DGR, i.e., pH values of 6.0 (studied previously) to 9.0 (studied herein) and a variety of small solution depths. The corrosion dynamics are determined by following the bulk concentration of cupric ions, pH, and morphology and composition of the surface oxides as a function of time.

8.2 EXPERIMENTAL

8.2.1 Materials and Solutions

All experiments were performed with high purity copper (99.9% purity) coupons made from wrought copper samples (provided by SKB, the Swedish Nuclear Waste Management Company) with an exposed surface area of 0.785 cm^2. Copper coupons were ground using silicon carbide papers with grit size 400, 800, and 1200 in succession. The coupons were then washed with deionized water, dried under flowing $Ar_{(g)}$ and placed in a 20 mL vial sealed with an aluminum crimp cap with a polytetrafluoroethylene (PTFE)-coated silicone septum (Thermo Fisher Scientific, Waltham, MA). More information on this procedure is provided in

S**ection 3.1**. All solutions used in this study were prepared using water purified with a NANOpure Diamond UV ultra-pure water system (Barnstead International, Dubuque, IA) to give a resistivity of 18.2 MΩ·cm.

8.2.2 Experimental Details Specific to Section 8.3.1

The pH was adjusted to 9.0 by adding a dilute solution of high-grade sodium hydroxide (≥ 98 %, Sigma Aldrich, St. Louis, MO) dropwise. Solutions were purged with compressed zero air (CO_2-free air, Praxair, Danbury, CT), 21% O_2 balance Ar (Praxair, Danbury, CT), or ultra high purity $Ar_{(g)}$ (Praxair, Danbury, CT) for 1 h. Aerated solutions were not purged. More details on the setup procedure can be found in **Section 3.1**. 100 µL of the sample solution was placed on the copper surface by injection into the sealed vial using a syringe. Radiation experiments were performed using a MDS Nordion Gamma Cell 220 Excel ^{60}Co irradiator, as described in **Section 3.2**, and non-radiation experiments were done by leaving the vials on the benchtop, in otherwise the same conditions.

8.2.3 Experimental Details Specific to Section 8.3.2

The solutions used in this section were prepared using NANOpure Diamond UV ultra-pure water (Barnstead International, Dubuque, IA) with a resistivity of 18.2 MΩ·cm. In experiments with a large solution depth (‘d_{sol}’), the copper coupons were embedded in poly-vinyl chloride heat shrink tubing (Techflex, Sparta, NJ) with an inner diameter of 15.88 mm and only the top, polished copper surface was exposed to the solution (left, **Figure 8.1**). The solution volumes were 2.0 mL (d_{sol} = 2.5 cm), 1.0 mL (d_{sol} = 1.27 cm), and 0.5 mL (d_{sol} = 0.80 cm). The experiment with the smallest solution depth (d_{sol} = 0.25 cm), was an immersion experiment, where the coupon was submerged in 2.0 mL of water (right, **Figure 8.1**). The coupon was covered with Parafilm (Bemis Company, Inc, Neenah, WI) so that only the top, polished surface was exposed to the solution (not imaged).

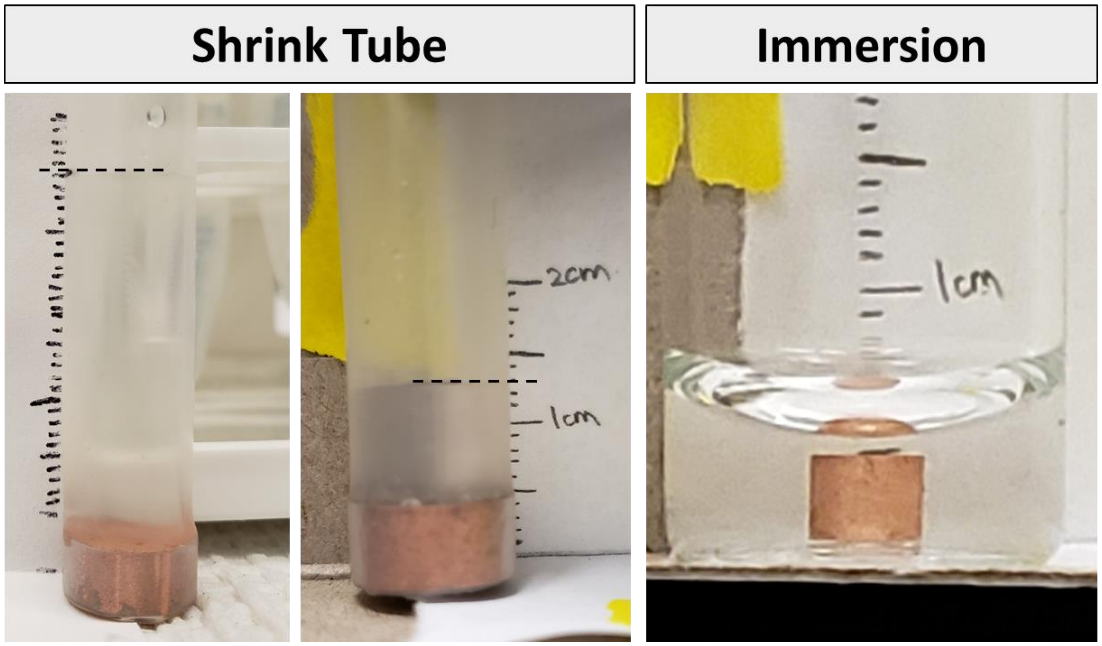

Figure 8.1 Copper coupons with different solution depths by using shrink tubing (left) and immersion (right). In the immersion experiments, coupons were covered with Parafilm on all sides other than the top surface (not shown).

8.2.4 Post-Test Analyses

Experiments were terminated by removing the solution using a Pasteur pipette. The copper coupon was washed and dried using $Ar_{(g)}$ gas (Praxair, Danbury, CT). Optical images were taken using a Leica DVM6A digital microscope, as outlined in **Section 3.3.1**, then the coupon was stored under vacuum. Scanning electron microscopy (SEM) was performed at the Western Nanofabrication Facility using Zeiss LEO 1530 and 1540XB instruments (**Section 3.3.2**).

The pH of the solution was determined using a Thermo Scientific Orion 9110DJWP Double Junction Micro-pH Electrode, as outlined in **Section 3.4.1**. The solution was then diluted for inductively coupled plasma optical emission spectroscopy (ICP-OES) (PerkinElmer Avio 200 ICP-OES) following the procedure outlined in **Section 3.4.2**.

8.3 RESULTS AND DISCUSSION

8.3.1 Effect of a Higher Starting pH

Increasing the initial pH (pH_0) from 7.0 to 9.0 does not significantly affect the transport *rate* of cupric ions. However, at pH 9.0, the solubility limit of cupric ions is at a minimum and is 2 orders of magnitude lower compared to at pH 7.0. Certainty, during corrosion, pH_t changes with t and z and the main form of cupric ions in solution is dependent on the $[OH^-]$ and $[Cu^{II}_{(sol'n)}]$:

$$Cu^{2+} + 2\ OH^- \rightleftharpoons Cu(OH)^+ + OH^- \rightleftharpoons Cu(OH)_{2(solv)} + H_2O \rightleftharpoons Cu(OH)_3^- + H^+ \qquad (8.2)$$

In this section, the effects of $pH_0 = 9.0$ are investigated in small solution droplets in the presence and absence of radiation. Although all cover gas compositions studied in **Chapters 6** and **7** (i.e., CO_2-free air, aerated, 21% O_2 (balance Ar), deaerated) were used, only the results from the CO_2-free air solution are presented herein; the time dependent behaviour for all cover gas compositions can be found in **Appendix C**.

8.3.1.1 In the Absence of Radiation

The time-dependent copper corrosion behaviour in the absence of radiation in a water droplet scrubbed of CO_2 is shown in **Figure 8.2**. Three kinetic stages were identified that are consistent with the corrosion mechanism developed in **Chapter 6** for droplets with $pH_0 = 7.0$. The observations which allowed for the identification of the stages are described below.

Stage 1a: By the first measurement (t = 16 h), $\log([Cu^{II}_{(sol'n)}]_t)$ increased to -4.4 ± 0.1 and pH_t decreased to 4.5 ± 0.1. That is, the production of $Cu^{II}_{(sol'n)}$ and H^+ were approximately the same. No significant granular oxide deposits were observed on the surface. These observations were the same as when $pH_0 = 7.0$, despite the significant difference in $[OH^-]_0$.

Stage 1b: For $16\ h < t \leq 40\ h$, both $[Cu^{II}_{(sol'n)}]_t$ and pH_t increased with time. The pH_t increased to a steady state value of 8.3 ± 0.1, corresponding to the pKa of $Cu(OH)^+$. The solution remained supersaturated with $Cu^{II}_{(sol'n)}$, but the surface generally remained free of granular oxide deposits.

Stage 2: For $48 \leq t < 200$ h, $[Cu^{II}_{(sol'n)}]_t$ and pH_t fluctuated with time around average values. The average $[Cu^{II}_{(sol'n)}]_t$ value was 0.2 ± 0.1 mM ($\log([Cu^{II}_{(sol'n)}] = -3.7$), which was slightly lower than in Stage 2 in $pH_0 = 7.0$ solutions. The average pH_t value was 8.3 ± 0.1, which corresponded to the $Cu(OH)^+$ pKa. The solution remained supersaturated with cupric ions. While some oxide growth was seen around the edge of the coupon, the surface in general remained free of granular oxide deposits. However, patches of dried $Cu(OH)_2$ hydrogel were observed on the surface during this stage.

Stage 3: After 480 h, some patches of Cu_2O were observed on the surface, however the general surface did not show signs of complete coverage with Cu_2O like in Stage 3 in $pH_0 = 7.0$ solutions. $[Cu^{II}_{(sol'n)}]_t$ continued to fluctuate around the average value in Stage 2, but the pH_t had decreased to 6.4 ± 0.1.

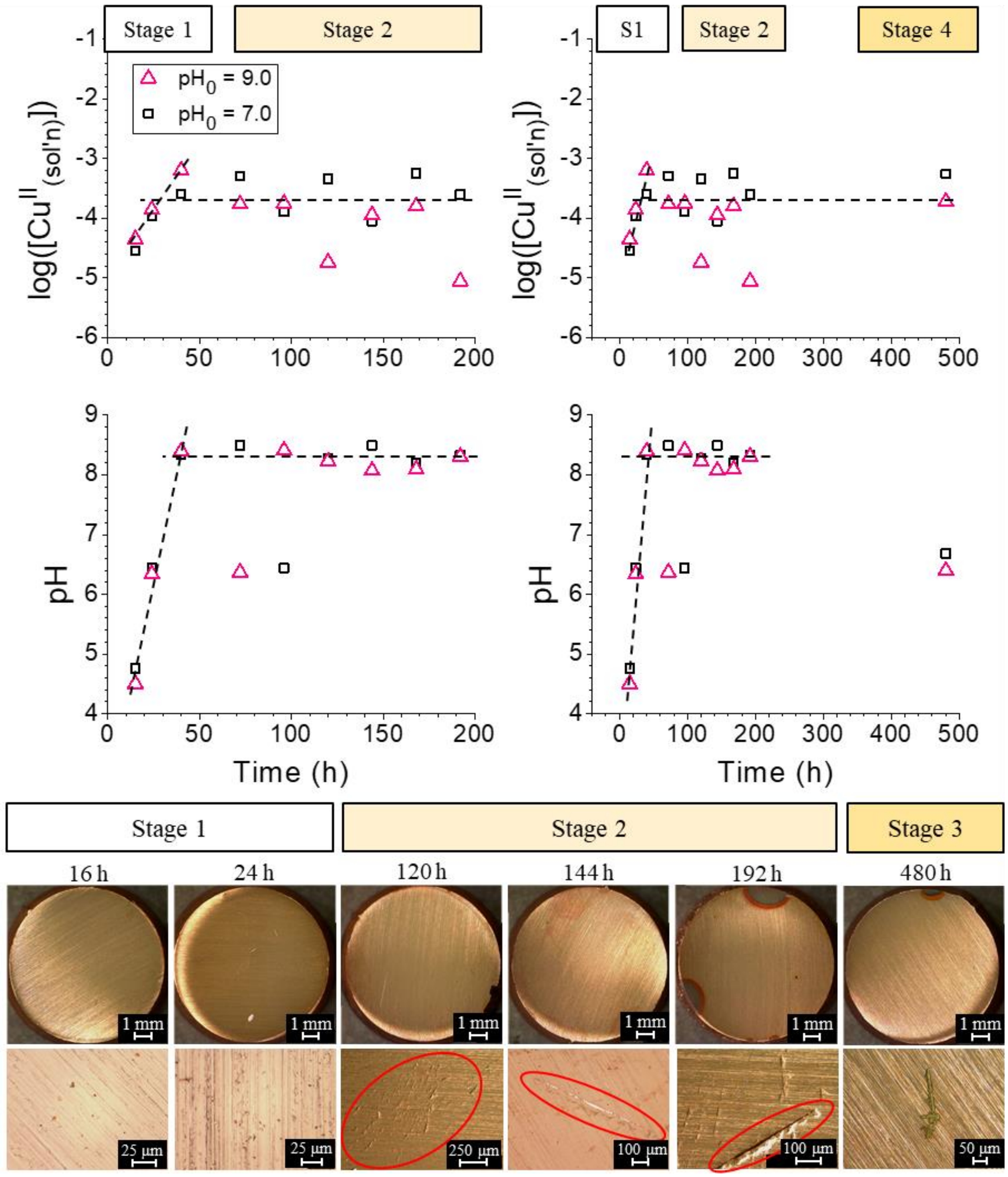

Figure 8.2 Time-dependent behaviour of [$Cu^{II}_{(sol'n)}$] (top row), pH (middle row), and the exposed surface (optical images, bottom rows) during copper corrosion after exposure to a 100 µL water droplet (previously purged of CO_2) with $pH_0 = 9.0$ in the absence of γ-radiation. The solution data is compared to that after exposure to $pH_0 = 7.0$ water (black squares, data from **Chapter 6**). Red circles in the optical images show the $Cu(OH)_2$ hydrogel. The black dotted lines show the general trend of the data (not based on regression analysis).

In **Chapter 4**, it was shown that when the pH_0 is near the equivalence point for water, small increases in $[OH^-]$ via **Eq. 8.1** can significantly increase the pH at $z = 0$. The high pH in turn causes a shift in the cupric ion hydrolysis equilibrium (**Eq. 8.2**) to the far right fast enough that the charge transfer, the mass transfer, and the cupric ion hydrolysis can be considered one elementary reaction:

$$Cu^0_{(m)} + \tfrac{1}{2} O_2 + H_2O \rightarrow Cu(OH)_3^- + H^+ \qquad \text{in } \underline{\text{Stage 1a}} \qquad (8.3)$$

The products from the initial elementary reaction diffuse from the metal surface, where they were formed, to the bulk solution.

$$Cu(OH)_3^-|_{z=0} \rightsquigarrow Cu(OH)_3^-|_{z=\delta_{diff}} \qquad \text{in } \underline{\text{Stage 1a}} \qquad (8.4a)$$

$$H^+|_{z=0} \rightsquigarrow H^+|_{z=\delta_{diff}} \qquad \text{in } \underline{\text{Stage 1a}} \qquad (8.4b)$$

With no other acid-base equilibria established in solution (i.e., in CO_2-free air), the rates of increase in $[Cu^{2+}_{(sol'n)}]_t$ and $[H^+]_t$ are the same.

Although solutions with $pH_0 = 9.0$ are not initially close to the equivalence point of water, the high $[OH^-]_0$ at $z = 0$ has a similar affect on the cupric ion hydrolysis. That is, the amount of $[OH^-]$ produced via **Eq. 8.1** combined with the already high $[OH^-]_0$ at $z = 0$ is sufficiently high enough to push the hydrolysis equilibrium towards the formation of $Cu(OH)_3^-$. Accordingly, the first measured pH_t (t = 16 h, pink in **Figure 8.2**) had decreased to 4.5 while $\log([Cu^{II}_{(sol'n)}]_t)$ increased to -4.7 ($[Cu^{II}_{(sol'n)}] = 40\ \mu M$), and their production rates are approximately the same. Therefore, in <u>Stage 1a</u>, corrosion occurs via **Eq. 8.3** and **8.4** for solutions with $pH_0 = 9.0$.

The increasing $[H^+]_t$ causes the hydrolysis equilibrium to shift to the left, which consumes H^+ and causes the rate of increase in $[Cu^{2+}_{(sol'n)}]_t$ and $[H^+]_t$ to deviate from each other. At the end of <u>Stage 1a</u>, pH_t reaches a minimum as $Cu(OH)_{2(solv)}$ begins to form, then increases with time in <u>Stage 1b</u> (**Figure 8.2**) due to the production of $Cu(OH)^+$.

$$Cu(OH)_3^- + H^+ \rightarrow Cu(OH)_{2(solv)} + H_2O \rightarrow Cu(OH)^+ + OH^- \qquad \text{in } \underline{\text{Stage 1b}} \qquad (8.5)$$

Because OH^- is produced at $z = 0$, the interfacial solution has a higher pH_t than the bulk solution during Stage 1b. As $Cu^{2+}_{(sol'n)}$ transports through the diffusion layer, its solubility decreases with z. The decrease in solubility causes $Cu^{2+}_{(sol'n)}$ to approach the solubility limit and $Cu(OH)_2$ precipitates as solid colloid particles ($Cu(OH)_{2(colloid)}$) in the bulk solution (away from the metal surface). These colloid particles remain dispersed in the bulk solution and are included in the measured [$Cu^{II}_{(sol'n)}$]. Despite the large changes in pH_t during Stage 1 (from 4.5 to 9.0), the increase in [$Cu^{II}_{(sol'n)}$] is linear at 15 ± 3 μM/h, shown in **Figure 8.2**.

As the concentration of $Cu(OH)_{2(colloid)}$ in the bulk solution increases, the frequency of their collision increases and when they collide, they agglomerate. The colloid particles will accumulate water molecules during aggregation due to strong hydrogen bonds between the colloid molecules and the surrounding water molecules.[3,4] The colloid agglomeration results in the formation of a hydrogel, which consists of a network of loosely connected $Cu(OH)_2$ colloid (solid) particles with a mobile phase of $Cu^{II}_{(sol'n)}$-saturated solution in the interstices.[5-7] The precipitation of $Cu(OH)_2$ hydrogel marks the beginning of Stage 2.

The hydrogel grows as the colloids dispersed in the bulk solution join the solid network (i.e., the colloid density increases within the hydrogel). The hydrogel growth, then, removes $Cu^{2+}_{(sol'n)}$, while metal oxidation produces $Cu^{2+}_{(sol'n)}$ and the removal and production rates of $Cu^{2+}_{(sol'n)}$ are approximately equal causing the [$Cu^{II}_{(sol'n)}$] to be constant with time in Stage 2, fluctuating around a value of 0.20 mM (log([$Cu^{II}_{(sol'n)}$] = – 3.7, **Figure 8.2**). Because the rates of production of $Cu^{2+}_{(sol'n)}$ (via **Eq. 8.3**) and of removal of $Cu^{2+}_{(sol'n)}$ (via hydrogel precipitation) are the same, the overall corrosion rate in this stage is equal to the precipitation rate of the hydrogel. Similarly, pH_t fluctuates around a value of 8.3 ± 1, due to $Cu(OH)_{2(solv)}$ and $Cu(OH)^+$ produced in Stage 1b buffering the pH.

$$Cu(OH)^+ + H_2O \rightleftharpoons Cu(OH)_{2(solv)} + H^+ \qquad pKa = 8.3 \qquad (8.6)$$

The growth of the hydrogel layer at $z = 0$ during Stage 2 creates a transport barrier for $Cu^{2+}_{(sol'n)}$ and they get trapped next to the metal surface. When cupric ions (as dissolved or dispersed colloidal species) get trapped next to the metal surface, they can more easily reduce to Cu^+ species, coupled with the oxidation of $Cu^0_{(m)}$ to $Cu^{2+}_{(sol'n)}$.[8] As $Cu^+_{(sol'n)}$ dissolves into the solution next to the metal surface, it establishes fast hydrolysis equilibria in the mobile phase of the hydrogel and is incorporated into the hydrogel as a solid species.

$$Cu^0_{(m)} + Cu^{2+}_{(sol'n)} \rightarrow 2\ Cu^+_{(sol'n)} + 2\ OH^- \rightleftharpoons 2\ CuOH_{(solid)} \qquad \underline{\text{in Stage 2}} \qquad (8.7a)$$

$$Cu^+_{(sol'n)}/CuOH_{(solid)} + Cu^{2+}_{(sol'n)}/Cu(OH)_{2(solid)} + OH^- \rightarrow \text{mixed } Cu^I/Cu^{II} \text{ hydroxide hydrogel} \qquad (8.7b)$$

The reduction of $Cu^{2+}_{(sol'n)}/Cu(OH)_2$ to $Cu^+_{(sol'n)}/CuOH$ via **Eq. 6.21** accelerates further precipitation of $Cu(OH)_2$ colloid particles. The faster growth of hydrogel, in turn, increases the rate of $Cu^+_{(sol'n)}$ formation. That is, a cyclic feedback loop between the formation of $Cu(OH)_2$ hydrogel (**Eq. 6.18**) and its reduction to $Cu^+_{(sol'n)}$ (**Eq. 6.21**) is established.

Localized areas of dried hydrogel were observed on the surface during Stage 2 (red circles in **Figure 8.2**). In the absence of radiation, the hydrogel is highly hydrated with a low colloid concentration, which dilutes the blue colour of the Cu^{2+} complex. Accordingly, the observed hydrogel was clear. The hydrogel precipitation occurs in thin strips that could not be correlated the metal grinding lines, and it will be shown later that patches of Cu_2O grow in a similar shape.

During Stage 2, the initial metal oxidation coupled with solution reduction reaction (**Eq. 8.3**), diffusion of cupric ions (**Eq. 8.4**), cupric ion hydrolysis (**Eq. 8.2**), and the precipitation of colloid particles are all in a steady state, while the growth of the hydrogel (including agglomeration of colloid particles and $Cu(OH)_2$ reduction to CuOH) is controlling the overall rate of metal loss. Due to the feedback loop established in this stage, the corrosion rate cannot simply be determined from linear dynamics.

Stage 3 begins when CuOH (formed via $Cu(OH)_2$ reduction) precipitates as Cu_2O:

$$2\ Cu^+_{(sol'n)} \rightleftharpoons 2\ CuOH_{(solid)} \rightarrow Cu_2O + H_2O \qquad \text{in } \underline{\text{Stage 3}} \qquad (8.8)$$

The rate of precipitation of Cu_2O crystals is dependent on the supersaturation concentration of CuOH within the hydrogel. $[Cu^{II}_{(sol'n)}]$ at the end of Stage 2 was low and the rate of $Cu(OH)_2$ reduction to CuOH was low, which suggests the precipitation rate of Cu_2O crystals was also low in these conditions. In $pH_0 = 7.0$ solutions, the entire surface was yellow after 480 h, which indicated that small Cu_2O crystals had forms uniformly across the surface. The uniform Cu_2O coverage was not observed in $pH_0 = 9.0$ solutions due to a lower $[Cu^{II}_{(sol'n)}]$ in Stage 2 (0.20 mM in $pH_0 = 9.0$ (**Figure 8.2**) compared to 0.38 mM in $pH_0 = 7.0$ (**Chapter 6**)). However, localized areas of Cu_2O growth were observed (bottom row in **Figure 8.2**), shaped similarly to the dried hydrogel imaged in Stage 2 further confirming Cu_2O precipitation from the $Cu(OH)_2$ hydrogel (**Eqs. 8.7** and **8.8**).

During Stage 3, $[Cu^{II}_{(sol'n)}]_t$ continued to fluctuate around 0.20 mM, while the pH_t decreased to 6.4 ± 0.1 and the solution to approach $Cu(OH)_2$ solubility equilibrium. This was the same time-dependent behaviour of solution species (i.e., $Cu^{II}_{(sol'n)}$ and OH^-) observed when $pH_0 = 7.0$.

Thus, the corrosion mechanism proposed for solutions of $pH_0 = 7.0$ is applicable to solutions of $pH_0 = 9.0$. This section has demonstrated that in each corrosion stage, the rate-determining steps, the corrosion rate, and the corrosion yields were similar regardless of the increase in pH_0. Although this section only discussed in detail CO_2-free solutions, the same conclusion was reached in all studied cover gas environments (air, 21% O_2 (balance Ar), and Ar, shown in **Appendix C**).

8.3.1.2 In the Presence of Radiation

As discussed in previous chapters, the energy of γ-radiation transferred to metal quickly dissipates as heat and does not induce any chemical change. However, water and humid air exposed to γ-radiation decompose into redox-active (mainly H_2O_2) and acidic species (mainly HNO_3). Under a continuous flux of γ-radiation, the radiolysis products reach steady-state concentrations and become homogeneously distributed in solution. The steady-state concentrations of radiolysis products depend on not only the radiation dose rate but also depend on solution pH, concentration of radical scavenger such as O_2 and Cl^-.[9-12] In the presence of a naturally corroding system, the production or consumption of the radiolysis species can also contribute to determining their long-term steady-state concentrations.

The time-dependent behaviours of $\log([Cu^{II}_{(sol'n)}])$, pH, and the surface morphology and colour during radiolytic corrosion in stagnant droplet solutions free of CO_2/carbonate are presented with an adjusted pH_0 to 9.0 are shown in **Figure 8.3**. Despite slight variations in dissolved product concentrations, copper corrosion in the presence of radiation progresses through similar dynamic stages regardless of pH_0 of 7.0 or 9.0. The key observations during radiolytic copper corrosion are:

Stage 1: When $t \leq 40$ h, $[Cu^{II}_{(sol'n)}]_t$ increased with time and the surface showed no granular oxide growth. The pH_t initially decreased with time, then reached a near constant value of about 4.7 at the end of the stage. The rate of increase in $[Cu^{II}_{(sol'n)}]_t$, the final yield of $[Cu^{II}_{(sol'n)}]$, and the steady state pH_t value in this stage were all similar to that for $pH_0 = 7.0$ solutions.

Stage 2: For $72 \text{ h} \leq t \leq 96$ h, $[Cu^{II}_{(sol'n)}]_t$ and pH_t were nearly constant while $Cu(OH)_2$ hydrogel grows. $[Cu^{II}_{(sol'n)}]_t$ fluctuates around a value of 4.8 mM and pH_t fluctuates around a value of 4.7. These values were similar to that observed in $pH_0 = 7.0$ solutions.

Stage 3: For $120 \text{ h} \leq t < 200$ h, $[Cu^{II}_{(sol'n)}]_t$ increased with time at a slower rate than in Stage 1, while the pH_t remained near its steady state value but fluctuated with time. The surface is covered with purple and pink-coloured oxides, indicate the presence of Cu_2O crystals covered with various thickness of $Cu(OH)_2$ hydrogel layer. The average size of Cu_2O crystals was smaller than in $pH_0 = 7.0$ solutions after the same amount of corrosion time.

Stage 4: After 480 h, $[Cu^{II}_{(sol'n)}]$ decreased to 8.5 ± 4.0 mM without a substantial change in pH_t from Stage 3. The surface was covered with pink and purple granular oxides and a very thick hydrogel layer. The clear, amorphous hydrogel layer was observed in optical and SEM images, and Raman analysis did not indicate the presence of nitrate, like in Stage 4 in $pH_0 = 7.0$ solutions.

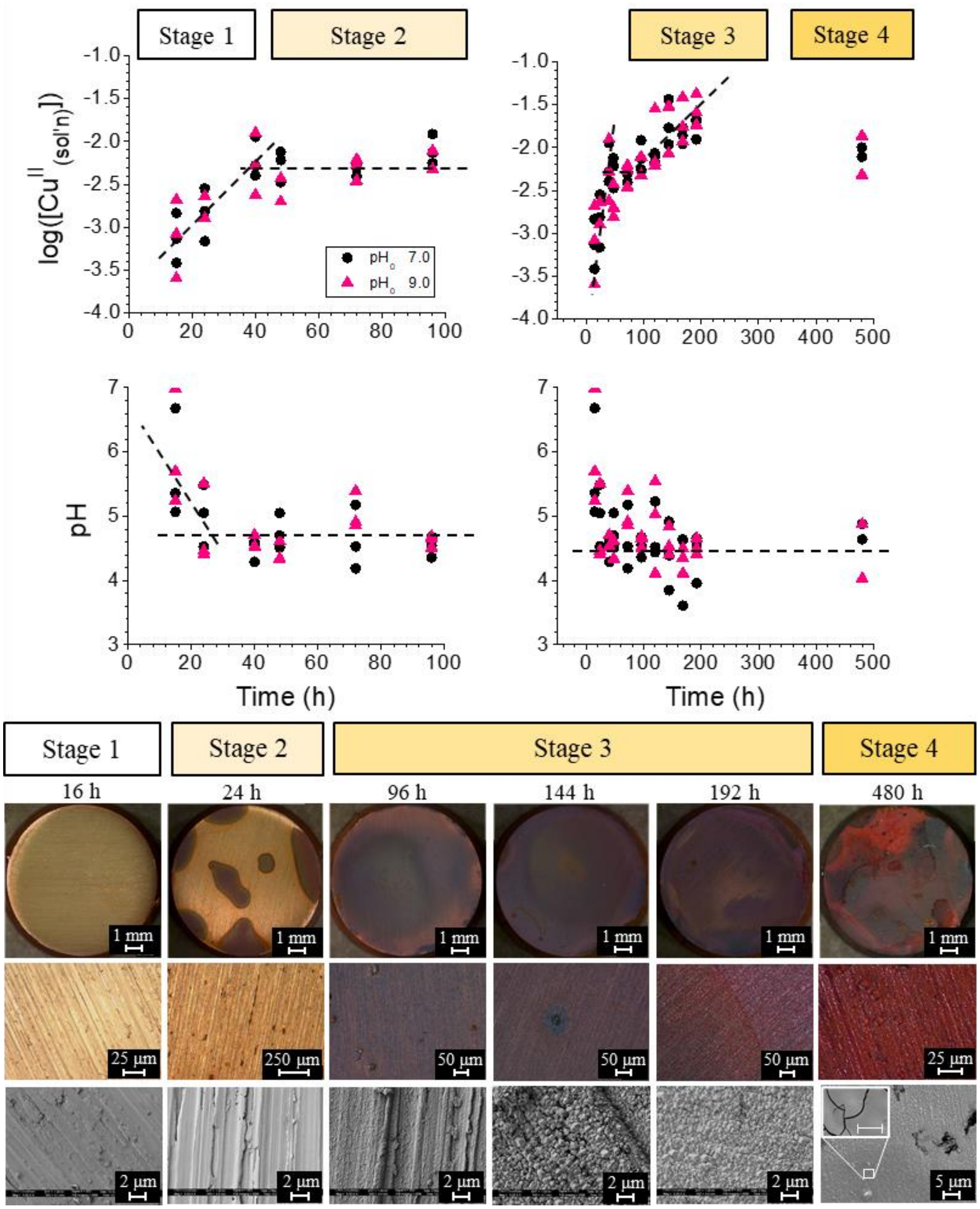

Figure 8.3 Time-dependent behaviour of [Cu^{II}$_{(sol'n)}$] (top row), pH (middle row), and the exposed surface (optical and SEM images, bottom rows) during copper corrosion after exposure to a 100 µL droplet of pure water (purged of CO_2) with pH_0 = 9.0 (pink triangles) in the presence of γ-radiation. The solution data is compared to that after exposure to pH_0 = 7.0 water (black circles, data from **Chapter 6**). The inset in the bottom right SEM image has a scalebar of 2.0 µm. The black dotted lines show the general trend of the data (not based on regression analysis).

In the presence of radiation, H_2O_2 produced via radiolytic water decomposition, is quickly produced at a low steady-state concentration. Thus, the initial oxidation of $Cu^0_{(m)}$ to $Cu^{2+}_{(sol'n)}$ is coupled with H_2O_2 reduction. As discussed in the previous section, in Stage 1a, the pH_0 is high enough that the fast cupric ion hydrolysis is pushed all the way to the right and the elementary reaction to be considered is:

$$Cu^0_{(m)} + H_2O_2 \rightarrow Cu(OH)_3^- + H^+ \tag{8.9}$$

The production of $Cu(OH)_3^-$ and H^+ at $z = 0$ and their subsequent diffusion to $z = \delta_{diff}$ cause $[Cu^{II}_{(sol'n)}]_t$ and $[H^+]_t$ to increase. The increase in $[H^+]_t$ causes a shift in hydrolysis equilibria towards the formation of $Cu(OH)_{2(solv)}$ and $Cu(OH)^+$ in Stage 1b (**Eq. 8.5**). The pH_t in the bulk solution decreases faster in the presence of radiation than in its absence, which causes Stage 1b to start earlier. This is shown after 16 h when the pH_t was higher in the presence of radiation (6.0, shown in **Figure 6.7**) compared to the absence (4.5 in Stage 1a, shown in **Figure 6.4**). This indicates that Stage 1b started before 16 h.

During Stage 1b, pH_t decreased indicating the rate of production of $[H^+]_t$ via radiolytic decomposition is faster than the rate of consumption of $[H^+]_t$ via cupric ion hydrolysis (**Eq. 8.5**). The pH_t value at the end of Stage 1b was unaffected by the higher pH_0 and was 4.7 ± 0.1 (**Figure 8.2**). The $[Cu^{II}_{(sol'n)}]$ yield at the end of Stage 1b in $pH_0 = 9.0$ solutions was 4.8 mM (pink in **Figure 8.2**), which was approximately the same as in $pH_0 = 7.0$ solutions (6.0 mM, black in **Figure 8.2**). Accordingly, the corrosion rate in Stage 1 in $pH_0 = 9.0$ solutions was nearly the same as in $pH_0 = 7.0$ solutions, at 11.5 ± 5.0 nmol $Cu/cm^2/h$ and the duration of this stage was the same in both solutions (rates, durations, and yields in each stage for both solutions are provided in **Table 8.1**).

In the presence of radiation, the rate of agglomeration of colloid particles is increased due to reactive radiolysis products that can lower the zeta potential of the colloid particles (increasing their intermolecular attraction),[13-15] and increase in rate of reduction to CuOH, discussed later.[16,17] Stage 2 was observed for $48\ h \leq t \leq 96\ h$, during which the characteristic plateaus in $[Cu^{II}_{(sol'n)}]_t$ and pH_t with time were observed and the $Cu(OH)_2$ hydrogel was observed on the surface. SEM images of patches of dried hydrogel that had grown after 48 h of corrosion are shown in **Figure 8.4**. The top images show small solid colloid particles aggregating between two grinding lines where the solution volume is limited, and the bottom images are of the smooth, dense hydrogel.

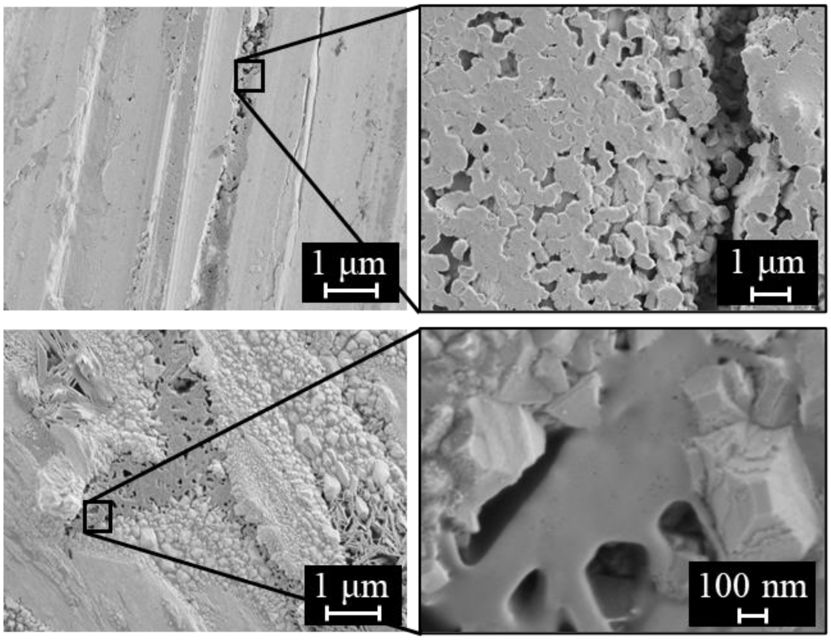

Figure 8.4 SEM images of the $Cu(OH)_2$ hydrogel after 48 h of corrosion in 100 μL of CO_2-free water droplet in the presence of radiation.

The plateau values of pH_t and $[Cu^{II}{}_{(sol'n)}]_t$ during Stage 2 were 4.7 and 4.8 ± 2.0 mM, respectively (top and middle row in **Figure 8.3**). That the pH_t plateau was the same in this solution as in $pH_0 = 7.0$ solutions confirm that the higher $[OH^-]_0$ had no effect on the steady-state pH value, which suggests that the long-term $[Cu^{II}{}_{(sol'n)}]$ value is unaffected by pH_0. Similarly, the steady-state $[Cu^{II}{}_{(sol'n)}]$ value was approximately the same in $pH_0 = 9.0$ solutions compared to in $pH_0 = 7.0$ solutions (6.0 ± 2.8 mM, black in **Figure 8.3**).

As $Cu^{2+}{}_{(sol'n)}$ and colloid particles accumulate, H_2O_2 can oxidize coupled with cupric ion reduction (**Eq. 8.10a**). The rate of oxidation of H_2O_2 by $Cu^{2+}{}_{(sol'n)}$ can only compete with its rate of reduction by $Cu^0{}_{(m)}$ when the concentration of $Cu^{2+}{}_{(sol'n)}$ is high, and so, this reaction pathway only becomes available at later stages of corrosion in the interfacial region. The solubility of cuprous ions is very low and will establish its solubility equilibrium very quickly (**Eq. 8.10b**). CuOH will be incorporated in the solid hydrogel network, forming a mixed Cu^I/Cu^{II} hydroxide hydrogel (**Eq. 8.10c**).

$$2\ Cu^{2+} + H_2O_2 + 2\ OH^- \rightarrow 2\ Cu^+ + O_2 + 2\ H_2O \tag{8.10a}$$

$$Cu^+_{(sol'n)} + x\ OH^- \rightleftharpoons CuOH_{(solid)} \tag{8.10b}$$

$$Cu^+_{(sol'n)}/CuOH_{(solid)} + Cu^{2+}_{(sol'n)}/Cu(OH)_{2(solid)} + OH^- \rightarrow \text{mixed } Cu^I/Cu^{II} \text{ hydroxide hydrogel} \tag{8.10c}$$

H_2O_2 accelerates the reduction of cupric to cuprous ions, which enhances the cyclic feedback loop between $Cu(OH)_2$ production and consumption. Therefore, CuOH formation is fast, and Stage 2 is short in the presence of radiation. However, the duration of Stage 2 was unaffected by the increase in pH_0 to 9.0, due to the same $[Cu^{II}_{(sol'n)}]$ yield during Stages 1 and 2 (summarized in **Table 8.1**).

Stage 3 begins when CuOH has reached its supersaturation capacity within the hydrogel and Cu_2O starts to precipitate.

$$2\ Cu^+_{(sol'n)} + x\ OH^- \rightleftharpoons 2\ CuOH_{(solid)} \rightarrow Cu_2O + H_2O \tag{8.11}$$

The start of the stage was determined by when the appearance of complete coverage of the copper metal surface by pink and purple oxides was observed in the optical images combined with a $[Cu^{II}_{(sol'n)}]$ increase with time (slower than in Stage 1). Thus, Stage 3 was observed for 120 h ≤ h < 200 h (**Figure 8.3**), which was the same duration as in $pH_0 = 7.0$ solutions. As discussed in **Chapter 6**, $[Cu^{II}_{(sol'n)}]$ is important in determining the rate of Cu_2O precipitation and the size of Cu_2O crystals. $[Cu^{II}_{(sol'n)}]$ in Stages 1 and 2 were slightly lower in pH_0 9.0 compared to 7.0 solutions and accordingly, the size of the Cu_2O crystals were slightly smaller (SEM images in **Figure 8.3** and from **Chapter 6** in **Figure 6.8**). Nevertheless, the stage lengths and rates were relatively unaffected (**Table 8.1**).

The fluctuations around the pH_t average value of 4.7 were large (± 0.5), which caused large fluctuations in the cupric ion solubility with time. The large solubility fluctuations ultimately resulted in a time-averaged increase in $[Cu^{II}_{(sol'n)}]$, although large variations in the measured value were observed. The dissolution rate of cupric ions in this stage was 0.12 ± 0.01 mM/h or a metal loss rate of 7.8 ± 0.8 nmol $Cu/cm^2/h$ (**Figure 8.3**).

$[Cu^{II}_{(sol'n)}]$ decreased substantially from its value of 29 ± 10 mM at 192 h to 8.5 ± 4.0 mM at 480 h. This decrease indicates that cupric ions were being consumed at the metal surface, and not produced via metal oxidation, which is consistent with Stage 4. In Stage 4, the oxide layer had grown thick enough to arrest the oxidation of the underlying metal, while the oxides on the surface ripen to approach equilibrium. In $pH_0 = 7.0$ solutions, nitrate was observed in the hydrogel layer in this stage due to the co-precipitation with cupric ions during Ostwald ripening of Cu_2O crystals. The hydrogel grown in the $pH_0 = 9.0$ after 480 h was observed ubiquitously on the surface (optical images in **Figures 8.3** and **8.4**) but did not have the blue colour indicative of the incorporation of nitrate.

Images of the hydrogel on the surface after 480 h in $pH_0 = 9.0$ solutions are shown in **Figure 8.6**. The optical images (top row) in **Figure 8.6** show a layer of a clear amorphous species in which bubbles have formed. The hydrogel layer is clear, suggesting a high degree of hydration (low $Cu(OH)_2$ colloid density). The SEM images (bottom row, **Figure 8.6**) show the cracks (due to *ex situ* drying) in the hydrogel layer, similar to the top layer of the hydrogel analyzed in aerated droplets in **Chapter 7**. The EDX Cu:O atomic ratio confirms that the cracked layer (area 1 in the bottom row in **Figure 8.5**) is $Cu(OH)_2$ (Cu:O atomic ratio of 0.7), and that the crystal layer underneath (area 2 in the bottom row in **Figure 8.5**) is Cu_2O (Cu:O atomic ratio of 1.9).

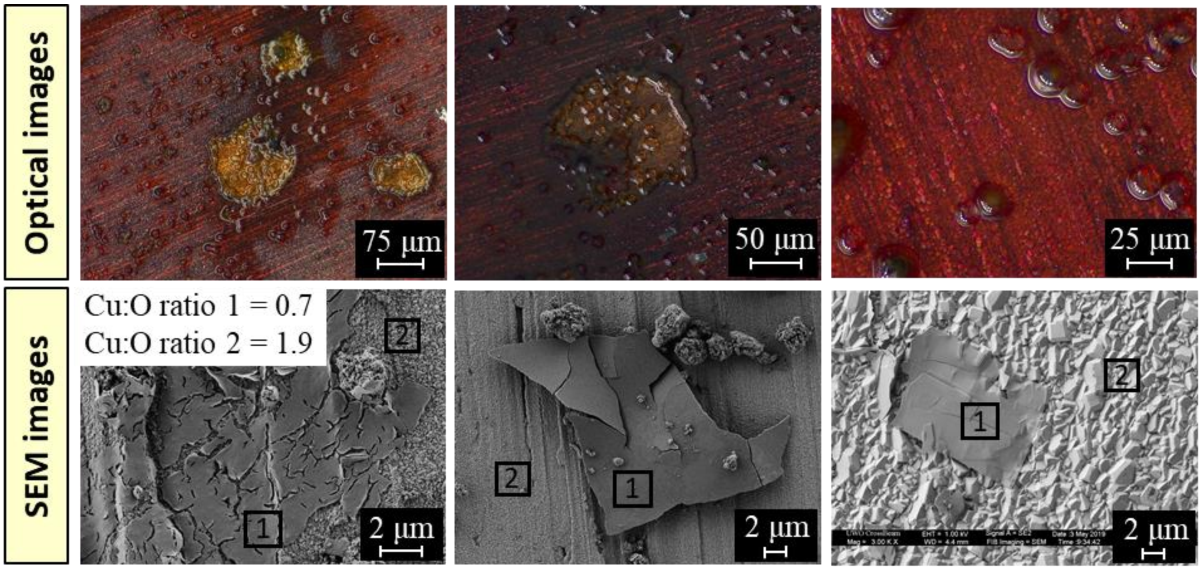

Figure 8.5 Optical (top row) and SEM (bottom row) images of the $Cu(OH)_2$ hydrogel grown after 480 h of corrosion in the presence of γ-radiation. Areas 1 and 2 were analyzed with EDX, and the Cu:O ratio was reported.

A summary of the rates and yields in each corrosion stage in CO_2-free droplet solutions with $pH_0 = 7.0$ (**Chapter 6**) and 9.0 is presented in **Table 8.1**. A comparison of the values in each corrosion stage shows that the pH_0 had little effect on the overall progression of radiolytic copper corrosion. This is because in both solutions the cupric ion hydrolysis was pushed towards the formation of $Cu(OH)_3^-$ in Stage 1a, resulting in similar corrosion product yields that carried through to the later corrosion stages. Increasing the pH_0 to 9.0 had little effect on the overall corrosion progression in any of the studied cover gas compositions (shown in **Appendix C**). The expected pH range of the groundwater that the copper layer of the UFC may be in contact with is 6 – 9.[2] Thus, this study has shown that the corrosion progression of the copper layer of the UFC will be the same at all expected groundwater pH_0 values.

Table 8.1 Summary of values obtained after radiolytic copper corrosion in CO_2-free solutions with $pH_0 = 7.0$ (**Chapter 6**) and 9.0.

	$pH_0 = 7.0$	**$pH_0 = 9.0$**
Stage 1		
Duration (h)	40	40
Dissolution rate of [$Cu^{II}_{(sol'n)}$] (nmol Cu/cm^2/h)	11.6 ± 1.2	11.5 ± 5.0
Stage 2		
Duration (h)	72	72
[$Cu^{II}_{(sol'n)}$] plateau (mM)	6.0 ± 2.8	4.8 ± 2.0
Steady-state pH	4.6 ± 0.4	4.7 ± 0.5
Stage 3		
Duration (h)	> 80	> 80
Dissolution rate of [$Cu^{II}_{(sol'n)}$] (nmol Cu/cm^2/h)	7.4 ± 1.3	7.8 ± 0.8
Stage 4		
Observed after (h)	480	480
$Cu^{II}_{(sol'n)}$ yield (mM)	8.9 ± 1.5	8.5 ± 4.0

8.3.2 Effects of Solution Depth in the Presence of Radiation

The length of Stage 1 is dependent on how quickly Cu^{2+} can accumulate in solution, reach the solubility limit of $Cu(OH)_{2(solid)}$, and begin precipitating. In solutions with a small depth (d_{sol}), such as the small water droplets (semi-oval shape with the maximum height of 0.20 cm) used in the previous section, $Cu^{2+}_{(sol'n)}$ can accumulate quickly and Stage 1 is short. In solutions with a large d_{sol}, Stage 1 is prolonged as it takes more time for the solution to reach the cupric ion saturation capacity. Previous studies on the effect of solution depth on copper corrosion in the absence of radiation, have found that increasing the solution volume does not change the rate but increases the duration of Stage 1.[18] The longer duration and same rate in larger solutions allows for more copper to dissolve into solution before moving into later stages. Thus, if the cupric ions are still able to accumulate (i.e., the solution is stagnant) in larger solutions, the rates of the later stages are accelerated. Certainly, the large solution depths can result in more overall metal loss. In this section, the effects of solution depth (d_{sol}) on the corrosion dynamics in the presence of radiation using d_{sol} values between 0.25 and 2.50 cm.

In small solution depths (defined in this study as $d_{sol} \leq 0.25$ cm, regardless of solution volume), the diffusion layer ($0 < z < \delta_{diff}$) is a non-negligible proportion of the overall d_{sol}, schematically shown in **Figure 8.6**. The diffusion layer thickness is dependent on the diffusing ion and for a given ion it is the same regardless of solution volume. In stagnant solutions, the Nernst diffusion layer is approximately 0.2 – 0.5 mm.[19] In small d_{sol}, the thickness of the diffusion layer, where large concentration gradients exist, is not negligible compared to the thickness of the entire solution. Conversely, in large depths (defined in this study as $d_{sol} \geq 0.80$ cm), the concentrations within the diffusion layer do not contribute significantly to the measured species values. In fact, the interfacial solution can be considered a point source of $Cu^{2+}_{(sol'n)}$ and other dissolved species formed via interfacial charge transfer (e.g., H^+/OH^-).

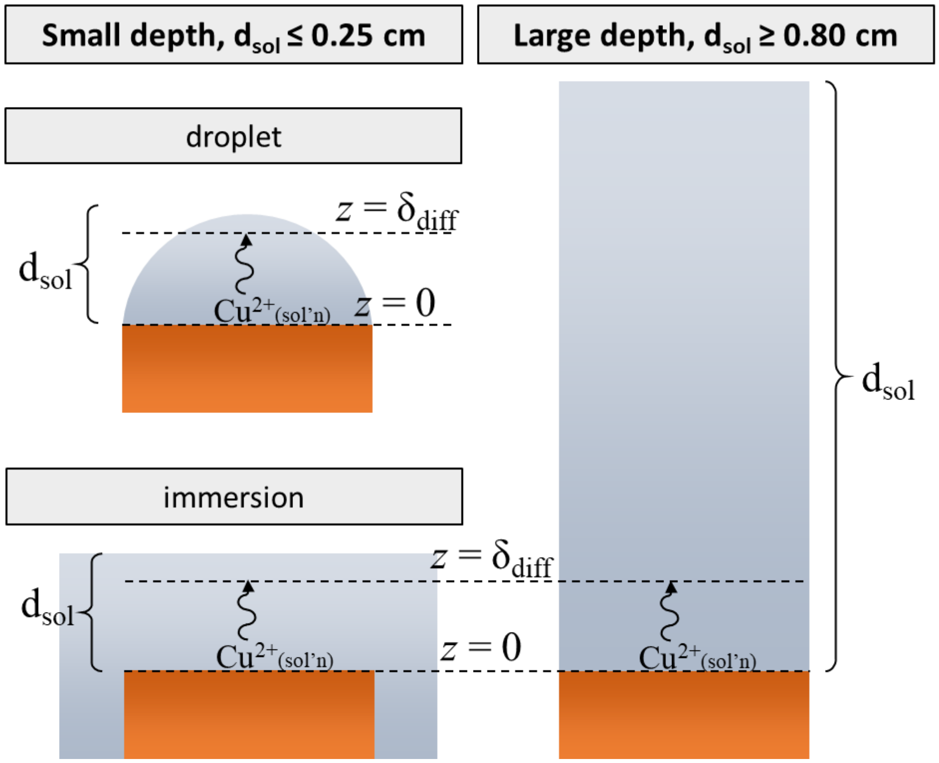

Figure 8.6 Schematic representation of the diffusion length (δ_{diff}) in small (left) and large (right) volumes, where d_{sol} is the solution depth.

8.3.2.1 Small Solution Depth

For $d_{sol} = 0.25$ cm solutions, the coupon was immersed in the solution so that the depth above the surface was similar to the maximum depth of the droplet solutions. However, the solution volume was larger in these immersion tests than in the droplet solutions (schematically represented in **Figure 8.6**). The time-dependent behaviours of $[Cu^{II}_{(sol'n)}]$, pH, and surface colour and morphology for $d_{sol} = 0.25$ cm solutions are shown in **Figure 8.7**. The solutions in this section are aerated (i.e., contain CO_2) and thus, are compared to the aerated droplet solutions from **Chapter 7**. The following are the key observations, which will be followed by a detailed discussion.

<u>Stage 1:</u> When $t \leq 40$ h, $[Cu^{II}_{(sol'n)}]_t$ increased while minimal oxide growth was observed on the surface. The pH_t first decreased from its initial value, but then increased for the rest of <u>Stage 1</u>. The pH_t reached at the end of this

stage was much higher in than other radiated solutions, but the rate and duration of this stage is the same as in aerated, droplet solutions.

Stage 2: For 48 h $\leq$ t $\leq$ 96 h, both the $[\mathrm{Cu}^{\mathrm{II}}{}_{(\mathrm{sol'n})}]_t$ and pH_t were mostly constant with time. $[\mathrm{Cu}^{\mathrm{II}}{}_{(\mathrm{sol'n})}]_t$ fluctuated around a value of 0.13 mM and pH_t fluctuated around 6.0. The surface remained clear of oxide deposits.

Stage 3: For t $\geq$ 144 h, $[\mathrm{Cu}^{\mathrm{II}}{}_{(\mathrm{sol'n})}]$ increased and pH decreased with time. Granular oxides covered the surface, with large spatial variations in colour. The Cu_2O particles are much smaller (in the hundreds of nm range) than those seen in droplet solutions (in the μm range) after the same amount of time.

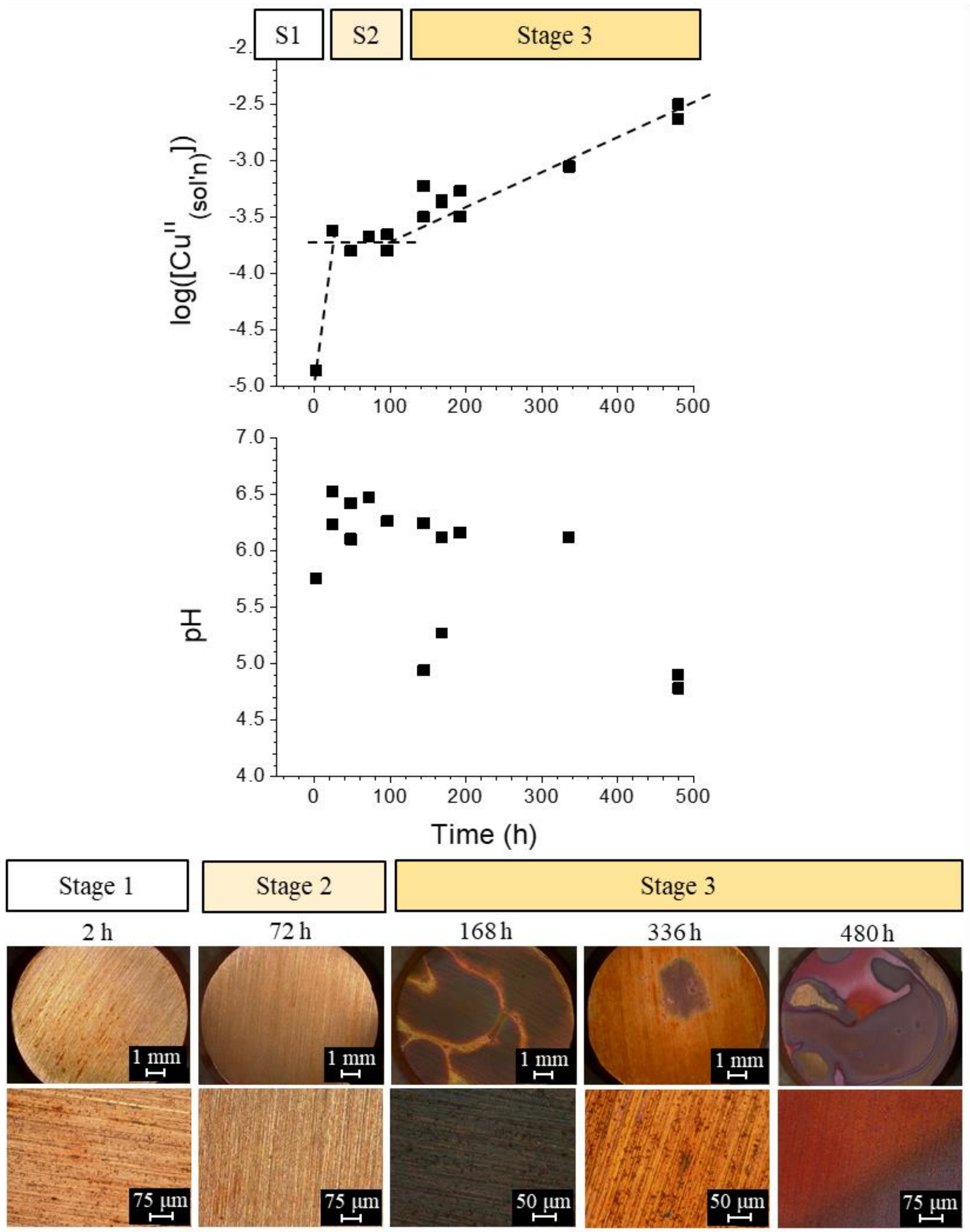

Figure 8.7 Time-dependent behaviour of [$Cu^{II}_{(sol'n)}$] (top row), pH (middle row), and the exposed surface (optical images, bottom row) during copper corrosion after exposure to pure water with d_{sol} = 0.25 cm (2.0 mL), in the presence of γ-radiation. The black dotted lines show the general trend of the data (not based on regression analysis).

In irradiated solutions, metal oxidation is coupled with H_2O_2 reduction, which is produced via water radiolysis at a low steady-state concentration. In aerated solutions in the presence of radiation (**Chapter 7**), corrosion in Stage 1 involves the full redox process at the metal surface and cupric ion hydrolysis in the interfacial solution to produce $Cu(OH)^+$ and $OH^–$.

$$Cu^0_{(m)} + H_2O_2 \rightarrow Cu(OH)^+ + OH^– \tag{8.12}$$

In the droplet solutions, the pH was constant during Stage 1, indicating the rate of production of $OH^–$ at the interfacial solution via **Eq. 8.12** was the same as the rate of production of $[H^+]$ in the bulk solution via water and humid air radiolysis (e.g., HNO_3).

In the immersion solutions, where d_{sol} is approximately the same as in the droplet solutions, but the bulk solution is much larger (see schematic in **Figure 8.6**), pH_t was observed to decrease from 7.0 to 5.7 after 2 h, then increase until t = 24 h (**Figure 8.7**). Because the bulk volume is larger, $[H^+]$ produced in the bulk solution via radiolysis is higher than $[OH^–]$ produced in the interfacial region via **Eq. 8.12**. Thus, the pH initially decreases (**Figure 8.7**). The production of $Cu(OH)^+$ and $OH^–$ at the metal surface will form a diffusion layer perpendicular and radially away the surface. This is the only corrosion condition studied in this thesis where radial diffusion away from the metal surface is possible. As $Cu(OH)^+$ diffuses into the bulk solution (i.e., the solution not above the metal surface), the lower pH_t (due to acidic radiolysis products) pushes the cupric ion hydrolysis equilibrium towards the formation of unhydrolyzed Cu^{2+}, releasing a $OH^–$. This shift in hydrolysis equilibrium in the bulk solution causes pH_t to increase (**Figure 8.7**), indicating the rate of production of $[OH^–]$ in this way is higher than the rate of production of $[H^+]$ via radiolysis. As the pH_t and cupric ion concentration in the bulk increases, the cupric ion hydrolysis equilibrium is again pushed towards the formation of $Cu(OH)^+$ and eventually $Cu(OH)_2$, causing the pH_t to plateau (**Figure 8.7**).

Regardless of the bulk changes in pH and main form of cupric ions, the main corrosion reaction at the interface in Stage 1 does not change (**Eq. 8.12**) and the corrosion rate is controlled by cupric ions away from the metal surface. Thus, Stage 1 is observed for the first 24 h, when the increase in $[Cu^{II}_{(sol'n)}]$ was constant and the surface remained clean from oxides

(**Figure 8.7**). The rate of increase in [$Cu^{II}_{(sol'n)}$] was much lower than in droplet solutions, at 4.8 ± 1.1 μM/h, but the rate of metal loss in Stage 1 was the same at 12.2 ± 3.5 nmol $Cu/cm^2/h$ (all rates are summarized in **Table 8.2**). That is, the rate of Stage 1 is unaffected by the large volume. Furthermore, because the length of Stage 1 is dependent on how quickly the interfacial solution can accumulate cupric ions, which then precipitate as a hydrogel network covering the surface, the duration of Stage 1 was also unaffected by the increase in solution volume. (However, the duration of Stage 1 is affected by increase in solution depth, shown in the next section).

As the concentrations of $Cu(OH)^+$ and OH^- at the interface increase, the cupric ion hydrolysis shifts towards the formation of $Cu(OH)_{2(solv)}$, which precipitate as colloidal particles. Shortly after colloid particles form, they aggregate into a hydrogel network, marking the start of Stage 2. During this stage, the rate of metal oxidation to produce $Cu^{2+}_{(sol'n)}$ is approximately the same as the rate of $Cu(OH)_2$ precipitation, and [$Cu^{II}_{(sol'n)}$] fluctuates around an average value (**Figure 8.7**). The steady-state concentration was 0.13 ± 0.04 mM, a much lower concentration than in droplet solutions, but an equal number of moles in both solution volumes with the same d_{sol} (0.25 μmol). Because the production of cupric ions at the interface ceased, so did the production of OH^-, and pH_t also finds a steady state with a value of 6.0 (**Figure 8.7**).

As $Cu(OH)_2$ hydrogel grows at the interface, the rate of reduction of $Cu^{2+}_{(sol'n)}$ coupled with the oxidation of H_2O_2 increases and a mixed Cu^I/Cu^{II} hydroxide hydrogel is formed (**Eq. 8.10**). Stage 3 begins when cuprous ions in the mixed hydrogel reach a supersaturation concentration and precipitates as Cu_2O crystals. The surface was covered with granular oxides when $t \geq 144$ h. There are large spatial variations in the oxide colour across the surface (optical images in **Figure 8.7**) despite a consistent solution height over the copper surface, suggesting that the colour variations are due to the spreading hydrogel, as opposed to solution height variations (in droplet solutions).

The Cu_2O crystals on the surface during Stage 3 in $d_{sol} = 0.25$ cm are compared to that in the aerated droplet solutions (**Chapter 7**) in **Figure 8.8**. Despite a similar d_{sol}, the crystal average crystal sizes are much smaller when the solution volume is large (immersion). The Cu_2O crystals grow because the redox reaction between $Cu^0_{(m)}$ oxidation to $Cu^{2+}_{(sol'n)}$ coupled with reduction of oxidant to OH^- (i.e., **Eq. 8.12**) can couple with the reduction of $Cu^{2+}/Cu(OH)_2$ to Cu_2O coupled with the reduction of oxidant to OH^- (i.e., **Eq. 8.10a** and **8.11**). Thus, $[Cu^{II}_{(sol'n)}]$ is important in determining the size of the Cu_2O crystals. With a larger solution volume, the lower $[Cu^{II}_{(sol'n)}]$ results in smaller Cu_2O crystals.

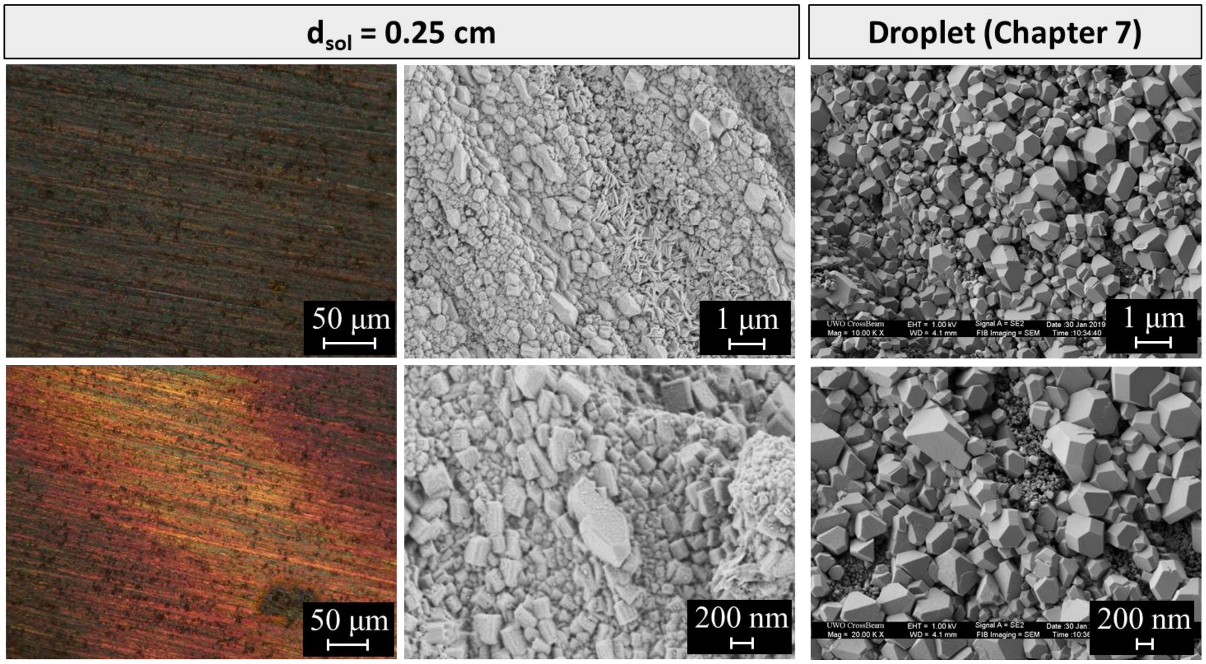

Figure 8.8 Optical (left column) and SEM (right two columns) images of the oxide growth after 168 h of corrosion (Stage 3) in d_{sol} = 0.25 cm (2.0 mL) and in aerated droplet solutions from **Chapter 7** for comparison (maximum d_{sol} = 0.20 cm).

Even after 480 h corrosion duration, Stage 4 was not observed in the immersion test, due to a lower $[Cu^{II}_{(sol'n)}]$ and thus less oxide growth during Stage 3. Thus, despite the same durations and molar yields in Stages 1 and 2 more overall metal loss can occur in Stage 3 in these larger volumes.

8.3.2.2 Large Solution Depth

To increase the solution depth while limiting radial diffusion, copper coupons were embedded in shrink tubing, shown in **Figures 8.1** and **8.6**. The solutions used were naturally aerated (containing CO_2). The time-dependent behaviours of $[Cu^{II}_{(sol'n)}]$ and pH in large solution depths ($d_{sol} \geq 0.80$ cm) are shown in **Figure 8.9**. The surface colour and morphology evolution with time is presented in **Figure 8.10** and **8.11**. Although the time-dependent behaviours were similar in each d_{sol} ($\geq$ 0.80 cm), the length and product yield in each stage varied with solution depth. The key time-dependent behaviours common to all large d_{sol} are:

Stage 1: $[Cu^{II}_{(sol'n)}]$ increases linearly with time, while no significant granular oxide growth was observed on the surface. The length of this stage increased with solution depth, but the metal oxidation rate (in nmol $Cu/cm^2/h$) was nearly independent of solution depth. The pH decreased during this stage.

Stage 2: $[Cu^{II}_{(sol'n)}]_t$ and pH_t fluctuate around a steady-state value that was nearly independent of solution depth. The duration of Stage 2 increased with increasing solution depth. The dried hydrogel network was observed in SEM images.

Stage 3: At $t = 480$ h, $[Cu^{II}_{(sol'n)}]$ increased to a maximum value proportional to d_{sol}, while pH remains at its steady state value. The surface darkened with the growth of some small granular oxides.

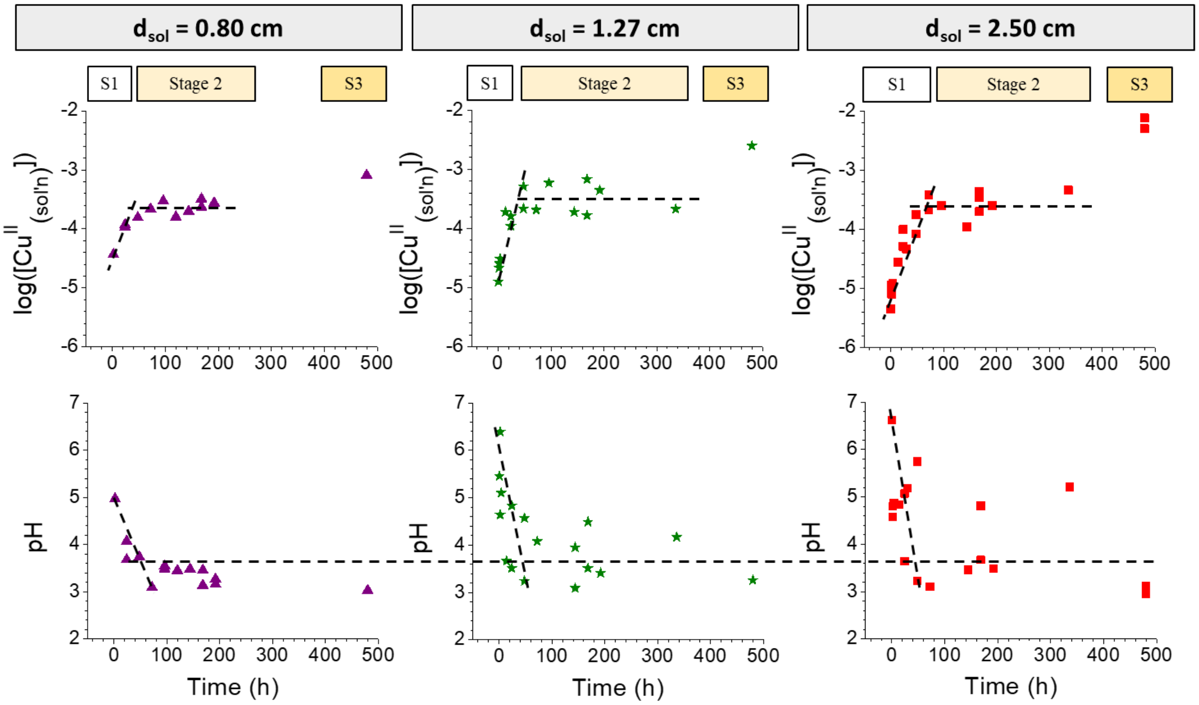

Figure 8.9 The time-dependent behaviours of $[\mathrm{Cu}^{\mathrm{II}}_{(\mathrm{sol'n})}]$ (top row) and pH (bottom row) in large solution depths ($d_{sol} \geq 0.80$ cm) during radiolytic copper corrosion. The black dotted lines show the general trend of the data (not based on regression analysis).

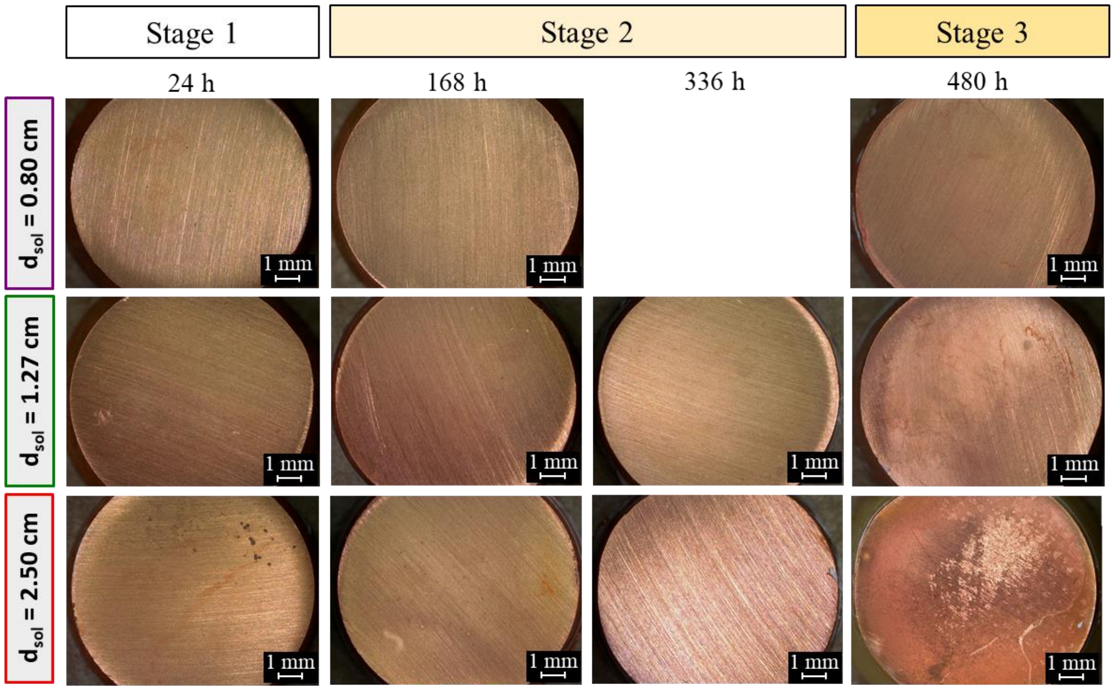

Figure 8.10 Optical images of the copper surface during the three observed corrosion stages after exposure to large solution depths ($d_{sol} \geq 0.80$ cm) in the presence of radiation.

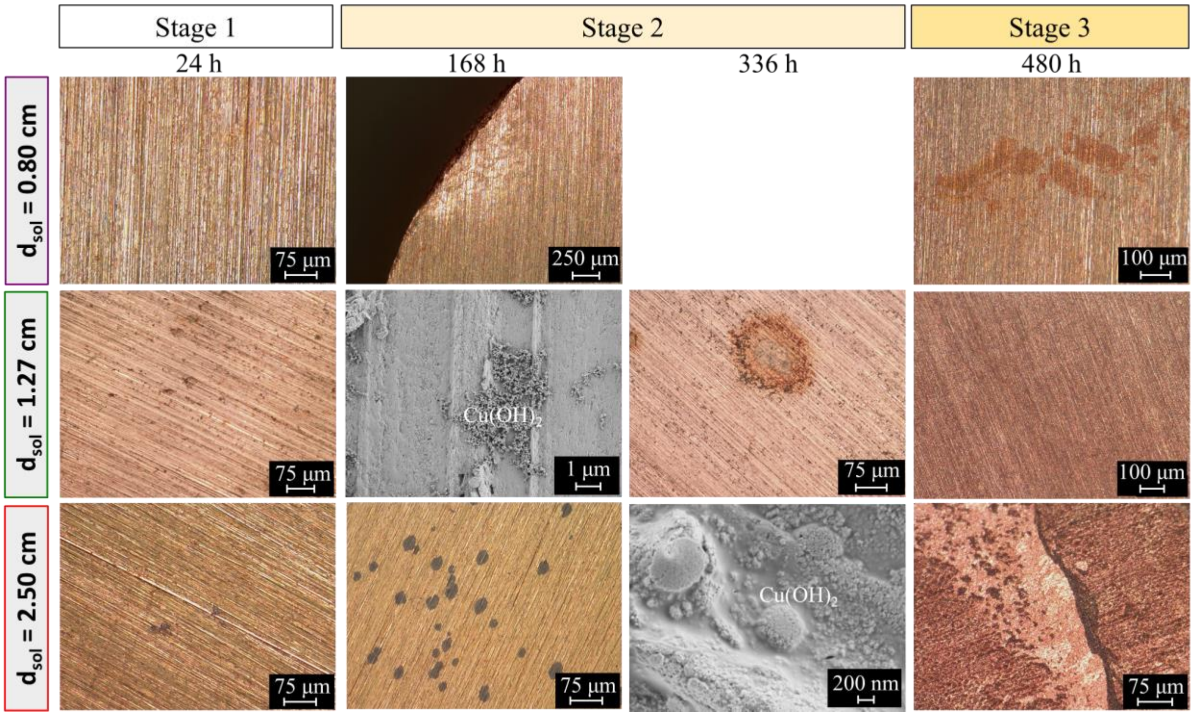

Figure 8.11 Optical and SEM images of the copper surface during the three observed corrosion stages after exposure to large solution depths ($d_{sol} \geq 0.80$ cm) in the presence of radiation.

$[Cu^{II}_{(sol'n)}]$ during radiolytic copper corrosion in all solution depths show the time-dependent behaviour characteristic of the first three stages of corrosion, shown in **Figure 8.9**. $[Cu^{II}_{(sol'n)}]$ increases linearly with time in <u>Stage 1</u>, remains constant with time in <u>Stage 2</u>, then increases as pH_t fluctuates around a low steady-state value in <u>Stage 3</u>. The solution depth (d_{sol}) affected the duration of the individual stages, the rate of $[Cu^{II}_{(sol'n)}]$ increase in <u>Stage 1</u>, and the overall yield after 480 h (the longest duration of the experiment).

When $d_{sol} \geq 0.80$ cm, the bulk volume is large and the OH^- production via the initial corrosion reactions (**Eq. 8.12**) has almost no effect on the overall pH. Thus, pH_t in all solutions begins decreasing almost immediately (less than 2 h, shown in **Figure 8.9**), and continues to decrease until a low steady-state value of 3.7 ± 0.3 is reached. This indicates that with d_{sol} above a critical value (between 0.25 cm and 0.80 cm), the OH^- produced at $z = 0$ has nearly the same effect on the pH in irradiated solutions.

The rate of $[Cu^{II}_{(sol'n)}]$ increase during <u>Stage 1</u> was inversely proportional to d_{sol} (**Figure 8.9** and exact values given in **Table 8.2**). However, the rate of metal loss (in units of nmol

Cu/cm^2/h) is nearly independent of d_{sol}. There is a slight decrease in rate with increasing d_{sol} because in larger volumes the $Cu^{2+}_{(sol'n)}$ concentration gradient is smaller. Nevertheless, the metal oxidation rate in Stage 1 is controlled by the diffusion rate of $Cu^{2+}_{(sol'n)}$ (mostly in the form of $Cu(OH)^+$) from $z = 0$ to the bulk solution. Regardless of d_{sol}, the surface during Stage 1 did not show a significant amount of oxide growth (**Figures 8.10** and **8.11**), consistent with the main corrosion product being a dissolved species.

Figure 8.9 shows that the duration of Stage 1 is directly proportional to d_{sol} (exact values given in **Table 8.2**). The duration of Stage 1 is dependent on how quickly $Cu^{2+}_{(sol'n)}$ can accumulate in the interfacial solution, which is consistent with the observed duration dependence on d_{sol}. That is, it takes longer for $Cu^{2+}_{(sol'n)}$ in the interfacial solution region in larger solution depths. Furthermore, with the same rate of metal loss, but increase in duration, there is much more overall corrosion damage during Stage 1 in larger solution volumes. The implication of this is that in large volumes or in flowing solutions, metal dissolution is expected to continue at the same rate for a very long time and the overall corrosion damage would be proportional to the service life of the copper component.

The steady-state $[Cu^{II}_{(sol'n)}]$ value was nearly independent of d_{sol} (when $d \geq 0.80$ cm, **Figure 8.9**), indicating the same $[Cu^{2+}_{(sol'n)}]$ had accumulated before it began precipitating as a hydrogel network. The hydrogel network was observed in the optical and SEM images in **Figure 8.11**. After 168 h, clear hydrogel was observed in $d_{sol} = 0.80$ cm at the edge of the coupon while blue (high colloid density) was observed in $d_{sol} = 2.50$ cm. In $d_{sol} = 1.27$ cm, the dried hydrogel solid network was observed in SEM. Copper hydroxide hydrogel that has been synthesized in previous studies has a similar solid network structure.[20] After a longer corrosion duration (t = 336 h), the hydrogel had covered the entire surface and increased in colloidal density. This can be seen in the SEM image in **Figure 8.11** in $d_{sol} = 2.50$ cm, where the hydrogel covers the surface as a thick layer.

As the saturated volume expands during Stage 2, the concentration of CuOH within the hydrogel increases and begins to precipitate as Cu_2O. At long corrosion times (t = 480 h), $[Cu^{II}_{(sol'n)}]$ increases and the granular oxide growth is visible on the surface, consistent with Stage 3. **Figure 8.9** shows that the $[Cu^{II}_{(sol'n)}]$ yield after 480 h as well as the rate of increase in $[Cu^{II}_{(sol'n)}]$ during Stage 3 was proportional to the d_{sol} in this stage. This is a result of the higher colloidal density in the hydrogel in larger d_{sol} during Stage 2. The implication of this is that if corrosion progresses past Stage 2, more material loss will occur when the solution depth is large, or the solution is flowing.

For all d_{sol} values, the surface had darkened by 480 h due to granular oxide growth along the polishing lines (**Figure 8.11**). The extent of oxide growth was also proportional to the d_{sol} (**Figure 8.10** and **8.11**). In largest d_{sol}, the oxides on the surface had aggregated into localized areas during the redox-assisted Ostwald ripening, shown in **Figure 8.10** and **8.11**, where the dark lines and islands are Cu_2O crystals, and the shiny reddish-orange areas are the bare $Cu^0_{(m)}$.

The depth of solution does not affect the corrosion progression but affects the duration of each stage. The results in this chapter confirmed that the solution depth, not solution volume, determines length of Stage 1. Ultimately, in larger solution depths, more corrosion damage can be expected. The rates, durations, and yields in each corrosion stage in all solution depths are summarized in **Table 8.2**.

Table 8.2 Summary of $Cu^{II}_{(sol'n)}$ dissolution rates in the observed corrosion stages in aerated solutions with different solution depths (d_{sol}) compared to droplet solutions (**Chapter 7**).

	Small solution depths		**Large solution depths**		
d_{sol} =	**0.20 cm (Chapter 7)**	**0.25 cm**	**0.80 cm**	**1.27 cm**	**2.50 cm**
Stage 1					
Duration (h)	24	24	2	50	100
$Cu^{II}_{(sol'n)}$ dissolution rate (nmol Cu/cm^2/h)	12.6	12.2	11.6	9.2	8.4
Stage 2					
Duration (h)	72	72	170	270	340
[$Cu^{II}_{(sol'n)}$] plateau (mM)	4.2	0.13	0.31	0.35	0.25
Amount of copper during plateau (µmol)	0.21	0.25	0.16	0.35	0.50

Steady-state pH	4.3	6.0	3.4	3.9	3.7
Stage 3					
Observed when	120 ≤ t ≤ 192	t ≥ 144 h	t = 480 h	t = 480 h	t = 480 h
$Cu^{II}_{(sol'n)}$ dissolution rate (nmol $Cu/cm^2/h$)	36	33	1.2	20	103
[$Cu^{II}_{(sol'n)}$] yield	65.2	2.7	0.80	2.5	6.3
Final copper yield (µmol)	3.3	5.5	0.40	2.5	12

8.4 CONCLUSIONS

This chapter investigated how the corrosion dynamics were affected by an increase in pH_0 and solution depth. In all conditions, the same elementary reactions control the overall corrosion progression. The time-dependent behaviours of [$Cu^{II}_{(sol'n)}$], pH, and surface morphology and colour were unaffected by the increase in pH_0 from 7.0 to 9.0. Furthermore, the rates of and yields in each stage were nearly independent of this pH_0 increase. This is true for all cover gas compositions studied in this thesis, although only CO_2-free solutions were discussed in detail in this chapter. These results indicate that the solution pH evolution is not dependent on pH_0 when between 6.0 (aerated), 7.0 (CO_2-free, 21% O_2, deaerated) and 9.0 (all cover gases), confirming the proposed corrosion mechanism. In effect, these results show that it is unnecessary to know the exact initial pH (between 6 and 9) of the groundwater solution when it interacts with the copper layer of the UFC.

This chapter also showed that the elementary stages that determine the corrosion dynamics are unaffected by d_{sol}. However, the durations and yields in each stage varies with d_{sol}, but not solution volume. Ultimately, the results in this chapter show that a larger d_{sol} will result in more metal loss. These results are consistent to previous studies done by our group of the effect of d_{sol} without radiation[18] and further confirm the corrosion mechanism.

8.5 REFERENCES

1 Standish, T. E. "Galvanic Corrosion of Copper-Coated Carbon Steel for Used Nuclear Fuel Containers" Doctor of Philosophy, The University of Western Ontario, Electronic Thesis and Dissertation Repository. (2019). 6705.

2 King, F., Ahonen, L., Taxén, C., Vuorinen, U., Werme, L. *Copper Corrosion Under Expected Conditions in a Deep Geologic Repository*. (SKB, 2001).

3 Rustad, J. R., Casey, W. H. A Molecular Dynamics Investigation of Hydrolytic Polymerization in a Metal−Hydroxide Gel. *J. Phys. Chem. B* **110**, 7107-7112, (2006).

4 Gustafson, R., Martell, A. Formation of Polynuclear Complexes in Aqueous Solution. *Ann. N.Y. Acad. Sci.* **88**, 322-331, (2006).

5 Holmes, H. N. The Formation of Crystals in Gels. *J. Franklin Inst.* **184**, 743-773, (1917).

6 Durand-Keklikian, L., Matijević, E. Needle-Type Colloidal Copper (II) Hydroxide Particles. *Colloid. Polym. Sci.* **268**, 1151-1158, (1990).

7 Shin, Y. G. "Nonlinear Dynamics of Carbon Steel Corrosion under Gamma Radiation" Doctor of Philosophy, The University of Western Ontario, Electronic Thesis and Dissertation Repository. (2020). 7339.

8 Baes, C. F., Mesmer, R. E. *The Hydrolysis of Cations*. (Wiley, 1976).

9 Joseph, J. M., Choi, B. S., Yakabuskie, P., Wren, J. C. A Combined Experimental and Model Analysis on the Effect of pH and $O_{2(aq)}$ on Gamma-Radiolytically Produced H_2 and H_2O_2. *Radiat. Phys. Chem.* **77**, 1009-1020, (2008).

10 Yakabuskie, P., Joseph, J., Wren, J. The Effect of Interfacial Mass Transfer on Steady-State Water Radiolysis. *Radiat. Phys. Chem.* **79**, 777-785, (2010).

11 Yakabuskie, P. A., Joseph, J. M., Stuart, C. R., Wren, J. C. Long-Term γ-Radiolysis Kinetics of NO_3^- and NO_2^- Solutions. *J. Phys. Chem. A* **115**, 4270-4278, (2011).

12 Morco, R. P., Joseph, J. M., Hall, D. S., Medri, C., Shoesmith, D. W., Wren, J. C. Modelling of Radiolytic Production of HNO_3 Relevant to Corrosion of a Used Fuel Container in Deep Geologic Repository Environments. *Corros. Eng. Sci. Technol.* **52**, 141-147, (2017).

13 Galante, R., Rediguieri, C. F., Kikuchi, I. S., Vasquez, P. A. S., Colaço, R., Serro, A. P., Pinto, T. J. A. About the Sterilization of Chitosan Hydrogel Nanoparticles. *PLOS ONE* **11**, e0168862, (2016).

14 Zheng, J., Clogston, J. D., Patri, A. K., Dobrovolskaia, M. A., McNeil, S. E. Sterilization of Silver Nanoparticles Using Standard Gamma Irradiation Procedure

Affects Particle Integrity and Biocompatibility. *J. Nanomed. Nanotechnol.* **2011**, 001, (2011).

15 Ulanski, P., Rosiak, J. M. The Use of Radiation Technique in the Synthesis of Polymeric Nanogels. *Nucl. Instrum. Methods Phys. Res. B* **151**, 356-360, (1999).

16 Wren, J. C. *Steady-State Radiolysis: Effects of Dissolved Additives* in *Nuclear Energy and the Environment* Vol. 1046 *ACS Symposium Series* (eds C. M. Wai & B. J. Mincher) 271-295 (2010).

17 Bessho, K., Oki, Y., Akimune, N., Matsumura, H., Masumoto, K., Sekimoto, S., Osada, N., Kinoshita, N., Monjushiro, H., Shibata, S. Corrosion of Copper in Water and Colloid Formation Under Intense Radiation Field. *J. Radioanal. Nucl. Chem.* **303**, 1117-1121, (2015).

18 Naghizadeh, M. "Copper Corrosion Dynamics under Deep Geologic Repository Conditions" Doctor of Philosophy, The University of Western Ontario, Electronic Thesis and Dissertation Repository. (2021). 7894.

19 Pohl, P., Saparov, S. M., Antonenko, Y. N. The Size of the Unstirred Layer as a Function of the Solute Diffusion Coefficient. *Biophys. J.* **75**, 1403-1409, (1998).

20 Fukumoto, S., Nakanishi, K., Kanamori, K. Direct Preparation and Conversion of Copper Hydroxide-Based Monolithic Xerogels with Hierarchical Pores. *New J. Chem.* **39**, 6771-6777, (2015).

CHAPTER 9. THESIS SUMMARY AND FUTURE WORK

9.1 SUMMARY

Predicting the long-term corrosion behaviour of the copper layer of the UFC is challenging. The copper layer will be exposed to uncommon solution conditions that change throughout its lifetime, including a continuous flux of γ-radiation. The small solution volumes expected in the DGR could lead to the accumulation of cupric ions next to the metal surface, and their (electro)chemical reactions can increasingly affect the initial charge transfer rate. Cyclic feedback loops between multiple elementary reactions can be established that affect the overall metal loss rate. Furthermore, solution conditions can affect the rate of individual elementary reactions and thus the overall rate of corrosion. The combined effects of solution parameters and γ-radiation on the copper corrosion dynamics were investigated in this thesis. The solution parameters investigated were the initial pH, cover gas composition, and the solution depth, all in the absence and presence of radiation. The corrosion dynamics were determined by following the corrosion products (i.e., $[Cu^{II}_{(sol'n)}]$, $[OH^-]$, and oxide deposits) evolution as a function of corrosion duration. Based on the results, a corrosion mechanism was proposed that was can be used to explain the corrosion behaviour in all studied conditions.

In **Chapter 4**, the time-dependent evolution of $[Cu^{II}_{(sol'n)}]$ and pH during the early corrosion stages (<u>Stages 1</u> and <u>2</u>) were investigated in all the redox and solution environments studied in this thesis. The elementary steps involved in the overall metal oxidation process are the same for all solution conditions but change as corrosion progresses. It was shown that the relationship of $[Cu^{II}_{(sol'n)}]$ versus $[H^+]$ evolves with time and follows that of the metal cation solubility versus $[H^+]$. However, the time-dependent evolution of these species influences their final yield along the solubility curve. This indicates that the values of $[Cu^{II}_{(sol'n)}]$ and pH can be determined by the solubility equilibrium of $Cu(OH)_2$ if the initial conditions and the evolution with time are known. The data presented in this chapter provides insight into the relationship between cupric ion dissolution and pH during copper corrosion and the fundamental understanding gained from these results could simplify the approach to long-term corrosion modelling.

In **Chapter 5**, the individual effects of key radiolysis products during the initial period of corrosion were determined using chemically-added oxidants in the absence of radiation. The results showed that the time-dependent behaviour of $[Cu^{II}_{(sol'n)}]$ and pH and their overall yields were nearly independent of the oxidant concentration and type. However, decreasing the initial pH from 7.0 to 4.0 increased the concentration of copper in solution (accordingly with the $Cu(OH)_2$ solubility), thereby increasing the copper yield and duration of Stage 1. It was also shown that an increase in H_2O_2 concentration increased the rate of cupric ion reduction to cuprous ion, increasing the amount of Cu_2O precipitation. The results from this chapter will permit the decoupling of the effects of radiolysis products on the corrosion evolution. Furthermore, the results presented in this chapter demonstrate that the dissolution behaviour and final yield of cupric ions are unaffected by the initial concentration and identify of the oxidant. These findings can simplify copper corrosion modelling in the presence of radiation.

Chapter 6 proposed a copper corrosion mechanism in the presence and absence of γ-radiation in CO_2-free water droplets. The results of this chapter showed that the elementary reactions involved in the overall corrosion process evolve with time in a stepwise manner. The metal oxidation dynamics evolve through distinct periods (stages), each with its own characteristic oxidation rate. Four stages were identified. In Stage 1, the overall corrosion process involves copper oxidation to the dissolved cupric ion, which quickly establishes a hydrolysis equilibrium and diffuses from the metal surface. The main corrosion products in this stage are dissolved cupric species, and thus the corrosion rate can be determined from the dissolution rate. The main effect of radiation in this stage is the production of acidic species, which cause the pH to decrease, rather than increase with time, and increase the solubility of cupric ions. Thus, the copper yield in Stage 1 is much higher in the presence of radiation and this stage was much shorter because the agglomeration and reduction of $Cu(OH)_2$ colloids is accelerated.

Stage 2 begins when cupric ions have accumulated, and $Cu(OH)_2$ begins to grow as a hydrogel network. Cupric ions trapped next to the metal surface are reduced to form a mixed Cu^{I}/Cu^{II} hydroxide hydrogel. During this stage, the net corrosion process is production of this mixed hydrogel and $[Cu^{II}_{(sol'n)}]_t$ is constant. The production of H_2O_2 in the presence of radiation accelerates the reduction of cupric ions, and thus Stage 2 is short in the presence of radiation.

Once CuOH is supersaturated, it precipitates as Cu_2O, marking the start of Stage 3. In unirradiated solutions, the CuOH concentration is low and H_2O_2 is absent, and thus the rate of Cu_2O precipitation is low and corrosion does not progress past Stage 3. In the presence of radiation, Cu_2O growth during Stage 3 is fast and individual particles can grow large. Cu_2O crystals undergo redox-assisted Ostwald ripening throughout this stage, and hindered diffusion through the hydrogel layer creates Liesegang bands on the surface. Once electron transfer through the oxide layer ceases, Stage 4 begins. During this stage, the metal oxidation rate is zero, but the oxide particles continue to age. In the CO_2-free solutions investigated in this chapter, nitrate was incorporated into the mixed Cu^I/Cu^{II} hydrogel and it is postulated that nitrate-containing copper crystals will precipitate with increasing time.

In **Chapter 7**, the combined effects of cover gas composition and the presence of γ-radiation were investigated. For all cover gas compositions, the corrosion progression involves the same elementary reactions, showing the same characteristic oxidation stages, with slight variations in rate and/or duration. The presence of CO_2 in solution introduced an important acid-base equilibrium and complexing anion, which allowed a significant amount of the hydrogel to grow in the presence of radiation. A higher concentration of hydrogel led to a faster progression through Stages 3 and 4. In HNO_3-free solutions, the opposite was observed: less hydrogel was formed and progression through Stage 3 to Stage 4 was slower. In deaerated (Ar-purged) solutions, the total yield of dissolved copper was the same as in oxygenated solutions in both irradiated and unirradiated conditions, further indicating that the oxidant concentration does not affect the cupric ion yield. However, $Cu(OH)_2$ reduction to form Cu_2O (Stage 3) was more efficient and began earlier in deaerated solutions. Stage 4 was not observed and therefore, metal loss continued for longer in deaerated compared to oxygenated solutions. That is, more copper was oxidized in deaerated than in oxygenated solutions. In summary, the elementary reactions that control the metal oxidation rate throughout the corrosion progress are consistent across all the solution and cover gas compositions studied, although the composition of the solution can cause the rates of particular elementary reactions to vary slightly.

In **Chapter 8**, the mass transport conditions of cupric ions were investigated by increasing the initial pH and solution depth. An increase in initial pH in a given cover gas environment had no significant effect on the corrosion dynamics or the time-dependent behaviour of $[\mathrm{Cu^{II}}_{(sol'n)}]$ or pH. However, increasing the solution depth prolonged <u>Stage 1</u> but did not change its rate, which led to more metal loss in later corrosion stages. While the length of and overall corrosion yields in each stage were dependent on solution depth, the observed time-dependent behaviours were unaffected by the change in solution depth.

9.2 CONCLUSIONS

The work presented in this thesis has shown that in small, stagnant water volumes, corrosion progresses through multiple time-dependent stages. The elementary steps involved in the overall metal oxidation process are the same for all solution conditions but change as corrosion progresses. The solution conditions affect the rates of the elementary steps involved in each stage and thereby the overall metal oxidation rate in each stage. The changes in the rates, not the nature of the elementary reactions, influence how fast the overall corrosion dynamics evolve during the different dynamic stages. If cupric ions are able to accumulate, the charge transfer and transport processes can strongly couple and establish strong feedback loops. Thus, the corrosion rate in later stages cannot be determined based on linear chemical dynamics. Furthermore, this work has elucidated the combined effects of solution environment (i.e., cover gas composition, initial pH, solution volume) and the presence of a continuous flux of γ-radiation on the time-dependent behaviours and the overall yields of corrosion products.

The results from this work will be used in the development of a radiolytic copper corrosion model that can accurately predict the required corrosion allowance of the copper layer of the UFC. The key conclusions from this thesis that contribute to the development of a robust radiolytic copper corrosion model are (i) that copper corrosion evolves through many steady states (corrosion stages) if copper ions can accumulate in solution, (ii) the copper dissolution rates in <u>Stage 1</u> as a function of solution conditions, (ii) the validation of hydrogel formation during <u>Stage 2</u>, (iii) the establishment of cyclic feedback during <u>Stages 2</u> and <u>3</u> and the acceleration of the feedback in the presence of radiation, and (iv) the relationship between dissolved copper concentration and pH at all corrosion stages beyond <u>Stage 1</u>.

9.3 FUTURE WORK

The longer-term goal that this project is contributing to is to develop a high-fidelity corrosion dynamic model that can predict the long-term corrosion behaviour of copper in the

DGR environment. The model will couple the rate and flux equations of the elementary processes involved in the overall corrosion process. The elementary processes include electrochemical reactions (metal oxidation coupled with solution reduction), solution reactions (hydrolysis, radiolysis), transport processes, and oxide particle nucleation and growth. The model must accurately and quantitatively deal with the feedback loops that can established throughout the corrosion process.

APPENDIX A. RADIATION-INDUCED pH EVOLUTION

The pH evolution in 100 µL water droplets in the presence of radiation is presented in **Figure A1**. This shows the pH decrease exclusively due to water radiolysis products without a corroding system. The irradiated droplets were in contact with CO_2-free air (**Chapter 6**) and Ar purged (**Chapter 7**) with an initial pH 7.0 (**Chapter 6**/**Chapter 7**) and 9.0 (**Chapter 8**). The final steady state pH in all solutions is 2.7 ± 0.1.

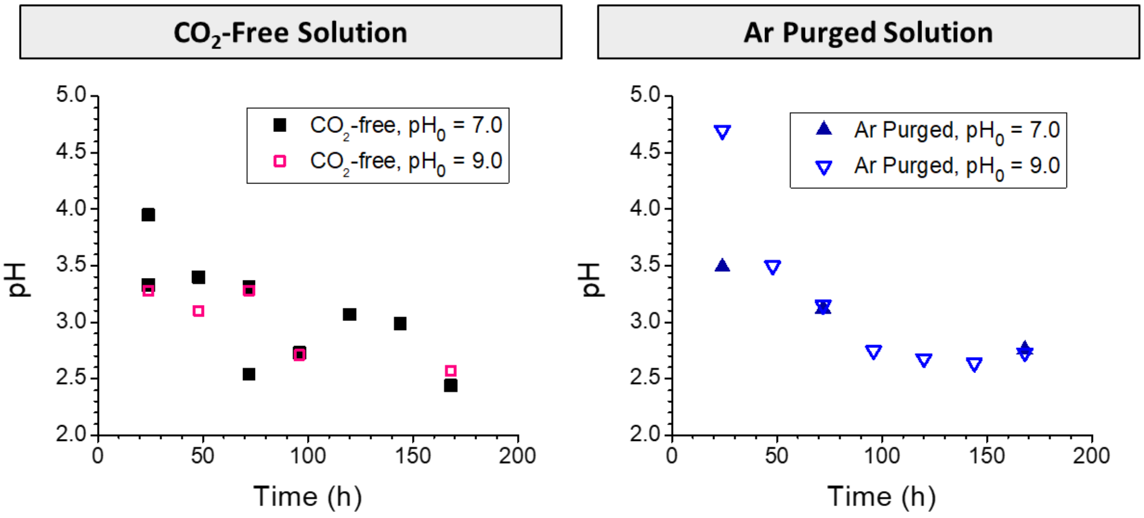

Figure A.1 The pH evolution in water droplets exposed to γ-radiation (without copper).

APPENDIX B. SOLUTION CHEMISTRY DURING Cu_2O GROWTH BY H_2O_2 REDUCTION

The effect of $[H_2O_2]_0$ on Cu_2O precipitation was investigated in **Section 5.3.2** by exposing a copper surface to a Cu^{2+}-saturated solution ($Cu(OH)_2$, Sigma Aldrich, St. Louis, MO) mixed with different $[H_2O_2]_0$ (0 M, 0.1 mM, 10 mM). **Figure B.1** shows the pH and the $[Cu^{II}_{(sol'n)}]$ remained constant throughout this experiment. More details are given in **Chapter 5**.

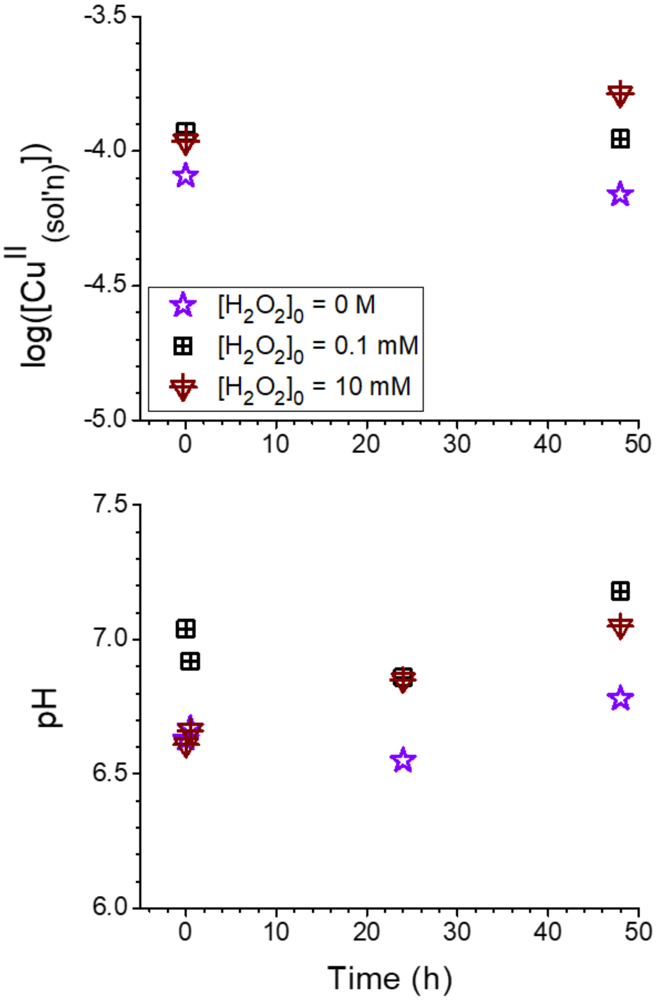

Figure B.1 Time-dependent behaviours of $[Cu^{II}_{(sol'n)}]$ (top row) and pH (bottom row) in the presence of various $[H_2O_2]_0$ solutions with $pH_0 = 7.0$.

APPENDIX C. CORROSION DYNAMICS IN WATER DROPLETS WITH pH₀ 9.0 IN THE PRESENCE AND ABSENCE OF RADIATION

The time-dependent behaviours of dissolved copper concentration, pH, and surface morphology are presence after copper exposure to aerated (**Figure C.1** and **C.2**), 21 % O_2 (balance Ar) (**Figure C.3** and **C.4**), and deaerated (**Figure C.5** and **C6**) in the presence and absence of radiation. The pH_0 = 9.0 solutions showed the same behaviour described in **Chapter 7** for the specific cover gas environment.

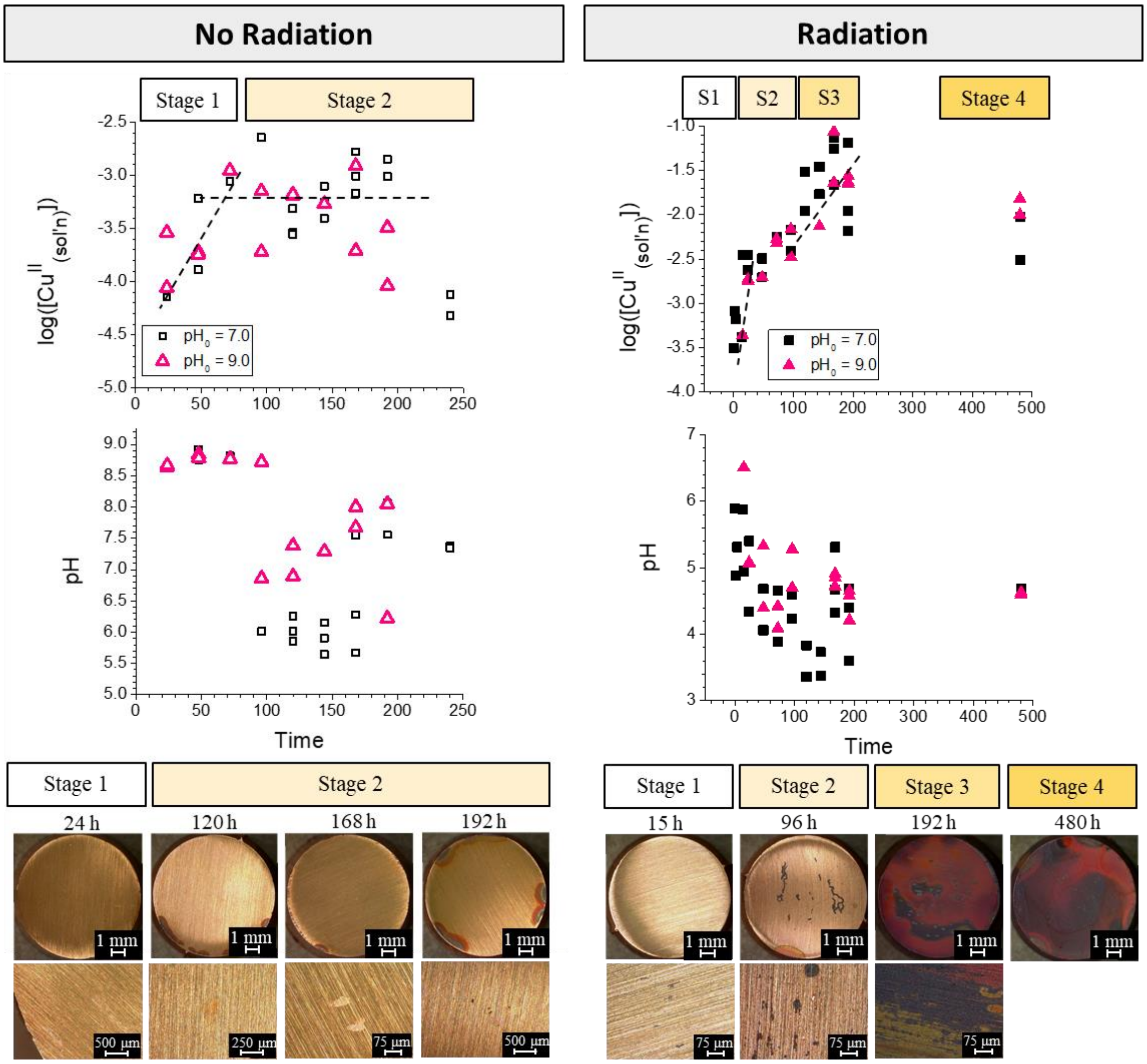

Figure C.1 Time-dependent behaviour of [$Cu^{II}_{(sol'n)}$] (top row), pH (middle row), and the exposed surface (optical images, bottom rows) during copper corrosion after exposure to a 100 µL aerated water droplet with pH_0 = 9.0 in the absence (left column) and presence (right column) of γ-radiation. The solution data is compared to that after exposure to pH_0 = 7.0 water (black squares, data from **Chapter 7**). The black dotted lines show the general trend of the data (not based on regression analysis).

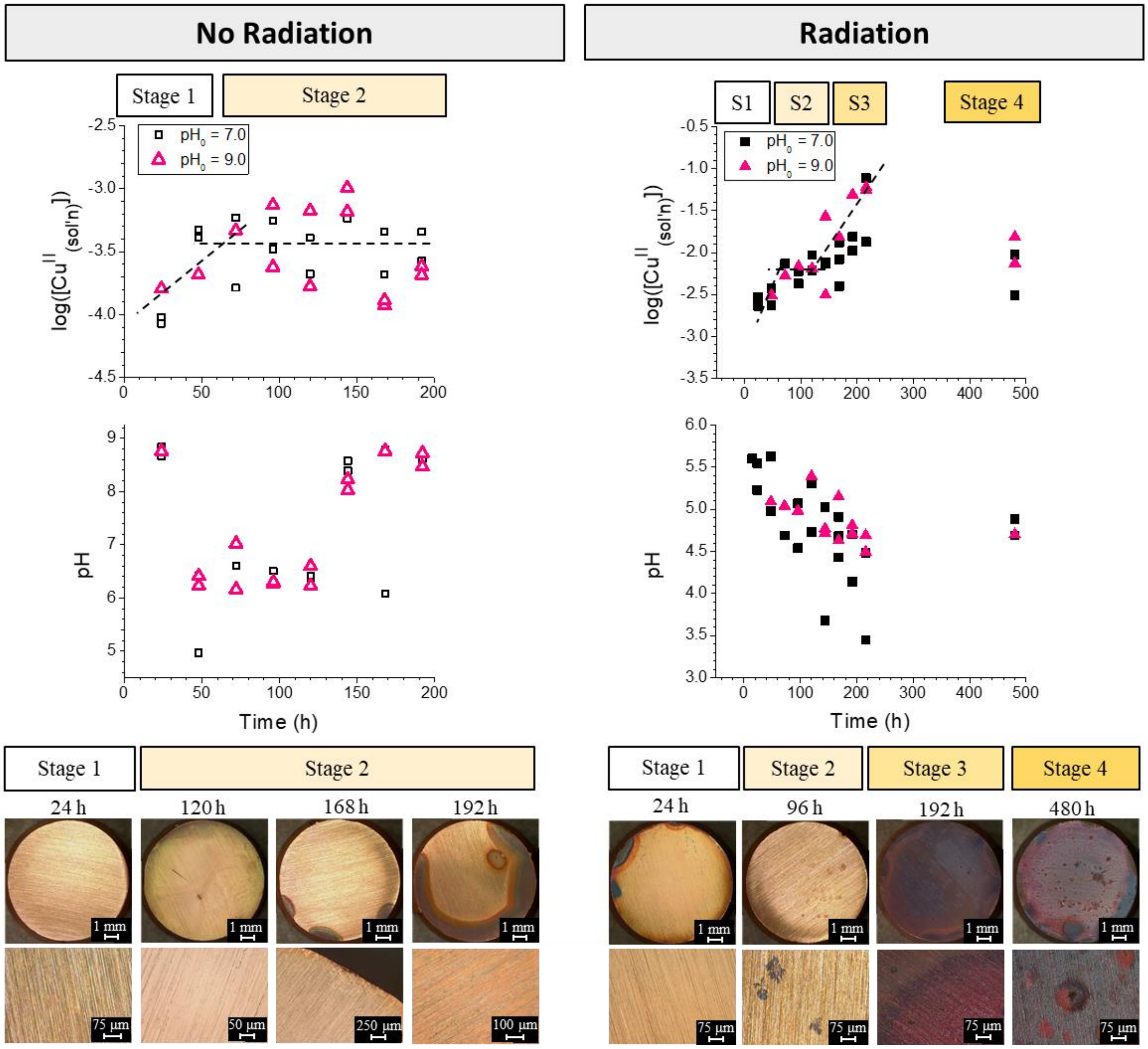

Figure C.2 Time-dependent behaviour of [$\text{Cu}^{\text{II}}_{\text{(sol'n)}}$] (top row), pH (middle row), and the exposed surface (optical images, bottom rows) during copper corrosion after exposure to a 100 µL water droplet previously purged with 21% O_2 (balance Ar) with $pH_0 = 9.0$ in the absence (left column) and presence (right column) of γ-radiation. The solution data is compared to that after exposure to $pH_0 = 7.0$ water (black squares, data from **Chapter 7**). The black dotted lines show the general trend of the data (not based on regression analysis).

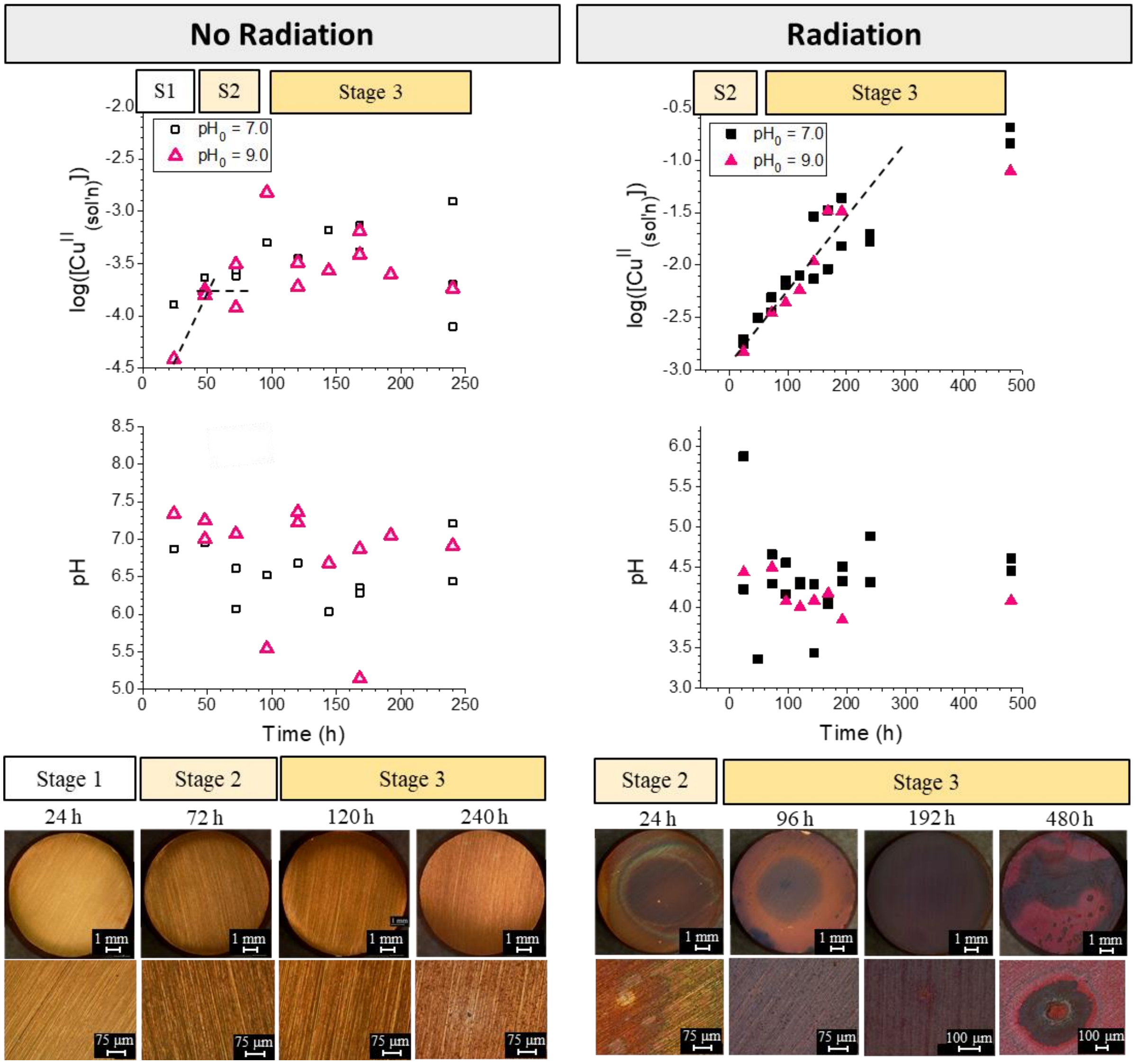

Figure C.3 Time-dependent behaviour of $[\mathrm{Cu^{II}}_{(\mathrm{sol'n})}]$ (top row), pH (middle row), and the exposed surface (optical images, bottom rows) during copper corrosion after exposure to a 100 µL deaerated water droplet with pH_0 = 9.0 in the absence (left column) and presence (right column) of γ-radiation. The solution data is compared to that after exposure to pH_0 = 7.0 water (black squares, data from **Chapter 7**). The black dotted lines show the general trend of the data (not based on regression analysis).

APPENDIX D. CURRICULUM VITAE

Lindsay Grandy

Education

Ph.D Physical Chemistry, Western University, London, ON 2017 – 2021

- Research on the radiation-induced corrosion of copper for use in nuclear fuel disposal under the supervision of Dr. Jungsook Clara Wren.
- Worked with funding partner Nuclear Waste Management Organization (NWMO), who required regular updates and explicit details on how the research was applicable to their project.

B.Sc. Honours Chemistry, Wilfrid Laurier University, Waterloo, ON 2011 – 2015

- Fourth year undergraduate thesis project: "Bulk Studies on the Reaction of Selected Phenols with Soluble and Insoluble Iron" under the supervision of Dr. Hind Al-Abadleh.

Work Experience

Graduate Research Assistant, Western University Jan 2017 – Present

- Developed and carried out various corrosion experiments, including electrochemical and immersion experiments, followed by surface and solution analysis.
- Created research presentations and updates applicable to both academic researchers and industry partners.
- Obtained certificates for: Radiation Safety, Laser Training, and WHIMIS.
- Received advanced training in the operation of the SEM from Western Nanofabrication Facility, Raman Spectroscopy from Surface Science Western, Gamma Irradiation Cell, and Gas Chromatography (GC-MS).

Graduate Teaching Assistant, Western University Jan 2017 – April 2020

- CHEM1301, 1302, 3372.
- Effectively communicated expectations for students to complete their laboratory session and their assessments, while providing constructive feedback on laboratory techniques and written assignments.

- Taught laboratory and course material to support student's learning and provided a safe space for discussions and to ask questions.

Publications

J.C. Wren, A. Jean, M. Naghizadeh, L. Grandy, R. Morco, J.M. Joseph, M. Behazin, and P.G. Keech. (2019) Radiation Induced Corrosion of Copper in Deep Geological Repositories – 19493. *Waste Management 2019 Conference Proceedings*.

S. Slikboer, L. Grandy, S.L. Blair, S.A. Nizkorodov, R.W. Smith, H.A. Al-Abadleh. Formation of Light Absorbing Soluble Secondary Organics and Insoluble Polymeric Particles from the Dark Reaction of Catechol and Guaiacol with Fe(III). *Environ. Sci. Technol.* 2015, 49 (13) 7793–7801.

Conference Presentations

"Determination of Key Elementary Reactions to Develop a Long-Term Copper Corrosion Mechanism" L. Grandy. *Presentation*. National Association of Corrosion Engineers (NACE) National Symposium, Virtual, May 19, 2021.

"Teaching Methodologies in STEM" Panel Presentation, Own Your Future May Conference on Teaching, Virtual, May 1, 2021.

"The Effects of γ-Radiation on Copper Corrosion Dynamics in Stagnant Water." L. Grandy, M. Naghizadeh, J.M. Joseph, G. Whitaker, M. Behazin, P.G. Keech, and J.C. Wren. *Poster*. University Network of Excellence in Nuclear Engineering (UNENE) Conference, Toronto, ON, Dec 16-17, 2019.

"Effects of Radiation on the Progression of Copper Corrosion in Stagnant Pure Water." L. Grandy, M. Naghizadeh, J.M. Joseph, G. Whitaker, M. Behazin, P.G. Keech, and J.C. Wren. *Poster*. Waste Management Symposia, Pheonix, AZ, Mar. 3-7, 2019.

"Effects of Radiation on the Progression of Copper Corrosion in Stagnant Pure Water." L. Grandy, M. Naghizadeh, J.M. Joseph, G. Whitaker, M. Behazin, P.G. Keech, and J.C. Wren. *Poster*. University Network of Excellence in Nuclear Engineering (UNENE) Conference, Toronto, ON, Jan. 14-15, 2019.

"Effects of Radiation on the Progression of Copper Corrosion in Stagnant Pure Water." L. Grandy, M. Naghizadeh, J.M. Joseph, G. Whitaker, M. Behazin, P.G. Keech, and J.C. Wren. *Poster*. Gordon Research Student Conference: Aqueous Corrosion, New London, NH, Jul. 6, 2018.

"Effects of Radiation on the Progression of Copper Corrosion in Stagnant Pure Water." L. Grandy, J.M. Joseph, G. Whitaker, M. Behazin, P.G. Keech, J.C. Wren. *Oral*. National Association of Corrosion Engineers (NACE) Southern Ontario Student Section Conference, Toronto, ON, Jul. 26, 2018.

"Radiolytic Corrosion of Copper in Small Water Droplets." L. Grandy, A.M. Jean, J.M. Joseph, G. Whitaker, M. Behazin, P.G. Keech, and J.C. Wren. *Poster*. Nuclear Waste Management Organization (NWMO) Facility Tour, Toronto, ON, Feb. 22, 2018.

"Kinetic Study of Gamma-Radiation on Copper Corrosion under Droplets and Humid Air." L. Grandy, J.M. Joseph, J.C. Wren. *Oral*. Electrochemical Society Western Student Chapter Conference, London, ON, Dec. 15, 2017.

"Radiolytic Corrosion of Copper in Small Water Droplets." L. Grandy, A.M. Jean, J.M. Joseph, G. Whitaker, M. Behazin, P.G. Keech, and J.C. Wren. *Poster*. University Network of Excellence in Nuclear Engineering (UNENE) Conference, Toronto, ON, Dec. 11, 2017.

Awards & Certificates

Queen Elizabeth II Graduate Scholarship in Science and Technology (QEII-GSST), Government of Ontario 2019 – 2021

- Two-year recipient of research merit-based scholarship for Ph.D. research in STEM, where $15,000/ year was awarded.

Western Certificate in University Teaching and Learning, Western University

- Certificate is awarded after five components, including specific courses and written components, are completed, and is designed to prepare graduate students for faculty positions.

Executive Committees

President, Chemistry Graduate Student Association (CGSA) Sept 2020 – Aug 2021

- Led VPs to complete the CGSA mission of connecting chemistry graduate students to each other through academic and social events.
  - Previous events include biweekly trivia nights, snow tubing, scholarship presentation (presented by me), finances in graduate school presentation, graduate student advice panel, and NSERC scholarship drop-in sessions.
- Organized and led meetings between myself and the five VPs, discussing events, policy documents, finances, and communications.

Executive Member, Electrochemical Society Western University Chapter
Oct 2018 – Feb 2021

- Organized and hosted events for general members.
  - Previous events include fundamentals and applications of electrochemistry workshop (presented by Dr. James Noël), fundamentals and applications of X-ray Photoelectron Spectroscopy (presented by Dr. Mark Biesinger), and the 4th Annual ECS Western Student Chapter Symposium with keynote speakers Dr. Yolanda Hedberg and Dr. Jeffrey Dahn.
- Took meeting minutes during executive meetings and distributed tasks amongst executive members to ensure events run smoothly.
- Communicated with general members through social media and emails.

Graduate Student Representative, Graduate Education Committee Sept 2019 – Aug 2020

- Represented the chemistry graduate students at meetings for the development and implementation of updated or new educational policy for chemistry graduate students.
- Responsible for developing policy documents, such as the agreement for joint students in the international study abroad 2+2 program, academic standards within the department, such as those for yearly reports, and departmental funding decisions, especially during the 2020 lockdown.

Instrument Training

- Gamma Irradiation Cell.
- Scanning Electron Microscopy.
- Raman Spectroscopy.
- Gas Chromatography (GC-MS).
- Ultraviolet-Visible Spectroscopy.
- Fourier Transform Infrared Spectroscopy.

Software Experience

- COMSOL Multiphysics, for simulating chemical systems.
- DaVinci Resolve, for creating and editing videos.
- OriginLab, for advanced graphing and data analysis.
- OWL, Western University's online course portal.
- Zoom.
- MS Office.

Volunteer Work

- Mentor for the HARK After-School Program by Investing in Children.
    - Free program for students in grade 6 – 8 to encourage healthy eating, active living, and overall personal wellness.
- Volunteer at Science Rendezvous.
    - Annual festival to promote science within the community, where the chemistry department organized a table to showcase chemical concepts.
- Supervision of completion of labs for high school students.
    - Western University's chemistry department allowed high school science and chemistry classes to use our facilities to complete a first-year lab with our guidance to promote our community and science.
- Judge at Science Fairs: Thames Valley Science & Engineering Fair, Bluewater Regional Science and Technology Fair.
    - Youth science fairs encourage young students to engage in science, while obtaining meaningful guidance and support from judge.